Numerical Modelling of Impact Crater Formation: Material Excavation and Interaction between Ejecta and Atmosphere

Dissertation

zur Erlangung des akademischen Grades
doctor rerum naturalium
(Dr. rer. nat.)

eingereicht von

Robert Luther

Freie Universität Berlin
Fachbereich Geowissenschaften
Institut für Geologische Wissenschaften
Fachrichtung Geophysik

2019

Erster Gutachter (FU):	Prof. Dr. Kai Wünnemann
Zweiter Gutachter (FU):	Prof. Dr. Lena Noack
Tag der Disputation:	12.06.2019

Zusammenfassung

Von großen planetaren Einschlägen bis hinunter zu kleinsten Impakten auf Asteroiden laufen ähnliche Prozesse ab, deren Verständnis bedeutsam für zahlreiche darauf aufbauende Fragestellungen ist. In dieser Dissertation liegt der Fokus auf einem Teilaspekt der Kraterbildung – dem Materialauswurf. Kraterauswurfdecken sind typische Merkmale der allermeisten Krater im Sonnensystem. Zwar ist der eigentliche Prozess der zum Auswurf des Materials führt verstanden, aber eine systematische Untersuchung der Abhängigkeit der Auswurfcharakteristika (wie z.B. Geschwindigkeit oder Auswurfwinkel) von Materialeigenschaften ist noch nicht erfolgt. Ebenso fehlt eine systematische Untersuchung des Verhaltens des Auswurfmaterials in einem gasförmigen Medium. In dieser Dissertation greife ich auf numerische Methoden zurück, um Einschlagsprozesse zu simulieren. Das hierfür genutzte und von mir erweiterte Stoßwellensimulationsprogramm *iSALE* ist in der Fachliteratur etabliert und gut beschrieben. Insbesondere gehe ich auf die vorhandenen Festigkeitsparametrisierungen und das Porositätskompaktionsmodell ein, da sie für die folgenden systematischen Untersuchungen der Auswurfmassen grundlegend sind. Das Porositätskompaktionsmodell wird in einer Studie angewandt, um die Verdichtung von hochporösem Schnee unter Beaufschlagung durch ein Meteoritenfragment zu quantifizieren. In diesem Extremfall wird nahezu kein Material ausgeworfen. Das Festigkeitsmodell zur Beschreibung von Festgestein wird zur Simulation der Kraterbildung in Quarzit und Marmor eingesetzt, um die für die Materialexkavation relevanten Festigkeitsmodelle anhand von Laborvergleichen zu validieren. Eine auffallende Besonderheit des Marmors ist, dass er im Vergleich zu der erwarteten Kratergröße gemäß der einaxialen Druckfestigkeit (UCS) deutlich kleinere Krater aufweist. Der Effekt der dynamischen Verhärtung wird mit dem Festigkeitsmodell angenähert, um die experimentellen Krater nachzustellen. Auf den Materialmodellen aufbauend erfolgt die systematische Untersuchung des Verhaltens der Auswurfmassen, wobei hier erneut Labordaten experimenteller Krater zur Validierung herangezogen

werden. Abhängig von verschiedenen Porositäten und Reibungskoeffizienten einer Parametrisierung der Festigkeit als Funktion des Druckes werden die Auswurfcharakteristika beschrieben und genutzt, um materialabhängige Auswurfdecken im Vakuum zu beschreiben. Außerdem werden analytische Skalierungsgesetze angewandt, um die entsprechenden Parameter basierend auf den Modelldaten zu bestimmen. Im folgenden Schritt wird dann die Wechselwirkung von Auswurfmaterial und einer vorhandenen Atmosphäre erläutert. Atmosphärische Effekte beeinflussen die ballistische Reichweite des ausgeworfenen Materials. Diese sind stark größenabhängig und die Reichweite nimmt mit kleiner werdenden Staubkorngrößen ab. In Bezug auf die Kratergröße nimmt die Reichweite ebenfalls ab, wenn die Kratergröße zunimmt. Zur Simulation und Beschreibung dieser Abhängigkeiten wurde ein neues Unterprogramm implementiert, in *iSALE* integriert und für eine systematische Parameterstudie herangezogen. Die Ergebnisse dieser Studie werden in dieser Arbeit dargestellt.

Abstract

From large planetary impacts down to the smallest impacts on asteroids, similar processes take place, and understanding them is relevant for numerous further questions. In this thesis, I focus on one of the sub-aspects of crater formation, namely material ejection, as ejecta blankets are typical features of most craters in the solar system. Even though the basic process of ejection is understood, a systematic study on the correlation between ejection characteristics (e.g. ejection speed and angle) and material properties is still missing. Likewise, a systematic study on the behaviour of ejected material in a gaseous medium is lacking. In this thesis, I use a numerical approach to simulate impact processes. The used shock physics code *iSALE*, to which I added new features, is established in the literature and well described. Specifically, I focus on the strength models and the porosity-compaction model because the following systematic study of material ejection builds upon these models. The porosity-compaction model

is applied in a study to quantify the compaction of highly porous snow after being impacted by meteorite fragments. In this end-member scenario, nearly no material is ejected. The strength model that is used for the representation of competent rock is applied to simulate craters in quartzite and marble in order to validate these rheology models, which are highly relevant for simulating excavation flow, against laboratory results. A striking characteristic observed for craters in marble is the smaller crater size compared to the expected crater size based on the uniaxial compressive strength (UCS) of marble. Here, I approximate the dynamic hardening of the marble target with the strength model of competent rock in order to reproduce the observed experimental craters. Based on these material models, I conduct a systematic parameter study on the behaviour of ejected material, which I again validate against laboratory data from experimental craters. Depending on material properties like porosity or the coefficient of friction for a parametrisation of the yield surface as function of pressure, the ejection characteristics are described and applied to derive the ejecta deposit in a vacuum case. In addition, analytical scaling relationships are fitted to the derived model data in order to obtain the corresponding parameters. In a next step, I explore the interaction of ejected material with an atmosphere. Atmospheric effects influence the ballistic range of the ejected material, and these effects are strongly size dependent, such that the range decreases with decreasing dust particle size. Further, relative to the crater size, the range decreases with increasing crater size. For the simulation and description of these correlations, a separate subroutine was written, integrated into *iSALE*, and applied for a systematic parameter study. The results of this study are presented in this thesis.

Erklärung zur Beteiligungen an Publikationen

Diese Dissertation wurde in meiner Zeit als Promovend und wissenschaftlicher Mitarbeiter am Museum für Naturkunde zu Berlin im Rahmen der zweiten Phase der DFG Forschergruppe *Multidisciplinary Experimental and Modeling Impact Crater Research Network* (MEMIN II) durchgeführt. Hierin war ich im Teilprojekt IX *Numerical modeling of impact cratering processes* angestellt. Die Finanzierung erfolgte durch die Deutsche Forschungsgemeinschaft: DFG Projekt WU 355/6-2. Darüber hinaus war ich zeitweise im Sonderforschungsbereich TRR170 *Late Accretion onto Terrestrial Planets* im Teilprojekt A4 angestellt und wurde außerdem durch die DAAD Förderung 57159947 unterstützt.

Diese Dissertation wurde kumulativ erstellt und beinhaltet mehrere Publikationen, die sich einer gemeinsamen Fragestellung widmen, welche in Kapitel 1 erläutert wird. Die Kapitel 6, 7, und 8 stehen jeweils für eigenständige veröffentlichte und wissenschaftlich begutachtete Publikationen. Kapitel 9 ist ebenfalls eine eigenständige Publikation und wurde vor kurzem bei einem wissenschaftlichen Journal zur Veröffentlichung akzeptiert. Der Promovend ist Erstautor der Publikationen der Kapitel 7, 8 und 9; und Zweitautor der Publikation des Kapitels 6. Die Referenzen wurden dabei am Ende der Dissertation in einer Liste zusammengefasst. Die Kapitel 1 (Einleitung), 2 (Hintergrund), 3 (Methodik), 4 (Beschreibung von Auswurfmaterial) und 5 (Validierung und Auflösung) wurden von mir als übergeordneten Rahmen der Promotionsschrift erstellt, um in die Thematik einzuführen, Hintergrundwissen bereitzustellen, welches nicht in den Publikationen genannt wird und um die wissenschaftlichen Fragestellungen zu formulieren. Kapitel 10 (Diskussion/Fazit) wurde ebenfalls von mir verfasst und bietet neben einer Ergebniszusammenfassung einen Ausblick auf weiterführende Forschungsrichtungen.

Im Folgenden werden die einzelnen Publikationen, auf denen diese Promotionsschrift aufbaut genannt und mein Anteil daran erläutert.

Publikationen in wissenschaftlichen Journalen aus dieser Dissertation:

Kapitel 6: Winkler R., **Luther R.**, Poelchau M. H., Wünnemann K., Kenkmann T., *Surface deformation of experimental hypervelocity impacts in quartzite and marble targets*, Meteoritics & Planetary Science, Band 53, Nr. 8 (Sonderband MEMIN), S. 1733-1755.

Diese Studie basiert auf einer Schusskampagne in Freiburg, an der sich alle Autoren in der Vor- oder Nachbereitung sowie Durchführung beteiligten. Die komplette Auswertung der Versuche (Mikroanalyse der Gesteinsproben, Auswertung der Krater) erfolgte durch R. Winkler in Freiburg. Der Promovend hat die komplette Modellierung und Modellauswertung durchgeführt. Der Text wurde abgesehen von den Passagen, die die numerischen Simulationen betreffen und vom Promovenden geschrieben wurden, vornehmlich von R. Winkler formuliert. M. Poelchau hat den transienten Krater im Quarzitgestein abgeschätzt, welcher wichtig für den Vergleich der experimentellen und numerischen Ergebnisse ist. Darauf aufbauend konnten R. Winkler und der Promovend die Schädigungen im Zielgestein aus den Experimenten mit physikalischen Größen aus den Modellierungen verknüpfen und die Ergebnisse mit den anderen Autoren diskutieren.

Kapitel 7: **Luther R.**, Artemieva N., Ivanova M., Lorenz C., Wünnemann K. (2017), *Snow carrots after the Chelyabinsk event and model implications for highly porous Solar System objects*, Meteoritics & Planetary Science, Band 52, Nr. 5, S. 979-999.

Der Promovend hat die Berechnung der numerischen Modelle zur Kraterbildung sowie deren Auswertung durchgeführt. Er hat zudem den größten Teil des Textes formuliert und die Modelle mit den Beobachtungen der Feldkampagne verknüpft. Die Feldkampagne wurde von M. Ivanova und C. Lorenz durchgeführt. Der Atmosphäreneintritt der Fragmente wurde von N. A. Artemieva simuliert. Der Promovend hat des Weiteren eine auf den Modellergebnissen aufbauende analytische Lösung für die Röhrenbildung im Schnee für andere Fragmentgrößen aufgestellt und den postimpaktalen Prozess dargestellt.

Kapitel 8: **Luther R.**, Zhu M.-H., Collins G. S., Wünnemann K., *The effect of Target Properties on Ejection Dynamics and Ejecta Deposition*, Meteoritics & Planetary Science, Band 53, Nr. 8 (Sonderband MEMIN), S. 1705-1732.

Der Promovend hat die Berechnung der numerischen Modelle zur Kraterbildung sowie deren Auswertung durchgeführt. Der Ansatz der Auswurfmassenanalyse basiert auf der Idee von M.-H. Zhu und wurde vom Promovenden um ein Höhenkriterium erweitert. Der Promovend hat die Funktionsanpassung an die Modelldaten für Kraterskalierungsgesetzte durchgeführt. K. Wünnemann und G. Collins haben den Text sprachlich korrigiert.

Kapitel 9: **Luther R.**, Artemieva N., Wünnemann K., *The Effect of Atmospheric Interaction on Impact Ejecta Dynamics and Deposition*, ICARUS, Band 333, S. 71-86.

Der Promovend hat die Berechnung der numerischen Modelle zur Kraterbildung sowie deren Auswertung durchgeführt. Der Promovend hat das den Ergebnissen des Kapitels zugrundeliegende Programm über die gesamte Dauer der Promotion selbst geschrieben und kontinuierlich verfeinert. Dabei wurde er von N. Artemieva in den Bereichen unterstützt, die die repräsentativen Partikel betreffen. K. Wünnemann hat die Anbindung an das Programm *iSALE* begleitet. Das Kapitel wurde vom Promovenden selbst verfasst.

Über die in dieser Arbeit abgedruckten Kapitel hinaus entstanden weitere Arbeiten. Sind diese in der vorgelegten Arbeit referenziert, so werden sie fett hervorgehoben. Folgende Liste fasst diese Publikationen in wissenschaftlichen Journalen zusammen:

<u>Publikationen in wissenschaftlichen Journalen mit Bezug zu dieser Dissertation:</u>

Raducan S., Collins G., **Luther R.**, Davison T., *The Role of Asteroid Strength, Porosity and Internal Friction in Impact Momentum Transfer*, Icarus (eingereicht).

Wilk J., Hamann C., Fazio A., **Luther R.**, Hecht L., Langenhorst F., Kenkmann T. (2018), *Melt Formation on Shatter Cones Recovered from the MEMIN Impact*

Experiments in Sandstone, Meteoritics & Planetary Science, Band 53, Nr. 8 (Sonderband MEMIN), S. 1569-1593.

Kenkmann T., Deutsch A., Thoma K., Ebert M., Poelchau M. H., Buhl E., Carl E., Danilewsky A. N., Dresen G., Dufresne A., Durr N., Ehm L., Große C. U., Gulde M., Güldemeister N., Hecht L., Hiermaier S., Hoerth T., Hamann C., Kowitz A., Langenhorst F., Lexow B., Liermann H., **Luther R.**, Mansfeld U., Moser D., Raith M., Reimold W. U., Sauer M., Schäfer F., Schmitt R. T., Sommer F., Wilk J., Winkler R., Wünnemann K. (2018), *Experimental impact cratering: A summary of the major results of the MEMIN research unit*, Meteoritics & Planetary Science, Band 53, Nr. 8 (Sonderband MEMIN), S. 1543-1568.

Prieur N. C., Rolf T., **Luther R.**, Wünnemann K., Xiao Z., Werner S. C. (2017), *The effect of target properties on transient crater scaling for simple craters*, Journal of Geophysical Research: Planets, Band 122, S. 1704-1726.

Ebert M., Hecht L., Hamann C., **Luther R.** (2017), *Laser-induced melting experiments: Simulation of short-term high-temperature impact processes*, Meteoritics & Planetary Science, Band 52, Nr. 7, S. 1475-1494.

Hamann C., **Luther R.**, Ebert M.., Hecht L., Deutsch A., Wünnemann K., Schäffer S., Osterholz J., Lexow B. (2016), *Correlating laser-generated melts with impact-generated melts: An integrated thermodynamic-petrologic approach*, Geophysical Research Letters, Band 43, Nr. 20, S. 10,602-10,610.

Statement of Contributions

This doctoral thesis was written during my time as doctoral student and scientific assistant within the DFG research group *Multidisciplinary Experimental and Modeling Impact Crater Research Network* (MEMIN II) at the Museum für Naturkunde in Berlin. I was employed in the sub project IX *Numerical modeling of impact cratering processes*. The project was funded under DFG grant number WU 355/6-2. In addition, I received funding through sub-project A4 of the research project TRR170 *Late Accretion onto Terrestrial Planets*, and I was supported by the DAAD grant 57159947.

This thesis is presented in a cumulative form and includes several publications that address a common scientific interest, as stated in chapter 1. Chapter 6 to 8 are each articles that are published in peer-reviewed journals. Chapter 9 is a manuscript for an article that has recently been accepted for

publication. I am the first author of the publications in chapters 7, 8, and 9; I am the first co-author of the publication in chapter 6. All references from the individual publications are given at the end of this thesis. The chapters 1 (introduction), 2 (background), 3 (method), 4 (treatment of ejecta) and 5 (validation and resolution) were written by me to frame the individual publications presented in the thesis, to introduce the topic, to give further information that is not included in the publications, and to raise the main scientific questions the thesis addresses. Chapter 10 (discussion and conclusion) was written by me to sum up the results of the individual chapters and to point toward further directions of study based on the content of the previous chapters.

In the following, I list the publications on which this thesis is based and describe my contribution to each.

Publications in scientific journals from this thesis:

Chapter 6: Winkler R., **Luther R.**, Poelchau M. H., Wünnemann K., Kenkmann T., *Surface deformation of experimental hypervelocity impacts in quartzite and marble targets*, Meteoritics & Planetary Science, Volume 53, Issue 8 (Special Issue MEMIN), pp. 1733-1755.

This study is based on a shooting campaign in Freiburg to which all authors contributed to the preparation of the campaign or participated in conducting the experiment. The complete analysis of the experiments (micro-analysis of rock samples, analysis of the crater) was done by R. Winkler in Freiburg. I modelled the experiment and analysed the models. The text was mainly written by R. Winkler, apart from the text passages about numerical modelling, which I wrote. M. Poelchau estimated the size of the transient crater in the quartzite target, which is important for the comparison of experimental and numerical results. Based on this comparison, R. Winkler and I were able to correlate subsurface deformations in the target rock from the experiments with the physical properties taken from the numerical models, and we discussed these results with the other authors.

Chapter 7: **Luther R.**, Artemieva N., Ivanova M., Lorenz C., Wünnemann K. (2017), *Snow carrots after the Chelyabinsk event and model implications for highly porous Solar System objects*, Meteoritics & Planetary Science, Volume 52, Issue 5, pp. 979-999.

I modelled the crater formation and analysed the models. I also wrote the majority of the text and correlated field observations with modelling results. The field campaign was organised by M. Ivanova and C. Lorenz. The atmospheric entry of the fragments was modelled by N. Artemieva. I developed an analytical solution for the funnel formation in snow of fragments of different sizes, and I described the post-impact process.

Chapter 8: **Luther R.**, Zhu M.-H., Collins G. S., Wünnemann K., *The effect of Target Properties on Ejection Dynamics and Ejecta Deposition*, Meteoritics & Planetary Science, Volume 53, Issue 8 (Special Issue MEMIN), pp. 1705-1732.

I modelled the crater formation and analysed the models. The approach for analysing the ejecta was based on an idea from M.-H. Zhu, and I expanded it by adding an altitude criterion. I fitted the crater scaling relationships to the model data. K. Wünnemann and G. Collins refined the text language-wise.

Chapter 9: **Luther R.**, Artemieva N., Wünnemann K., *The Effect of Atmospheric Interaction on Impact Ejecta Dynamics and Deposition*, ICARUS, Volume 333, pp. 71-86.

I modelled the crater formation and analysed the models. I also developed the programme (throughout all of my thesis work) on which the results of this chapter are based, and, thereby, I continuously improved the code. For the part on representative particles, I was supported by N. Artemieva. Also, K. Wünnemann supervised the coupling of the new programme to *iSALE*. I also wrote the chapter.

Besides the presented publications, additional articles have been published with relation to this thesis. When these publications are

referenced within the thesis, the reference is marked in bold letters. The following list summarises these publications in scientific journals:

Publications in scientific journals related to this thesis:

Raducan S., Collins G., **Luther R.**, Davison T., *The Role of Asteroid Strength, Porosity and Internal Friction in Impact Momentum Transfer*, Icarus (submitted).

Wilk J., Hamann C., Fazio A., **Luther R.**, Hecht L., Langenhorst F., Kenkmann T. (2018), *Melt Formation on Shatter Cones Recovered from the MEMIN Impact Experiments in Sandstone*, Meteoritics & Planetary Science, Volume 53, Issue 8 (Special Issue MEMIN), pp. 1569-1593.

Kenkmann T., Deutsch A., Thoma K., Ebert M., Poelchau M. H., Buhl E., Carl E., Danilewsky A. N., Dresen G., Dufresne A., Durr N., Ehm L., Große C. U., Gulde M., Güldemeister N., Hecht L., Hiermaier S., Hoerth T., Hamann C., Kowitz A., Langenhorst F., Lexow B., Liermann H., **Luther R.**, Mansfeld U., Moser D., Raith M., Reimold W. U., Sauer M., Schäfer F., Schmitt R. T., Sommer F., Wilk J., Winkler R., Wünnemann K. (2018), *Experimental impact cratering: A summary of the major results of the MEMIN research unit*, Meteoritics & Planetary Science, Volume 53, Issue 8 (Special Issue MEMIN), pp. 1543-1568.

Prieur N. C., Rolf T., **Luther R.**, Wünnemann K., Xiao Z., Werner S. C. (2017), *The effect of target properties on transient crater scaling for simple craters*, Journal of Geophysical Research: Planets, Volume 122, pp. 1704-1726.

Ebert M., Hecht L., Hamann C., **Luther R.** (2017), *Laser-induced melting experiments: Simulation of short-term high-temperature impact processes*, Meteoritics & Planetary Science, Volume 52, Issue 7, pp. 1475-1494.

Hamann C., **Luther R.**, Ebert M.., Hecht L., Deutsch A., Wünnemann K., Schäffer S., Osterholz J., Lexow B. (2016), *Correlating laser-generated melts with impact-generated melts: An integrated thermodynamic-petrologic approach*, Geophysical Research Letters, Volume 43, Issue 20, pp. 10,602-10,610.

Contents

Numerical Modelling of Impact Crater Formation: Material Excavation and Interaction between Ejecta and Atmosphere i

Zusammenfassung i

Abstract ii

Erklärung zur Beteiligungen an Publikationen iv

Statement of Contributions vii

List of Figures xvi

List of Tables xxi

Notations xxii

1 Introduction 1

1.1 Setting the Stage 1

1.2 Objectives and Goals 5

1.3 The Multidisciplinary Experimental and Modeling Impact Crater Research Network (MEMIN) 7

1.4 Structure of the Thesis 10

2 Background 13

2.1 Mechanics of Impact Cratering 13

2.1.1 Contact- and Compression Stage 13

2.1.2 Excavation Stage 16

2.1.3 Modification Stage 18

2.2 Atmospheric Traverse of the Impactor 19

2.3 Ejecta Plume 20

3 Methodology 21

3.1 Numerical Approach 21

3.2 iSALE 2D 24

3.2.1 Spatial and Temporal Discretisation 25

3.2.2 Equation of Motion 27

3.2.3 Rheology Model 29

3.2.4 Equation of State 32

3.2.5 Porosity-Compaction Model 36

4 Treatment of Ejecta in iSALE 41

4.1 Continuum Assumption *41*
4.2 Tracer *42*
4.3 Representative Particles *45*
5 Validation and Resolution Tests 53
6 Subsurface deformation of experimental hypervelocity impacts in quartzite and marble targets 65
6.1 Abstract *66*
6.2 Introduction *67*
6.3 Methods *69*
6.3.1 Target materials 69
6.3.2 Experimental Setup 69
6.3.3 Sample preparation and image acquisition 71
6.3.4 Porosity determination and deformation mapping 71
6.3.5 Numerical Modelling 72
6.4 Results *73*
6.4.1 Crater morphology 73
6.4.2 Porosity 75
6.4.3 Grain size analysis 77
6.4.4 Deformation microstructures 79
6.4.5 Numerical modelling 83
6.5 Discussion *87*
6.5.1 Deformation microstructures 87
6.5.2 Cratering efficiency 96
6.5.3 Experiment-Model Comparison 97
6.6 Conclusions *101*
6.7 Acknowledgements *103*
6.8 Appendix *103*
6.8.1 Determination of pre – and post-impact porosity 103
6.8.2 Grain size distribution 104
6.8.3 Different deformation micro-features 104
6.8.4 Orientation analysis of these micro-features 105
6.8.5 Numerical modelling 105
6.8.6 Parametrization table of the models 110

7 Snow carrots after the Chelyabinsk event and model implications for highly porous Solar System objects 111
7.1 Abstract *111*
7.2 Introduction *113*
7.3 Recovery of meteorites in the field *114*
7.4 Methods in use and Initial Conditions *117*
7.4.1 Atmospheric entry model 117
7.4.2 Heat transfer with mass loss 119
7.4.3 Impact into snow: numerical model 120
7.4.4 Impact into snow: analytical model 122
7.5 Results *123*
7.5.1 Atmospheric entry dynamics 123
7.5.2 Heating and cooling during the entry 124
7.5.3 Snow Penetration 127
7.5.3.1 Best fit model 127
7.5.3.2 Influence of strength parameters on a funnel depth 129
7.5.3.3 Funnel walls 131
7.6 Discussion *134*
7.6.1 Sensitivity to input parameters 134
7.6.2 Analytical solutions for smaller and larger fragments 136
7.6.3 Tagish Lake Meteorite Fall 137
7.6.4 Post-Impact Processes 138
7.6.5 Applications to other impacts in the Solar System 141
7.7 Conclusions *144*
7.8 Acknowledgements *146*
7.9 Appendix *146*
7.9.1 Details on the ε-α porosity compaction model 146
7.9.2 Numerical resolution and artefacts 148
7.9.3 Model Parameters 150
8 The Effect of Target Properties on Ejection Dynamics and Ejecta Deposition 151
8.1 Abstract *152*
8.2 Introduction *153*

8.3 Theoretical Background *155*
8.4 Methods *161*
8.5 Comparison to experimental data and scaling models *166*
8.6 Results *169*
8.6.1 Coefficient of friction 169
8.6.2 Porosity 171
8.6.3 Cohesion 173
8.6.4 Effects of impact velocity 175
8.7 Discussion *177*
8.7.1 Effects of different impact velocities for constant crater size 177
8.7.2 Target properties and excavation flow 180
8.7.3 Implications for ejecta scaling 183
8.7.4 Ejecta deposits 186
8.7.5 Ejecta deposits at natural impact craters 193
8.8 Conclusion *196*
8.9 Acknowledgements *198*
8.10 Appendix *198*
8.10.1 Ejection criterion 198
8.10.2 Resolution 200
8.10.3 Model Parameters 201
8.10.4 Unprocessed model launch angles 202
8.10.5 Model Results - Overview 203
9 The Effect of Atmospheric Interaction on Impact Ejecta Dynamics and Deposition 205
9.1 Abstract *206*
9.2 Introduction *207*
9.3 Methods and Useful Analytical Solutions *210*
9.3.1 Analytical solutions 211
9.3.1.1 Sedimentation and free fall 211
9.3.1.2 Scaling of ejecta 212
9.4 Verification, Validation, and Benchmarks *213*

9.4.1 Sedimentation of individual particles in undisturbed atmosphere. ... 213
9.4.2 Settling of dust-laden layers ... 214
9.4.2.1 Different Regimes of Settling ... 217
9.5 Motion of ejecta curtains through the atmosphere ... 221
9.5.1 Curtain Evolution ... 221
9.5.2 Thickness of deposited Ejecta ... 223
9.5.3 Deposition Velocity of Ejecta ... 226
9.5.4 Ballistic Range ... 227
9.5.5 Crater Fall Back ... 228
9.5.6 Influence of different particle sizes ... 229
9.6 Laboratory Scale Impacts ... 232
9.6.1 Thickness of deposited Ejecta ... 234
9.6.2 Ejecta curtain angle ... 236
9.7 Discussion and Perspectives ... 239
9.8 Conclusions ... 242
9.9 Acknowledgements ... 243
9.10 Appendix ... 244
9.10.1 Model Parameters ... 244
10 Discussion and Conclusion ... 245
10.1 Objectives & Key Questions ... 245
10.2 Discussion and Limitations ... 252
10.3 Conclusions & Outlook ... 259
11 Bibliography ... 265
12 Appendix ... 291
12.1 Publications at scientific conferences and workshops related to this thesis ... 291
Eidesstattliche Erklärung ... 295
Lebenslauf ... 297
Danksagung ... 299

List of Figures

Figure 1-1: Map of Earth's craters on the Earth Impact Database as of November 2017. 4
Figure 1-2: The MEMIN research network. 9
Figure 2-1: Cratering process in three stages. 15
Figure 2-2: Pressure-volume relationship for a hypothetical silicate that undergoes shock-induced phase changes. 16
Figure 3-1: Example of the Lagrangian formulation (a, grid moves with material flow), the Eulerian formulation (b, static grid), and of the Smoothed Particle formulation (c, SPH – mesh free) to describe the motion of material in fluid dynamic computations. 22
Figure 3-2: Cylindrical mesh geometry in iSALE. 27
Figure 3-3: Yield strength of the two materials. 32
Figure 3-4: Pore compaction versus volumetric strain 39
Figure 4-1: Impact of a 16-m radius projectile with 12 km/s after 0.32 s. 42
Figure 4-2: Sketch of ejecta motion in a vacuum. 44
Figure 4-3: Cumulative particle size-frequency distribution. 51
Figure 5-1: Representative particle motion. Panel 56
Figure 5-2: Material settling (determined with iSALE) 58
Figure 5-3: Effect of resolution on material settling (determined with iSALE) 58
Figure 5-4: Material settling under four grid resolutions for 5 km: 10, 50, 100, and 500 cells (determined with iSALE). 60
Figure 5-5: Material settling for two resolutions regarding the number of representative particles: 100, and 10000. 62
Figure 6-1: Marble and quartzite craters. 74
Figure 6-2: Subsurface damage mapping 76
Figure 6-3: Development of the grain size frequency density with increasing depth beneath crater floor (given in projectile diameters; 1 d_p = 2.5 mm) of the marble (a) and the quartzite (b) experiment. 78

Figure 6-4: Examples of tensile fractures (dotted arrows), intra-granular cracks (solid-line arrows) and grain boundaries (dashed arrows) in a) marble and b) quartzite. 79
Figure 6-5: Photomicrographs and SEM images of the marble target subsurface. 81
Figure 6-6: Comparison of the 18 measured crater profiles from the experiment (grey lines) and the numerical crater profile (black line) 84
Figure 6-7: Total plastic strain distribution during the crater formation. 85
Figure 6-8: Pressure isobars within the quartzite (left half) and marble (right half) target. 86
Figure 6-9: Sketch of impact-generated deformation features 92
Figure 6-10: Yield strength of the two materials. 108
Figure 7-1: “Snow carrots”. 115
Figure 7-2: Fragment velocities (i) and masses (ii) as a function of altitude. 124
Figure 7-3: Heating of meteoroids of various masses (same as in Figure 7-2) in the vapor cloud after the end of ablation. 125
Figure 7-4: Comparison of the free-fall time (solid line) with the cooling time as a function of meteorite mass for various temperature profiles..... 126
Figure 7-5: Snapshots of the funnel formation. 128
Figure 7-6: Fragment deceleration (i) and funnel depth evolution (ii). 129
Figure 7-7: Influence of snow rheology on funnel depth. 131
Figure 7-8: Density profiles for four different models at different times that correspond to the same depth relative to the final depth 133
Figure 7-9: Snapshot of a fragment at its final depth in a snow target with a cohesion of 100 kPa. 138
Figure 7-10: Post-impact filling of snow funnels due to thermal transpiration. 141
Figure 7-11: Snapshots of larger scale funnel formation..... 144
Figure 7-12: Pore compaction versus volumetric strain 147
Figure 7-13: Resolution study. 148
Figure 7-14: Funnel depth evolution for a 2D and a 3D model..... 149
Figure 8-1: Excavation and material displacement. 157

Figure 8-2: Ejection behaviour 167
Figure 8-3: Launch velocity (i, iii) and launch angle (ii, iv) versus launch positions on the target surface. 171
Figure 8-4: Launch velocity (i) and the launch angle (ii) versus launch positions on the target surface. 172
Figure 8-5: Launch velocity (i) and the launch angle (ii) versus launch positions on the target surface. 173
Figure 8-6: Ejection velocity for the same cases as shown in Figure 8-3 - Figure 8-5 ((i)-(iv), respectively).....175
Figure 8-7: Absolute launch velocity (i) and the launch angle (ii) versus absolute launch positions on the target surface for different impact velocities. 176
Figure 8-8: Ejection velocity and angle for the same cases as shown in Figure 8-7. 180
Figure 8-9: Peak pressure contours and gradients for two different coefficients of friction. 182
Figure 8-10: Peak pressure contours for three different materials. 183
Figure 8-11: Ejecta velocity fitting results. 186
Figure 8-12: Distribution of the ejecta thickness for different target properties. 188
Figure 8-13: Ejecta deposit fitting results.....190
Figure 8-14: Distribution of the ejecta thickness for a nonporous, cohesionless target with different impact velocities. 191
Figure 8-15: Crater and ejected mass for the cases of different impact velocities. 192
Figure 8-16: Ejecta deposit fitting results.....193
Figure 8-17: Launch angles (i) and mass weighted averages of launch angles (ii) for different ejection criteria. 199
Figure 8-18: Launch velocity (i) and the launch angle (ii) versus launch positions on the target surface. 200
Figure 8-19: Unprocessed model launch angles for all scenarios from this study. 202

Figure 9-1: Sedimentation velocities for particles of different sizes as a function of altitude..... 214
Figure 9-2: Model (iSALE) snapshots showing settling of a dusty layer in atmosphere..... 215
Figure 9-3: Deceleration of an individual particle (i) and surrounding gas velocity (ii)..... 216
Figure 9-4: Normalised horizontal velocities versus normalized vertical velocities of particle..... 218
Figure 9-5: Three Regimes of settling..... 219
Figure 9-6: Deposition thickness (determined with iSALE) of material with r_{dust} = 100 μm..... 220
Figure 9-7: Formation of the ejecta curtain during 4-km-diameter crater formation (simulated with iSALE)..... 222
Figure 9-8: Ejecta curtain evolution from 20s to 120 s (simulated with iSALE)..... 223
Figure 9-9: Ejecta deposits for a 4-km-radius transient cavity and two particle sizes..... 225
Figure 9-10: Normalised total deposition velocities (determined with iSALE) for a crater with R = 200m..... 227
Figure 9-11: Ballistic range of ejecta deposition..... 228
Figure 9-12: Average crater fall back for our simulated crater sizes from 200 m – 4 km (determined with iSALE)..... 229
Figure 9-13: Ejecta curtain for a 1 km sized crater after 5, 20 and 40 s (simulated with iSALE)..... 231
Figure 9-14: Ejecta deposits (determined with iSALE) for a 1-km-radius transient cavity and five particle sizes..... 232
Figure 9-15: Laboratory-scale ejecta curtains (simulated with iSALE)..... 233
Figure 9-16: Ejecta deposits from numerical simulations for a target chamber pressure of 1 kPa and 100 kPa (determined with iSALE)..... 235
Figure 9-17: Normalised (to parabolic deposition) ejecta deposits from numerical simulations with iSALE for a target chamber pressure of 6 MPa 235

Figure 9-18: Evolution of angle of ejecta curtain for different chamber pressures 238
Figure 9-19: Ejecta deposits (determined with iSALE) as in Figure 9-14. 242
Figure 10-1: Representation of momentum multiplication factor. 260

List of Tables

Table 6-1**:** Overview of target and experimental parameters 70
Table 6-2**:** Overview of experimental parameters and crater morphology.. 74
Table 6-3**:** Overview of experimental and modelled crater dimensions..... 98
Table 6-4**:** Maximum observed depths of subsurface deformation features and their corresponding numerically modelled strain and shock pressure values. 101
Table 6-5: Model data. 110
Table 7-1**:** Results for four initial fragment sizes. Case III is studied in detail using the iSALE model. 127
Table 7-2**:** Model Parameters of our best fit model. 150
Table 8-1**:** Model parameters for all 50 models. 201
Table 8-2**:** Overview of target materials and dimensionless parameters of the models used in this study and fitting results from Eqs. (93), and (96) & (97). 203
Table 9-1: Impacts and Planetary & Lunar atmospheres. 207
Table 9-2: Model parameters for vertical settling. 244
Table 9-3: Model parameters for ejecta curtain. 244

Notations

Symbol	Meaning	SI-Unit
A, a	Tillotson parameters (A=bulk modulus, also K)	Pa, -
A	cross sectional area (not to confuse with A_{Tillo})	m²
a	projectile radius (not to confuse with a_{Tillo})	m
B, b	Tillotson parameters	Pa, -
B	ejecta decay (not to confuse with B_{Tillo})	-
C	specific heat capacity	J/(kg K)
C_D	drag coefficient	-
C_h	heat transfer coefficient	-
c	speed of sound	m/s
D	damage, model parameter	-
d	depth	m
E	Energy	J
E_Y	Young's modulus	Pa
F	free energy	J
f	Degree of freedom	-
G	external forces (e.g. gravity)	N
G_μ	shear modulus	Pa
g	gravity (acceleration)	m/s²
h	thickness/height	m
I	exponent of size frequency distribution	
J_2	2nd invariant of deviatoric stress tensor	Pa²
K	Bulk modulus (= A)	Pa
K_1, K_2, K_3, K_4	scaling constants	-
k	thermal conductivity	W/(m K)
k_B	Boltzmannkonstante	J/K
m	mass	kg
N	number of particles	-
n	Iteration index	-
P or p	pressure	Pa
Q	vaporisation heat	J/kg
q	heat flux	W
R	crater radius	m
r	radial / horizontal position (= x)	m
r_i, r_d	dust/particle radius	m
S	entropy	J/K

s	deviatoric stress (stress tensor s_{ij})	Pa
T	Temperature	K
T_e, T_0	ejecta thickness	m
t	time	s
U	wave velocity	m/s
v	material / impact velocity	m/s
V	volume	m^3
x	horizontal / radial position (= r)	m
Y	material strength	Pa
y	vertical position (= z in 2D)	m
z	vertical position (= y in 2D)	m
α	ejection / launch angle	°
α_d	distension	-
β	coefficient of friction	-
β_p	Momentum multiplication factor	-
Γ	Grüneisenparameter	-
γ	adiabatic exponent	-
δ	projectile density	kg/m^3
ε	strain (also for ε-α-compaction model)	-
$\dot{\varepsilon}$	strain rate	1/s
η	viscosity	Pa s
Θ	Coupling parameter	-
κ	compaction rate	-
μ	scaling parameter	-
ν	scaling parameter	-
ν_P	Poisson ratio	
ξ	Sedimentation parameter	-
π	scaled size	-
ρ	density	kg/m^3
σ	stress (stress tensor σ_{ij})	Pa
σ_a	ablation coefficient	s^2/m^2
σ_B	Stefan-Boltzmann-constant	W/K^4
τ	iteration time step	s
Φ	porosity	-, or %
χ	speed of sound ratio	-
Ψ	effective drag acceleration	1/s
ω_α, ω_β	Tillotson parameters	-
ω_n, ω_p	scaling parameters	-

1 Introduction

1.1 Setting the Stage

Since the beginning of the existence of the solar system and the formation of the Sun around 5 billion years ago, the matter within this system has been continuously undergoing a dynamic evolution. Dust first agglomerated to planetesimals, and then this system full of planetesimals and planetary embryos evolved large bodies that we call planets. Throughout this evolution, one process continues to happen over and over again, namely, the colliding of bodies with one another. This process, called *impact cratering*, can result in the growth of the planetesimals and planetary embryos when the impacts are rather "slow", or it can result in the complete disruption of an entire object[1]. Impact craters are the most abundant surface features on most atmosphere-less bodies, and they are present on most bodies that possess an atmosphere, including the terrestrial planets, their moons, the moons of the gas giants, and the asteroids in the asteroid belt. Hence, understanding this phenomenon is crucial for understanding the history of the solar system.

As impact craters cover so many surfaces of solar system objects, they have been used as a measure of chronology in planetary science (see e.g. Fassett 2016 for a recent review). By counting craters of different sizes, a crater size distribution can be produced for a defined geologic surface terrain. Under the assumption that different terrains undergo a similar impact flux (i.e. the impactor population's characteristics remain constant over time), these crater size distributions can be compared, and older

[1] Certainly, "slow" is not a quantitative characterisation of the velocity. However, the velocity range necessary for accretion on the body is restricted by the escape velocity of the body. As long as the majority of the post-impact material is ejected with a velocity slower than the escape velocity, the body grows in mass. The escape velocity on Earth is 11.2 km/s, the escape velocity on Itokawa, a ~ 530m x 300 m x 200 m asteroid, is ~0.2 m/s. In contrast, disruption is defined by the impact energy that is required to let escape half the mass of the original major body (see e.g. Jutzi et al. (2010) for a study on the influence of projectile and material properties on disruption). The topic of material accretion is far too complex to give an overview, here, but an overview is given e.g. by Izidoro and Raymond (2018).

terrains will have accumulated more craters than younger terrains. However, different target properties could tend to produce different crater sizes between different surface areas (e.g. due to different target rheology), thus care must be taken when making these comparisons. The question is: How important is the decrease in crater size for an increase in strength between two neighbouring geologic surfaces? A recent intense numerical parameter study by **Prieur et al. (2017),** to which I contributed (but which is not part of this thesis), gives answers to this and similar questions.

In order to assign absolute ages instead of relative ages, a crater chronology function is required. Therefore, the age of some probed materials must be sampled by radiogenic dating methods (e.g. Stöffler and Ryder 2001) and correlated with the crater density of the tested region (Neukum 1983). However, one question (among others) remains uncertain in this approach: Does the dated melt-bearing material originate from the region where it was found, or does it represent material from a different region (and thus calibrates the age of this different region) that was ejected during an impact? How much ejecta from distant locations could be present in a sample area?

Melt rocks also occur in lunar regolith samples. Regolith forms not only by large impacts, but also by the continuously ongoing process of micro-impacts, i.e. impacts on a very small scale: Fast impacts cause fracturing of target rocks, transform material e.g. by melting, and finally also mix and re-distribute material laterally and from different depths (e.g. Colwell et al. 2007). However, so far, differences between lunar regolith and the regolith from asteroids (e.g. Itokawa) have been found. On Itokawa, melt seems to be absent while melt agglutinates are common on the Moon (Yoshikawa et al. 2015). As both kinds of regolith are thought to form due to impacts, the question arises as to how the processes of crater formation and material ejection are different on both bodies. Is this process unique for Itokawa, or is it common to asteroids?

A size-class larger than micrometeorite impacts is the class of decimetre-sized (i.e. tens of centimetres) meteoroids, which can help constraining today's impactor flux. Their impacts on the Moon can be

observed even by Earth-bound observing systems due to the emitted light, which has prompted the development over the last ~20 years of the field of lunar impact flash observations. Such impact flashes, which typically last from the tens to hundreds of milliseconds (Bouley et al. 2012), are thought to be caused by an impact plume (Melosh et al. 1993; Ortiz et al. 2000). However, the longer-lasting observed flashes (duration of several frames up to 1 - 8 s, Madiedo et al. 2014; Suggs et al. 2014) cannot be explained by a short-lived vapour phase, and the idea arose that such radiation can be caused by hot melt droplets in the ejecta (Yanagisawa and Kisaichi 2002). But, is there enough hot ejected material available to cause a light flash that can be observed from Earth? A better understanding of the processes involved in flash formation might help to better constrain the impactor flux in the decimetre- to metre-size range.

Only few years ago, a ~20 m meteoroid entered Earth's atmosphere in the Chelyabinsk area and caused injuries and damage. What would happen, if an object of even larger size were detected to be on an Earth-crossing trajectory? To avoid the danger of an asteroid impact on Earth, different techniques have been considered to deflect or destroy the hazardous object. One approach is to use a kinetic impactor that transfers momentum onto the asteroids and, thus, changes its orbit. However, a fraction of the momentum is carried by ejected material. Hence, the total momentum transfer depends on the ejection dynamics and, as such, on the target properties of the body. But, these are not well known, and, so far, few studies have dealt with this question. Only recently, interest has arisen due to the Asteroid Impact & Deflection Assessment mission AIDA (Cheng et al. 2016).

If the deflection of an asteroid fails, the consequences of the impact on Earth could be dramatic. On Earth, 190 impact structures have been found up to date (Figure 1-1), and more are expected to be discovered. In comparison to other bodies in the solar system, Earth's crater record is small due to the high rate of erosion (e.g. due to winds, precipitation, freezing water) and tectonic activity. At least one crater structure has been correlated with an event of mass extinction: The Chicxulub impact on the Yucatan

peninsula, Mexico, marks the time of transition from the Cretaceous to the Paleogene at ~66 Ma ago and ended the era of the dinosaurs (Alvarez et al. 1980). The impact caused local devastation, but furthermore, it caused a change in Earth's climate due to the release of climatically active gases and dust (Pierazzo et al. 1998; Artemieva and Morgan 2017; Brugger et al. 2017). The study of such cratering events is crucial to quantify the consequences for the ecosystem. How much gas can be released in an impact event? How much dust is set free, and how much time does the dust need to settle? Such questions require studying the interaction of ejected material with an atmosphere. Furthermore, this approach allows for studying the distribution of ejected tektites and crater infill material. These questions are transferable also to other planets and bodies that possess an atmosphere, like Venus, Mars, or Saturn's moon Titan.

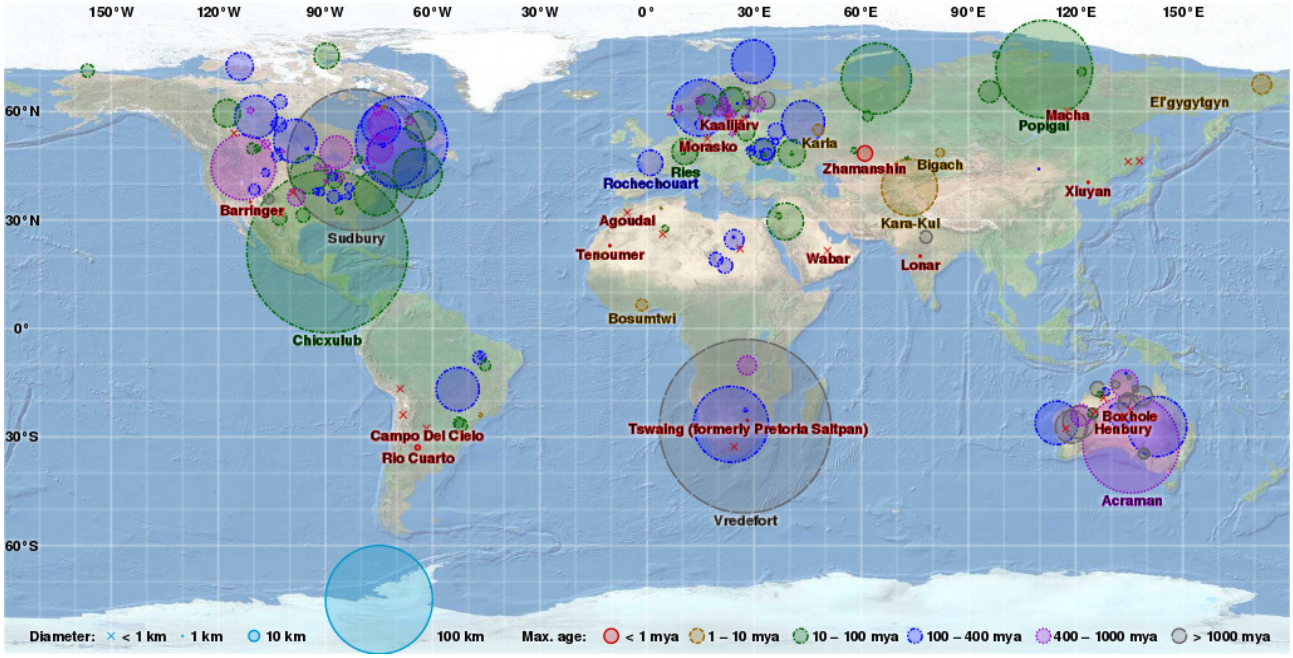

Figure 1-1: Map of Earth's craters on the Earth Impact Database as of November 2017. Circles represent the size of the craters, colour represents the age.[2]

Overall, there are likely many further examples of where the study of ejected material plays a major role. Certainly, there are more aspects

[2] Map from CMG Lee, United States Geological Survey, Earth Impact Database

regarding ejecta processes that are not addressed here, which are beyond the scope of this thesis.

1.2 Objectives and Goals

Ejecta blankets are a prominent and characteristic feature of impact craters. Ejected material plays a major role in planetary science, as summarised above. In this thesis, I study the ejection behaviour during impact cratering and the trajectories of ejecta until they are deposited. The ejection behaviour and, consequently, the deposition of the ejecta are expected to depend on the properties of the target material.

The excavation flow has been the subject of numerous previous studies (e.g. Oberbeck 1975; Maxwell 1977; Thomsen et al. 1979; Croft 1980; Austin et al. 1981; Melosh 1985). In laboratory experiments, mostly sand or powders have been used as the target material (Stöffler et al. 1975; Hartmann 1985; Cintala et al. 1999; Anderson and Schultz 2003; Hermalyn and Schultz 2011; Tsujido et al. 2015; Yamamoto et al. 2017). Previous studies found that an analytical model could describe the observed ejection angles on the basis of few parameters: An analytical expression for deriving ejection characteristics was developed by Maxwell (1977), who used the Z-model to describe material trajectories within the target. Further improvements have been implemented by Thomsen et al. (1979) and by Croft (1980), as they buried the centre of trajectories in a depth of about one projectile diameter. Further improvements to this model include the time dependence of its parameters in order to account for the evolution of the ejection behaviour (Austin et al. 1981; Anderson et al. 2004). However, the Z-model does not account for effects of target properties like porosity, nor for characteristics related to projectile velocity and mass. Furthermore, it is difficult to measure a systematic change of just one individual parameter in an experimental study. Therefore, I use numerical modelling to simulate cratering in different target materials and study the ejection behaviour for each case. I validate numerical results derived with different material models against experimental craters and naturally observed impact funnels, and I compare laboratory ejecta data with modelling results in order to show

the reliability of the model results. Based on the ejection characteristics, I derive the positions where the ejected material is deposited.

All points mentioned above are an important step when simulating the distribution of ejected material. However, the approach assumes vacuum conditions for calculating the trajectories of the ejecta, and a more sophisticated approach is required when ejecta trajectories shall be derived in the presence of a vapour plume or on a body that possesses an atmosphere. In this thesis, I implement a new feature to the iSALE shock physics code, which already has been successfully used before in the SOVA shock physics code (Shuvalov 1999), in order to simulate ejecta movement in an atmosphere. Solutions derived for vacuum conditions might hold true in a limited range, but in general, the ejecta distribution will deviate from results under vacuum conditions.

In light of the previous paragraphs, I formulate the key questions of this thesis as:

S I. **Ejecta and Target Properties:** In what ways does the ejection behaviour of different target materials differ, and how does ejection depend upon single material parameters? How does this influence the ejecta deposition?

S II. **Ejecta and Atmosphere:** What is the difference between ejecta trajectories in a vacuum and ejecta trajectories in an atmosphere? To what extent is the deposition of material affected by the atmosphere?

In order to answer these key questions, I address the following objectives:

M I. **Material Models:** The numerical parametrisations implemented in iSALE need to be tested if they sufficiently describe complex materials like competent rock or highly porous materials. Therefore, experimentally derived craters shall be reproduced in a model by using the rheology parametrisations in iSALE. Similarly, naturally observed funnels in a highly porous material shall be reproduced in a model by using the porosity-compaction model. Validating

the material models in iSALE is crucial for giving a reliable description of the ejection behaviour for different target properties.

M II. **Ejecta Analysis:** An approach to determine ejected material in an impact simulation has to be developed. A tool to analyse ejected material needs to be implemented and validated.

M III. **Representative Particles:** A reasonable approach for simulating the interaction of ejecta with a gaseous medium within iSALE is required to study ejection processes in an atmosphere. A new feature needs to be developed for iSALE and requires validation and/or benchmarking to test its applicability.

In the next section, I describe the project in which I embed the scientific work expressed by the questions and objectives above. The project provides ideal conditions to address these questions in an interdisciplinary environment and to validate numerical parameterisations, such as by comparing the material models against laboratory experiments.

1.3 The Multidisciplinary Experimental and Modeling Impact Crater Research Network (MEMIN)

This thesis was written as part of the DFG-funded MEMIN Research Network – *Multidisciplinary Experimental and Modeling Impact Research Network*. As natural craters are an end product of a cratering event itself and the long-term modification processes thereafter, the MEMIN Research Network was initiated in order to improve the understanding of crater formation processes by direct real-time observations of the cratering event

and the analysis of the cratering products, i.e. crater size, petrophysical subsurface material modifications, and material ejection. The experiments were set up to match natural systems as closely as possible. Within MEMIN, a unique network of scientists with different backgrounds and working techniques was organised to study the topic of impact cratering. The expertise covers field geologists, geochemists, mineralogists and (geo-) physicists from different locations in Germany, and their methods to study impact cratering range from field campaigns, experimental shooting campaigns, shock recovery experiments, diamond anvil cells, laser irradiation techniques, split-Hopkinson-pressure bar set-ups, laboratory micro-analysis, and numerical modelling, allowing for an interdisciplinary research approach (**Kenkmann et al. 2018**). The network is subdivided into 9 sub-projects that focus on different aspects and objectives, contributing to the common aim of understanding impact cratering in more detail.

A central aspect to MEMIN are the shooting campaigns with two-stage light gas guns at the Frauenhofer Ernst-Mach-Institut in Freiburg (SLGG, Figure 1-2 i). Each shot requires the preparation and weighing of the target blocks, the preparation of seismic sensors attached to the target blocks, mounting of ejecta catchers, and the adjustment of measuring devices like high-speed cameras (cf. Figure 1-2 iv) and spectrometers before the shot, and the careful recovery of the target block, ejecta catchers (Figure 1-2 iii), and ejected fragments from the target chamber after the shot. The target was then weighed once more to derive the mass loss due to the cratering. Targets in the SLGG campaigns were 20 – 25 cm in edge length (Figure 1-2 ii), while target blocks at the larger two-stage light gas gun were up to 80 cm in edge length. In the shooting campaigns, different types of competent rocks, such as marble, sandstone, or quartzite, were used as targets and were impacted with real iron meteorites (Campo del Cielo), steel, aluminium or basalt spheres (2.5-12 mm in diameter) with speeds in the range from ~2.5-7.8 km/s, resulting in craters in the decimetre range. The usage of these natural target materials was motivated by the objective of MEMIN to study the impact-induced effects on competent rock. This had not been done is such detail before, which explains the novelty of the

experiments conducted within MEMIN. Different parameter studies were conducted, including impact speed, projectile size and material, target porosity and target water saturation of pores, aiming on studying the effects of these parameters on crater mechanics, shock metamorphism, and projectile distribution during cratering (Poelchau et al. 2013; Poelchau et al. 2014).

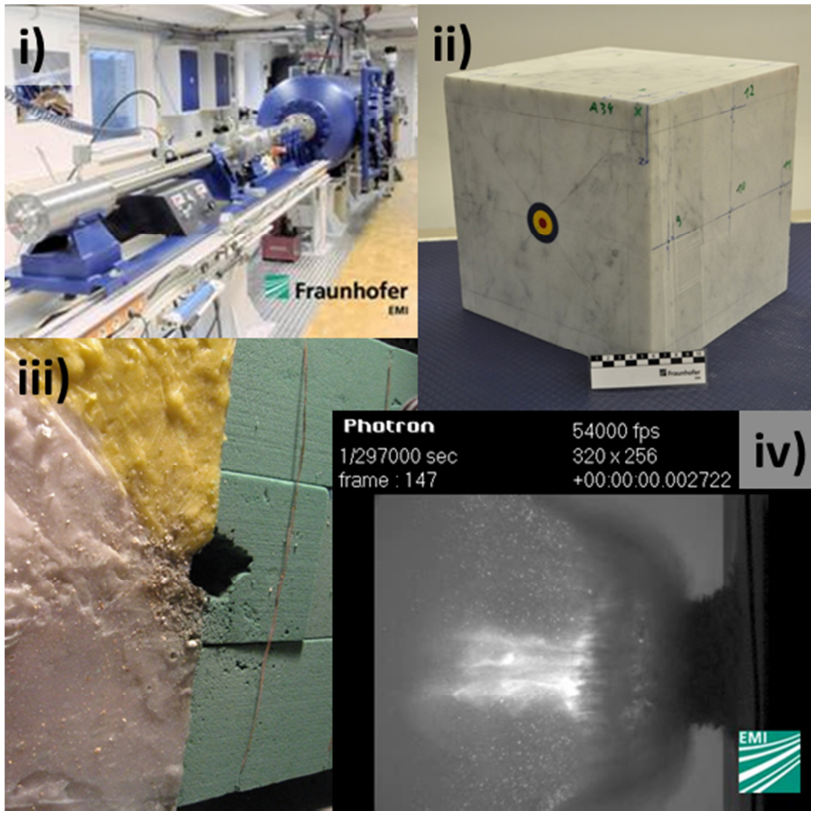

Figure 1-2: The MEMIN research network. The shooting campaigns at the Frauenhofer Ernst-Mach Institut in Freiburg were a central element to the research group. i) two-stage light gas gun, ii) marble target block (~25 cm edge length) prior to the impact, iii) ejecta catchers after the impact, and iv) snapshot from an impact plume ~0.4 ms after the impact.

This thesis was conducted in sub-project IX *Numerical modelling of impact cratering processes*. This project aimed at i) extending and generalising newly developed material models based on results from MEMIN I, ii) modelling the generation and formation of an ejecta plume (impact flashes were observed in high-speed videos captured during the shooting campaigns), iii) simulating the formation of natural crater structures, iv) implementing an atmosphere model that accounts for the interaction of ejected material with a gas phase, and v) supporting the other

sub-projects with modelling work for their analysis, and thus, giving insight into the processes that yielded the results observed on the experimental side. Conversely, modelling also requires testing and verification by observational constraints and, hence, takes advantage of the results from experiments. Based on such comparisons, modelling allows for studying cratering events on a larger natural scale.

1.4 Structure of the Thesis

This thesis is structured in ten chapters. Chapter 1 introduced the topic of impact cratering and presented the research questions to which this thesis is devoted. It also presented the research group MEMIN, including the sub-project in which this thesis was developed.

In chapter 2, a short background to the processes that occur during impact cratering is given. The Hugoniot equations are introduced, which describe the shock state of a material that is impacted with a given velocity. A short excurse gives some information on atmospheric effects that include atmospheric entry of meteoroids, but also the ejection of material from the ground.

Chapter 3 describes the methods used in this thesis. Numerical approaches, and in specific the iSALE shock physics code, are shown. The ejecta analysis and the newly programmed feature of iSALE that tackles the question of atmospheric interaction are explained in chapter 4. Chapter 5 shows validation tests and resolution tests for this newly implemented feature in iSALE.

Chapter 6 and 7 are each individually published and peer-reviewed articles in international journals. They relate to the first objective in this thesis, and they showcase studies where iSALE material models are tested: Chapter 6 relates to the strength models, chapter 7 to the porosity-compaction model. Here, I test the porosity-compaction model for an impact scenario with a snow target with high porosity. This scenario is an end-member case where ejection is suppressed nearly completely. Furthermore, I test the strength model and reproduce experimental MEMIN craters that were produced during shooting campaigns using quartzite and marble

targets. A reliable description of real materials is the basis for doing parameter studies for further materials.

Chapter 8 is published in a peer-reviewed international journal and is part of a MEMIN special issue (the same issue as chapter 6). It answers the first key question and the second objective shown above. The ejection dynamics for different target materials are described. The parameter study also includes the effects of increasing impact velocities on the ejection behaviour and material deposition. It does not include the effect of atmospheric interaction, which is part of chapter 9. In chapter 9, which refers to the second key question and the third objective, a parameter study of material movement in an atmosphere is presented for different size distributions and impact crater scales.

Finally, chapter 10 summarises and discusses the points taken up by the previous chapters and the key questions and objectives. Furthermore, this chapter offers an outlook on ongoing research activities and possible applications of the developed methods for further topics.

2 Background

2.1 Mechanics of Impact Cratering

When a projectile hits a target with high (supersonic) velocity, it forms a crater that is substantially larger than the original projectile, and material is ejected from the cavity. The process of impact cratering is typically described by three main phases: the contact- and compression stage, the excavation stage, and the modification stage (Gault et al. 1968). Although this distinction is somewhat artificial, as the different stages are not clearly separated and they grade into one another – i.e. material can start to be excavated in some area of the crater while at a different location, compression is still ongoing – this subdivision of the cratering process is helpful to understand the physical principles of cratering. In the following, I describe each of these stages of crater formation focusing on the most important aspects relevant to the work this thesis is based on. A much more detailed and sophisticated description of the impact cratering process in general can be found in the textbook "Impact Cratering – A Geological Process" by Melosh (1989) or in "Impact Cratering: Processes and Products" edited by Osinski and Pierazzo (2013). As some basic understanding of shock physics is essential for understanding hypervelocity impact processes, I also summarise the fundamental principles here. A comprehensive compilation on shock physics is given by Zel′dovich and Raizer (2002). As the following sections (2.1.1 – 2.1.3) represent a summary of textbook knowledge, I have foregone stating references and refer to Melosh (1989) and Osinski and Pierazzo (2013).

2.1.1 Contact- and Compression Stage

When two bodies collide with a high relative velocity that is faster than the speed of sound of the material, the pressure increases instantaneously at their contact surface. From the highly compressed interface, a shock wave emanates hemispherically into both objects (Figure 2-1 i). Typically, a smaller projectile impacts a larger, resting target,

transferring most of its momentum and kinetic energy onto the target. The material is compressed, heated and accelerated to high velocity. Shock pressures in this stage reach amplitudes on the order of several hundreds of GPa (e.g. a dunite rocky projectile impacting a rocky target with 20 km/s initially generates a shock pressure of ~650 GPa as estimated by impedance matching with the parameters as given by Melosh 1989) and, thus, far exceed the yield strength of the materials. The shock state of the material is defined by the Hugoniot equations that relate the initial (uncompressed) state of a material (index *0*) with a shock (compressed) state:

$$\rho(U - v) = \rho_0 U \quad , \quad (1)$$

$$P - P_0 = \rho_0 v U \quad , \quad (2)$$

$$E - E_0 = (P + P_0)(V_0 - V)/2 \quad , \quad (3)$$

with the internal energy E, pressure P, density ρ, specific volume $V = 1/\rho$, particle velocity v, and shock wave velocity U. In a phase diagram that shows e.g. P versus V, the uncompressed and the compressed state (e.g. A and C in Figure 2-2, respectively) are connected by the Rayleigh line (orange dotted line, Figure 2-2) that marks the loading path of the material and ends in a shock state on the Hugoniot curve. Note, the Hugoniot curve does not represent a thermodynamic path, but connects different possible shock states.

The shock wave runs through the projectile and reaches the rear of the projectile. Due to the zero pressure boundary condition at the free surface, it is reflected as a rarefaction wave that runs back through the projectile and into the target, releasing the compressed material (Figure 2-1 ii). The material releases adiabatically and might melt or vaporise upon release. The contact- and compression stage lasts until the projectile is released from the high pressure. Processes of this short first stage (e.g. ~10^{-3} s for a 10-m projectile at 10 km/s impact velocity) are located in a small volume that is similar to the size of the projectile.

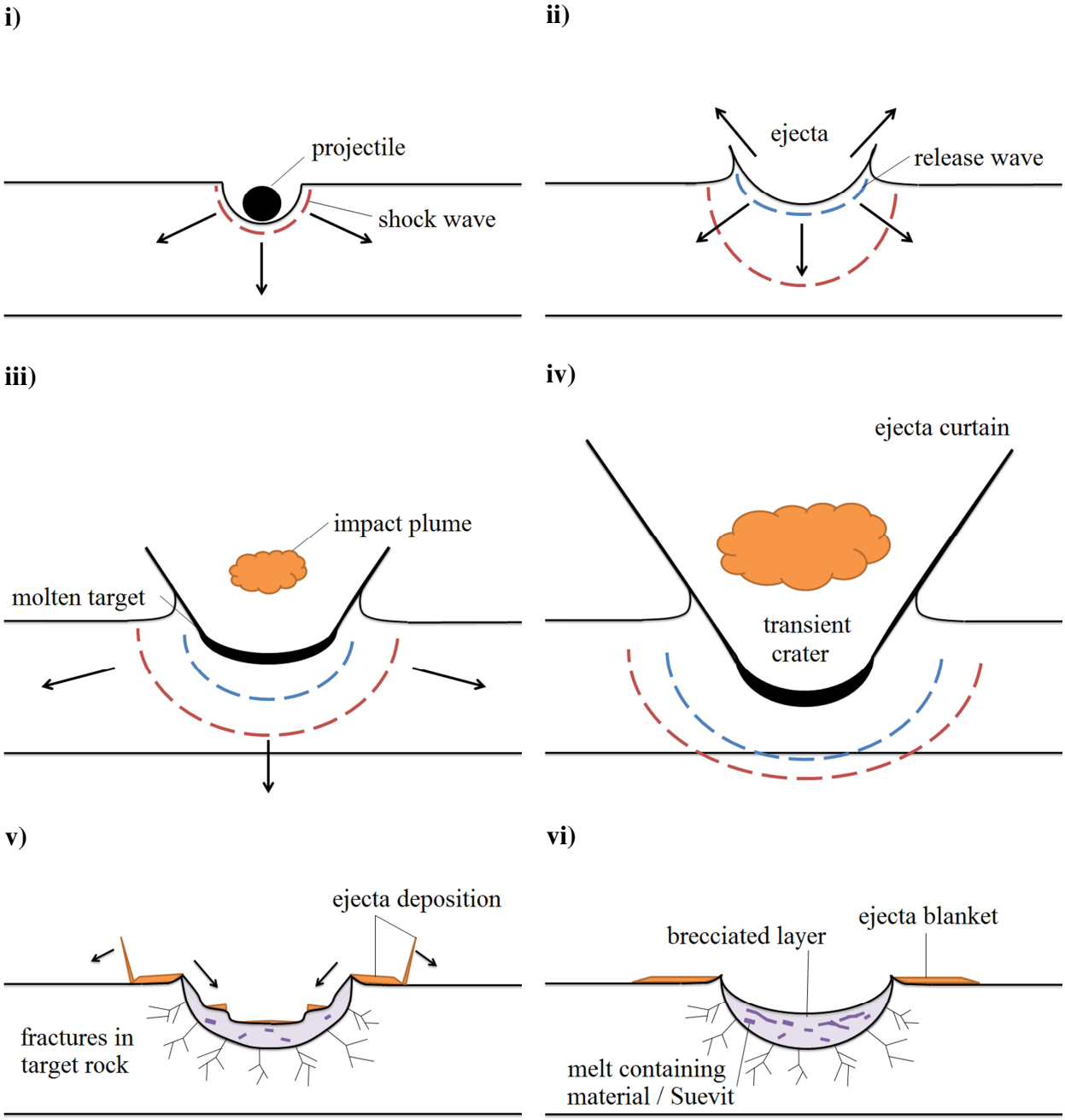

Figure 2-1: Cratering process in three stages. Contact- and compression stage (i, ii), excavation stage (iii, iv), and modification stage (v, vi). Shock and rarefaction waves are illustrated in red and blue, respectively. The sequence shows the formation of a simple crater.

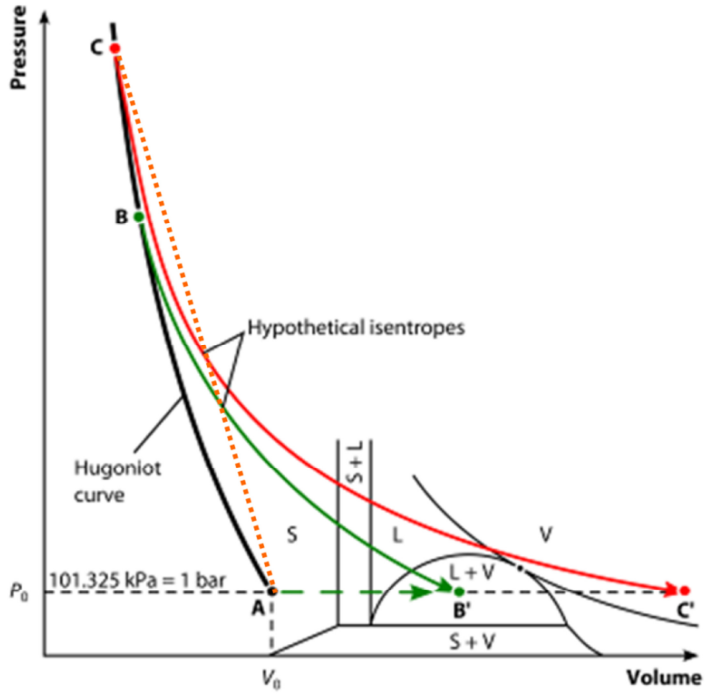

Figure 2-2: Pressure-volume relationship for a hypothetical silicate that undergoes shock-induced phase changes. Point B corresponds to an impact scenario in which the material is compressed to state B and released to state B', inducing melting and incipient vaporisation. Shocking the material to higher pressure (state C) induces complete vaporization (state C'). The orange dotted line is the thermodynamic compression path called the Rayleigh line. S = solid; L = liquid; V = vapour. The figure is based on Melosh (1989) and modified by **Hamann et al. (2016)**.

2.1.2 Excavation Stage

During the excavation stage, a hemispherical shock wave that is followed by the rarefaction wave propagates through the target, whereupon material is set into motion. The material motion is directed radially outwards, approximately, resulting in the subsonic excavation of a crater. Driven by the shock-induced excavation flow, the cavity grows to 10 to 20 times the projectile size. Depending on the initial location of the material, it is either displaced into the crater (outward and downward motion) or ejected from it (outward and upward motion; Figure 2-1 iii & iv). Material that is expelled from the crater forms a cone-shaped ejecta curtain that evolves outward with time. Material ejected from nearby the impact point leaves with the fastest velocity. The ejection velocity decreases with radial distance and, thus, with the time of ejection. A direct consequence is that nearby

material is ejected to the largest distances whereas material originating from areas close to the crater rim is ejected only to short distances out of the rim. At the top of the rim, an overturn flap of inverted rock units, which were ejected with very low velocities, can be observed on top of uplifted ground surface. The ejecta blanket covers the ground outside the crater. A continuous blanket reaches out several crater radii – in theory, as far as the thickness of the blanket is thicker than the grains it consists of. Ejected material interacts with the target upon landing. This process of ballistic sedimentation (e.g. Hüttner 1969; Oberbeck 1975; Hörz et al. 1983) refers to the admixture of target material into the ejecta deposit. The mixture of target and ejecta material depends on the deposition velocity, which is larger at larger distances from the crater (the fastest ejecta travels the farthest distance and is deposited with a velocity equal to the ejection velocity if atmospheric interaction is absent).

The peak shock pressure is the maximum pressure the material experiences during the compression-unloading cycle as the shock wave passes by. The peak shock pressure decreases with distance to the point of impact mostly because of three reasons: i) energy is dissipated into the target in terms of heat and material motion (shock wave compression is an unisentropic process), ii) geometric spreading of the shock wave as it propagates hemispherically into the target, and iii) the rarefaction wave that unloads the material from shock pressure and propagates in compressed material travels faster than the shock front and overtakes the shock wave, which results in a rapid decrease of the peak shock pressure. The more the shock decays, the more important the resisting forces due to gravity-driven litostatic pressure and material strength become, as these forces alter the excavation flow so that the crater growth is stopped. Depending on which resisting force controls the deceleration of the excavation flow, it is either called gravity or strength dominated. The stage when crater growth is stopped is called the transient crater, and its size is a good measure of the kinetic energy of the impact. Although it is very useful, the concept of the transient crater is only a virtual crater, because different locations within the crater reach the transient stage at different times. However, the virtual

transient crater can be approximated by a real crater at a given time; e.g. when the crater volume is largest. This approximation gets worse the bigger the crater is because it starts to grade into the modification stage. Nevertheless, the concepts of the transient crater and the three crater stages are useful for making analytical calculations of crater size and crater energy, as will be shown later. The excavation stage lasts longer than the contact- and compression stage (seconds to minutes; e.g. ~5 s for a 50-m projectile at 5 km/s impact velocity).

2.1.3 Modification Stage

The modification stage includes processes that alter the shape of the transient crater, leading to the final crater morphology (Figure 2-1 vi). These processes are mostly gravity driven, and the duration of this stage is the longest of the three stages. Consequently, strength-dominated craters do not undergo a significant modification stage.

For simple natural craters, oversteepened material at the crater rim becomes unstable and slides into the cavity, forming a lens of brecciated material (Figure 2-1 v). Hence, the transient depth-to-diameter ratio of typically 0.2 is modified, and the crater diameter increases by about 20% (Melosh 1989). Larger, complex craters suffer more significant modifications by the formation of a central uplift or peak rings. Large units of rock slump into the cavity, thus forming terraced terrains from the final rim inwards (e.g. Sturm et al. 2016). Final complex craters are much wider in diameter than the transient crater. As this stage is not the focus of this thesis, I refer to more specific literature on this subject (e.g. Kenkmann et al. 2013; Krüger et al. 2017).

2.2 Atmospheric Traverse of the Impactor

Where no atmosphere is present, impact events occur on a planetary body at every size scale. In contrast, for planetary bodies that possess an atmosphere – like Titan, Venus, Mars, or the Earth – the atmospheric shielding due to radiation, ablation and asteroid break-up prevents small-scale cratering events. A meteoroid that encounters such a body and penetrates into the atmosphere forms a bright meteor, and most of the mass of the entering meteoroid ablates away. The remaining piece that hits the Earth is called a meteorite. For a detailed physical description of the ablation process, please see chapter 7.4.1-7.4.2.

When larger objects enter the atmosphere of a planetary body, shock waves are generated that propagate through the atmosphere, and effects can be observed on the ground. The very recent atmospheric entry of the Chelyabinsk meteoroid (see chapter 7 for details) at a size of ~20 m caused the destruction of windows and the collapse of a roof (Borovička et al. 2013). An even larger observed event is the Tunguska event from 1908 in Siberia, which had an equivalent energy of 10-20 Mt of TNT (Chyba et al. 1993) and resulted in about 2000 km² of forest trees being torn down by the shock wave. While both stony objects mentioned above were disrupted upon atmospheric entry, small stony objects can also penetrate the atmosphere if atmospheric entry conditions favour the penetration and survival of the body, and they can form a crater, as demonstrated by the formation of the ~14 m diameter Carancas crater in 2007 in Peru (Kenkmann et al. 2009). Upon atmospheric disruption, meteoroids can also form crater strewn fields (Bronikowska et al. 2017).

Atmospheric disruption of meteoroids occurs when the aerodynamic stresses exceed the internal strength of the meteoroid. When the initial object is crushed, the fragments are accelerated laterally, increasing the material surface area. This surface area increase causes an increase in drag and, consequently, in aerodynamic stress, leading to further separation of the fragment cloud (see e.g. Artemieva and Shuvalov 2001).

2.3 Ejecta Plume

Similar effects described above for atmospheric penetration of an impactor also occur when material is ejected from a forming crater. During excavation, the velocity of the particles in the growing ejecta curtain decreases, whereas the size of the fragments increase radially due to the lower pressures that the material experiences. Hence, initial ejecta will be affected the most by atmospheric interaction. A typical example of early, highly shocked ejecta are tektites, such as the moldavites that originate from the Ries crater in South Germany (Artemieva et al. 2013). Furthermore, as described in section 2.1.1, large shock pressures of several hundred of GPa cause vaporisation of material (cf. Figure 2-2: path from Hugoniot state B to release state B' for incipient vaporisation). **Hamann et al. (2016)** show shock pressures ~100 GPa and ~270 GPa for incipient vaporisation of quartz and basalt, respectively. Similarly to an atmosphere, the impact vapour would interact with ejected material and modify the ejecta trajectories. As the released impact vapour exhibits high velocities, it can also cause the acceleration of ejected dust.

The forming ejecta blanket within an atmosphere will deviate from an ejecta blanket on an atmosphere-less body (Shuvalov and Dypvik 2013). Instead of an ideal parabolic trajectory, particles will be subject to wind and turbulence. Smaller particles will be dissolved in the atmosphere for a longer time than larger particles; hence, the deposition of ejecta is size dependent. Very small dust grains can also cause climate perturbations by decreasing the solar irradiation. The study of atmospheric interaction is the subject of key question *S II "Ejecta and Atmosphere"* (chapter 9).

3 Methodology

This chapter describes the methods that have been used to address the key questions. The first key question *S I – Ejecta and Target Properties*, which is addressed by a parameter study to analyse the effects of target properties on the ejection dynamics, requires the availability of many different target materials, each of which varies only by individual material parameters. Of course, it is possible to study the size of natural craters in different target materials or geological units by observation and remote sensing. But, the target properties will remain mostly unconstrained, and the characteristics of natural craters are affected by post-impact factors like erosion. A laboratory study seems more appropriate to tackle the question. However, such a study is hardly possible in a laboratory experiment because a change in one material parameter (e.g. porosity) is likely to change another material parameter (e.g. material strength). The most promising approach is to use numerical modelling with a shock physics code that is capable of simulating different material models, providing further insight into the cratering process. Hence, numerical modelling is the approach I decided to use. As the following sections in chapter 3 partly refer to textbook knowledge, I do not give references to such knowledge and refer to Anderson (1987), Ferziger and Perić (1997) or Collins et al. (2013).

3.1 Numerical Approach

So-called hydrocodes were developed in the 1970s to simulate the propagation of shock waves, primarily in gases and fluids (Amsden et al. 1980). They are also applicable to solid matter, as material behaviour can be approximated by a hydrodynamic approach during high shock pressure conditions. However, for the modelling of impact cratering, it is also important to consider the behaviour of material after unloading, when matter regains its solid-state properties. Therefore, I follow the suggestion by Pierazzo et al. (2008) to use the term shock physics code. Shock physics codes simulate material motion based on the compressible Navier-Stokes

equations and, thus, conserve momentum, energy, and mass. These three differential equations are formulated in a material description (Lagrangian formulation, or Smoothed Particle formulation as mesh-free Lagrangian formulation; Gingold and Monaghan 1977) or in a spatial description (Eulerian formulation). Furthermore, a hybrid method also exists where the grid can move in space but does not necessarily follow the material motion (ALE – Arbitrary Lagrangian-Eulerian). As Lagrangian formulations suffer from disadvantages when there are high material deformations causing mesh distortions, Eulerian descriptions are often preferred for the simulation of hypervelocity impacts.

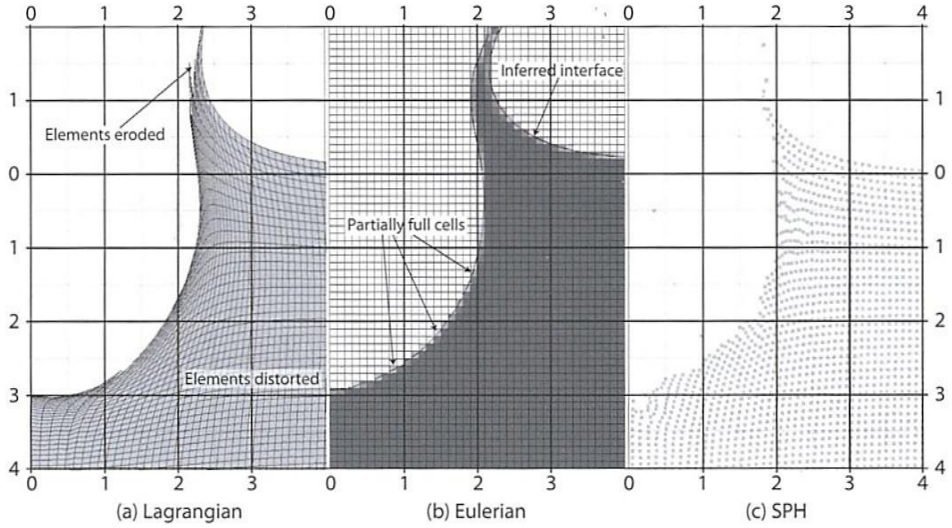

Figure 3-1: Example of the Lagrangian formulation (a, grid moves with material flow), the Eulerian formulation (b, static grid), and of the Smoothed Particle formulation (c, SPH – mesh free) to describe the motion of material in fluid dynamic computations. The figure is taken from Collins et al. (2013). (a) and (c) were generated by Mark Price with AUTODYN.

To complete the set of equations (5 unknowns, 3 equations), and in order to consider the behaviour of highly compressed and unloaded solid matter, two more equations are required. An equation of state relates the thermodynamic state variables and allows for working out e.g. the pressure in a material from its temperature and density. Also, a constitutive model relates material stress, strain, and temperature. Further advances required for the applicability of shock physics code simulations for natural solid materials include the implementation of an elasto-plastic constitutive model

and a parametrisation for porous material behaviour. The set of equations is solved at discrete points in the space-time domain. Different approaches exist for discretisation and solving these equations, three of which I will mention below: The finite-difference method approximates the derivatives of the differential equations by a finite difference between different equidistant points in a mesh. More advanced methods are the finite-volume and the finite-element methods. In a finite-element approach, the simulated material is subdivided into small (often unstructured) sub-domains (elements) where the equations are approximated individually. Between elements, specific continuity conditions are required. Finally a global system of equations for the entire domain has to be solved under consideration of the boundary conditions. The third approach is the finite-volume method, which uses the integral from of the conservation equations. The domain is discretised by cells (volumes), and each cell has to fulfil the conservation conditions. The flux of a given quantity from one cell to another is given by the surface integral, and this flux causes a change in the corresponding variables of the neighbouring cell. Thus, this approach guaranties the conservation of this quantity.

In this thesis, I use the *impact Simplified Arbitrary Lagrangian-Eulerian* (iSALE) shock physics code in its 2D version, which I will describe further in the next section. The grid-based code uses finite differences with an interface reconstruction algorithm, an advanced rheology and porosity compaction model, and includes Lagrangian features like tracer particles that allow for material tracking and detailed studies of "individual" material evolution.

3.2 iSALE 2D

The iSALE 2D code[3] is a multi-material, multi-rheology shock physics code that is based on the SALE hydrocode developed at Los Alamos (Amsden et al. 1980). Different versions of SALE, which originally could only describe Newtonian fluid flow for one material, have been or are still used within impact-related sciences (e.g. SALEB, SALE-3MAT, SALES-2, see e.g. Ivanov et al. 1997; Collins and Melosh 2002; Pierazzo et al. 2005; Wünnemann et al. 2005). Important developments for applying SALE to the simulation of impacts into solid materials and that are incorporated in iSALE are the implementation of an elasto-plastic constitutive model and a model of material fragmentation (Melosh et al. 1992). However, this had been done only for the Lagrangian formulation of SALE, and important improvements to the strength model with regard to the applicability for Eulerian-mesh calculations have been incorporated by Ivanov et al. (1997) and later by Collins et al. (2004), including a model for damage accumulation and strain-dependent material weakening (details follow in chapter 3.2.3). In order to describe many natural materials, a porosity model is required. The ε-α porosity-compaction model was added (Wünnemann et al. 2006) and later improved by Collins et al. (2011). Recently, a model for dilatancy was implemented to simulate the creation of impact-induced porosity due to shearing in geological material (Collins 2014). Details on the ε-α porosity model can be found in section 3.2.5.

The thermodynamic behaviour of material is simulated by various equations of state. Most often used are a Tillotson equation of state (Tillotson 1962) and the semi-analytical equation of state, ANEOS, (Thompson and Lauson 1972), which were developed in the Hopkins Laboratory for Pure and Applied Science and the Sandia National Laboratories, respectively. But, simple equations of state like for an ideal gas are also available. More details on the evolution of iSALE can be found in Wünnemann et al. (2006) or the current iSALE manual (Collins et al. 2017). The results derived with the iSALE code are continuously compared

[3] Webpage: http://www.isale-code.de

to natural and experimental data at small (meso) scales as well as at large (macro) scales (Collins et al. 2011; Kowitz et al. 2013; Collins 2014; Güldemeister et al. 2015; Davison et al. 2016; Wünnemann et al. 2016). The current distribution of iSALE is the fourth version, called iSALE-Dellen. Results in chapter 7 are based on the previous version, iSALE-Chicxulub.

3.2.1 Spatial and Temporal Discretisation

The numerical grid in iSALE 2D is set up either in a cylindrical symmetry (see Figure 3-2), or in Cartesian coordinates with two dimensions (horizontal and vertical direction). A system of regularly spaced nodes defines the location of velocity vectors that are used for momentum calculations and material advection. These positions are the vertices of the cells, in the centre of which are defined the scalar quantities like mass, pressure, energy, or temperature. This kind of mesh is known as a *staggered mesh*. It has some characteristics that are typical for a finite-volume approach of solving the partial differential equations, especially because iSALE calculates the mass flux out of a cell and uses it as influx for the neighbouring cell. However, in iSALE the partial differential equations (in their Lagrangian formulation) are solved by a finite-difference approach in an explicit way in order to derive new velocities at the nodes. These velocities are used to deform the mesh (material movement). Relative to the old cell boundary, a mass flux can be calculated. In iSALE, this calculation is done in an upwind direction. Based on the mass flux, the parameters in the undeformed (space-fixed) mesh are updated. For each cell, the in- and outflow at cell boundaries are equal. The iSALE advection scheme is accurate in first-order. Simulation results can be affected by numerical diffusion due to this advection scheme, which is one of the reasons why the simulation results have to be tested in a resolution study.

The time discretisation is done in accordance with the Courant-Friedrichs-Levy stability criterion that restricts the movement of material within a time step Δt to a cell with the size Δx:

$$\Delta t \leq \frac{\Delta x}{c} \quad (Lagrangian), \tag{4}$$

$$\Delta t \leq \frac{\Delta x}{c + |v|} \quad (Eulerian), \tag{5}$$

with the speed of sound c of the material and the material velocity v.

The computational grid covers a finite space that is confined by boundary cells, where specific boundary conditions are required. Boundary conditions can describe how material enters or leaves the computational domain, but they can also inforce material and wave reflections into the domain.

In iSALE, three boundary conditions are implemented. Two of them do not allow for material to cross the boundary by setting the velocity component normal to the boundary to zero. If the velocity component along the boundary is set to zero (option *noslip*), material is not allowed to move. If only the normal component is set to zero (option *freeslip*), material is allowed to move tangentially along the boundary. A boundary that allows material to pass is implemented with the option *outflow*. However, all these boundary conditions do not work well for highly non-linear shock waves, as they produce reflections of the shock waves back into the mesh. To avoid this problem, a special approach is required to reduce the effect of shock wave reflections: All processes that are relevant for a given study are supposed to happen inside the high-resolution zone, where the cells with the smallest spatial extent are located. The high-resolution zone is surrounded by a zone of cells with growing space increment. The extended cells in the extension zone cover a larger space in the computational domain, which allows the shock wave to decay over the larger distance without increasing the computational costs. In addition, numerical diffusion has a damping effect on the shock wave. The goal of this approach is to reduce, e.g. the amplitude of an expanding shock wave such that any reflections are negligible when the wave hits the boundary of the computational domain. An approach using a zone with an increasing cell size has previously been

successfully applied in numerous shock wave simulations (e.g. Wünnemann and Ivanov 2003; Wünnemann et al. 2011; Bronikowska et al. 2017).

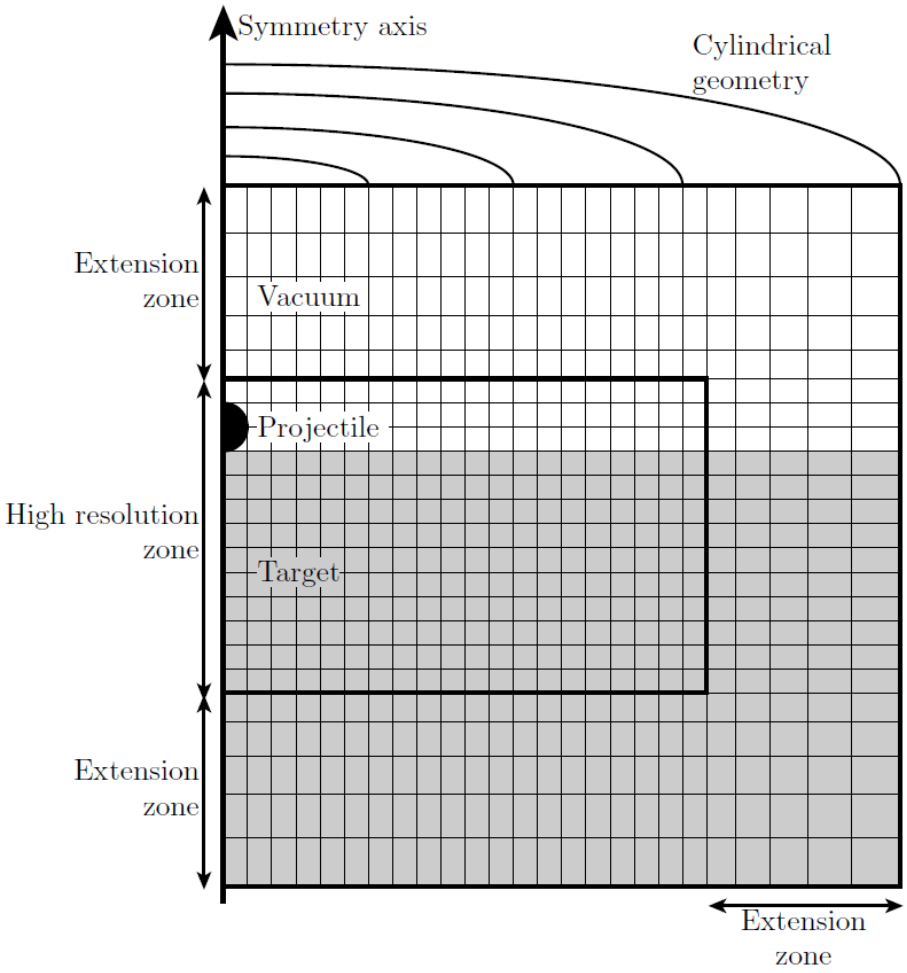

Figure 3-2: Cylindrical mesh geometry in iSALE. The mesh is rotated along the symmetry axis on the left. The inner bold line shows the high resolution zone that is surrounded by the extension zone, where cells grow by a fixed percentage in size. The target material is shown in grey. Adapted from Wünnemann and Lange (2002).

3.2.2 Equation of Motion

As stated above, a shock physics code simulates the motion of material by approximating it as a continuum, solving a set of partial differential equations that describe the conservation of mass, momentum and energy. In iSALE, these are formulated in cylindrical coordinates as[4]:

[4] This is the formulation given for SALE by Amsden et al. (1980). By replacing the index r with x, and by equalling $r = 1$ in all equations, the formulations can be used for a Cartesian

$$\frac{\partial(\rho\, v_r)}{\partial t} + \frac{1}{r}\frac{\partial(r\rho\, v_r^2)}{\partial r} + \frac{\partial(\rho\, v_r v_z)}{\partial z} = -\frac{\partial P}{\partial r} + \frac{1}{r}\frac{\partial(r s_{rr})}{\partial r} + \frac{\partial(r s_{rz})}{\partial z} - \frac{s_\theta}{r} + \rho G_r \quad , \tag{6}$$

in the radial direction and

$$\frac{\partial(\rho\, v_r)}{\partial t} + \frac{1}{r}\frac{\partial(r\rho\, v_r^2)}{\partial r} + \frac{\partial(\rho\, v_r v_z)}{\partial z} = -\frac{\partial P}{\partial r} + \frac{1}{r}\frac{\partial(r s_{rr})}{\partial r} + \frac{\partial(r s_{rz})}{\partial z} - \frac{s_\theta}{r} + \rho G_r \quad , \tag{7}$$

in the vertical direction for the conservation of momentum (Navier-Stokes equations) with the density ρ, velocity v, time t, space coordinates r and z, pressure P, the deviatoric stress tensor s_{ij}, and external forces G like gravity. Mass conservation is described as:

$$\frac{\partial \rho}{\partial t} + \frac{1}{r}\frac{\partial(r\rho\, v_r)}{\partial r} + \frac{\partial(\rho\, v_z)}{\partial z} = 0 \quad , \tag{8}$$

and energy conservation as:

$$\frac{\partial(\rho\, E)}{\partial t} + \frac{1}{r}\frac{\partial(r\rho\, E\, v_r)}{\partial r} + \frac{\partial(\rho\, E v_z)}{\partial z} = -P\left(\frac{1}{r}\frac{\partial(r\, v_r)}{\partial r} + \frac{\partial v_z}{\partial z}\right) + s_{rr}\frac{\partial v_r}{\partial r} + s_{rz}\frac{\partial v_r}{\partial z} + \frac{v_r s_\theta}{r} + s_{rz}\frac{\partial v_z}{\partial r} + s_{zz}\frac{\partial v_z}{\partial z} \quad , \tag{9}$$

with the internal energy E.

2D scenario without radial symmetry. The stress s_θ is zero in Cartesian coordinates. Here, I skip the artificial viscosity term Q in the equation, which would be summed to each time the pressure occurs in the equation. It is not in the focus of this thesis, but it is required for shock physics computations.

3.2.3 Rheology Model

In general, stress σ is a function of strain ε, strain rate $\dot{\varepsilon}$, temperature T, and damage D, where D is a scalar parameter to describe the degree of fracturing in the material, where D=0 is fully intact and D=1 corresponds to the maximum degree of fragmentation:

$$\sigma_{ij} = f\left(\varepsilon_{ij}, \dot{\varepsilon}_{ij}, T, D\right) \ . \tag{10}$$

The stress matrix can be subdivided into the deviatoric stress matrix s_{ij} that describes pure shear deformation and the pressure P (pure compression, trace components of the stress matrix if it is oriented according to the principle stress directions):

$$s_{ij} = \sigma_{ij} - P\,\mathbb{1} \ . \tag{11}$$

The deviatoric stresses for an elasto-plastic material are worked out in iSALE based on the deviatoric components in Hooke's law:

$$s_{ij}^{n+1} = s_{ij}^{n} + 2G_{\mu}\,\dot{\varepsilon}_{ij}^{n}\,\Delta t \ , \tag{12}$$

with the shear modulus G, the deviatoric strain rate $\dot{\varepsilon}$, and the time step Δt. The stress is capped according to the yield strength (see below). The strain rate components are calculated based on the velocities as follows:

$$\dot{\varepsilon}_{rr} = \frac{\partial v_r}{\partial r} - Tr\left(\dot{\varepsilon}_{ij}\right) \ , \tag{13}$$

$$\dot{\varepsilon}_{zz} = \frac{\partial v_z}{\partial z} - Tr\left(\dot{\varepsilon}_{ij}\right) \ , \tag{14}$$

$$\dot{\varepsilon}_{\theta} = \frac{v_r}{r} - Tr\left(\dot{\varepsilon}_{ij}\right) \ , \tag{15}$$

$$\dot{\varepsilon}_{rz} = 0.5\left(\frac{\partial v_r}{\partial z} + \frac{\partial v_z}{\partial r}\right) . \quad (16)$$

The strain rate is added to the strain variable each cycle, which is then advected in each time step. The shear modulus G_μ is calculated from the bulk modulus K and the Poisson ratio ν_P as follows:

$$G_\mu = 3\,K(P)\frac{1-2\nu_P}{2(1+\nu_P)} . \quad (17)$$

Consequently, for liquids G_μ=0 follows from ν_P=0.5. As mentioned above, for the simulation of solid materials that can only take a limited amount of stress, the stress is capped according to the yield strength. A yield strength Y that is defined for a material can depend e.g. on pressure, strain, or temperature. If the square root of the second invariant of the deviatoric stress tensor $\sqrt{J_2}$ exceeds the yield strength, shear failure occurs and the deviatoric elastic stress and strain components need to be reduced to the yield envelope. The difference between the elastic strain components before and after this procedure yields the plastic strain. J_2 in iSALE is defined in cylindrical coordinates as (Collins et al. 2004):

$$J_2 = \frac{1}{6}[(s_{rr}-s_{zz})^2 + (s_{zz}-s_\theta)^2 + (s_\theta - s_{rr})^2] + s_{rz}^2 . \quad (18)$$

Details on the rheology models used in this thesis are given in each chapter. However, a short description is given in the following[5]: To model the strength, Y, of a complex target like a competent rock during crater formation, the constitutive model proposed by Collins et al. (2004) is used in a default setting. The strength of the target depends on the confining pressure P and the state of damage D that the material has witnessed (Figure 3-3). Increasing the damage of the material causes a weakening of its strength according to:

[5] This paragraph is consistent with the Appendix of chapter 4.

$$Y(P) = (1 - D)\, Y_i(P) + D\, Y_d(P) \ . \qquad (19)$$

The subscripts i and d denominate the intact (D=0) and damaged (D=1) material properties, respectively. A detailed description of the determination of the damage is given Collins et al. (2004). The shear damage is given by the ratio of total plastic strain to the accumulated strain at the point of failure. Failure occurs when the stress in the material exceeds the strength of the material, i.e. $J_2 > Y^2$. Due to fracturing and pulverization during the cratering process, the damaged material has a much lower strength than the intact material. As described by Collins et al. (2004) and successfully applied to previous sandstone target experiments (Güldemeister et al. 2015), we use a parametrisation by Lundborg (1968) for the intact state of the material (solid lines in Figure 3-3):

$$Y_i(P) = Y_i^0 + \frac{\beta_i P}{1 + \frac{\beta_i P}{Y_i^m - Y_i^0}} \quad , \qquad (20)$$

where Y^0 describes the shear strength at zero pressure (i.e. this is the cohesion of the intact material for P=0), β the coefficient of friction, and Y^m the Von Mises Plastic Limit, which can be estimated from the Hugoniot elastic limit (e.g. Melosh 1989, p. 35). The strength of the damaged material is described by a Drucker-Prager yield surface that is capped by a maximum value of strength (dashed lines in Figure 3-3):

$$Y_d(P) = min(Y_d^0 + \beta_d\, P\, , Y_d^m) \, . \qquad (21)$$

In addition, thermal weakening is considered (Ohnaka 1995). This rheology model is used in chapter 6 because it is suited for modelling the material behaviour of competent rock. In chapters 7 and 8, the simpler Drucker-Prager model is used.

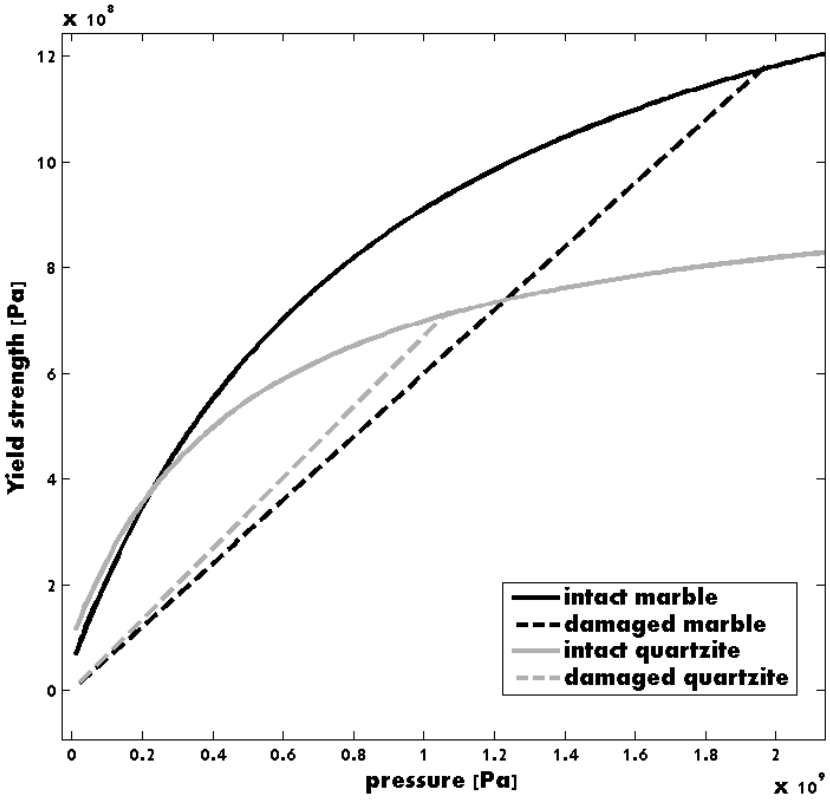

Figure 3-3: Yield strength of the two materials. Solid lines give intact material, dashed lines show damaged material yield envelopes. Black shows the strength of marble, grey the strength of quartzite.

3.2.4 Equation of State

As stated above, an equation of state is required to complete the set of equations and to include the thermodynamic response of a material. An example for a simple equation of state is the equation for an **ideal gas**. It is often found in a form that correlates the internal energy with the degrees of freedom f_d of the gas molecules, the amount of particles N, the Boltzmann constant k_B, and the temperature T:

$$E = \frac{f_d}{2} N k_B T \ , \tag{22}$$

where $f_d = 3$ for a monoatomic gas and $f_d = 7$ for a two-atomic gas (3 for translation, 2 for rotation, and 2 for vibration), or in a form that correlates pressure with volume V and temperature:

$$P\,V = N k_B T \ . \tag{23}$$

However, in iSALE and hydrocode computations in general, density and inner energy are often results of a computational iteration, based on which the pressure is computed in the next cycle:

$$P = f(\rho, E) \ . \tag{24}$$

The temperature is often derived from the internal energy and generally not considered very reliable (Melosh 1989). Hence, the equation of an ideal gas is better formulated in the form of Eq. (24) as:

$$P = (\gamma - 1)\,\rho\,E \ , \tag{25}$$

with the adiabatic exponent γ (ratio of the specific heat capacity at constant pressure C_P and constant volume C_V). The ratio γ can be determined by the internal degrees of freedom of the gas, or by the Grüneisen parameter Γ:

$$\gamma = \frac{C_P}{C_V} = \frac{f+2}{f} = \Gamma + 1 \, . \tag{26}$$

The ideal gas is used for simulating the behaviour of air in chapter 9.

A more complex equation of state available in iSALE is the **Tillotson equation of state** (Tillotson 1962). This equation reproduces experimentally derived linear relations between the particle velocity in a material and the shock wave velocity at lower pressures, and it extrapolates to the Thomas-Fermi limit at high pressures where the solid behaves like an electron gas. For material unloading from high shock pressures, the Tillotson equation of state accounts for vaporisation if sufficient internal energy is added to the material. The equation is defined for two regions in the phase space. For the compression range $\left(\frac{\rho}{\rho_0} \geq 1\right)$ and for expanded

states with an energy lower than the energy of initial vaporisation ($E<E_{iv}$), it is formulated as:

$$P = \left[a + \frac{b}{\frac{E}{E_0}\left(\frac{\rho_0}{\rho}\right)^2 + 1} \right] \rho\, E + A\left(\frac{\rho}{\rho_0} - 1\right) + B\left(\frac{\rho}{\rho_0} - 1\right)^2 \ , \qquad (27)$$

and for expanded states $\left(\frac{\rho}{\rho_0} < 1\right)$ with an energy larger than the energy of complete vaporisation ($E>E_{cv}$) it is formulated as:

$$P = \ a\, \rho\, E + \left[\frac{b\, \rho\, E}{\frac{E}{E_0}\left(\frac{\rho_0}{\rho}\right)^2 + 1} + A\left(\frac{\rho}{\rho_0} - 1\right) e^{-\omega_\beta \left(\frac{\rho_0}{\rho} - 1\right)} \right] e^{-\omega_\alpha \left(\frac{\rho_0}{\rho} - 1\right)^2} \ , \qquad (28)$$

with the Tillotson parameters a, b, A (bulk modulus), B, E_0, ω_α and ω_β. E_0 is a parameter that is often set close to the vaporisation energy. α and β are constants that govern the rate of the equation to converge to the ideal gas law. The initial energy for an initial pressure P=0 is zero. At zero pressure, a and b relate to the Grüneisen parameter as follows:

$$a + b = \Gamma(\rho_0) \ . \qquad (29)$$

Although a value of a = 2/3 is predicted as a limit from the Thomas-Fermi model for a monoatomic electron gas, it is often set to 0.5 because it better fits the observational data (Melosh 1989).

For partial vaporisation $\left(\frac{\rho}{\rho_0} < 1; \ \ E_{iv} < E < E_{cv}\right)$, a transition formulation is used:

$$P = \frac{(E - E_{iv})P_v + (E_{cv} - E)P_s}{E_{cv} - E_{iv}} \ , \qquad (30)$$

with P_v and P_s derived from Eqs. (28) and (27), respectively. The Tillotson equation is used in chapter 7 to describe the behaviour of basalt and snow (i.e. water). It is sufficient in the low-pressure range studied there.

A more sophisticated equation of state, which is widely used in hypervelocity impact studies, is the **ANEOS** software package (ANalytical Equation Of State, Thompson and Lauson 1972; Thompson 1990). Based on the Helmholtz free energy F, ANEOS calculates not only pressure and density, but it also provides estimates for temperature and entropy S (in contrast to the Tillotson equation of state):

$$E = F + TS \ , \tag{31}$$

$$P = \rho^2 \left.\frac{\partial F}{\partial \rho}\right|_T \ , \tag{32}$$

$$S = -\left.\frac{\partial F}{\partial T}\right|_\rho \ . \tag{33}$$

The free energy is approximated to be separable into three parts:

$$F(\rho, T) = F_{cold}(\rho) + F_{thermal}(\rho, T) + F_{electronic}(\rho, T) \ . \tag{34}$$

The "cold" term does not depend on temperature and describes the atomic interaction based on the interatomic potential at zero temperature ($E_c = F_c$). The "thermal" term describes thermal motion of atoms and ions, and it equals zero for $T = 0$. For low densities and high pressure, it approaches an ideal gas. The "electronic" term represents thermal motion, excitation, and ionisation of electrons and is important at very high temperatures and low densities. From Eqs. (32)-(34), it follows that also pressure or entropy are separated into these three components.

Recent improvements to ANEOS have been implemented by Melosh (2007), who modified the treatment of the vapour phase. So far, ANEOS has treated vapour as a monoatomic gas, which has a larger energy and entropy than a more realistic gas that contains molecular clusters. As consequence of

the high energy required for vaporisation in a monoatomic gas, only little vapour is produced in shock physics calculations. Changes have been incorporated in the "thermal" and the "cold" terms of ANEOS.

Based on an input file for each material, where ~50 input parameters have to be specified, the ANEOS programme supplies iSALE with tabulated files that contain the thermodynamic states. Two phases apart from the vapour phase can be described by ANEOS. Typically, two solid phases, or one solid and one molten phase, are required in impact simulations. Apart from using tabulated files, it is possible to directly calculate thermodynamic states with ANEOS during the simulation with iSALE. In chapters 6 and 8, I use the ANEOS for quartzite, which is one of the most accurate equations of states in impact simulations. In chapter 6, I also use the calcite ANEOS (Pierazzo et al. 1998).

3.2.5 Porosity-Compaction Model

The ε-α porosity-compaction model in iSALE was originally implemented by Wünnemann et al. (2006) and gives the possibility of simulating the behaviour of porous material under compressive strain (pressure), as typically occurs during shock wave compression. The model was refined by Collins et al. (2011) who included thermal material expansion during compaction.

In this model, a change in material distension α_d that relates to the material porosity Φ as

$$\alpha_d = \frac{1}{1-\Phi} = \frac{\rho_S}{\rho} \tag{35}$$

is calculated from a change in volumetric strain ε_V. Note that compaction is defined as negative. The subscript S denotes parameters for the non-porous state of a material. Based on the calculated distension, the pressure can be updated according to the assumption:

$$P = f(\alpha_d, \rho, E) = \frac{1}{\alpha_d} P_S(\alpha_d\, \rho, E) = \frac{1}{\alpha_d} P_S(\rho_S, E) \tag{36}$$

from Carroll and Holt (1972). The ε-α compaction model treats four different regimes of compaction: i) elastic compaction, ii) exponential compaction, iii) power-law compaction, and iv) complete compaction (see Figure 3-4). Regime i) is valid for $0 > \varepsilon_V > \varepsilon_e$, where ε_e is the volumetric strain at the elastic limit. Compaction in this regime is reversible and the change from the initial distension $\alpha_{d,0}$ to the distension at the elastic limit $\alpha_{d,e}$ ($\alpha_{d,e} < \alpha_{d,0}$) is given by:

$$\frac{d\alpha_d}{d\varepsilon} = \alpha_d \left[1 - \left(\frac{c(\alpha_d)}{c_{S0}}\right)^2\right] \quad , \tag{37}$$

with the sound speed c_{S0} of the solid matrix at zero pressure and the bulk sound speed of the porous material c:

$$c(\alpha_d) = c_{S0} + \frac{\alpha_d - 1}{\alpha_{d,0} - 1}(c_0 - c_{S0}) \quad , \tag{38}$$

where c_0 is the bulk sound speed of the porous material at zero pressure. For larger volumetric strain, $\varepsilon_e > \varepsilon_V > \varepsilon_X$, where the subscript X denotes the transition from the exponential to the power-law compaction regime, distension is defined as:

$$\alpha_d = \alpha_{d,e} e^{\kappa(\varepsilon - \varepsilon_e)} \quad , \tag{39}$$

with the compaction rate parameter κ. This rate is typically close to 1 (e.g. 0.98 in Wünnemann et al. 2006). For smaller porosities, κ can be set to smaller values like ~0.8. The change in distension (which is used together with the strain rate and the time step within iSALE for updating the distension from the previous iteration) is then given simply as:

$$\frac{d\alpha_d}{d\varepsilon} = \kappa\alpha_d \quad . \tag{40}$$

In the third regime, $\varepsilon_X > \varepsilon_V > \varepsilon_C$, where the subscript C denotes complete compaction, distension and the rate of compaction are given as:

$$\alpha_d = 1 + \left(\alpha_{d,X} - 1\right)\left(\frac{\varepsilon_c - \varepsilon}{\varepsilon_c - \varepsilon_e}\right)^2 \quad , \tag{41}$$

and:

$$\frac{d\alpha_d}{d\varepsilon} = 2\left(1 - \alpha_{d,X}\right)\frac{\varepsilon_c - \varepsilon}{(\varepsilon_c - \varepsilon_e)^2} \quad . \tag{42}$$

For the last regime, $\varepsilon_C > \varepsilon_V$, it is simply the case where $\alpha_d = 1$ and the compaction rate is zero.

Collins et al. (2011) improved the ε-α compaction model by adding the elastic compaction as described by Eq. (37), and by accounting for thermal expansion of highly porous materials that have been extremely heated due to compaction of the pore space. They introduce a thermal volumetric strain ε_h, which sums up together with the mechanical volumetric strain to the total strain. Small thermal volumetric strain can be approximated for $\kappa \sim 1$ as:

$$\varepsilon_h = \frac{\Gamma}{c_{S0}^2}\left(E - E_0\right) \quad , \tag{43}$$

with the Grüneisen parameter Γ (cf. Eq. (29)) and the specific internal energy E. The additional term of the thermal volumetric strain is accounted for when using the mechanical volumetric strain $\varepsilon_m = \varepsilon_{total} - \varepsilon_h$ in Eqs. (37) - (42).

In general, the compaction of porosity is not reversible, apart from an elastic component. However, an additional dilatancy model is available in iSALE (Collins 2014), which allows for an increase of porosity due to

shearing (shear-bulking). This model was not used for the simulations within this thesis.

The ε-α compaction model is a key parametrisation for modelling results in the chapters 7 and 8.

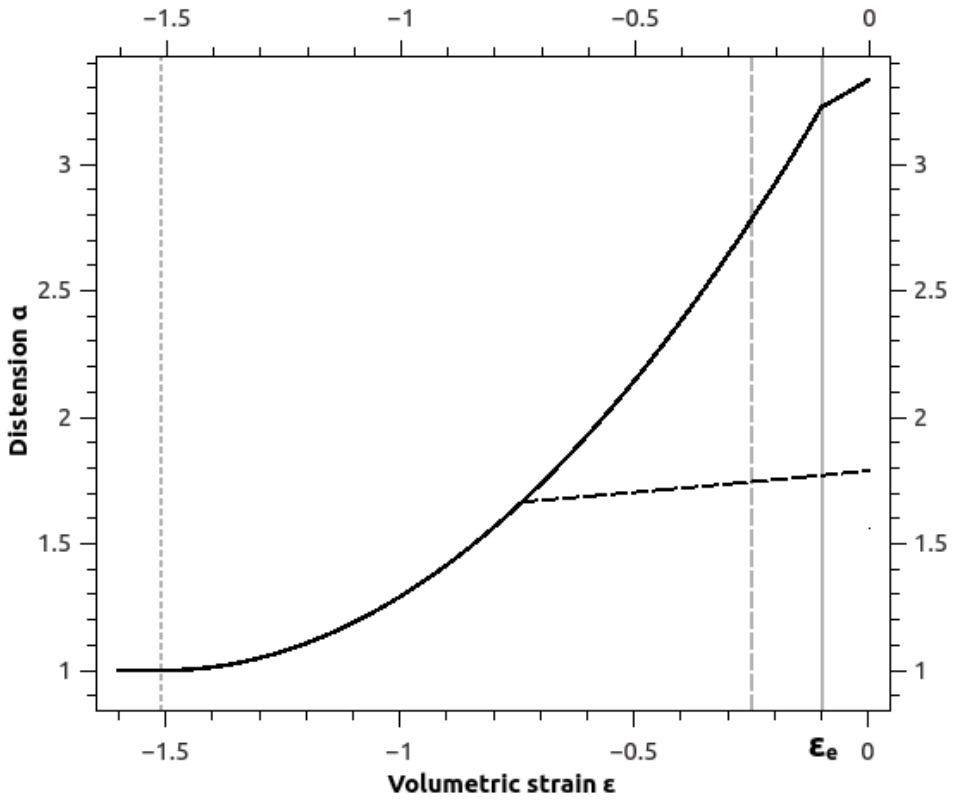

Figure 3-4: Pore compaction versus volumetric strain for the case of $\chi = 0.5$ during the compression (black solid line) and during the release after reaching half of the initial distension (black dashed line). Note the differences in slope for elastic compaction and release for equal differences in distension. The thin vertical lines represent the transitions from the elastic to the exponential regime according to the ε-α porosity-compaction model (grey solid line), from the exponential to the power law regime (grey dashed line) and to the fully compacted regime (grey dotted line). If $\chi = 1$, the distension remains constant during the elastic compaction and the elastic release.

4 Treatment of Ejecta in iSALE

Explosion and impact events generate shock waves, which cause the so-called excavation flow (section 2.1.2), whereby material is displaced such that a crater opens or is ejected out of the growing cavity. In this chapter, material ejection is discussed with respect to the computational methods that are used for describing material motion when the continuum assumption is no longer satisfied.

4.1 Continuum Assumption

Material motion and, hence, crater formation and the excavation flow, is approximated by the assumption of a continuum material flow, which is described by the equations of motion (chapter 3.2.2). This approximation works well for iSALE even when the material becomes completely damaged (D=1). As material is damaged, it may become granular, but granular material adjacent to the crater wall can still be well described as a continuum with an adequate rheology model. However, when material is ejected, this assumption no longer holds true. Ejected material may move differently when it is treated as a continuum (Figure 4-1 left panel) or as individual particles (Figure 4-1 right panel).

Describing ejecta motion as a continuum is problematic because the ejecta curtain is poorly resolved. Material movement and crater formation in general are well resolved in an Eulerian grid code like iSALE, and resolution studies help for estimating when a sufficient degree of convergence of the simulation results is reached. However, for ejection processes, the normal resolution of an impact simulation is insufficient to describe the movement of the ejected material because the ejecta curtain is resolved by a very limited number of cells, and it thins out at larger altitudes as the curtain evolves (cf. cell illustration in Figure 4-1). Mesh refinement procedures (e.g. adaptive mesh refinement) could significantly increase the reliability of the results if the material continuum is used for assessing ejected material. In the next section, I will discuss a different approach to

tackle the issue of the resolution and the continuum approach based on tracking the material movement with tracer particles.

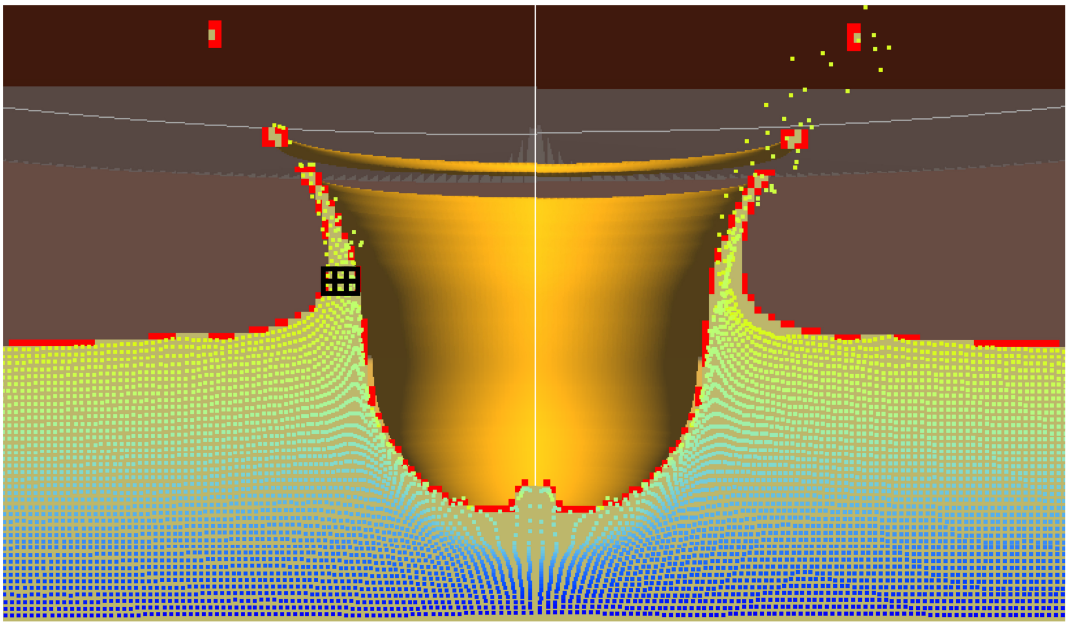

Figure 4-1: Impact of a 16-m radius projectile with 12 km/s after 0.32 s. All materials are granitic. Tracers are shown as yellow to blue dots according to their vertical position. On the left panel, tracers are coupled to the movement of the material continuum in the grid; on the right, tracers above the surface are decoupled from the continuum and move according to Earth's gravity without atmospheric drag. For illustration, a few numerical cells are included on the left panel in black.

4.2 Tracer

In iSALE, Lagrangian particles (tracers) are used to track the material during the flow within the computation grid. Tracers are massless, i.e. they are passive and do not interact with the material within the grid. However, tracers represent the material from their initial location at the start of the simulation. Typically, tracers are set in the centre of each computational cell, and they allow for tracking the conditions experienced by the material during the simulation, such as the peak pressure or temperature. The peak shock pressures can be useful for determining the amount of melt or vapour that is produced by an asteroid impact (e.g. Pierazzo et al. 1998).

Tracer velocities are interpolated from the velocities at the four nodes of the cell where the tracer is located. Here, an example of this is

shown for a cell with node indices 1 and 2 (11 bottom left node, 12 upper left node, 21 bottom right node, 22 upper right node), and a tracer at position *r*:

$$\begin{aligned} v_{x,y} = (1-t_x)\big(1-t_y\big)v_{x,y}^{11} \\ + \quad t_x \ \big(1-t_y\big)v_{x,y}^{21} \\ + \quad t_x \quad t_y \ v_{x,y}^{22} \\ + \ (1-t_x) \quad t_y \ v_{x,y}^{12} \ , \end{aligned} \tag{44}$$

with

$$t_x = \frac{r_x - x_{11}}{x_{21} - x_{11}} \ , \qquad t_y = \frac{r_y - y_{11}}{y_{12} - y_{11}} \ . \tag{45}$$

New tracer positions at a later time step *n*+1 are calculated by a simple explicit Euler scheme:

$$r_{x,y}^{n+1} = r_{x,y}^{n} + \Delta t \ \ v_{x,y} \ . \tag{46}$$

As discussed in the previous section, modelling the movement of ejecta is erroneous when using the continuum approach of material motion. In contrast, this thesis uses the movement of tracer particles to determine ejection characteristics for different materials. Therefore, tracers are assessed in a specific altitude over the target. With increasing altitude, the ejecta curtain is resolved by increasingly fewer cells (Figure 4-1), and more problems related to the continuum assumption will affect the results from tracking tracer particle motion. At low altitudes, issues arise because ejection characteristics can still be influenced by pressure gradients within the target material. A minimum altitude of one projectile radius avoids such issues and gives stable results for ejection characteristics. A more detailed discussion on this approach and uncertainties in the ejection characteristics can be found in chapter 8.

Based on the derived ejection dynamics, the vacuum trajectories of the ejected material are only affected by gravity and can be calculated as parabolas (Figure 4-2). Thus, it is possible to derive the location where the ejected material will land. By summing up the material at one landing position, the thickness of the landed material can be calculated. However, this approach neglects, secondary effects like secondary mass wasting or material slumping. This point is discussed in more detail in chapter 8.

The tracer approach is useful when dealing with vacuum conditions. However, many planetary objects possess an atmosphere that interacts with ejected material. Furthermore, fast impacts cause the formation of a vapour plume that will interact with the ejecta, as well. As the tracer approach does not include such interaction, it needs to be calculated within the model itself. Also, tracers as implemented in iSALE do not have characteristics (e.g. particle size, mass) that are required for calculating such an interaction. A new implementation of a method is required for such purposes and will be described in the next chapter.

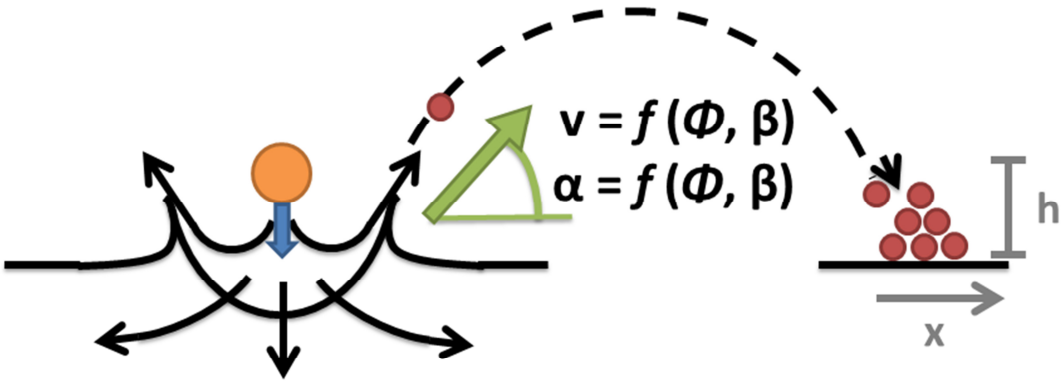

Figure 4-2: Sketch of ejecta motion in a vacuum. The material is ejected from the crater with a certain velocity and angle that depend on the target properties (e.g. porosity Φ, coefficient of friction β). The material follows a parabolic trajectory until it is deposited at a certain distance from the crater.

4.3 Representative Particles

As stated in the previous section, the description of ejecta trajectories under the presence of a vapour plume or an atmosphere requires the implementation of a new feature in iSALE. The approach followed in this thesis is the representative particles (RP) approach as presented by Shuvalov (1999). Even though chapter 9 deals with this approach specifically, here I discuss the approach and its implementation, as this is a major part of the thesis.

The representative particles technique is an approach to model a dusty flow as a second material phase within a medium that is described by a material continuum, allowing for different velocities between the continuum medium and representative particles. Furthermore, using representative particles allows for modelling particles of different size and with different individual velocities.

A dusty flow is described by the movement of a large number of representative particles (10^3 - 10^5) within a medium. A representative particle mimics the behaviour of a certain amount of real dust grains N_{grain} of a certain size traveling on similar trajectories (N_{grain} ~10^5 - 10^{10}). They have a certain mass and are subject to acting forces like gravity or drag. The equation of motion for the i^{th} dust grain is given by:

$$m_i \frac{d\vec{\boldsymbol{v}}_{\boldsymbol{i}}}{dt} = m_i \vec{\boldsymbol{g}} + 6\pi\, r_i \eta \left|\vec{\boldsymbol{v}}_g - \vec{\boldsymbol{v}}_{\boldsymbol{i}}\right| \vec{\boldsymbol{e}}_{\boldsymbol{g-i}} + C_D \pi {r_i}^2 \rho_g \left|\vec{\boldsymbol{v}}_g - \vec{\boldsymbol{v}}_{\boldsymbol{i}}\right|^2 \vec{\boldsymbol{e}}_{\boldsymbol{g-i}} \quad , \quad (47)$$

where C_D is the drag coefficient, g the gravitational acceleration, m_i and r_i the dust grain mass and radius, respectively, ρ_g and η are gas density and viscosity, respectively, $\boldsymbol{v_i}$ and $\boldsymbol{v}_g$ are the dust and gas velocity, respectively, and $\vec{e}_{g-i}$ is the unity vector of relative movement between gas and the i^{th} dust grain, defined as: $\vec{e}_{g-i} = \left(\vec{v}_g - \vec{v}_i\right) / \left|\vec{v}_g - \vec{v}_i\right|$. The first term on the right side of Eq. (47) describes gravity, the second term represents a low-velocity flow regime (Stokes drag), and the third term represents the high-velocity flow regime (sometimes referred to as Newton drag). The gas

velocity is inferred from the velocity components on the nodes of the cell according to Eqs. (44) and (45) for each representative particle, individually.

In the following, I show the equations for two dimensions with a vertical component *z* and a radial component *r*, as cylindrical symmetry is used in the iSALE 2D shock physics code. However, the method can be extended into 3D. Eq. (47), separated into two components and using the norm of the velocity difference, $\Delta v_{g-i} = \left|\vec{\boldsymbol{v}}_g - \vec{\boldsymbol{v}}_{\boldsymbol{i}}\right|$, then reads as:

$$\frac{dv_{i,z}}{dt} = -g + \frac{C_D \pi {r_i}^2 \rho_g}{m_i} \Delta {v_{g-i}}^2 e_{g-i}^z + \frac{6\pi\, r_i \eta}{m_i} \Delta v_{g-i}\, e_{g-i}^z \quad , \tag{48}$$

$$\frac{dv_{i,r}}{dt} = \frac{C_D \pi {r_i}^2 \rho_g}{m_i} \Delta {v_{g-i}}^2 e_{g-i}^r + \frac{6\pi\, r_i \eta}{m_i} \Delta v_{g-i}\, e_{g-i}^r \quad . \tag{49}$$

Following the approach from Shuvalov (1999), an implicit implementation is used to approximate Eq. (49) (radial direction) as:

$$\frac{v_{i,r}^{n+1} - v_{i,r}^n}{\tau} = \left[\frac{C_D \pi {r_i}^2 \rho_g}{m_i} \Delta v_{g-i}^n + \frac{6\pi\, r_i \eta}{m_i}\right] \left(v_{g,r}^{n+1} - v_{i,r}^{n+1}\right) \quad , \tag{50}$$

with time step τ and the index n corresponding to the n^{th} time step. The implicit implementation is required to obtain correct results for large time steps. Reordering for the updated representative particle velocity (= dust grain velocity) gives:

$$v_{i,r}^{n+1} = \frac{v_{g,r}^{n+1}}{1 + \frac{1}{\tau\, \Psi_i}} + \frac{v_{i,r}^n}{1 + \tau\, \Psi_i} \quad , \tag{51}$$

with the drag acceleration:

$$\Psi_i = \frac{C_D \pi {r_i}^2 \rho_g}{m_i} \Delta v_{g-i}^n + \frac{6\pi\, r_i \eta}{m_i} = \frac{3\, C_D\, \rho_g}{4\, \rho_i\, r_i} \Delta v_{g-i}^n + \frac{4.5\, \eta}{\rho_i\, {r_i}^2} \quad . \tag{52}$$

Eq. (52) yields a strong acceleration for small particles and slow acceleration for large particles. Momentum conservation and Eq. (51) yield an expression from which the updated gas velocity in the cell that includes N_{RP} representative particles can be derived:

$$m_g v_{g,r}^n + \sum_{i=1}^{N_{RP}} N_{grain}^i m_i \, v_{i,r}^n = m_g v_{g,r}^{n+1} + \sum_{i=1}^{N_{RP}} N_{grain}^i m_i \left(\frac{v_{g,r}^{n+1}}{1 + \frac{1}{\tau \, \Psi_i}} + \frac{v_{i,r}^n}{1 + \tau \, \Psi_i} \right). \quad (53)$$

For Eq. (48) (vertical component), if $v_{g,z}^n > v_{i,z}^n$, a more complex implementation is used that allows the transition to sedimentation velocity at large time steps (Shuvalov 1999). The sedimentation velocity can be derived from an equilibrium condition of the acting forces by setting Eq. (47) equal to zero. Chapter 9 discusses the equation for calculating the stationary sedimentation velocity v_{sed}, but for now it is enough to see that the sedimentation velocity is derived as one solution of a parabolic equation:

$$0 = -g + \frac{6\pi \, r_i \eta}{m_i} \, v_{sed} + \frac{C_D \pi {r_i}^2 \rho_g}{m_i} \, \xi \, v_{sed}^2 \quad , \quad (54)$$

$$\xi = min\left(\frac{1}{{e_{g-i}^z}^n}, \xi_K \right) = min\left(\frac{\Delta v_{g-i}^n}{v_{g,z}^n - v_{i,z}^n}, \xi_K \right) \quad , \quad (55)$$

where ξ_K is a big constant (e.g. ξ_K=100) that avoids numerical division problems for small velocity differences between gas and dust. Stationary sedimentation is given for $v_{g,r}^n = v_{i,r}^n$, i.e. ξ=1. Reordering Eq. (54) for g and replacing g in Eq. (48) yields:

$$\frac{dv_{i,z}}{dt} = \left(v_{g,z} - v_{g,i} + v_{sed} \right) \left[\frac{C_D \pi {r_i}^2 \rho_g}{m_i \, e_{g-i}^z} \xi \left(v_{g,z} - v_{g,i} - v_{sed} \right) + \frac{6\pi \, r_i \eta}{m_i} \right] . \quad (56)$$

The numerical approximation for this equation is:

$$\frac{v_{i,z}^{n+1} - v_{i,z}^{n}}{\tau} = \left(v_{g,z}^{n+1} - v_{i,z}^{n+1} + v_{sed}\right) \widetilde{\Psi}_i \quad , \qquad (57)$$

with

$$\widetilde{\Psi}_i = \frac{C_D \pi {r_i}^2 \rho_g}{m_i} \xi\left(v_{g,z}^{n} - v_{i,z}^{n} - v_{sed}\right) + \frac{6\pi\, r_i \eta}{m_i} \quad , \qquad (58)$$

which results in the solution for the updated particle velocity:

$$v_{i,z}^{n+1} = \frac{v_{g,z}^{n+1} + v_{sed}}{1 + \frac{1}{\tau\, \widetilde{\Psi}_i}} + \frac{v_{i,z}^{n}}{1 + \tau\, \widetilde{\Psi}_i} \quad . \qquad (59)$$

For the case of $v_{g,z}^{n} < v_{i,z}^{n}$, the approximation for Eq. (48) follows the approach for the radial direction:

$$\frac{v_{i,z}^{n+1} - v_{i,z}^{n}}{\tau} = -g + \Psi_i \left(v_{g,z}^{n+1} - v_{i,z}^{n+1}\right) \quad , \qquad (60)$$

yielding:

$$v_{i,z}^{n+1} = \frac{v_{g,z}^{n+1}}{1 + \frac{1}{\tau\, \Psi_i}} + \frac{v_{i,z}^{n} - g\tau}{1 + \tau\, \Psi_i} \quad . \qquad (61)$$

Similar to the radial component, the updated gas velocity can be derived from momentum conservation:

$$m_g v_{g,z}^{n} + \sum_{i=1}^{N_{RP}} N_{grain}^{i} m_i \left(v_{i,z}^{n} - g\tau\right) = m_g v_{g,z}^{n+1} + \sum_{i=1}^{N_{RP}} N_{grain}^{i} m_i\, v_{i,z}^{n+1} \quad , \qquad (62)$$

with $v_{i,z}^{n+1}$ as given in Eq. (59) or (61). The radial and vertical positions x_r and x_z of particles are calculated as follows:

$$x_{i,r}^{n+1} = x_{i,r}^{n} + 0.5\left(v_{i,r}^{n} + v_{i,r}^{n+1}\right)\tau \quad , \tag{63}$$

$$x_{i,z}^{n+1} = x_{i,z}^{n} + 0.5\left(v_{i,z}^{n} + v_{i,z}^{n+1}\right)\tau \quad . \tag{64}$$

Drag forces are dissipative terms in the equation of motion, causing a transformation of energy from kinetic to thermal energy. In the approach of representative particles, the increase in thermal energy ΔE_{therm} can be calculated based on the energy balance equation (including potential energy):

$$\begin{aligned} &\frac{m_g}{2}\left|v_g^n\right|^2 + \sum_{i=1}^{N_{RP}} N_{grain}^{i} m_i \left(\frac{\left|v_i^n\right|^2}{2} + g x_{i,z}^{n}\right) \\ &\quad = \frac{m_g}{2}\left|v_g^{n+1}\right|^2 + \sum_{i=1}^{N_{RP}} N_{grain}^{i} m_i \left(\frac{\left|v_i^{n+1}\right|^2}{2} + g x_{i,z}^{n+1}\right) + \Delta E_{therm} \ . \end{aligned} \tag{65}$$

The kinetic energy of the gas is calculated as the sum of one fourth of the kinetic energy at each node.

Following the approach from Shuvalov (1999), all representative particles are sorted by their position relative to the cells of the grid, starting in an alternating manner either at the central bottom or the outer top corner of the grid. I implemented a heapsort sorting algorithm.

Velocity changes for the gas in the material continuum in iSALE are implemented in a similar way to the SOVA shock physics code. The difference in the approach between iSALE and SOVA lies in the position of the velocity in the grid. SOVA velocities are calculated at the centre of the cell boundaries and allow for movement only across this boundary, whereas in iSALE, two velocity components are stored in each node of a cell.

The whole representative particle routine is called from the iSALE main cycle each iteration. Several positions within the cycle have been tested, but finally the routine is included at a position such that it is called after updating the time step and prior to the calculation of the artificial viscosity. In this way, the new updated gas velocity is included in the

calculations of the stability routines, and updated gas velocity is taken into account for gas advection. Furthermore, the state of the materials and the time step are updated prior to calling the representative particles routine. For calculating the new time step *dt*, a Courant-Friedrichs-Lewy condition for the representative particles was implemented in the following way:

$$dt^{n+1} = min\left(2\ dt^{n}, 0.2\ \frac{\min(dx, dz)}{\max(v_{i,x}^{n}, v_{i,z}^{n})}\right) \quad . \qquad (66)$$

In its current implementation, the representative particle approach allows for simulating scenarios with all equally sized particles as well as with differently sized particles that follow a constant size-frequency distribution. Particle sizes are included in calculations according to a power law description, as given, e.g. by Buhl et al. (2014b):

$$N_{cum}(> r) = C\ r^{-I} \quad , \qquad (67)$$

with the exponent *I*. A short implementation test is shown in Figure 4-3: The size-frequency distribution is defined as input for the formation of representative particles according to Eq. (67) for the following four particle sizes: 1 mm, 1 cm, 1dm, and 1 m (*I*=2.66). After setting up the model, the produced representative particles from the simulation are compared with Eq. (67). The model exactly reproduces the analytical input and the size distribution in the model is implemented correctly.

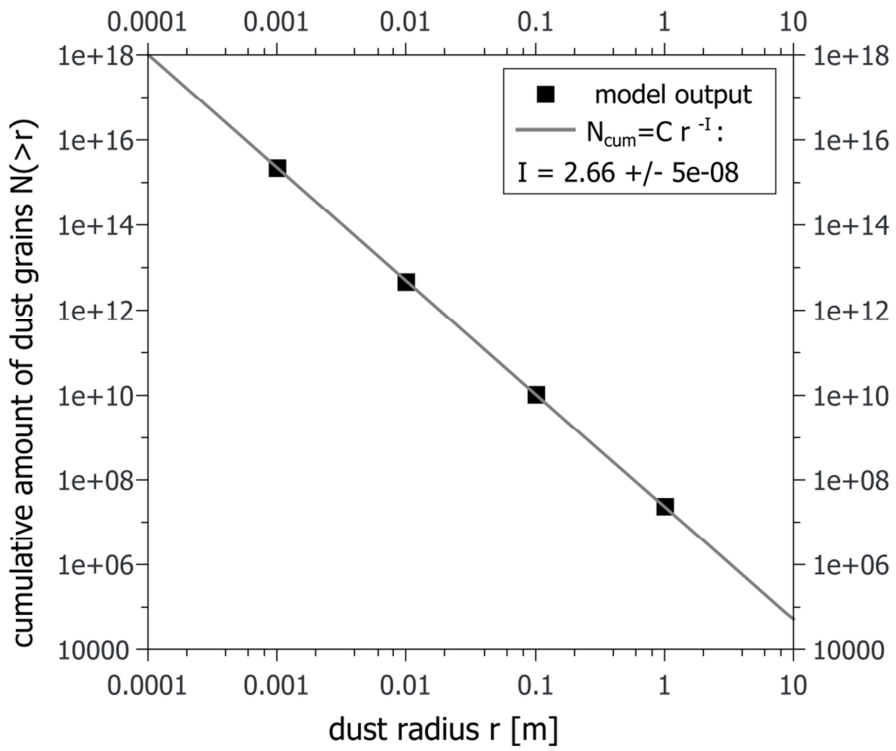

Figure 4-3: Cumulative particle size-frequency distribution. The absolute number of particles is not important for this test and depends on the scale of the test scenario. The relative distribution of the particle sizes is important, and the simulated particles (black squares) reproduce the input power law (solid line).

The new implementation of the code allows for producing representative particles in three ways: i) representative particles can be set manually, ii) representative particles are produced according to scaling relationships (see chapter 8.3 for details), or iii) representative particles are produced during an impact simulation. While the first two approaches require input values or parameters that are used to set the representative particles, the latter approach is a self-consistent way to produce the representative particles directly from the ejected material within the simulated impact event. Once that ejected continuum material in the grid fulfils a transformation criterion (e.g. crossing a predefined altitude), the mass is deleted from a cell of the grid and transferred onto newly produced representative particles. The sizes of the representative particles are defined prior to starting the simulation according to the size-frequency distribution.

For assessing the simulation results of the representative particles calculation, the particle data is stored in an extra file in the “PROGRESS” directory. Furthermore, three fields are stored by iSALE: i) the amount of representative particles per cell (*fRP*), ii) material density of representative particles in a cell (*fRd*), and iii) number density of dust grains per cell (*fRn*).

5 Validation and Resolution Tests

Material models that describe the physical behaviour of a material have to be tested to check if they reproduce a realistic material behaviour. Further, newly developed numerical programmes like the representative particle approach need to be rigorously tested to ensure correct functionality. Both aspects (testing a material model and a new programme) are addressed by this thesis, and testing is performed in different ways:

i) Benchmarking compares numerical results of a programme or material model with results from an already existing code that has already been proven to yield reliable results.

ii) Laboratory experiments deliver a ground truth for any numerical model that can be used for validating the model in order to increase the reliability.

iii) Analytical solutions are exact and provide the best comparison for validating a numerical model.

Benchmarking seems like the weakest form of testing and proving the reliability of the code, but it is better than not performing any kind of comparison. However, it raises the question of why a new programme had to be developed if there was already an existing code to tackle the same task. For example, the representative particles approach is already implemented in the SOVA shock physics code. The new implementation in iSALE allows for combining the strength of iSALE, which lies in the variety of available material models, with the behaviour of ejecta in a gaseous environment, which is the strength of SOVA. As shown in chapter 8, the ejection behaviour depends on the target properties, and simulating ejecta trajectories in a gas benefits from realistic initial ejection conditions.

Laboratory experiments deliver a ground truth with observations under controlled conditions. However, their outcomes also have to be discussed carefully. How well controlled is the experimental set-up? Are there effects that influence the outcome of the experiment that need to be taken into account (e.g. a blast wave in impact experiments)? What are the properties of target materials used in impact experiments? Given such

uncertainties, the most reliable validation that can be done is against an analytical solution of a given problem. Yet, analytical solutions often apply only to simplified problems, which is why numerical modelling is required to solve complex problems.

In this thesis, I validate material models against laboratory experiments and natural observations. These comparisons are important to see if the simulated cratering flow reproduces constraints such as the crater size, so that these material models can, consequently, be applied for the study of ejection processes. In the chapters 3.2.3 and 6, I describe details of the strength model, and I compare the simulated crater (using the material model with a set of experimentally derived strength parameters) with cratering experiments into marble and quartzite targets. This comparison shows good agreement between observed and simulated craters, and it supports the credibility of the material models in iSALE on the laboratory scale. Previous tests of the strength models have been done e.g. by Ivanov et al. (1997), Collins et al. (2004), Elbeshausen et al. (2009), Davison et al. (2011) or Güldemeister et al. (2015).

In chapter 7, I compare simulated funnels in highly porous snow with natural snow funnel observations, which serve as a natural experimental constraint. The material model that is validated in this chapter is the ε-α compaction model, as described in chapter 3.2.5. I also tested the influence of the model input parameters on the funnel formation process. The high porosity and the low impact velocity serve as a kind of end-member scenario in which crater shapes and excavation flow differ from typical cratering processes, and ejection is suppressed nearly completely. Again, the comparison shows that iSALE is capable of reproducing natural observations, and the code seems appropriate for the study of material ejection. Previous tests of the porosity model have been conducted by Wünnemann et al. (2006), Wünnemann et al. (2008), Collins et al. (2011) or Güldemeister et al. (2015).

Having shown that the material models discussed above yield reasonable results not only on a natural scale but also on a laboratory scale, and having shown that porosity compaction is reproduced realistically in the

model, I apply these material models to derive ejection characteristics for a wide range of model material parameters. I validate the approach of ejection analysis, which is shown in chapters 4.2 and 8, by comparing the numerically determined ejection characteristics of a representative material with experimental results of ejection velocity and ejection angles. This validation against experimental results does support the numerical approach for studying material ejection, allowing for a thorough parameter study to determine the influence of material properties on the ejection processes in a vacuum.

In addition to the ejection processes in a vacuum, I studied the interaction of ejected material with a gaseous medium. Including this effect in iSALE required the implementation of a new approach, which was carefully checked during programming and finalisation of the code. This newly implemented representative particle approach was tested in various ways: i) it was tested for correct trajectory calculation in a vacuum for a simple shot scenario; ii) it was tested for trajectory calculation in an atmosphere and determination of correct sedimentation velocities in a simple sedimentation scenario; iii) the code results were tested in a more complex settling scenario by benchmarking against the SOVA code, and iv) the code behaviour was tested under different resolutions. Results of the first test are shown in Figure 5-1 i): Representative particles that are ejected with a velocity of 707 m/s at an angle of 45° move on a trajectory (black line), which matches the ideal analytical parabolic solution in vacuum (red dashed line). Once drag forces are acting on the particles in a gaseous environment, no analytical solution is available for the trajectory in a 45°-shot scenario. Hence, I compare the code results for vertical sedimentation to the analytical equilibrium solution (Eq. (47)) for individual grains of different sizes, which start settling from an initial altitude of 5 km in a resting gas. The scenario and the results are shown in chapter 9, and numerical and analytical results for the velocity agree to within 10%. For demonstrative purpose, I also show the trajectory for the previous 45° shot scenario when drag deceleration by a gas at rest reduces the range of a grain (grey line in Figure 5-1 i). The grain size and mass of the particles for which

I show the trajectory (r=10 m, ρ=2650 kg/m³) is large with respect to the laboratory scale, and the representative particle represents 100 of such big fragments, so that drag deceleration affects the trajectory only at distances larger than 10 km, where the trajectory increasingly bends downwards.

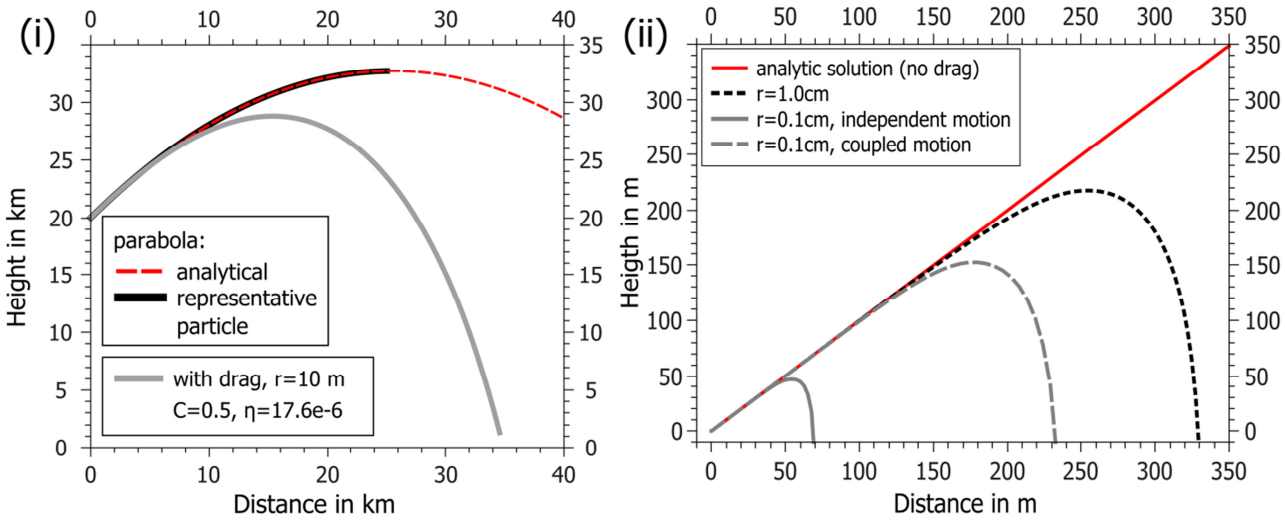

Figure 5-1: Representative particle motion. Panel i) shows results for a representative particle (representing 100 real particles with r=10 m, ρ=2650 kg/m³) that initially moves with a speed of 707 m/s in a 45° direction. The red line depicts the analytical parabolic trajectory under Earth's gravity. The black line shows the trajectory of the representative particle without drag. The grey line shows the movement of the same RP under drag (ρ_{air}=1.3 kg/m³, η=17.6e-6 Pa s, C_D=0.5). ii) Trajectories of different sized dust (1 cm and 1 mm) in an ideal atmosphere. Drag decelerates the particles from their initial velocity of 1 km/s (45°) according to their size, and in the individual model runs, the 1 mm and 1 cm sized dust reaches a distance of ~70 m and ~330 m, respectively. In a coupled run, the cm sized dust follows exactly the same trajectory as in the individual run, but the 100 million mm-sized particles move more than 3 times farther in the coupled run than in the individual run.

The drag force is sensitive to the size of representative particles. Smaller dust grains are decelerated more efficiently than larger ones (Figure 5-1 ii). However, dust with a small size can travel to longer distances if its movement is coupled with dust of a larger size ("drag shielding"). In other words, dust of a larger size can accelerate the gas, and, as such, reduce the velocity difference between gas and dust grains, which inhibits the deceleration of smaller dust grains. In the next test scenario, I show this effect for two particle sizes, 1 mm and 1 cm, in individual model runs as well as in a coupled simulation (Figure 5-1 ii). The initial velocity is 1 km/s

at an angle of 45°. The total mass of the cm-sized dust is about ten times bigger than the mm-sized dust, so that the total dust mass in the individual run (for cm size) and the coupled run (cm and mm size) is about equal. In both the individual and the coupled runs, the cm-sized dust moves along similar trajectories up to a distance to ~330 m. However, the deposition distance of the mm-sized dust increases by more than a factor of 3 from ~ 70 m to 230 m. Although I do not have any benchmark or validation data to check the quantitative outcome of this test, the results support the plausibility of the code and give a qualitative validation.

In order to further support the credibility of the newly implemented representative particle approach, I benchmark it against the SOVA shock physics code, which has gained credibility through various publications using such particles (e.g. Shuvalov 1999; Artemieva and Ivanov 2004; Artemieva et al. 2013; Shuvalov and Dypvik 2013). However, some differences between the results from the two codes in a benchmark test are expected due to code characteristics. For the benchmark, I have chosen a more complex scenario of vertical settling, where the analytical solution does not hold true. The scenario is explained and shown in chapter 9. A large number of representative particles of a given size start settling vertically from an initial altitude of 5 km, and the process is more turbulent than the simple settling of individual particles. In chapter 9, I compare the behaviour of two representative particles derived from iSALE and SOVA, respectively. I also compare the vertical velocity of the gas, which is initially at rest and starts accelerating according to the particle movement. The overall behaviour between both codes agrees, and the error between their results is approximately 10-20%.

Modelling results depend on the resolution that was used for a numerical study, and the results should converge with increasing model resolution. In the following, I show some resolution analyses for the vertical settling scenarios shown before.

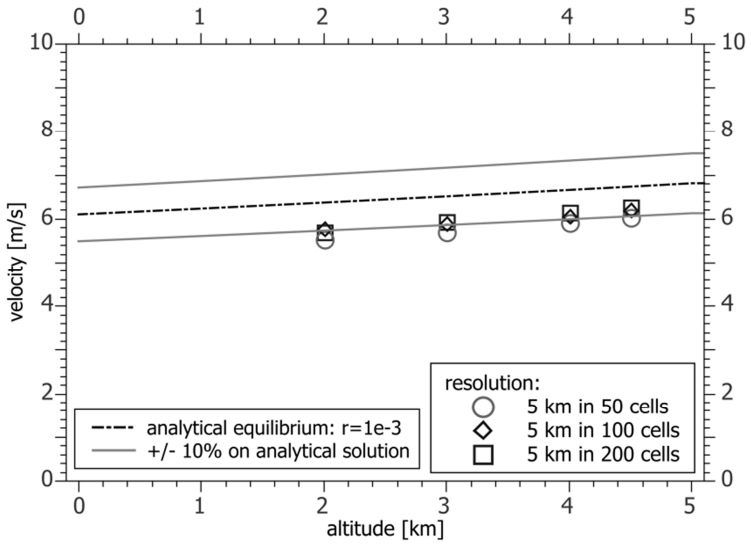

Figure 5-2: Material settling (determined with iSALE): Vertical velocity versus altitude under three grid resolutions for 5 km: 50, 100, and 200 cells. The black dash dotted line shows the equilibrium sedimentation velocity and the grey lines show a 10% range of uncertainty. Representative particles include 1 dust grain with a size of r = 1 mm and an initial velocity of 1 km/s. Note that the surface density in this scenario (1.8 kg/m³) is slightly larger than density of Earth's atmosphere.

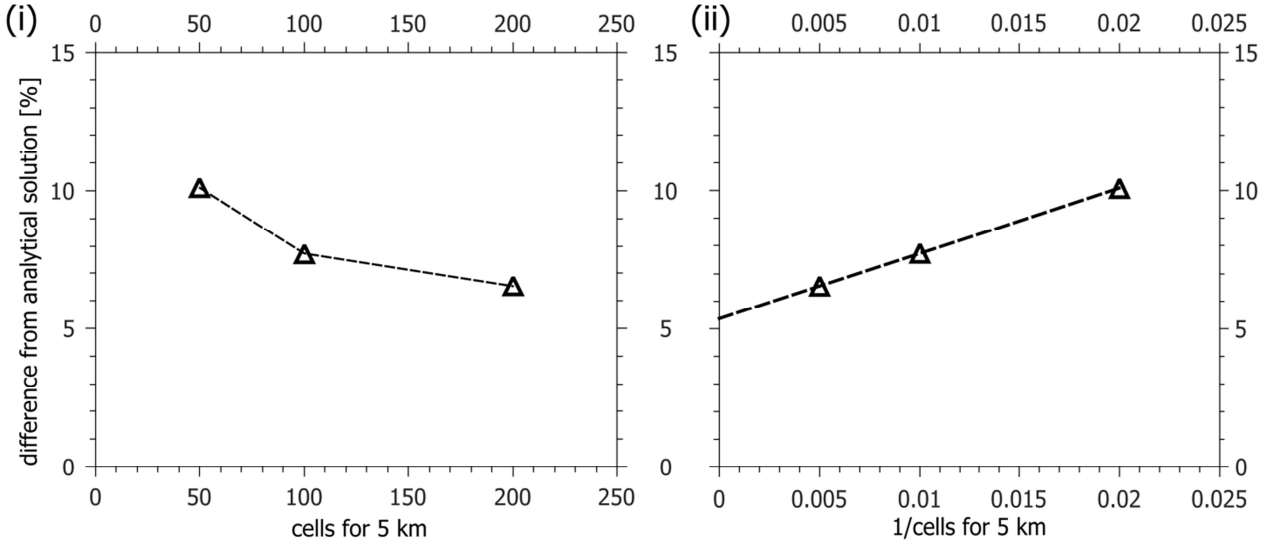

Figure 5-3: Effect of resolution on material settling (determined with iSALE): The difference of the vertical velocity at an altitude of 4 km to the analytical solution is shown for i) different resolutions (amount of cells for an altitude of 5 km), and ii) against the inverse of the amount of cells for an altitude of 5 km. The scenario is the same as in Figure 5-2.

In the representative particle approach, two model resolutions have to be distinguished: i) grid resolution and ii) resolution of dust grains by representative particles, i.e. how many representative particles are used to represent a certain dust mass. I test the dependence on the grid resolution for

the scenario of independent single dust grains settling in equilibrium for dust with a size of r = 1 mm and an initial velocity of 1 km/s at a 5-km altitude resolved by 50, 100 and 200 cells, respectively (Figure 5-2 and Figure 5-3). The results of the different resolution runs fall within 6-10% uncertainty of the analytical solution for the best and the lowest resolution, respectively (Figure 5-3 ii). Linear regression yields a value of ~5% of convergence for increasing resolution. Further differences to the analytical solution might occur due to slight variations in the density of the surrounding gas. Although the resolution does influence the results, this effect is small enough that even the lowest resolution of 50 cells per 5 km yields reliable results.

Furthermore, I test both kinds of resolutions for the scenario of dust settling, with an initial dust layer that has a corresponding thickness of 0.1 m at an initial altitude of 5 km. For testing the grid resolution, 10000 representative particles are distributed equally over a horizontal distance of 5 km. Dust grains are of r = 1 cm in size, and they have an initial velocity of 1 km/s. The initial altitude is resolved by 10, 50, 100, or 500 cells and I compare the evolution of the average altitude of the representative particles (Figure 5-4 i) and the evolution of the vertical velocity component normalised to the sedimentation velocity at zero altitude (Figure 5-4 ii). The results from the model run with a grid resolution of 10 cells for a 5-km altitude deviate from the other resolutions, and particles take about double the time (~80 s) to reach an altitude of 1500 km. The resolutions of 50 and 100 cells show a better agreement with the best resolution. The deviation in altitude from the best resolution model at a time of 20 s is ~12% and ~4% for the 50 and 100 cells resolution, respectively. Similar results can be shown for the evolution of the vertical velocity. The velocities of the three models with better resolutions are similar to each other. Only for the lowest resolution of 10 cells are there significant deviations from the best resolution (Figure 5-4 ii).

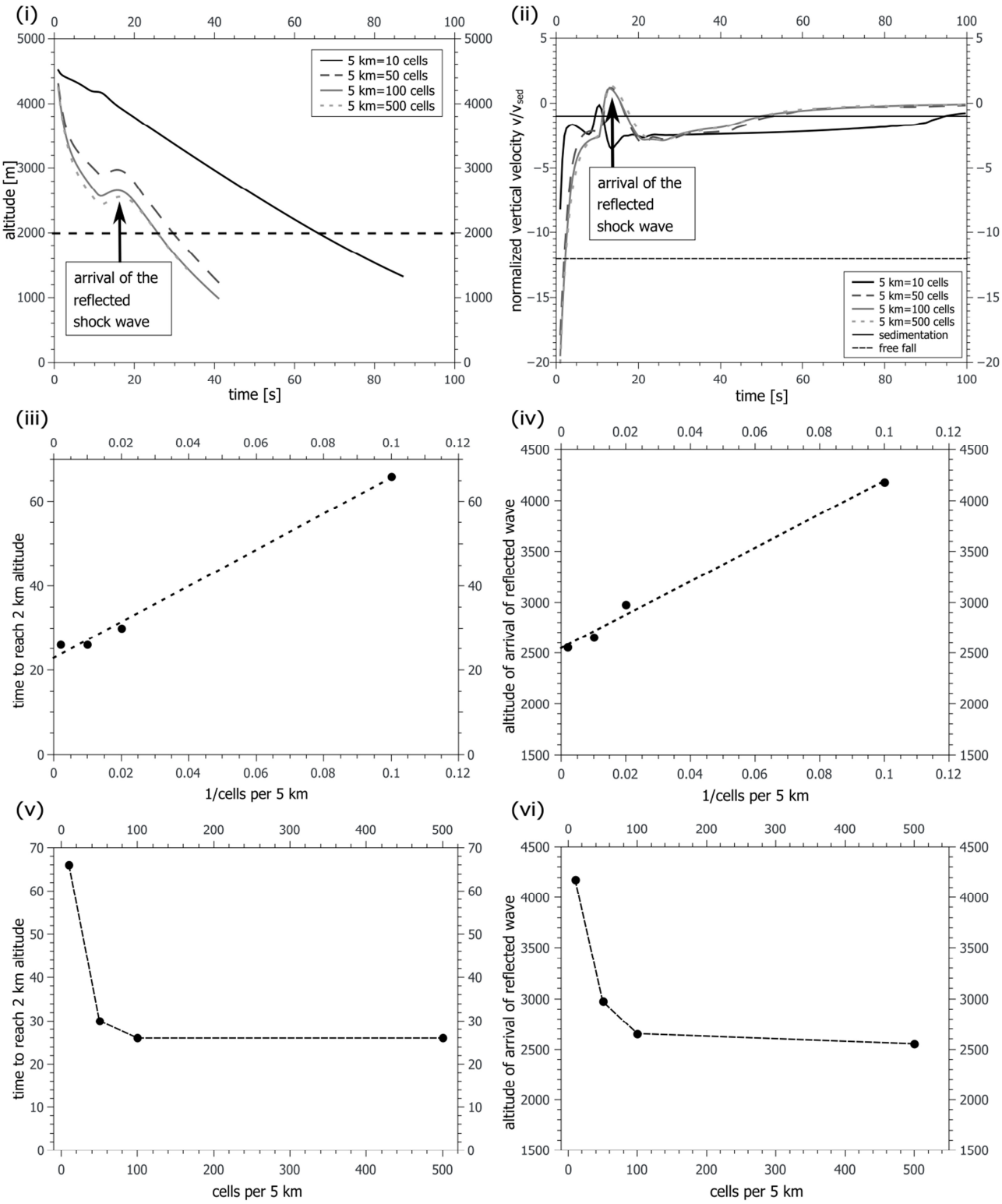

Figure 5-4: Material settling under four grid resolutions for 5 km: 10, 50, 100, and 500 cells (determined with iSALE). Altitude i) and normalised vertical velocity ii) are shown as functions of time. The velocity is normalised to the sedimentation velocity at the surface level. The solid and dashed horizontal lines in ii) depict the sedimentation velocity and the free fall velocity, respectively. The resolution is analysed against the inverse of the amount of cells for an altitude of 5 km by comparing the following values: iii) settling time of representative particles to reach the altitude of 2 km (dashed line in i), and iv) the altitude of the arrival of the

reflected shock wave in air from the surface, which can be recognised by the bump in i) and ii). Panels v) and vi) show the convergence of the analysed values against the resolution. The initial layer thickness is 0.1 m with dust particles of a size of r = 1 cm and an initial velocity of 1 km/s. The dashed lines in iii) to vi) depict the convergence against the resolution.

The convergence with increasing model resolution is shown for the settling time to reach an altitude of 2 km (Figure 5-4 iii, v), and for the altitude of the arrival of the surface-reflected shock wave (Figure 5-4 iv, vi), which affects the particle motion by temporarily inverting the vertical velocity (Figure 5-4 ii) and lifting up the particles for a moment (Figure 5-4 i). In principle, only the resolution of 10 cells per 5 km shows large deviations in the results, which must be considered as too large to be reliable. All other tested resolutions yield reasonable results close to the convergence values for "infinite resolution". In chapter 9, I use a resolution for the vertical settling scenarios of 50 cells, which has a slightly larger error than other tested resolutions of 100 and 500 cells, but it allows for running more models in a parameter study without spending too much computation time.

The second kind of resolution is given by the number of representative particles that represent the same mass of dust. I test resolution regarding the number of representative particles for the same scenario as for the grid resolution, and I choose 100 and 10000 representative particles to represent the total mass of dust; i.e. one representative particle for the lower resolution contains 100 times more dust grains than in the model with better number resolution. Hence, I set 1 and 100 representative particles per cell, respectively. An even lower resolution would imply that some cells do not contain representative particles, which was not tested. Again, I plot the evolution of the average altitude (Figure 5-5 i) and the average vertical velocity normalised to the sedimentation velocity (Figure 5-5 ii). For an increase in the particle resolution by two orders of magnitude, the difference of the average particle altitude is less than ~4% (Figure 5-5 i). Also the vertical velocities of both models agree with each other. Due to this level of agreement between the two resolutions, I do not show any convergence plot. The general (i.e. average) evolution is equal in both models, and the first

representative particles reach the ground after 40 s in both cases. As a consequence, the model with the lower resolution of 1 representative particle per cell is sufficient to simulate the average material flow, and it requires less computational effort (regarding memory and computation time).

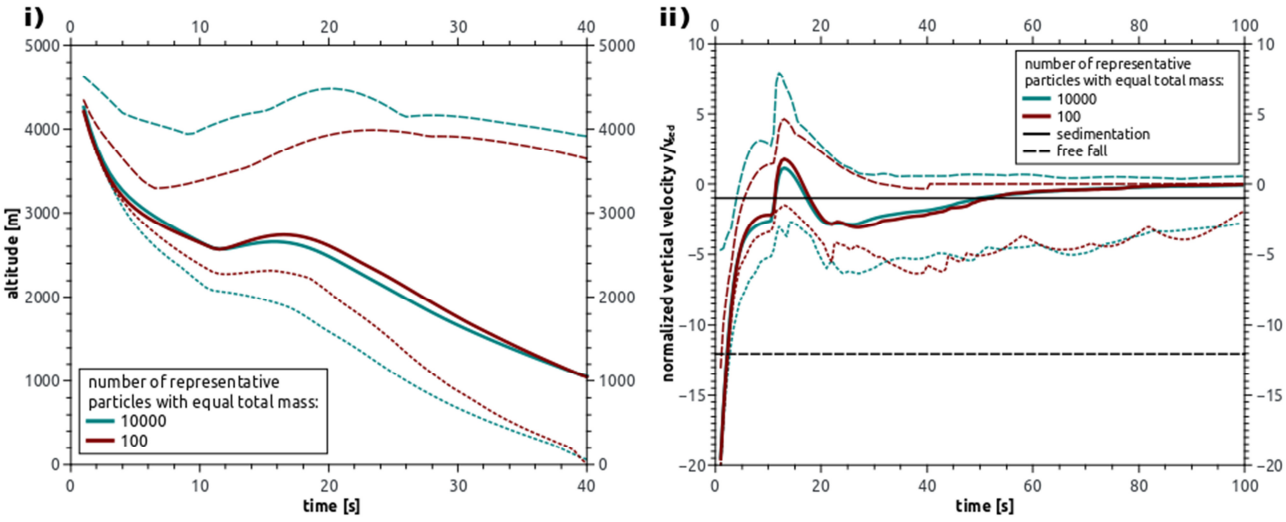

Figure 5-5: Material settling for two resolutions regarding the number of representative particles: 100, and 10000. Altitude i) and normalised vertical velocity ii) are shown as a function of time (determined with iSALE). Initial layer thickness is 0.1 m with dust of a size of r = 1 cm and an initial velocity of 1 km/s. The velocity is normalised to sedimentation velocity. The black solid line shows the sedimentation velocity, and the dashed line shows the free fall velocity. Dashed and dotted coloured lines give the maximum and minimum values of all representative particles, respectively.

In addition to the average values, I also plot the maximum and minimum values of altitude and velocity for all representative particles. Maximum and minimum values for both altitude and vertical velocity depend much more on the resolution and deviate to a larger extent than the average values (e.g., there is a difference of ~20% in the maximum altitude of representative particles after ~10 s of sedimentation, Figure 5-5 i). The model with a lower representative particle resolution shows a smaller spread between minimum and maximum values. This can be explained by the larger initial scatter in the distribution of representative particles per cell for the better resolution scenario, and by the ability to simulate more details in the dust evolution when a better resolution is used. Consequently, a larger particle resolution is required for deriving detailed results, including the

range of minimum and maximum outcomes, while the lower resolution is sufficient for analysing the average results. In chapter 9, I studied the average behaviour of vertical settling, and I used the lower resolution of 1 representative particle per cell in the scenario of dust with an initial velocity of 1 km/s, but I also included the average values of the model runs with a resolution of 100 representative particles per cell when dust is initially at rest.

Having done thorough testing, as shown above, to answer objective *M III – Representative Particles*, the representative particle approach was applied to tackle the key question *S II – Ejecta and Atmosphere* on the deposition of ejecta in an environment with an atmosphere in chapter 9. However, before I come to key question *S II*, I show results that address objectives *M I – Material Models* and *M II – Ejecta Analysis* in chapters 6 - 8, and address the key question *S I – Ejecta and Target Properties* on ejection dynamics with respect to different target properties and the ejecta deposition in a vacuum in chapter 8.

6 Subsurface deformation of experimental hypervelocity impacts in quartzite and marble targets

This chapter has been published as the following peer-reviewed article:

Rebecca Winkler, Robert Luther, Michael H. Poelchau, Kai Wünnemann, Thomas Kenkmann (2018). *Subsurface deformation of experimental hypervelocity impacts in quartzite and marble targets*. Meteoritics & Planetary Science 53 (8), 1733-1755, http://dx.doi.org/10.1111/maps.13080.

This chapter addresses the objective *M I – Material Models*: Does iSALE allow for modelling impact craters, and does iSALE reproduce experimental results? The code is capable of simulating rheologies of increasing complexity from constant yield surfaces to parametrisations that include damaging of material and a corresponding reduction in strength (cf. chapter 3). However, detailed comparisons between numerical experiments and laboratory studies have mostly be conducted in granular (sand-like) targets (Wada et al. 2006; Hermalyn and Schultz 2011; Wünnemann et al. 2016) or metals, like aluminium (Pierazzo et al. 2008). Within the framework of MEMIN, shooting campaigns were conducted using competent rock targets like sandstone, quartzite, or marble. Comparisons for sandstone and quartzite were done during the first phase of MEMIN by Güldemeister et al. (2015). In the following chapter, laboratory marble craters are compared to numerical results. In contrast to previous studies with quartzite and sandstone, marble shows a much more pronounced dynamic hardening (Zwiessler et al. 2016), i.e. craters are smaller than what would be expected from static strength measurements.

All authors prepared or participated in the shooting campaign at the Ernst-Mach Institut in Freiburg in 2014, such that all authors made decisions on the target and projectiles used, prepared the experimental set-up before the shot, and recovered the cratering results, e.g. the ejecta catchers. After the campaign, I modelled the impacts into marble and quartzite with iSALE, and I produced the corresponding figures and text. I also looked for further experimental constrains to explain the deep-reaching

"fingers" of volumetric strain that could not be observed by the analysis in this article. However, Raith et al. (2018, same Special Issue) was able to show deeper-lying impact effects within the target.

The editorial work was done by the first author, Rebecca Winkler, who wrote most of the text. She did the laboratory analysis together with M. Poelchau and T. Kenkmann. M. Poelchau estimated the transient crater size for the quartzite target, which is important for comparing numerical and experimental results. I carefully discussed the manuscript with R. Winkler, and together we correlated modelling results and the laboratory data. During the review process, we were suggested to enhance this interdisciplinary presentation of the results, which I intensively discussed with R. Winkler, so that we intensified the interlinkage between model and laboratory craters in the discussion section.

6.1 Abstract

Two impact cratering experiments on non-porous rock targets were carried out to determine the influence of target composition on the structural mechanisms of subsurface deformation. 2.5 mm diameter projectiles were accelerated to ~5 km s^{-1} and impacted into blocks of marble or quartzite. Subsurface deformation was mapped and analysed on the microscale using thin sections of the bisected craters. Additionally, both experiments were modelled and the calculated strain zones underneath the craters were compared to experimental deformation features. Microanalysis shows that the formation of radial, tensile and intra-granular cracks is a common response of both non-porous materials to impact cratering. In the quartzite target, the subsurface damage is additionally characterized by highly localized deformation along shear bands with intense grain comminution, surrounded by damage zones. In contrast, the marble target shows closely spaced calcite twinning and cleavage activation. Crater diameter and depth as well as the damage lens underneath the crater are unexpectedly smaller in the marble target compared to the quartzite target, which is in contradiction to the marble's much weaker compressive and tensile strengths. However, numerical models result in craters that are similar in size as well as in strain

accumulation at the end of transient crater formation, indicating that current models should still be viewed cautiously when compared to experimental details.

6.2 Introduction

During a hypervelocity collision with a spherical projectile a large fraction of the projectile's kinetic energy is deposited in the target and emanates from the point of impact as a hemispherically spreading shock wave. Peak shock pressures near that point of impact may reach several 100 GPa. Shock pressures decrease as the wave expands due to spatial spreading, energy consumption by rock deformation, and decay through a rarefaction wave that propagates faster than the shock wave (e.g. Melosh 1989). While the initial shock pressure near the impact point is well above the rock´s Hugoniot elastic limit (HEL) - the pressure at which the elastic stress trajectory exceeds the compressional failure envelope - it falls with increasing radial distance first to pressures around the HEL in the elastic decay regime and then to compressional pressures below the HEL. Note that rocks typically have higher compressive than tensile strengths, thus tensile failure can still occur after pressures have fallen below the compressional HEL (Melosh 1989). The different pressure stages create different deformation microstructures in target rocks characteristic for the distance from the point of impact. The exact material response, i.e. fracture propagation and localization behaviour of damage, is intrinsic to the type of rocks in use (Holsapple and Schmidt 1982). This, in turn, is related to the mechanical properties of its minerals phases that constitute the rock. Non-porous rock types can develop distinct deformation patterns under similar impact conditions owing to varying material properties (Hörz 1969; Polanskey and Ahrens 1990). Shape and crystallographic preferred orientations of the mineral constituents may lead to strength anisotropies and add complexity to the mechanical response to dynamic loading of the rocks.

To investigate the deformation of different targets, we conducted two hypervelocity impact experiments using quartzite and marble under

similar impact conditions. These two target materials were chosen because roughly one third of the Earth´s known impact craters formed in sedimentary targets of which many contain carbonates as an important sedimentary rock and another third formed in mixed crystalline and sedimentary targets (Earth Impact Database, 2016). A number of experiments into non-porous rocks like granite (Hörz 1969; Burchell and Whitehorn 2003), basalt and gabbro (Gault and Heitowit 1963; Moore et al. 1963; Lange et al. 1984) have been investigated, but only a few cratering experiments have been conducted in carbonates (Schneider and Wagner 1976; Lindgren et al. 2011; Kurosawa et al. 2012). The crater subsurfaces of these experiments have only been analysed macroscopically, without correlating them with stress stages induced by the shock wave. To date few studies by, e.g., Polanskey and Ahrens (1990), Ai and Ahrens (2004), Lindgren et al. (2011) as well as Buhl et al. (2013, 2014a) and Winkler et al. (2016) have focused on fracture patterns and their corresponding stress stages in experimentally generated crater subsurfaces. Despite differences in lithology and porosity, certain deformation features like cracks with radial orientation to the impact point, or tensile fractures oriented subparallel to the crater surface, are common in all targets. The former result from hoop stresses that develop as a consequence of the hemispherically expanding compression wave (Ai and Ahrens 2004), the second occur when the rarefaction wave passes through the rock (Polanskey and Ahrens 1990).

This paper presents a detailed analysis of microscopic deformation features of two impact cratering experiments conducted with quartzite and marble targets and links the findings to specific deformation phases created by the expanding shock wave. Both experiments were also modelled, utilizing the state-of-the-art shock physics code iSALE-2D. This code has successfully been compared to experimental and observational constraints of natural materials (e.g. Güldemeister et al. 2013; Wünnemann et al. 2016; Luther et al. 2017a) and uses validated parametrizations of target characteristics (e.g. Collins et al. 2004; Wünnemann et al. 2006; Melosh 2007).

6.3 Methods

6.3.1 Target materials

Quartzite and marble were used as natural target materials with a very low porosity. Quartzite and marble are chemically relatively pure and mineralogically homogenous and hence suited to test impact cratering on metamorphic silicate and carbonate targets.

Carrara Marble of White Carrara Venatino type was quarried by the Amso International Company in northern Tuscany, Italy. All Carrara marbles belong to the lower to middle Liassic carbonate platform of the former Italo-Adriatic continental margin. During the Apennine orogeny, the limestones underwent a greenschist facies metamorphism and form today's homogenous Carrara marbles with ~98 vol% calcite and traces of quartz, mica and dolomite. Grain boundaries are slightly sutured, but the grains show little undulose extinction. The mean grain size is 80 – 100 µm and the average porosity is ≤ 1%. There is no recognizable anisotropy of grain size.
Taunus Quartzite was quarried by the Taunus-Quarzit-Werke GmbH & Co. KG, Wehrheim, Germany. The Taunus Quartzite was formed by a low-grade Variscan metamorphosis that overprinted a 405 Ma old sandstone. It consists of ~91 vol% quartz and additionally comprises a greenish, fine-grained phyllosilicate-bearing matrix (~8 vol%) along with small amounts of rutile, chromite, zircon, monazite, and iron oxides. Some grain boundaries are sutured, and grains show undulose extinction. The average size of the quartz grains is 100 - 125 µm and the average porosity is ≤ 1%. There is only negligible anisotropy of grain size, which does not influence the impact experiment.

6.3.2 Experimental Setup

Two impact experiments were carried out with a two-stage light gas gun at the Fraunhofer Ernst-Mach-Institute for High-Speed Dynamics in Freiburg (EMI), Germany. The so-called space light-gas gun (SLGG) with an 8.5 mm calibre launch tube was employed to accelerate spheres (iron

meteorite or steel) of 2.5 mm diameter to impact speeds of ~5 km s^{-1}. The steel and iron meteorite projectiles impacted onto a cube of marble (25 cm edge length) and quartzite (20 cm edge length), respectively. The ambient pressure in the target chamber was reduced to 0.001 bar and 0.1 bar for marble and quartzite, respectively, during the experiments. The varying impactor materials and speeds, as well as different ambient pressures used in the experiments lead to a difference in impact energy of ~20%. The varying shot parameters have their origin in the composition of the multidisciplinary experimental campaigns of the MEMIN network that make compromises necessary. As the focus of this study is on subsurface deformation styles and not on crater sizes, the twenty percent difference in impact energy is acceptable. It cannot explain the observed differences in deformation. The different ambient pressure in the target chambers is negligible for our study, since it doesn't affect subsurface deformation. All experimental parameters are listed in Table 6-1. For details of the accelerator and the exact experimental assembly we refer to Schneider and Schäfer (2001), Kenkmann et al. (2011), Poelchau et al. (2013), and **Kenkmann et al. (2018)**.

Table 6-1**:** Overview of target and experimental parameters

	A34–5614	A20–5339
Target material	Marble	Quartzite
Target density [g/cm³]	2.7	2.6
Target UCS[a] [MPa]	60 ± 8	292 ± 39
Target tensile strength [MPa]	7.3 ± 2.6	16.7 ± 1.3
Target dimensions [cm]	25 x 25 x 25	20 x 20 x 20
Projectile material	Campo del Cielo iron meteorite	D 290-1 steel
Projectile diameter [mm]	2.5	2.5
Projectile density [g cm^{-3}]	7.76	8.1
Projectile mass [g]	0.0635	0.0669
Impact velocity [km s^{-1}]	~5 [b]	5.43
Kinetic energy [J]	~794 [b]	986

[a] Uniaxial Compressive Strength

[b] Velocity was not measured due to technical issues

6.3.3 Sample preparation and image acquisition

The target blocks were weighed to determine the excavated masses directly after the experiments. Crater sizes and morphologies were analysed with a high-resolution 3D laser scanner (Dufresne et al. 2013). For thin section preparation, the crater cavities were impregnated with low-viscosity epoxy to preserve porosity and microstructures. The target blocks were bisected through the crater centre and thin sections of the crater subsurface were prepared.

Photo-mosaics of scanning electron micrographs acquired with a Zeiss Leo 1525 field-emission scanning electron microscope (FE-SEM, ALU Freiburg) in secondary electron (SE) mode, at 20 kV accelerating voltage and 9 mm working distance, were stitched together and cover the whole crater subsurface of both craters. 450 micrographs were used for the marble mosaic and 600 micrographs for the quartzite mosaic. The micrographs of both experiments were taken with identical 100-fold magnification and a resolution of 3072 x 2304 px (1 px equals 380 nm). The stitched composite images cover the complete width of the thin section, approximately 2.3 cm, and about half its length (1.8 cm).

In addition, individual back-scattered electron (BSE) images, at 20 kV accelerating voltage and 8.5 mm working distance were taken of both marble and quartzite targets. The resolution is again 3072 x 2304 px and the magnification varies between 1000-fold and 3000-fold.

6.3.4 Porosity determination and deformation mapping

The acquired images and photo-mosaics were used to quantitatively analyse microstructural deformation in the crater subsurface. The digital image analysis software ImageJ was used for porosity determination, using a grey-scale threshold approach. To analyse the diverse and ubiquitous microstructures the geographic information system ArcGIS (ESRI Inc.) was used. Cracks within mineral grains, fractures extending over several grains, and grain boundaries were mapped as polylines. Area-measured features

that include several grains and grain fragments were mapped as polygons. In detail the following deformation markers were determined:

1) Pre- & post-impact porosity
2) Grain size distribution
3) Different deformation micro-features and
4) Orientation analysis of these micro-features.

For a detailed description of the procedural methods, see appendix 1 A - D.

6.3.5 Numerical Modelling

The experimentally produced deformation features as well as the depth of the impact-influenced zone were compared to numerical simulations. The simulations provide information about the total plastic strain distribution and strain rate decay with distance from the crater floor. The experimental setup is simulated using the iSALE-2D Eulerian shock physics code (Wünnemann et al. 2006) in the "Chicxulub" version , which is based on the SALE hydrocode solution algorithm (Amsden et al. 1980). To simulate impact processes in solid materials SALE was modified to include an elasto-plastic constitutive model, fragmentation models, various equations of state (EoS), and multiple materials (Melosh et al. 1992; Ivanov et al. 1997). More recent improvements include a modified strength model (Collins et al. 2004) and the ε-α porosity compaction model (Wünnemann et al. 2006; Collins et al. 2011).

The thermodynamic material response was modelled using the Analytical Equation of State (ANEOS) for iron (projectile material, Thompson and Lauson 1972), marble (experiment A34–5614, Pierazzo et al. 1998), and quartzite (experiment A20–5339, Melosh 2007).

To model the strength Y of the target during crater formation, the constitutive model proposed by Collins et al. (2004) was used. The strength of the target depends on the confining pressure and the state of damage that the material has witnessed. Details are given in the appendix 2. The strength of the spherical projectile was neglected, since its strength does not control the crater size.

For the projectile a resolution of 30 cells per projectile radius (CPPR) was used. The grid was set up with 1200-1300 horizontal and 1600 vertical cells for the targets. 100-125 cells were added to the sides with 5% increase in cell-size from each cell to the neighbouring cell, and 200 and 50 of these cells to the bottom and top of the grid, respectively. The grid size represents the target in size for the models. Due to the available target geometry in the model setup, the cubic target is approximated by a cylinder of equal length and diameter as the block size. For a more detailed description of the simulation and a table summarizing all input parameters see appendix 2.

6.4 Results

6.4.1 Crater morphology

Both craters have shallow dipping rims and low depth/diameter (d/D) ratios (Figure 6-1). The marble crater has a volume of 3.9 cm^3, a diameter of 56.6 ± 4.2 mm and a depth of 6.0 ± 0.4 mm, resulting in a d/D ratio of 0.11 (Table 6-2). The crater formed in marble has no central depression that could be distinguished from the spallation surface based on slope angles or textural differences. Instead, the crater has a thin rim of 7 – 9 mm width along its outer margin with very shallow slope angles of only 5 – 15°, while the rest of crater has homogenous slope angles of 20 – 25°. The crater volume of the quartzite crater is 5.7 cm^3, and the crater diameter is 73.0 ± 12.8 mm with a depth of 10.6 mm, resulting in a d/D ratio of 0.15 (Table 6-2). The crater shows a central depression zone with a diameter of ~15 – 10 mm that contains brighter, highly fragmented target material, surrounded by an outer spallation zone. The central depression has an angle of 20 - 30° to the target surface, while the spallation zone has a slope angle of 15 – 20° (Figure 6-1). The outer part of the quartzite crater morphology is characterized by deep spall fractures that form a nearly complete second rim around the inner spallation surface. The crater in the quartzite target is thus bigger and deeper than the crater in the marble target, partly owing to a

bigger impact energy in the quartzite experiment. The calculated equivalent depth of burial is defined as:

$$d_b = d_p \sqrt{\frac{\rho_p}{\rho_t}} \tag{68}$$

where d_p is the projectile diameter, ρ_p is the projectile density and ρ_t is the target density (Melosh 1989). It is nearly identical for both experiments with 4.4 mm and 4.3 mm for the quartzite and marble experiment, respectively.

Table 6-2**:** Overview of experimental parameters and crater morphology.

	A34–5614 (marble)	A20–5339 (quartzite)
Crater diameter (mm)	57 ± 4	73 ± 13
Crater depth (mm)	6 ± 0.4	11
Diameter/depth ratio	0.11	0.15
Crater volume (mm³)	3869 ± 120	5670 ± 140
Depth of burial (mm)	4.3	4.4

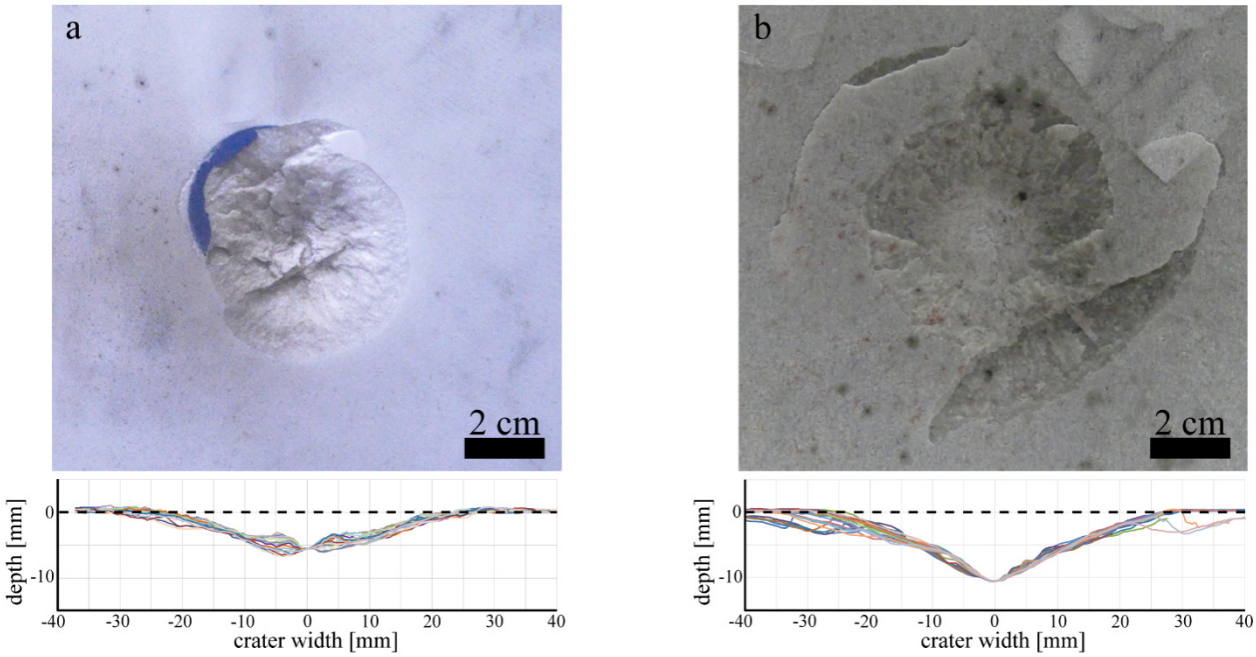

Figure 6-1: Marble and quartzite craters. a) Plan view of the marble crater (A34-5614). The profile lines (bottom) are generated from 3D scans at 10° steps rotated around the crater centre. The profiles show a lack of a central depression compared to the quartzite crater. b) Plan view of quartzite crater (A20-5339). Note the outer second rim of pervasive incipient spall, as well as the brighter crater centre. The profile lines show a steepening of the crater slope towards central depression, visible as the bright central area in the photograph.

6.4.2 Porosity

The two cratering experiments show increased impact-induced secondary porosity in the crater subsurface, which decreases with depth from the crater floor (Figure 6-2c & g). Both target materials have less than 1% initial porosity. The measured porosity is caused by dilatation processes during the impact, which create tensile fractures and open voids.

In the marble experiment (A34-5614) (Figure 6-2a-d) the impact-induced porosity directly at the crater floor is 12% and thus much lower than in the quartzite target (Figure 6-2g). Porosity increases up to ~14% at 1.3 mm or 0.5 d_p (projectile diameters; 1 d_p = 2.5 mm) depth, where a dominant tensile fracture crosscuts the depth profile. From this point, porosity decreases down to a depth of ~1.75 d_p (4.4 mm), where the pre-impact porosity of the target is reached. Due to a breakout during thin section preparation at 1.25 d_p (3.1 mm) depth this porosity value is not measured. Instead the values of porosity at 1.0 d_p (2.5 mm) and 1.5 d_p (3.75 mm) depth are directly connected on Figure 6-2.

The quartzite experiment (A20-5339) shows a very high value of impact-induced secondary porosity (32%) directly at the crater floor (Figure 6-2e). This is a result of the formation of extensive tensile fractures, which partially or completely separate large flake-like pieces from the more continuous crater floor. These tensile fractures become narrower with increasing distance to the crater floor. At a depth of ~1 d_p (2.5 mm), the ratio between tensile fractures, open grain boundaries and intra-granular fractures is balanced. Between 1 d_p and ~2.75 d_p (6.9 mm) depth, secondary porosity values decrease constantly until the initial porosity of < 1% is reached.

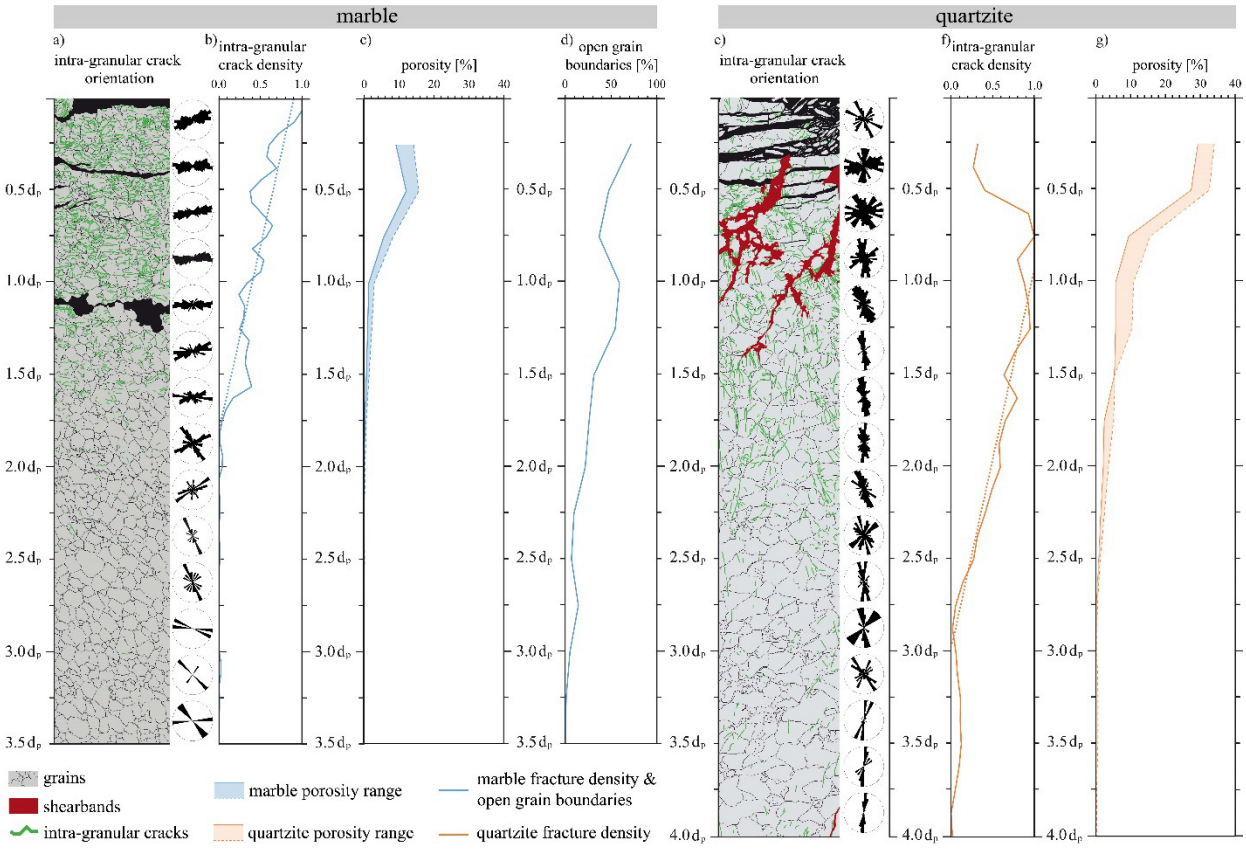

Figure 6-2: Subsurface damage mapping in marble (a) and quartzite (e) targets showing intra-granular crack orientation (a & e), intra-granular crack density (b & f), impact-induced porosity (c & g) and open grain boundaries (d) versus depth in projectile diameters (d_p). a) and e) show rose diagrams of intra-granular crack orientations in 0.25 d_p (0.625 mm) sections of marble and quartzite. The marble in a) shows a preferred orientation of intra-granular cracks subparallel to the crater floor down to a depth of 1.75 d_p (4.4 mm). Below that depth no preferred orientation is visible. In the quartzite target in e) cracks show a bimodal preferred orientation with sub-horizontal and radial cracks within 1 d_p (2.5 mm) below the surface. Below 1 d_p cracks show a preferred radial orientation. b) and f) show the intra-granular crack density of marble (b) and quartzite (f) target, normalized to the highest value. Both density curves decrease linearly with distance to the crater floor. However, the quartzite curve shows an increase in intra-granular cracks over the first 0.5 d_p (1.25 mm), due to the intense tensile fracturing (see black areas in e) before it decreases. Background density levels are reached for marble at 1.75 d_p (4.4 mm) depth and for quartzite at 2.9 d_p (7.25 mm) depth. c) and g) show the impact-induced porosities of the marble (c) and quartzite (g) target. Deviations between min and max values are caused by applying different gray-scale thresholds for the image analyses. We estimate the error in porosity values to be ± 2%. d) Open grain boundaries in the marble target. Within the first 0.25 d_p (0.63 mm) open grain boundaries dominate. Between 0.25 d_p and 1.00 d_p (0.63 – 2.5 mm) depth the percentage of open and closed grain boundaries is roughly equal. Below 1.00 d_p (2.5 mm) depth closed grain boundaries dominate.

6.4.3 Grain size analysis

Both quartzite and marble have a fairly uniform pre-impact grain size distribution with mean grain sizes of ~125 µm and ~90 µm, respectively. Grain sizes beneath the crater floor, however, are strongly influenced by impact-induced fractures and led to a notable decrease in overall grain size in both experiments. The grain size distribution analysis also reflects the degree and depth of deformation in the crater subsurface. For both experiments only, grains larger than 10 µm² were taken in account, due to image resolution.

Figure 6-3a shows the distribution curves of the marble experiment (A34-5614). A decrease in large grain sizes along with a strong increase in very small grain sizes can be seen within the first 0.75 d_p (1.9 mm). The depth interval between 0.75 d_p and 1.25 d_p (1.9 – 3.1 mm) is a transition zone. Its grain size distribution seems to reflect an intermediate stage for both small and large grain sizes between a heavily influenced rim region and the undisturbed pre-impact distribution. Below 1.25 d_p (3.1 mm) no further changes in grain size occur.

The grain size distribution of the quartzite experiment (A20-5339; Figure 6-3b) shows a pronounced concentration of small grain sizes, combined with a lack of large grain sizes directly at the crater floor (0 – 0.25 d_p/ 0 – 0.63 mm). To a depth of 1.75 d_p (4.4 mm) grain sizes gradually become more evenly distributed. Between 1.75 d_p (4.4 mm) and 3.00 d_p (7.5 mm) depth the background scatter of the very small grain sizes (10 – 200 µm²/ 4 – 8 µm) is reached, as compared to the pre-impact grain size distribution. However, average pre-impact grain size is not yet restored. Below 3.00 d_p (7.5 mm) the grain size distribution reaches the undeformed distribution.

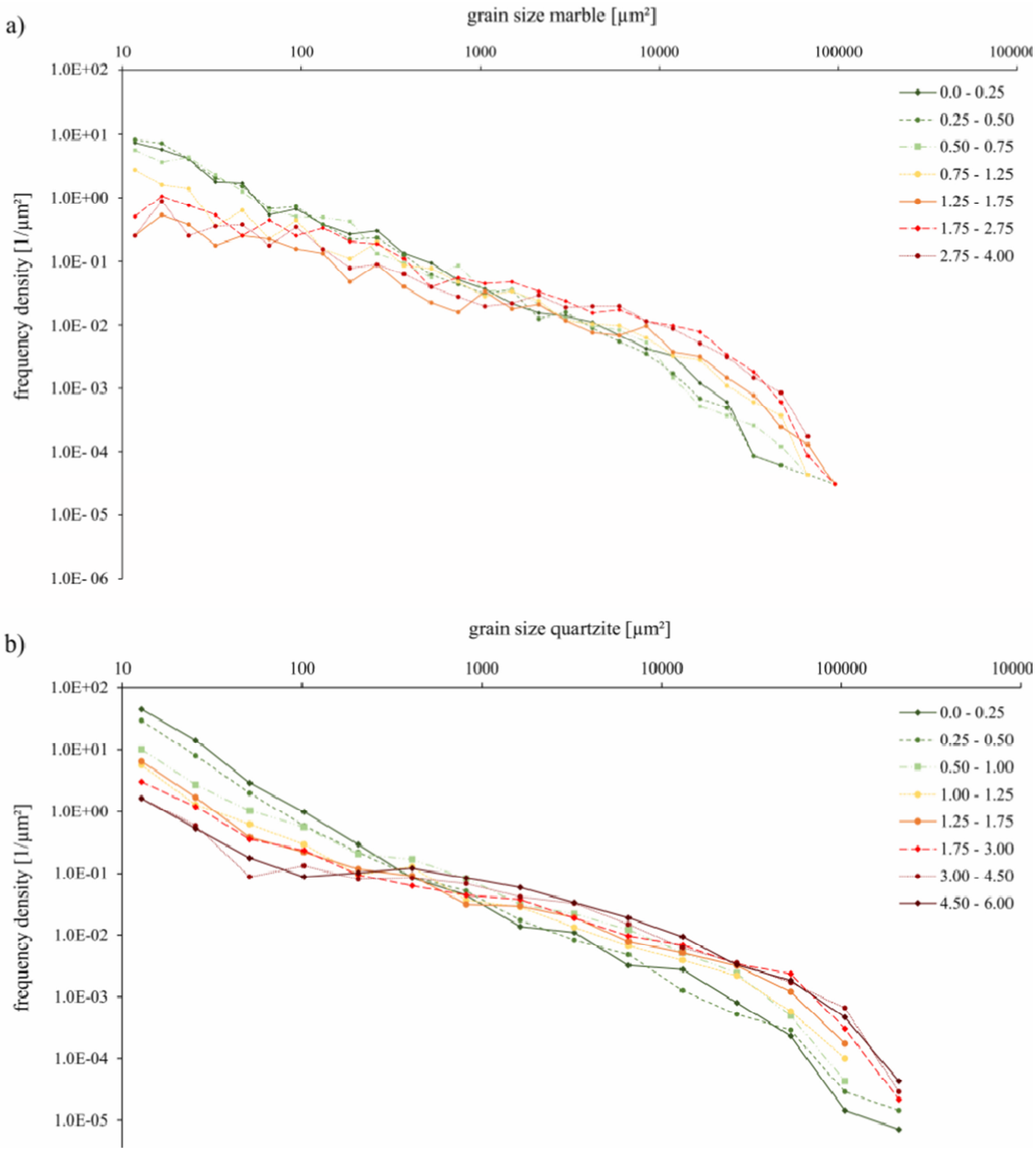

Figure 6-3: Development of the grain size frequency density with increasing depth beneath crater floor (given in projectile diameters; 1 d_p = 2.5 mm) of the marble (a) and the quartzite (b) experiment. A) The uppermost three distribution curves (green) show very little difference in grain size, while the yellow curve (0.75 d_p - 1.25 d_p/ 1.9 – 3.1 mm) shows an intermediate grain size distribution between the highly comminuted rim and undamaged deep regions. B) The distribution curves show a successive shift from a highly comminuted crater floor (green) towards the original grain size below 3.00 d_p (7.5 mm) depth (dark red). Note that step sizes for the depths of the curves (given in d_p) are variable.

6.4.4 Deformation microstructures

Deformation microstructures of the two impact experiments have been mapped based on SEM-BSE micrograph mosaics. Tensile fractures and intra-granular cracks (Figure 6-4 a, b) are found in the subsurfaces of both experiments. All concentrically oriented fractures that exceed the grain scale were mapped as tensile fractures. In marble, grain boundaries are only occasionally included in tensile fractures. In quartzite, grain boundaries are more commonly included within tensile fractures. Intra-granular cracks in quartzite are straight or only slightly bent, while intra-granular cracks in marble are more typically kinked. The formation of twin lamellae and open cleavage is restricted to marble, while quartzite deformation is characterized by the formation of shear bands with intense grain comminution (Figure 6-4c).

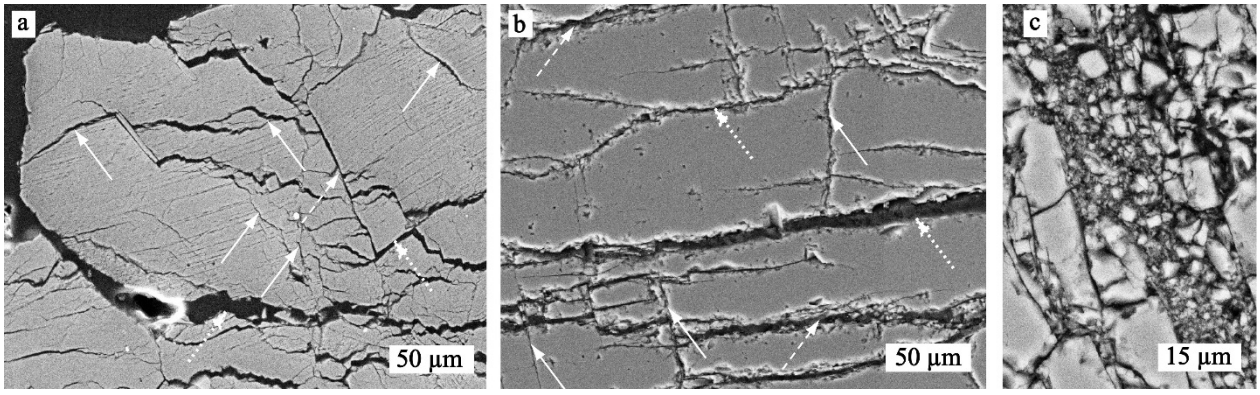

Figure 6-4: Examples of tensile fractures (dotted arrows), intra-granular cracks (solid-line arrows) and grain boundaries (dashed arrows) in a) marble and b) quartzite. C) shows a shear band in quartzite with intense grain comminution.

Marble

Intra-granular cracks in marble are < 5 to ~300 µm in length and have widths of at least 2 µm. An intra-granular crack density was calculated along the central profile down to 3.5 d_p (8.8 mm). Figure 6-2b shows that the intra-granular crack density decreases with increasing distance to the crater floor until the background values are reached between 1.75 and 2.00 d_p (4.4 – 5.0 mm). The decrease follows a roughly linear trend with distance.

Additionally, an orientation analysis of the intra-granular cracks of that profile was conducted. The number of cracks per segment area (0.25 x 0.25 d_p) ranges from 700 at the crater floor to 9 at 2.75 d_p (3.9 mm) depth. Crack orientations of each segment are plotted as rose diagrams. The cracks show a preferred orientation subparallel to the crater floor (Figure 6-2a) down to 1.75 d_p (4.4 mm). At greater depths, the number of fractures is very low, however, taking neighbouring areas into account, no impact-related orientation is noticeable.

The crater subsurface of the marble target is also characterized by large tensile fractures oriented subparallel to the crater floor. These fractures transect at least two grains, do not follow grain boundaries and decrease in width from up to 80 µm at the crater floor to as little as 2 µm in greater depths. The lower boundary of the zone of tensile fractures is at 1.5 d_p (3.75 mm) depth.

A distinct feature of marble subsurface deformation is the opening of grain boundaries. Within the uppermost 0.25 d_p (0.63 mm) 72% of all grain boundaries are open. Between 0.25 d_p and 1.25 d_p (0.63 – 3.1 mm) depth approximately half of all grain boundaries are open (Figure 6-2d), and this value decreases further below 1.25 d_p (3.1 mm). At 3.25 d_p (8.1 mm) depth all grain boundaries are closed.

Apart from intra-granular cracks and tensile fractures the main deformation features in the marble crater subsurface are twin lamellae and open cleavage. Polarized light microscopy images of the uppermost crater subsurface show heavily deformed grains. In plane polarized light calcite grains show a brownish colour; in cross polarized light they show a lack of extinction and reduced interference colours (Figure 6-5a, b). The intensity of the features decreases with depth down to ~1.5 d_p (3.75 mm), below which they are no longer observed (Figure 6-5c, d). In thin section and SEM microscopy these features were recognized as twins. Unlike tectonic calcite twins that show an average thickness of ~ 35 µm in our sample material, the impact-generated twins have a thickness of less than 1 µm and thereby classify as microtwins (Groshong 1972).

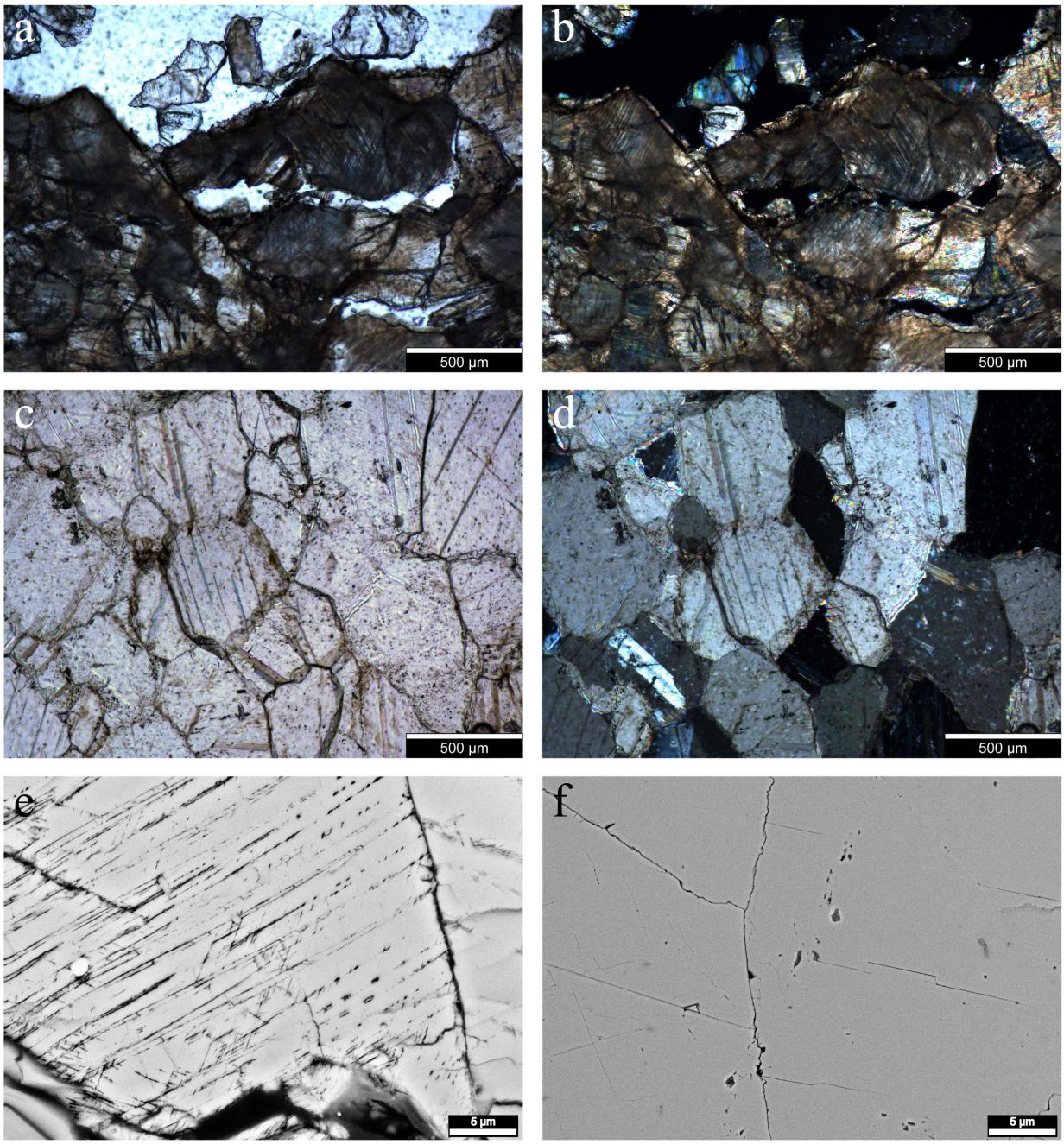

Figure 6-5: Photomicrographs and SEM images of the marble target subsurface. a) and b) show the most proximal crater subsurface of the marble target directly at the crater floor in plane polarized (a) and crossed-polarized (b) light. A) shows the brownish coloration of calcite grains and b) the low interference colors and general lack of extinction in the proximal subsurface. c) and d) show micrographs of the marble subsurface at ~ 1.5 d_p depth. In plane-polarized light (c) the calcite grains are transparent, while in d) with crossed-polarized light the grains reach their usual interference colors. e) SEM-BSE image of several sets of parallel open cleavage planes in a calcite grain close to the crater floor. f) SEM-BSE image of undeformed calcite grains at 1.7 d_p (4.2 mm) distance to the crater floor. Only few, slightly opened cleavage cracks are present.

High resolution SEM-BSE images of the crater subsurface additionally show many open cracks. These cracks correspond to open cleavage and run as slightly bent parallel sets through the grains. In many cases two or three set per grain exists (Figure 6-5e). In the same fashion as impact induced twins the creation and opening of cleavage decreases with depth. At a distance of ~ 1.7 d_p (4.2 mm) only rare and isolated cleavage cracks are present.

Quartzite

The crater subsurface of the quartzite target also shows the formation of intra-granular cracks. As in marble they range in length from < 5 µm to ~300 µm and have a width of at least 2 µm. The intra-granular crack density (Figure 6-2f) was calculated down to 4.0 d_p (10.0 mm). Since the uppermost 0.5 d_p (1.25 mm) in quartzite are dominated by secondary porosity due to tensile fractures the intra-granular crack density reaches its maximum only at 1.0 d_p (2.5 mm). It then decreases linearly down to a depth of 2.9 d_p (7.25 mm), where pre-impact background levels are reached.

The orientation analysis of the intra-granular cracks in quartzite shows a rough bimodal distribution of preferred orientations (Figure 6-2e). The main orientation down to 1 d_p (2.5 mm) depth is sub-horizontal with a subordinate radial direction. Below 1 d_p (2.5 mm) the cracks clearly show a preferred radial orientation and in few cases additionally a shear component. Tensile fractures in quartzite have a similar appearance to those in marble, although they are generally shorter in length, since they are restricted by shear bands. It is also common that tensile cracks in quartzite in part follow grain boundaries. Their width varies between 100 µm and 2 µm, depending on their distance to the crater floor. The zone of tensile fractures reaches down to a depth of 2.2 d_p (5.5 mm).

Unlike the marble target, grain boundaries in quartzite are only rarely open and occur as tensile fractures oriented subparallel to the crater floor. The deepest open grain boundary is found at 1.75 d_p (4.4 mm) depth.

The most prominent deformation features beside intra-granular cracks and tensile fractures, are highly localized shear bands, surrounded by broader damage zones. The orientation of these shear bands is roughly

radial and they all originate at the crater floor. Their individual length varies largely between ~2.5 mm and ~8.5 mm.

The shear bands are between 30 µm and 300 µm thick with an average thickness of ~100 µm. They are characterized by very intense grain comminution with the median of the particle size (above cutoff) of 0.9 µm, compared to the original quartzite grain size of ~125 µm. The average particle size within the shear bands remains constant with radial distance to the crater floor, and is independent of the angle to the impact direction. The porosity within the shear bands is strongly enhanced. Average shear band porosity is ~28% and can reach ~33% near the crater floor to due to tensile fractures. The maximum shear displacement observed along the shear bands is 30 µm, but commonly the displacement is significantly smaller than that. No correlation could be found between the angle of the shear band to the impact direction and the sense of shear or the magnitude of displacement.

The boundaries of the shear bands are sharp and clearly traceable so that the borders between shear bands and surrounding damage zones are distinctly defined. The damage zones themselves are characterized by a network of fractures emanating from the shear band. The fracture density in the damage zones varies strongly and cannot be correlated with the radial distance to the crater floor or the relative orientation to the impact direction. However, the width of damage zones is narrower in the central crater region close to the symmetry axis than in the shallower regions sideways towards the target surface. The central damage zones have average thicknesses between ~160 µm to ~190 µm, become successively thicker (~240 µm at 45°) until they reach a thickness of ~370 µm to ~460 µm in the shallowest region.

6.4.5 Numerical modelling

Crater profiles

For direct comparison the modelled crater profiles of both experiments at the transient crater stage of maximum crater volume are plotted with the crater profiles measured from the experimental craters (Figure 6-6). Note that both numerical models show a small region of

artificially increased depth in the crater centre due to the boundary conditions of the 2D model. The numerical model of the marble crater (A34-5614) a depth of 6 mm (7.4 mm including the artificial effects) and a diameter of ~27.6 mm, resulting in a depth diameter (d/D) ratio of 0.22 (Table 6-3). The ratio is thus smaller than the final experimental crater, but since the numerical model aims at the transient crater and does not include modification processes (e.g. spallation) this result is to be expected. The numerically modelled quartzite crater (A20-5339) has an actual depth of 6.2 mm (7.2 mm including the artificial effects) and a diameter of ~27.8 mm, resulting in a depth diameter (d/D) ratio of 0.22 (Table 6-3). As the modelled crater in marble it is smaller than the experimentally produced crater.

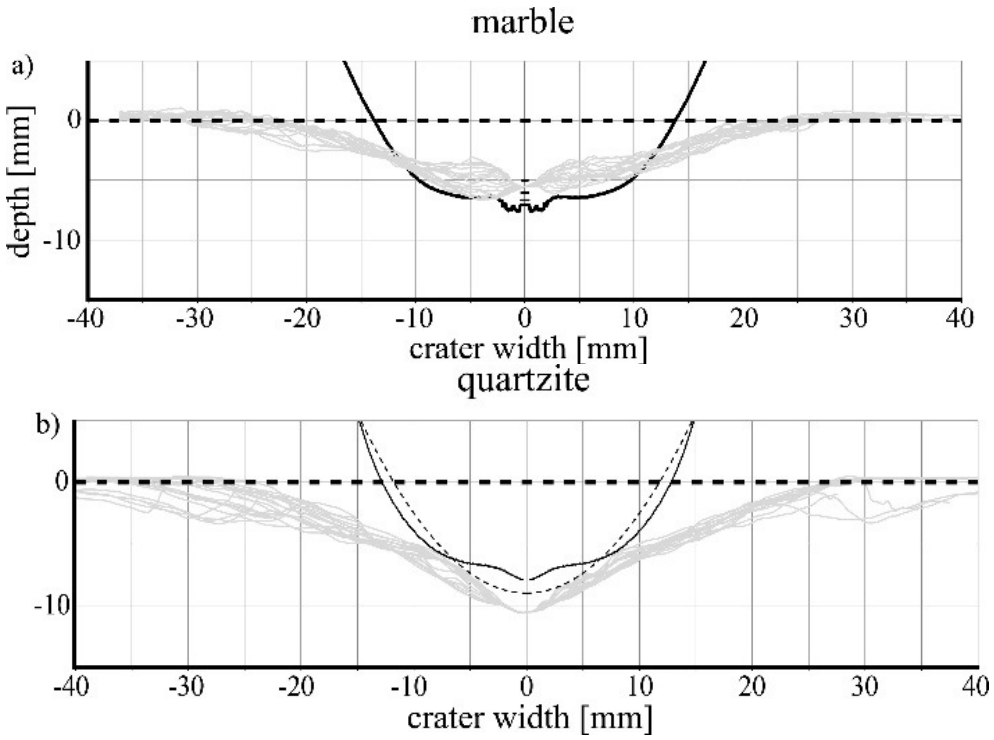

Figure 6-6: Comparison of the 18 measured crater profiles from the experiment (grey lines) and the numerical crater profile (black line) of the marble target (a) and the quartzite target (b) at the stage of transient crater (defined by maximum volume). The dashed line in (b) shows the paraboloid of the transient crater determined on the basis of the high-speed video of the experiment (Dufresne et al. 2013), which was used as a constraint for the model.

Total plastic strain distribution

Figure 6-7 shows the total plastic strain distribution of the marble and quartzite models. The total plastic strain is a combination of shear and tensile strains that occur locally to different degrees of intensity. Based on Collins et al. (2004), who give a detailed description of modelling deformation and strain in iSALE, plastic deformation of the target rocks begins at compressive shear strain values >0.001 for low confining pressures, although the threshold strain for plastic failure can increase up to 0.05 for high confining pressures.

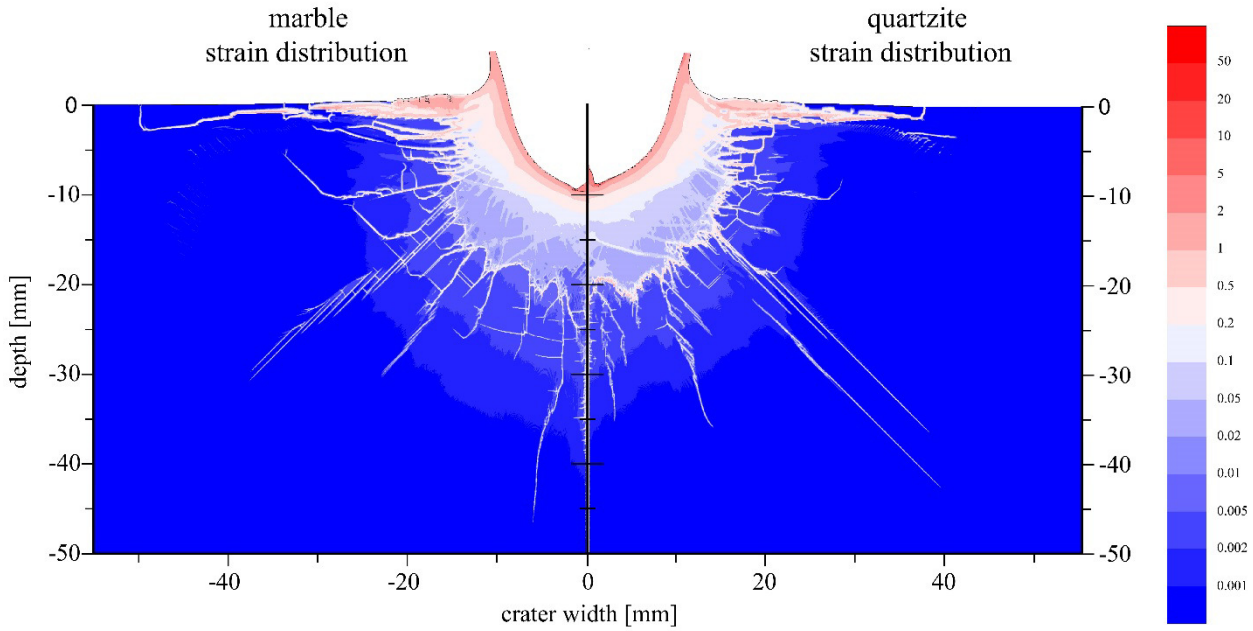

Figure 6-7: Total plastic strain distribution during the crater formation. The snapshots show the stage of the craters 44 µs after the impact – after the passage of the shock wave and prior to the arrival of reflected waves from the block/model boundaries. Both marble and quartzite target show a lens of continuously decreasing strain levels ~20 mm below the target surface (~12 mm below crater floor). Beyond that lens strain decreases significantly and a few mainly radially oriented narrow lines occur that exhibit high strain levels. Additionally, both targets show high strain regions along the target surface, which become narrower away from the crater rim and eventually terminate at the target surface.

Both marble and quartzite models show similar strain behaviour, with regions of high strain (>0.5) found at the crater floor and at the immediate target subsurface outside of the crater. Strain intensities decrease with depth and radial distance from the impact point, with only slight variations noticeable between the quartzite and marble models. With

decreasing strain, strongly localized zones of high strain extend into the deeper target subsurface. Models from Collins et al. (2004) show that tensile strains dominate to the left and right of the crater rim, whereas compressional shear failure is dominant beneath the crater floor.

Pressure regions

Figure 6-8 shows shock pressure isobars calculated for the marble and quartzite targets. The material within the uppermost 4 mm (1.6 d_p) underneath the crater floor in the marble model experienced pressures over 3.5 GPa (Figure 6-8). Within the next 3 mm (1.2 d_p) below that depth the calculated pressures decrease to 2.0 GPa. From that depth downwards the rate of pressure decrease is reduced so that the 1.0 GPa isobar is only reached in 10 mm (4 d_p) depth. The 0.5 GPa isobar is finally reached at a depth of 31 mm beneath the crater floor (5.6 d_p).

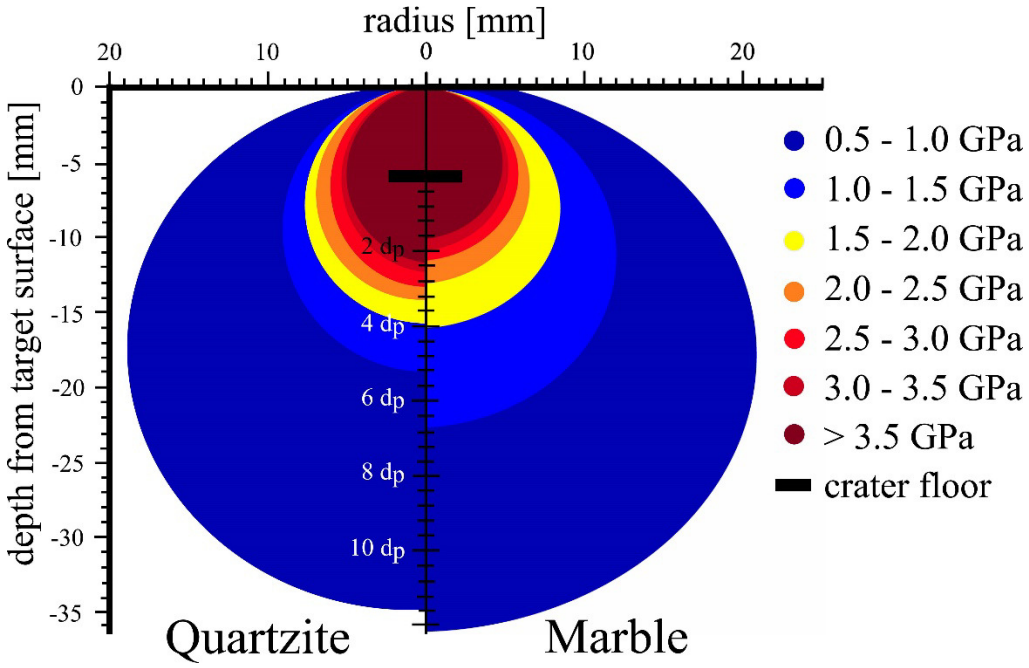

Figure 6-8: Pressure isobars within the quartzite (left half) and marble (right half) target. The colour map denotes the peak pressure reached by the marked material.

The rate of pressure decrease in quartzite (Figure 6-8). Here the high pressure region underneath the crater floor extends down to a depth of 6 mm (2.4 d_p) beneath the crater floor. It only needs 2 mm (0.8 d_p) for pressures to decrease to 2.0 GPa and another 5 mm (2 d_p) to decrease to 1.0 GPa. The

0.5 GPa isobar is already reached at 29 mm (6.4 d_p), so 2 mm above that mark in marble.

6.5 Discussion

6.5.1 Deformation microstructures

Microstructural mapping of deformation features in the marble and quartzite targets reveal some common types of deformation, including spall and tensile fractures, as well as intragranular cracks, but differences in the style of deformation are also apparent (Figure 6-9). Subsurface deformation in the marble is dominated by pervasive and omnipresent fracturing and twinning that dies out with radial distance to the crater floor. The quartzite's crater subsurface on the other hand is characterized by intense localized deformation along roughly radial shear bands separated by lenses with only limited fracturing.

For both targets a relative succession of deformation regimes can be inferred based on the orientation and superposition relationships of various deformation microstructures. These regimes can be assigned to different stress states created by the hypervelocity impact, and we will refer to them as regimes I-III in the text below:

- Regime I: Shock pressures decrease with distance from the impact point but are well above the Hugoniot elastic limit (HEL) of quartz and calcite near the central crater floor (Figure 6-8) and lead to features formed under high confining pressures and shear stresses.
- Regime II: As the wave continues to propagate, pressures fall to compressional stresses below the target's HEL, because of geometric spreading and the rarefaction wave that gradually catches up with the pressure pulse. Here, hoop stresses that are oriented concentrically to the impact point dominate and can form radially oriented deformation features.
- Regime III: The tensile pulse from the rarefaction wave generates tensile stresses that are radial to the impact point which in turn induce tensile fractures with concentric orientations.

Note that shock features indicating higher shock metamorphic conditions, such as planar deformation features, are found in the ejecta of the quartzite experiment (Ebert et al. 2014). In the craters' subsurfaces merely low- and sub-shock deformation is preserved. In the following both targets are discussed separately.

Furthermore, note that the experimental conditions of the two impact experiments differed slightly (Table 6-1), leading to a variation of the impact energy by ~20%. While that difference may partly be responsible for the smaller crater dimensions and damage lens underneath the crater for the marble target, it should not influence the substantially different micro-structural deformation responses between the two crater subsurfaces to any major degree.

Marble

In the marble target, the following three successive groups of microstructural features are distinguished:

1) Pervasive twinning and cleavage activation,
2) Opening of grain boundaries and intra-granular cracks
3) Tensile fracturing on the grain scale or larger.

The implications for their respective formation conditions are discussed below.

Pervasive twinning and cleavage activation

Twinning in calcite is a widespread phenomenon, and occurs if calcite experiences differential stress (Turner and Weiss 1963; Rybacki et al. 2013). A critical resolved shear stress of only ~5-15 MPa is needed to initiate twinning (Lacombe and Laurent 1996; Laurent et al. 2000). The formation of calcite twins during impact has been reported for natural impacts, as well as impact experiments by several authors (e.g. Robertson and Grieve 1977; Langenhorst 2002; Schedl 2006; Lindgren et al. 2013). Lindgren et al. (2013) estimate that shock-derived calcite twins begin to form at pressures of ~110-480 MPa based on cratering experiments. The formation of two to three twin sets per grain in the direct vicinity of the

crater floor suggests compression with a shear strain ≥0.1 (Barber and Wenk 1979).

In experiment A34-5614, two or more twin sets per grain (microtwins with <1 µm thickness, opposed to ~35 µm thick tectonic twins) are present down to 1.0 d_p (2.5 mm) depth, with the number of sets, as well as the number of twins per set decreasing constantly with depth. The blue line in Figure 6-9 indicates the radius, where roughly half of each grain's area is comprised of impact-induced twins. The line was determined semi-quantitatively, since that area wasn't measured, but estimated. It coincides with the transition from several twin sets per grain to only one set. From the modelling results, the material with several twin sets per grain can be correlated with shock pressures of at least ~3.5 GPa (Figure 6-8), as well as strains larger than 0.5 (Figure 6-7a), which is considerably larger than the shear strain value of ≥0.1 by Barber and Wenk (1979). Below a depth of 1.0 d_p (2.5 mm) one set of twin lamellae per grain dominates. Following Barber and Wenk (1979), this requires strains ≥0.02. The numerical model calculated strains ≥0.02 down to a depth of 9 mm (3.6 d_p). Impact-induced twinning, however, was only observed down to a depth of ~4.5 mm (1.8 d_p; Figure 6-9 a). At around that depth peak pressures drop below ~3.5 GPa. Given the fact that all other impact related deformation features in marble also cease between 4 - 5 mm (1.8 - 2.0 d_p) it is likely that the model overestimates the extent of strain at greater depth.

Along with pervasive twinning of calcite the crater's subsurface shows abundant activation and opening of cleavage planes (Figure 6-5e). Intense cleavage formation with depth occurs in the same manner as calcite twinning does.

From other impact experiments in non-porous rocks, e.g. Moore and Gault (1962), Hörz (1969), Polanskey and Ahrens (1990), it is known that if the HEL of the target material is exceeded, the rock will fail under compression due to shearing. The crystal structure of calcite allows mechanical twinning along different crystallographic planes. Calcite twins can therefore be considered as zones of simple shear with a known shear direction, shear sense and angular shear, with the angular strain being

proportional to the thickness of the twin (Burkhard 1993). Hence, both pervasive twinning and cleavage activation can be correlated with the first regime of deformation with pressures above the marble's HEL. However, since only ~5-15 MPa of critical resolved shear stress is necessary to initiate twinning, twin formation in later pressure stages at lower pressures cannot be excluded. It is not possible to define a zone of pervasive shear fracturing as done by Polanskey and Ahrens (1990), since both features disappear gradually with radial distance to the crater floor (Figure 6-9a).

Opening of grain boundaries and intra-granular crack formation

Intense twinning of calcite leads to heterogeneous shear deformation at the grain scale and spatial incompatibilities along grain boundaries. Further incompatibilities arise at the intersection of two twins. Both types of geometric complications, present in each grain, lead to open spaces along grain boundaries if deformation time is not sufficient to allow diffusion or dissolution-precipitation processes to close them (Burkhard 1993). Therefore, the opening of grain boundaries in our experiment, regardless of their orientation, is an inevitable consequence of pervasive twinning. Consequently, it occurs simultaneously to the twin formation during regime I of the deformation. At deeper levels of the crater subsurface where twinning is less intense, the orientation of the grain boundaries, as potential zones of weakness, becomes more important. Grain boundaries sub-parallel to the crater floor or in roughly radial direction are predominantly open. The tensile opening of radially oriented grain boundaries suggests that they open under hoop stresses during regime II, when the maximum principal stress axis is oriented radially and the minimum principal stress axis is oriented concentrically, as described by Ai and Ahrens (2004). Sub-horizontally oriented grain boundaries open during regime III, under the tensile pulse of the rarefaction wave.

Formation of intra-granular cracks with a preferential radial orientation is frequently reported from other impact experiments in a range of target materials (Moore et al. 1963; Polanskey and Ahrens 1990; Buhl et al. 2013; Winkler et al. 2016). In the marble experiment, however, very few radial cracks developed. The dominant orientation of intra-granular cracks is

sub-horizontal (Figure 6-2a). The lack of radial cracks is likely the consequence of early cleavage formation. The pervasive cleavage doesn't allow the grains to accumulate localized high strain zones. Hoop stresses can only form dispersively and do not reach the level needed for radial fracture formation (Ai and Ahrens 2004). The small radial cracks in marble find no equivalent in the model.

Tensile fracturing

The marble crater subsurface is marked by abundant tensile fractures from intra-granular scale to fractures over several mm in length (Figure 6-9a). Tensile failure occurs in the outer regions of the crater´s subsurface as long fractures aligned sub-parallel to the crater floor with a large degree of opening, and they resemble spallation fractures reported in other experiments (e.g. Hörz 1969; Polanskey and Ahrens 1990; Kenkmann et al. 2011; Winkler et al. 2016). Other microscopic deformation features like twins, cleavage or intra-granular cracks are not prevalent in these outer crater zones.

The numerical model shows long, localized, sub-horizontal strain lines, which terminate at the target surface (Figure 6-7a) and can be regarded as spallation fractures. However, the spallation fractures in the marble experiment are shorter and much more pervasively distributed than in the model. Due to the perfect cleavage in calcite and the low tensile strength of the marble, fractures are more easily generated than e.g. in quartzite and thus more of them form that are shorter on average. The model does not account for cleavage in calcite and may therefore not correctly calculate the spallation behaviour.

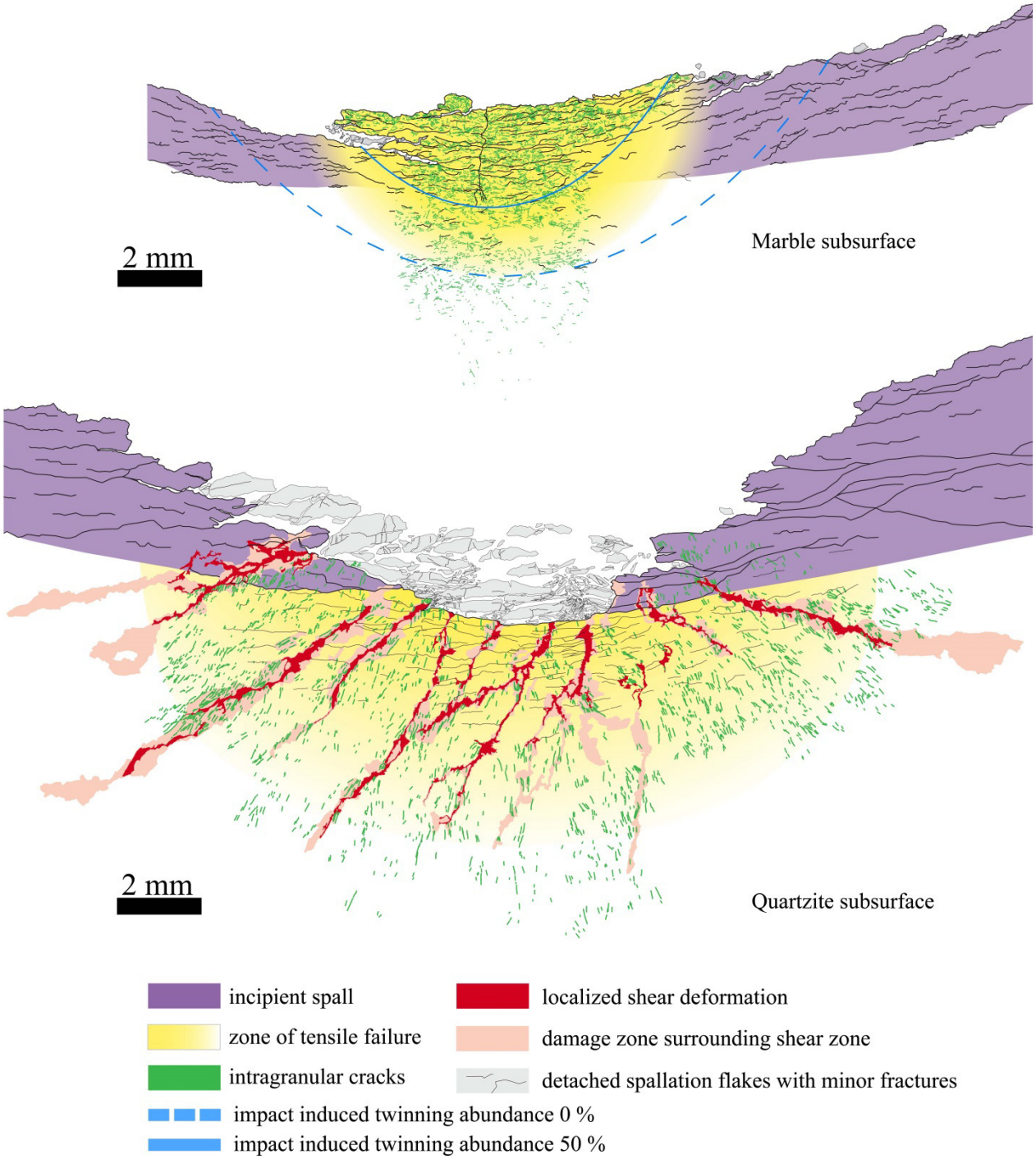

Figure 6-9: Sketch of impact-generated deformation features of a) a 2.5 mm iron meteorite projectile at ~ 5 km s^{-1} on a marble target, and b) a 2.5 mm steel projectile at ~ 5 km s^{-1} on a quartzite target.

The tensile fractures that occur beneath the crater centre are similar to spall fractures with respect to size and the degree of opening. They reach, however, to a greater depth and decrease in length and opening width with depth. Since the spall fractures in marble lack their typical characteristics

like e.g. a very large opening width, a net-like connection of several fractures or the termination at the target surface the transition from spallation fracture to tensile fracture can be considered as gradual (Figure 6-9a). The mapping of spallation and tensile fractures was therefore semi-quantitative. It was based on the disappearance of small tensile fractures as they are also known from other experiments, as well as the appearance of longer and wider spallation fractures. A separate zone of tensile failure along the crater floor has been observed microscopically by other authors for porous target materials (Buhl et al. 2013; Winkler et al. 2016). Polanskey and Ahrens (1990) did not find such a zone in non-porous basalt targets, but their study did not include microscopic analysis. The formation of tensile fractures can be attributed to the last deformation regime (Regime III) during pressure release.

Quartzite

In the quartzite target, the following three successive groups of microstructural features are distinguished:

1) Localized shear bands and grain comminution,
2) Intra-granular crack formation, and
3) Tensile fracturing.

The implications for their respective formation conditions are discussed below.

Localized shear bands and grain comminution

Several authors who conducted impact experiments on different non-porous target materials such as granite, basalt, gabbro and nephrite discriminated deformation zones in the target beneath the crater (Moore and Gault 1962; Moore et al. 1963; Hörz 1969; Lange et al. 1984; Polanskey and Ahrens 1990). According to these authors the uppermost part of the crater's subsurface is a very shallow zone of crushed rock, which is characterized by pulverization of grains and micro-fractures. This zone is followed by a zone of shear fractures that contain grooves and striae. In contrast to the above cited work we could not identify pulverized domains. However, we do recognize a zone of shear bands starting directly at the crater floor and

propagating in a roughly radial fashion with lengths between ~2.5 mm and 7.5 mm (Figure 6-9b). In contrast to Moore and Gault (1962) who described shear fractures in basalt to be smooth, we found such fractures to be very irregular and mostly cutting through grains. Grain size analysis of the fault gouge (Figure 6-3b) shows extreme grain comminution with a reduction of grain size to ~0.9 µm, irrespective of the distance to the crater floor. We were not able to quantify significant displacements along the shear bands, but shearing is evident. The formation of the shear bands occurs during regime I of the deformation sequence, in which high differential stresses occur and where shearing is possible. Comparing the depth at which the shear bands end with the model results of numerical simulations suggests that shock pressures of at least ~1 GPa (Figure 6-8) are required for their formation. The shear bands are surrounded by damage zones that are characterized by a dense, cross cutting fracture pattern. The widening of the damage zones with shallower orientations has its origin, probably, in a stronger shear component in that region. It is possible that the shear bands are analogous to the lines of increased total strain ($\varepsilon \sim 0.05$) underneath the region with a total plastic strain of ~ 0.1 (Figure 6-7b). The total plastic strain at those cracks is enhanced by a factor of ~2.5 relative to the material surrounding the cracks. However, these lines of increased total plastic strain reach deeper than the shear bands in the experiment.

Intra-granular crack formation

Numerous intra-granular cracks occur in the quartzite subsurface, most of which have radial orientations (Figure 6-2e), and thus resemble fractures and observed in other subsurface analyses of experimentally produced craters (Polanskey and Ahrens 1990; Buhl et al. 2013; Winkler et al. 2016). However, in the upper 2.5 mm (1 d_p) of the quartzite crater subsurface subhorizontal intra-granular cracks also occur. The frequency of intra-granular cracks decreases with depth, and correlates with the attenuation of the shock wave. Nonetheless, radially oriented intra-granular cracks could be mapped to a maximum distance of 12.5 d_p (31.5 mm). They formed most likely during regime II of the deformation, where compressive stresses are oriented radially and tensile stresses are oriented concentrically,

and thus, formed during the same regime as vertical grain boundaries in marble.

Tensile fracturing

The quartzite crater subsurface is marked by tensile fractures at two different locations. We found abundant spall fractures in the outer and shallower crater regions (Figure 6-9b). They emanate at various depths from the crater wall and propagate towards the target surface, where they terminate. Typical for the quartzite subsurface are very long and interlocked spall fractures that isolate incipient spall fragments that remain arrested to the target as long as some intact bridges remain (Figure 6-1). The quartzite numerical model shows high strain accumulations close to the surface that can be interpreted as spallation zones (Figure 6-7b). Additionally the model shows high strain lines underneath the most superficial high strain wedge. Each of these strain lines terminates in the larger one above it. That pattern can be observed in the fractures pattern of the spallation fractures in quartzite (Figure 6-9b).

The central crater subsurface is permeated by open tensile fractures of various dimensions down to the granular scale. Since the majority of the tensile fractures are bounded by shear bands on either side, it is obvious that they formed after the shear bands. Thus tensile failure in non-porous targets seems to be very pronounced. Compared to studies in higher porosity targets (Buhl et al. 2013; Winkler et al. 2016) the zones of tensile failure are not restricted to the vicinity of the crater floor, but reach far deeper into the target than in porous targets. While Buhl et al. (2013) and Winkler et al. (2016) identified the uppermost millimetre (0.4 d_p) and upper 2 mm (0.8 d_p), respectively, as zones of tensile failure, quartzite displays an expansion of this zone to a depth of 2.2 d_p (5.5 mm). Tensile failure is attributed to the deformation regime III, when the rarefaction wave unloads the target.

6.5.2 Cratering efficiency

The marble experiment has an unexpectedly low cratering efficiency (i.e. the ratio of excavated crater mass to projectile mass) at 164.5 compared to 220.4 for the quartzite experiment. This discrepancy is in part due to the ~20% smaller impact energy of the marble compared to the quartzite experiment. However, this result is remarkable considering that marble has a much lower uniaxial compressive strength (UCS) and tensile strength than quartzite (60 MPa and 7.3 MPa versus 292 MPa and 16.7 MPa; Table 6-1), which in theory should yield larger crater volumes in the strength-dominated cratering regime that the experiments occur in. In fact, using crater scaling methods, Poelchau et al. (2015) estimated for a range of experiments on Carrara marble that a roughly fourfold increase in UCS from 60 MPa to ~230 MPa would theoretically be needed for the smaller marble crater volumes to plot with their non-porous quartzite and basalt counterparts.

The small marble crater size may suggest that conventional measures of strength like UCS do not sufficiently represent the strength-dominated behaviour of these experimental craters. A possible dynamic increase in strength at high strain rates that occur experimentally may explain some variation; perhaps Carrara marble has a much stronger strain-rate related strength increase than the Taunus quartzite (see e.g. Zwiessler et al. 2017 for more details).

On the other hand, a second possible mechanism may be a faster dampening or attenuation of the shock wave, due to the consumption of energy by the formation of twins and the activation and opening of cleavage planes relative to the more resilient quartzite. A similar scaling behaviour was observed in porous target materials like sandstone, where the closing of pore space led to a strong attenuation of the shock wave and a reduction in cratering efficiencies relative to the target strength (e.g. Kowitz et al. 2013; Poelchau et al. 2013).

6.5.3 Experiment-Model Comparison

Crater profiles

When comparing experimentally and numerically produced craters it has to be taken into consideration that impact experiments in solid rock targets produce wide, flat craters due to the large amounts of spalled material that is removed from the target (e.g., Melosh 1984; Poelchau et al. 2014), whereas numerical models, in particular the iSALE code, do not directly account for the spallation process, modelling only the transient crater. This leads to comparatively smaller crater diameters and hence, higher depth-diameter (d/D) ratios of 0.22 for both numerical models (cf. Figure 6-1 and Figure 6-6).

However, based on the numerically modelled strain (Figure 6-7) we can estimate a "spallation diameter". Narrow zones of high tensile strain ($\varepsilon \geq 0.2$) near the target surface mark wedges with unstrained material on top that show a strong geometric resemblance to spall plates collected from impact experiments. Where these zones intersect the target surface, diameters can be estimated at 62 mm and 76 mm for marble and quartzite, respectively (Table 6-3). d/D ratios of the numerical "spall craters" are 0.10 and 0.09, respectively. Compared to the experimentally produced d/D-ratios of 0.11 and 0.15 the calculated "spallation d/D-ratios" are much closer the experiment than the transient crater d/D-ratios. However, this is probably only a phenomenological similarity, since the modelled strain lines along the target surface in marble do not correspond in appearance to the more evenly distributed spallation fractures in the experiment. Also, the spall plates in the experiments are more strongly wedge shaped than in the model. Based on video analysis of the cratering event and crater morphology, the transient depth and diameter of the experimental craters can be estimated, as described by Poelchau et al. (2014). Due to technical problems during the marble experiment, this procedure is only possible for the quartzite experiment. A paraboloid that forms the estimated transient crater of the experiment was determined. The crater floor and the basal extent of the ejecta cone at its largest stage were used as constraints for the depth and width of the paraboloid. The paraboloid has a height of 9 mm and a

diameter of 23.5 mm, resulting in a d/D-ratio of 0.38 (Table 6-3). Even though the experimental d/D ratio is larger than the one of the model at 0.27 (Table 6-3), the quartzite transient crater agrees well with the transient numerical crater (Figure 6-6b). The higher d/D ratio has its origin in the two negative deviations, i.e. in the greater depth, yet smaller diameter of the experimental paraboloid compared to the model.

Note that the experimental crater morphology of the quartzite crater is deeper than both the paraboloid fit and the numerical transient crater. Presumably parts of the crater floor were removed in the late stages of cratering through tensile failure. This would correspond to the tensile, regime III type deformation described above, and is in part represented by the grey-coloured areas of the crater floor mapped in Figure 6-9b. In comparison, the numerical model of the marble transient crater is too deep for the experimental crater floor morphology. This again may reflect a stronger attenuation of the shock wave in marble that is currently not incorporated in the numerical models.

Table 6-3**:** Overview of experimental and modelled crater dimensions.

	Experiment		Numerical model	
	A34–5614	A20–5339	A34–5614	A20–5339
Target material	Marble	Quartzite	Marble	Quartzite
Crater diameter (mm)	57 ± 4	73 ± 13	~ 62	~ 76
Crater depth (mm)	6 ± 0.4	10.6	6	6.2
Final depth/diameter (d/D) ratio	0.11	0.15	0.10	0.09
Transient diameter (mm)	-	~ 25.5	27.6	27.8
Transient depth (mm)	-	~ 9	6	6.2
Transient depth/diameter ratio	-	0.38	0.22	0.27
Max. thickness of damaged/strain lens (mm)/(d_p)	4.1/1.6	7.1/2.9	9/3.6	11/4.4
Max. thickness of strain detection (mm)/(d_p)	4.1/1.6	7.1/2.9	34/13.6	44/17.6

d_p = projectile diameter

Total plastic strain distribution

The total plastic strain in the numerical model (Figure 6-7) shows domains within which target material was deformed either through compressional shearing or through tension. Consequently, the material loses strength. The lower strength is described by the Drucker-Prager yield surface. The exact nature of that deformation or plastic work is not

accurately defined. It incorporates sand-like porosity, as well as cracks in otherwise solid rock. Direct comparison of the models to the experiments suggests that the zones of medium to high strain accumulations in the model represent: secondary porosity due to tensile fractures, various kinds of fractures on different scales, shear bands in the case of quartzite, and pervasive twinning and cleavage activation in the case of marble.

Marble

Plastic deformation in the marble experiment is evident as opened grain boundaries, twinning and cleavage activation, intra-granular cracks and tensile fracturing, and can at least partially be correlated with numerical modelling results. The experimental data show an opening of grain boundaries down to a depth of ~ 3.5 d_p (8.75 mm) (Figure 6-2d), which indicate a good correlation between experiment and model. Although it is not a perfect match between experiment and model, the model does at least reflect the necessary stress stage for radial crack formation. Groups of concentric fractures visible in the modelled strain lens (Figure 6-7) fit well to the tensile fractures, although they are located too deep underneath the crater floor. The large and deep reaching radial fractures beyond the strain lens find no analogue in the experiment.

The impact-influenced zone in marble reaches to a depth of 4.5 mm (Table 6-4), which is ~2.5 times smaller than the strained zone in the model. A reason for that could be that the used parametrization might be too simplistic. The formation of micro-twins with an average thickness in the sub-micrometre scale in the experiment, for example, consumes lots of the impact energy that is no longer available for crater formation. This energy consumption is not included in the model and can explain the larger strain lens in the model. Nonetheless, a number of experimental and numerical observations correspond well to each other, as described above (Table 6-3 and Table 6-4). However, this fit was reached only by increasing the strength parameters of the marble. To achieve the crater depth of the experiment a higher cohesive strength was used than originally determined for the target material. Poelchau et al. (2015) proposed a dynamic strength effect as reason for the smaller and shallower marble craters. This

suggestion has been taken into account for the numerical model of the marble crater and first dynamic strength measurements of Carrara Marble were used as constraints (Kenkmann et al. 2017; Zwiessler et al. 2017). Dynamic hardening increases the resistance against crater formation and finally leads to the formation of smaller craters. The same result is true for the phenomenon of twinning as it consumes impact energy. Hence, it seems possible that enhanced dynamic hardening of the marble in the experimental study and the formation of twinning could be phenomena based on the same process behind. Note that the quartzite target gives good model results without increasing the material strength and does not show twin formation.

Quartzite

In case of quartzite, the experiment shows shear bands with intense grain comminution, intragranular cracks and tensile fracturing as deformation features. The large radial fractures beyond the modelled strain lens correspond well to deep-reaching radial fractures in quartzite. As in the model these fractures show in parts an up to ~30° angle to the pure radial orientation. The minor concentric fractures in the model have at least one analogue in the experiment, even though this concentric fracture lies much deeper than the modelled one (9.6 d_p/24 mm). That is nearly as far as predicted by the model, where that zone reaches a depth of 11.2 d_p (28 mm) below the strain lens, and therefore, corresponds well. All other cracks that formed deeper than the strain lens zone are mostly short and isolated. Thus, they do not form an extensive fracture network, but represent rather a homogeneous deformation that decreases successively with depth. It is possible, though, that due to thin section limitations, as well as the limited 2D cutting effect, further large-scale radial or concentric cracks remained undetected.

The impact-influenced zone in quartzite reaches to a depth of 7.5 mm (Table 6-4), which is ~1.7 times smaller than the completely damaged zone of the model. The reason for the discrepancy between the modelled and experimentally damaged zone in quartzite could be a higher than expected energy consumption by the generation of the shear bands and the intense grain comminution within them.

Hence, further microscopic studies, as well as ultrasound measurements could give a hint on the reliability of the model data in predicting deep lying deformation features. For example, Moser et al. (2013) have found for sandstone targets a reduction of ultrasound velocities correlated to subsurface damaging at much deeper depths within the target than observed by micro-analysis (see also Raith et al. 2018).

Table 6-4**:** Maximum observed depths of subsurface deformation features and their corresponding numerically modelled strain and shock pressure values.

	Marble A34–5614			Quartzite A20–5339		
	Experiment [mm; d_p]	modelled strain [-]	modelled pressure [GPa]	Experiment [mm; d_p]	modelled strain [-]	modelled pressure [GPa]
Increased porosity (Figure 6-2)	4.4/1.75	> 0.1	> 3.0	6.9/2.75	> 0.05	> 2.5
Reduced grain size (Figure 6-3)	3.1/1.25	> 0.2	> 3.5	7.5/3.0	> 0.05	> 2.0
Tensile fractures (Figure 6-9)	3.75/1.5	> 0.1	> 3.5	5.5/2.2	> 0.05	> 3.5
Intra-granular crack density (Figure 6-2)	4.5/1.8	> 0.05	> 3.0	7.25/2.5	> 0.05	> 2.0
High-intensity Cc-twinning (Figure 6-9)	2.5/1.0	> 0.5	> 3.5	-	-	-
Low-intensity Cc-twinning (Figure 6-9)	4.5/1.8	> 0.1	> 3.0	-	-	-
Shear band depths, quartzite (Figure 6-9)	-	-	-	7.5/3.0	> 0.2	> 1.5

d_p = projectile diameter

6.6 Conclusions

In this study, an interdisciplinary approach including experimental analysis and numerical modelling was applied. We analysed the deformation characteristics of experimentally produced impact craters formed in marble and quartzite under similar impact conditions and compared them to results of numerical modelling. The crater morphology of both craters is strongly affected by spallation that widens the craters and reduces the d/D-ratio to values of 0.11 and 0.15 in marble and quartzite, respectively. The modelled craters, corrected for spallation, reached d/D-ratio values of 0.10 and 0.09 for marble and quartzite, respectively. The formation of radial, tensile and intra-granular cracks, accompanied by an overall grain size reduction along with the generation of secondary porosity, is a general response of non-porous materials to impact cratering. In addition to that, the marble target is characterized by widespread and

pervasive twinning, as well as cleavage activation. The quartzite target on the other hand developed localized shear bands with intense grain comminution surrounded by fractures. Except for spallation fractures, it is not possible to resolve any of these specific features on a total plastic strain map calculated by the model. As deformation is governed by the presence of localized shear bands in the quartzite experiment the strain distribution is more heterogeneous than in the model. In distal regions, models indicate still elevated strain levels, while our microanalyses of the experiments show no further deformation. Pressure ranges derived from the models can be correlated with damage processes in the experiment.

Based on progressive changes of stress conditions in the expanding shock wave, a relative formation sequence of the deformation features can be established:

In marble, pervasive twinning and cleavage activation occurs in the proximal crater subsurface beneath the crater floor under shock pressures above the HEL. The formation of radial cracks as well as the opening of radially oriented grain boundaries below the twinned zone occurs after the shock wave has attenuated to a compressional pressure wave with high differential stress. Tensile fracturing on different scales and at several locations of the crater subsurface results from the rarefaction wave passing through the target.

In quartzite, pervasive grain crushing as well as the formation of localized shear bands with grain comminution occurs under shock loading conditions above HEL close to the impact point and proximal in crater floor. The wide spread intra-granular fracturing is associated with the attenuation of the shock wave to pressures below the HEL. Tensile fracturing on different scales relates to pressure release and the passage of the rarefaction wave.

The reduced size of the damaged zone of the marble target (1.8 d_p marble versus 3.0 d_p quartzite) is mainly due to pervasive and intense twinning in calcite that consumes more energy of the passing shock wave compared to only localized shear deformation in the quartzite target.

The numerical models reach best fits with the experimental results when using target strengths larger than the quasi-statically determined UCS values. This suggests that the rate-dependent increase in strength during dynamic loading plays an important role in impact cratering. Further future modelling studies which include mesoscale approaches that are capable of simulating the observed deformation mechanisms may substantially improve the current modelling results.

6.7 Acknowledgements

This work has been carried out in the framework of the MEMIN Research Unit FOR 887, projects KE 732/16-2 and WU 355/6-2 and we would like to thank the German Research Foundation DFG for ongoing support. We specially thank Tobias Hoerth and Christoph Michalski, as well as the technicians of the Fraunhofer EMI for conducting the experiments. We greatly appreciate the support of Dr. Richard Wirth with the TEM analysis used in this study. We thank our lab technician Herbert Ickler for the preparation of all samples. We thank Nicole Güldemeister for fruitful discussions. We gratefully acknowledge the developers of iSALE-2D, including Gareth Collins, Kai Wünnemann, Dirk Elbeshausen, Boris Ivanov and Jay Melosh. We also acknowledge the developer of the pySALEPlot tool Tom Davison, and the developer of the VIMoD tool Dirk Elbeshausen. iSALE –Website: **www.isale-code.de**. Finally, we are grateful to John G. Spray and Auriol Rae for their constructive reviews.

6.8 Appendix

6.8.1 Determination of pre – and post-impact porosity

Both target materials have less than 1% detectable porosity and if porosity is present, it exists as small, unconnected intra-granular pockets. Pre- and post-impact porosity was measured to quantify the secondary porosity that developed as a result of dilatant deformation during the impact experiments. The digital image analysis software ImageJ (http://rsbweb.nih.gov/ij/) was used to determine porosity quantitatively via

image analysis. Grey-scale thresholds were applied to SE images of 100x magnification. The nominal resolution of pore space using that magnification is ≥ 2 µm. The determined porosity is given as the area percentage of each analysed image. Each image is a depth section defined as 0.25 d_p (projectile diameters; 0.25 d_p = 0.625 mm) in height and ~ 0.5 d_p in width. Individual depth sections do not overlap. The obtained 2D porosity is equivalent to the 3D volume porosity in percent (Bear 1972; Bear and Bachmat 1984).

6.8.2 Grain size distribution

Grain sizes in both experiments were determined along the symmetry axis of the crater. As with the porosity, depth sections of 0.25 d_p (0.625 mm) height and 0.5 d_p width were analysed individually using the Analyse Particles tool in ImageJ, which yields a grain size dataset. Due to the resolution of the SE micrographs, the smallest particle size that can be reliably measured is 4 µm. The particle sizes were binned in four particle size classes per order of magnitude grain size. The frequency density (i.e. the absolute frequency of grain sizes of a class in proportion to the bin size) was plotted against the binned grain sizes for increasing depth intervals.

6.8.3 Different deformation micro-features

The quartzite target subsurface also contains localized deformation zones of comminuted material. The grain size reduction along these zones were additionally analysed based on 1000-fold magnified BSE-images (90 x 120 µm), which were taken at ~ 150 µm intervals. Images were cropped to the deformation zone with Adobe Photoshop and the cropped section was analysed with the "analyse particles"-function of ImageJ. The smallest particle size that can be reliably measured is 0.3 µm. The determined grain size per image was plotted against radial distance to the crater floor, converted into depth in projectile diameter.

The intra-granular crack density of both experiments was calculated by summarizing crack lengths within bounding-box squares with an edge

length of 0.625 mm (0.25 d_p). The boxes were shifted vertically away from the crater floor in 0.25 mm (0.1 d_p) steps along the symmetry axis of the crater. The total crack length per square area was normalized by the maximum value obtained along the profile.

6.8.4 Orientation analysis of these micro-features

For an orientation analysis of the cracks in both marble and quartzite target, the azimuths were determined with the Field Calculator tool of ArcGIS and binned in the same way as for the crack density analysis. For each depth interval, a rose diagram was plotted to achieve the main orientation of that interval.

6.8.5 Numerical modelling

To model the strength, *Y*, of the target during crater formation, we used the constitutive model proposed by Collins et al. (2004) in default setting. The strength of the target depends on the confining pressure *p* and the state of damage *D* that the material has witnessed. Increasing the damage of the material causes a weakening of its strength according to:

$$Y(p) = (1 - D)\, Y_i(p) + D\, Y_d(p) \ . \qquad (69)$$

The subscripts *i* and *d* denominate the intact (*D*=0) and damaged (*D*=1) material properties, respectively. A detailed description of the determination of the damage is given by Collins et al. (2004). The shear damage is given by the ratio of total plastic strain to the accumulated strain at the point of failure. Failure occurs, when the stress in the material exceeds the strength of the material, i.e. $J_2 > Y^2$, where J_2 is the second invariant of the stress tensor:

$$J_2 = \frac{(s_1 - s_2)^2 + (s_2 - s_3)^2 + (s_3 - s_1)^2}{6} \ , \qquad (70)$$

where s_i are the principle deviatoric stresses. Due to fracturing and pulverization during the cratering process, the damaged material has a much lower strength than the intact material. As described by Popova et al. (2004) and successfully applied to previous sandstone target experiments (Güldemeister et al. 2015), we use a parametrization by Lundborg (1968) for the intact state of the material:

$$Y_i(p) = Y_i^0 + \frac{\beta_i p}{1 + \frac{\beta_i p}{Y_i^m - Y_i^0}} \quad , \tag{71}$$

where Y^0 describes the shear strength at zero pressure, β the coefficient of friction, and Y^m the Von Mises Plastic Limit. The strength of the damaged material is described by a Drucker-Prager yield surface that is capped by a maximum value of strength:

$$Y_d(p) = min(Y_d^0 + \beta_d\, p\, , Y_d^m)\, . \tag{72}$$

In addition, thermal weakening is considered (Ohnaka 1995). We oriented the choice of parameters for the strength model by the parameters chosen by Güldemeister et al. (2015) that gave consistent results between numerical and laboratory experiments with quartzite targets. Thus, we set β_i = 1.8 and β_d = 0.6 (note, that there is an error in table 2 of Güldemeister et al. 2015) for both the quartzite and the marble target. The cohesions Y_i^0 and Y_d^0 of the intact and damaged quartzite target were set to 96.9 MPa and 0 MPa, respectively (Figure 6-10). As the experimentally derived uniaxial compressive strength (UCS) of marble (60 MPa, Poelchau et al. 2015) is of the same order of magnitude as the UCS value of the porous sandstone studied by Güldemeister et al. (2015) (67 MPa, Poelchau et al. 2014), we tested to set Y_i^0 for marble to similar values in the order of 10 MPa and Y_d^0 to 0 MPa as shown by Güldemeister et al. (2015). However, recent results of dynamic strength hardening experiments at strain rates of 100 s^{-1} show a more extensive hardening for marble than for sandstone (Zwiessler et al.

2016). Strain rates during crater experiments reach even higher values and can be estimated as:

$$\dot{\varepsilon} = \frac{v_i \; r_{Pr}}{R^2} \quad , \tag{73}$$

where v_i is the impact velocity, r_{Pr} the projectile radius and R the reference size in the target. Those values are given with 5 km s^{-1}, 1.25 mm and ~10 mm, respectively, resulting in an estimate of the strain rate of ~ 6×10^5 s^{-1} (cf. Poelchau et al. 2014). This estimate is three orders of magnitude larger than the value from the split-Hopkinson pressure bar experiment and allows for a further increase of the dynamic increase factor above the value of 2.7 from the split-Hopkinson bar experiment. Thus, we also increased Y_i^0 up to 50 MPa, Y_i^m to 1.7 GPa, and Y_d^0 up to 10 kPa in order to include an effective strength hardening. Note that including some small cohesion in the damaged state gives some (small) tensile strength to the material. We also compared models with a Y_i^0 of 10, 60 and 100 MPa and a Y_d^0 of 100 kPa. Comparing transient crater depth and diameter, we find: decreasing Y_i^0 from 60 MPa to 10 MPa causes an increase in depth and diameter by ~ 20%. Increasing Y_i^0 from 60 MPa to 100 MPa causes a decrease in depth and diameter by ~10%. We are confident that our chosen value of Y_i^0 reproduces the crater well.

In the following, we describe the approach of calculating the dynamic equivalent to the strength of uniaxial compression experiments Y_{UCSd} using the 2nd invariant of the stress tensor in eq. (70) with the assumption $s_2 = s_3$:

$$J_2 = \frac{(s_1 - s_3)^2}{3} = \frac{{Y_{UCSd}}^2}{3} \quad , \tag{74}$$

and the assumption that $p = Y_{UCS}/3$, leading from eq. (71) to the following equation:

$$Y_i^0 + \frac{\beta_i \frac{Y_{UCSd}}{3}}{1 + \frac{\beta_i \frac{Y_{UCSd}}{3}}{Y_i^m - Y_i^0}} = \frac{Y_{UCSd}}{\sqrt{3}} \quad . \tag{75}$$

Solving this equation with the parameters chosen above results in Y_{UCSd} = 595 MPa. This value is one order of magnitude larger than the static UCS-value given by Poelchau et al. (2015). However, we might slightly overestimate the dynamic strength that we calculate based on the best-fit model due to the strength model used. For the purpose of numerical stability, the strength of the damaged state of the material cannot be set to too high values (e.g. cohesion). Consequently, the intact material must be defined to be stronger to absorb the effect of the low cohesion for damaged material.

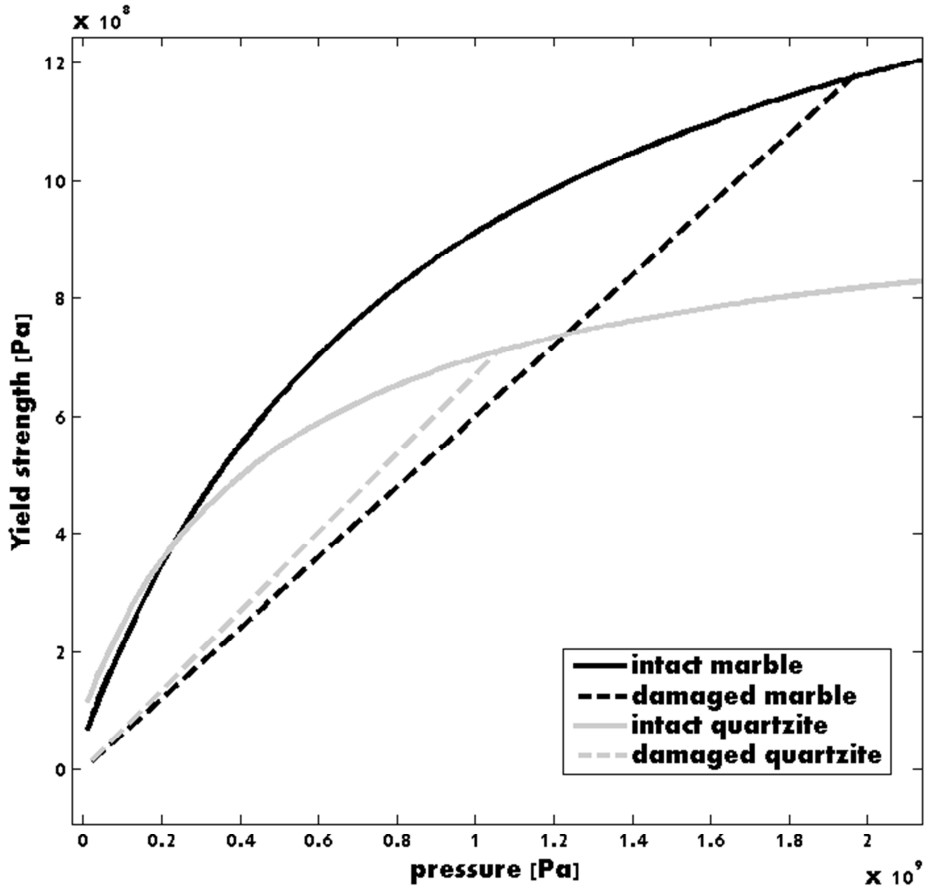

Figure 6-10: Yield strength of the two materials. Solid lines give intact material, dashed lines show damaged material yield envelopes. Black shows the strength of marble, grey the strength of quartzite.

In accordance with Güldemeister et al. (2015), we defined the transient crater in both models runs as the stage during crater growth when the maximum crater volume is reached. Due to technical problems, no video was available for the reconstruction of the transient crater parabola for the A34–5614 experiment. Hence, we consider the depth as the most important constraint for comparison of modelled and experimental craters in marble. The addition of some cohesion in the damaged state allows for taking the crater depths as a constraint, as we could not exclude further material displacement in the case of a cohesionless damaged material.

The spherical iron (Exp. A20–5339) and Campo de Cielo projectiles (Exp. A34–5614) were 2.5 mm in diameter. We use a resolution of 30 cells per projectile radius (CPPR) for the models. Previous studies using similar scaled targets used a resolution of 12 CPPR (Güldemeister et al. 2015) so that we consider our resolution of the projectile sufficient and at the same time still in an acceptable range in terms of computational costs. The impact velocity was set to 5 $km\ s^{-1}$, as estimated in the experiments. Note that in the aftermath of the experiments and simulations the impact velocity was re-calculated for the A34–5614 experiment with a different approach (the original triggers did not work properly) to be 5.4 km/s, and 5 km/s was used as a close estimate in the model. However, changes in crater size due to the small difference in velocity are small and expected to fall into the uncertainty range of the models. Furthermore, comparisons between the models exclude a velocity component when using the same velocity.

6.8.6 Parametrization table of the models

Table 6-5: Model data.

	Iron (projectile)	**Marble A34–5614**	**Quartzite A20-5339**
General parameters			
Poisson ratio (basalt)	0.25	0.3	0.3
Specific heat capacity [J/(kg K)]	200	880	800
Strength parameters			
Lundborg parametrisation			
intact yield surface:			
Y_i^0 [MPa]	-	50.0	96.9
β_i	-	1.8	1.8
Y_i^m [GPa]	-	1.7	1.0
damaged yield surface:			
Y_d^0 [kPa]	-	1.0	0.0
β_d	-	0.6	0.7
Y_d^m [GPa]	-	1.7	1.0
Thermal Softening (Ohnaka 1995)	-		
Softening constant	-	1.2	1.2
Melt temperature [K]	-	1100	1600
Simon approximation:			
Simon constant	-	$6 \cdot 10^9$	$6 \cdot 10^9$
Simon exponent	-	3.0	3.0

7 Snow carrots after the Chelyabinsk event and model implications for highly porous Solar System objects

This chapter has been published as the following peer-reviewed article:

Robert Luther, Natasha Artemieva, Marina Ivanova, Cyril Lorenz, Kai Wünnemann (2017). *Snow carrots after the Chelyabinsk event and model implications for highly porous Solar System objects*. Meteoritics & Planetary Science 52 (5), 979-999, http://dx.doi.org/10.1111/maps.12831.

This chapter addresses the objective *M I – Material Models* on the material models that are included in iSALE. In the previous chapter, I focused on the rheology models and crater simulations in competent rock. In this chapter, the focus lies on the description of the porosity parametrisation that is used with iSALE. To assess its applicability on porous materials, a scenario was chosen that includes a highly porous target. Hence, I chose to simulate characteristic features in snow that were found while recovering fragments after the Chelyabinsk airburst from 2013. My contributions to this article cover the study using iSALE that is described in the method, results and discussion sections. Furthermore, I edited the paragraphs from my co-authors. In addition, I added the explanation for the post-impact modification of the snow funnels that finally led to the formation of densely filled, ice "snow carrots". The section on the recovery of fragments and their initial description was done by M. Ivanova and C. Lorenz. Finally, N. Artemieva simulated the descent of the meteoroid fragments in the atmosphere.

7.1 Abstract

After the catastrophic disruption of the Chelyabinsk meteoroid, small fragments formed funnels in the snow layer covering the ground. We constrain the pre-impact characteristics of the fragments by simulating their atmospheric descent with the atmospheric entry model. Fragments resulting from catastrophic breakup may lose about 90% of their initial mass due to ablation and reach the snow vertically with a free fall velocity in the range

of 30-90 m/s. The fall time of the fragments is much longer than their cooling time and, as a consequence, fragments have the same temperature as the lower atmosphere, i.e. of about -20°C. Then we use the shock physics code iSALE to model the penetration of fragments into fluffy snow, the formation of a funnel and a zone of denser snow lining its walls. We examine the influence of several material parameters of snow and present our best-fit model by comparing funnel depth and funnel wall characteristics with observations. In addition, we suggest a viscous flow approximation to estimate funnel depth dependence on the meteorite mass. We discuss temperature gradient metamorphism as a possible mechanism which allows to fill the funnels with denser snow and to form the observed "snow carrots". This natural experiment also helps us to calibrate the iSALE code for simulating impacts into highly porous matter in the Solar System including tracks in the aerogel catchers of the Stardust mission and possible impact craters on the 67P/Churyumov-Gerasimenko comet observed recently by the Rosetta mission.

7.2 Introduction

At 9:22 a.m. (local time, 3:22 UTC) on February 15, 2013, an extremely bright fireball was seen by many wittnesses in the Kurgan, Tyumen, Ekaterinburg, and Chelyabinsk districts of Russia. Thousands of stones fell as a meteorite shower around Pervomaiskoe, Deputatsky and Yemanzhelinka villages ~40 km south of Chelyabinsk. The largest meteorite (~600 kg) formed an 8-m-diameter hole in the Chebarkul Lake ice (70 km west of Chelyabinsk) and was recovered in autumn (Popova et al. 2013). A few buildings were damaged and window glasses were broken within an area of ~1400 km^2 by the atmospheric shock waves. About 1600 people were injured by broken windows and required medical attention. Numerous video recordings allowed for the reconstruction of the trajectory and fragmentation history of the estimated ~20 m sized meteoroid revealing a low entry angle of about 17° to the horizon at 19 km/s, and an altitude of breakup between 45 and 30 km (Borovička et al. 2013). The first fragments were found by local residents immediately after the fall. An expedition from the *Vernadsky Institute* arrived 3 days later, on February 18 of 2013, to start the regular search. Many fragments were recognized due to small holes in the snow cover. Beneath the holes, a funnel leads to a narrow snow-filled cone with the fragment at its tip, which we refer to in the following as "snow carrot" due to its shape.

In this paper we test two hypotheses of "snow carrot" formation: 1) warm fragments fall onto the snow, cause melting of snow, and then sink into the mixture of water and snow which recrystallizes later to form the characteristic "carrots"; 2) cold falling fragments mechanically compact the fluffy snow without substantial heating and melting. In the following sections we present: a short description of the field work at the impact site, numerical modelling of atmospheric entry and penetration into snow, and possible mechanisms of post-impact modification of the funnels. Finally, we discuss potential applications of the presented models for impacts in the Solar System.

7.3 Recovery of meteorites in the field

Local residents collected the first meteorite pieces from the snow shortly after the meteorite fall. Some finders noted that stones were warm (in comparison with local temperature of -20^{o}C); however, temperature descriptions vary between the witnesses and may be biased. The *Vernadsky Institute* expedition arrived to the site on February 18 and worked in the field for one week until a snow storm impeded the recovery of meteorites from snow. During the expedition, 464 meteorite stones were recovered, weighing 3.66 kg in total. The weight of individual fragments ranges from 1 g to 120 g; their size ranges from a few mm up to 10 cm (Badyukov and Dudorov 2013). Other expeditions, meteorite hunters, and local residents recovered additional fragments weighing 0.001-2 kg, and one 24 kg piece was found much later. The recovered fragments have been described in detail in terms of mineralogy, petrography and their chemical composition by Galimov et al. 2013. Based on these analyses, the Chelyabinsk meteorite has been classified as LL5 ordinary chondrite that has experienced a moderate-degree of shock metamorphism at some point in its history before its encounter with the Earth: The fragments contain shock melt (~1/3 by volume); and isotopic characteristics suggest an earlier impact event about 290 Ma ago.

The *Vernadky Institute* team investigated a large area along the trajectory of the meteorite. All fragments were easily detected due to holes in the snow cover. Most of the excavated meteorite fragments were surrounded by a dense shell of coarse-grained snow continuing into a vertical column, which the expedition members named “snow carrots”, above which the channel in the snow led to the surface (Ivanova et al. 2013), (see Figure 7-1 i–iv) showing “snow carrots” in the field). The team excavated the snow around each hole, retrieved a “snow carrot”, and picked out the meteorite from its tip.

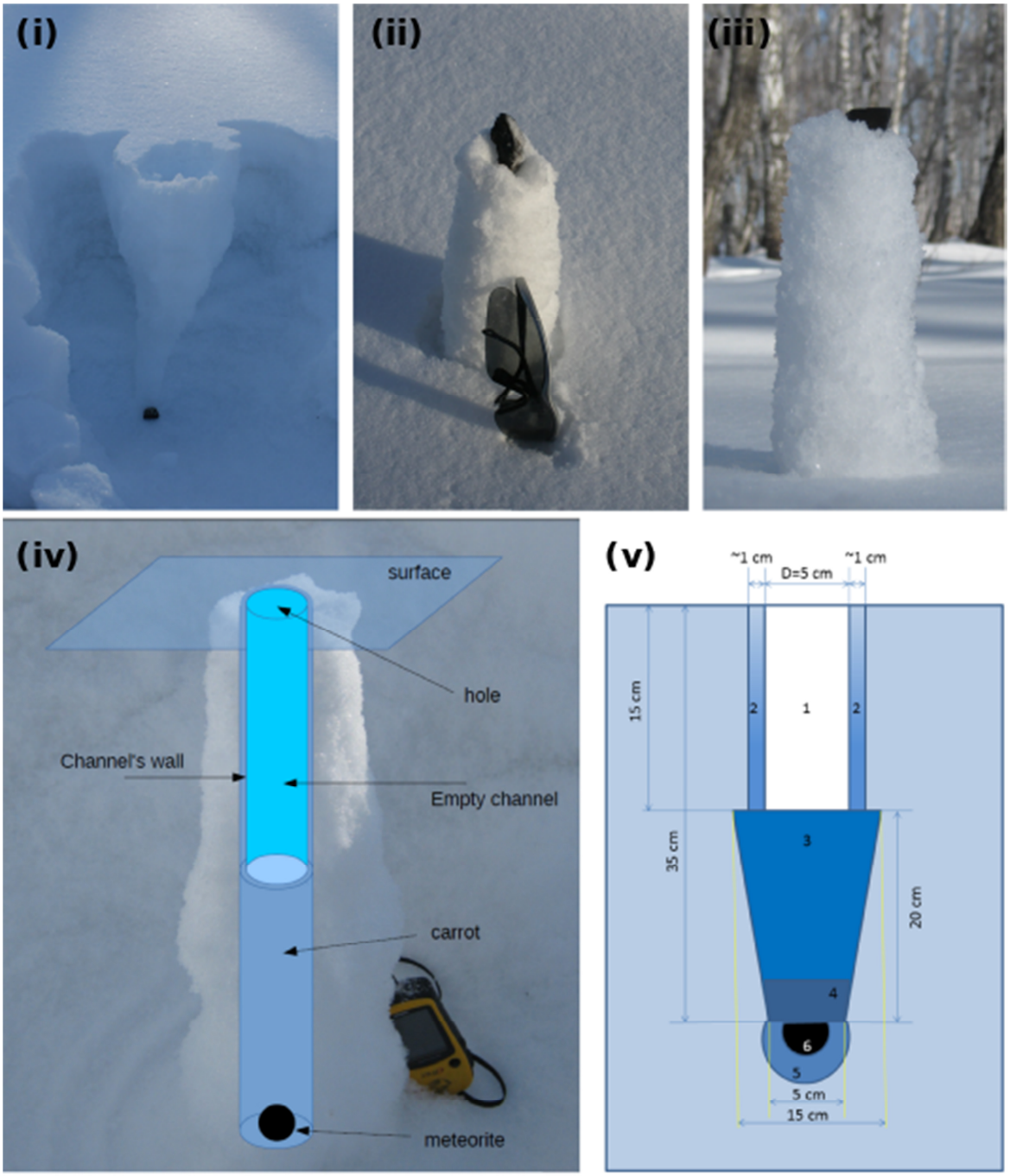

Figure 7-1: “Snow carrots”. In (i) and (iv) the “snow carrots” are shown in situ. In (ii) and (iii) the “snow carrots” are shown upside down and put on top the snow layer for photographic purposes. The fragments can be seen in (i), (ii) and (iii). The sunglasses in (ii) and GPS unit in (iv) serve as scale. A scheme is added for description in (iv). In addition, a Cross section of the snow funnel and the “snow carrot” created by a fragment with a mass of ~ 50 g is shown (v). Numbers show: 1 – channel in the snow; 2 – thin walls of the channel made of coarse-grained snow (note that the upper end of the funnel walls cannot be distinguished from the surrounding snow); 3-4 – “snow carrot”, 3 – dense snow with large crystals, 4- dense snow with small crystals ~1-2 cm thick; 5 – the envelope of dense fine-textured snow; 6 - meteorite fragment.

At first glance the funnel length correlates with meteorite mass (and hence with their terminal velocity). However, we cannot exclude deviations from this correlation due to the fragment's specific geometry, influence of local winds, or other unknown factors. The snow layer in the Chelyabinsk area that covered the frozen ground was about 70 cm thick at the time of the event and represents the maximum observable funnel length. Big fragments reach the frozen ground surface and are embedded into the soil whereas intermediate cm-sized fragments with a mass of more than 50 g penetrated to a depth of 30-40 cm (Figure 7-1 v) and small fragments with a mass of only few grams were stopped at a depth of about 10-15 cm. In rare cases and only in some places, the smallest fragments lie on the thin icy crust without penetration.

Each funnel begins at the snow surface with a 1-7 cm in diameter entrance hole. These entrance holes are usually about 1.5-2 times larger than the diameter of a sphere with the same mass as the fragment at the bottom of the funnel. The upper short part of the funnel does not show significant increase in structural strength and cannot be distinguished from the surrounding undisturbed snow. However, at depth funnel walls differ from the surrounding snow and are made of the coarse-grained snow with large crystals (number 2, Figure 7-1 v). Vertical funnel walls for intermediate-sized fragments are ~1 cm thick and 10-30 cm in length. Sometimes the walls deviate from vertical by 5-10°. This deviation could be explained by fragment's collision with tree branches shortly before the penetration (some meteorites had traces of bark). The upper layer of snow surrounding the funnels did not show any signs of subsidence, ejecta deposition or any other disturbances. Vertical cross-sections of the funnels are not cylindrical but have a slightly wavy structure that could be the result of either meteoroid's rotation during the penetration or the natural layering of the snow cover.

To about half of the penetration depth, the funnels are filled by dense snow with large crystals and, at the deepest part - by ~1-2 cm of dense snow with small crystals (number 3 and 4, respectively, Figure 7-1 v). These features, which we refer to as "snow carrots"Figure 7-1, are shorter than 10 cm for the smallest fragments and longer than 20 cm for the intermediate

size fragments. The diameters of the "snow carrots" equal the diameters of the snow funnels including the funnel walls. The fragment itself is located at the tip of the "snow carrot" and is surrounded by an envelope of dense, fine-textured snow.

The funnel walls and "snow carrots" consist of transparent crystals 2-5 mm in size whereas the surrounding snow characterizes by much finer structure. There is also a thin layer of frost crystals growing on the funnel walls.

The largest meteorite fragments are surrounded by 0.5-1 cm-thick envelopes of dense fine snow. In one case (a 100 g-weight fragment) the envelope was icy. Smaller fragments are surrounded by coarse-grained snow with variable thickness. Fragments weighing ~100 g penetrate close to the ground and have a thin fine snow layer between the fragment and the soil. In some cases the layer of fine-grained snow is ~1.5 times wider in diameter than the carrot (the carrot has a "foot") and it is not clear if this "foot" is a consequence of the penetration process, or if it is caused by some local pre-impact properties of soil/snow.

7.4 Methods in use and Initial Conditions

We use a two-stage modelling approach to describe the funnel formation. First we derive realistic initial conditions for this natural experiment (mass, velocity, temperature) by simulating the atmospheric motion of the fragments of the Chelyabinsk meteoroid after its catastrophic disruption at an altitude of ~30 km, including their thermal history and mass-velocity evolution. In the second stage, we simulate the impact into snow using the mass and velocity constraints from the first stage as initial conditions.

7.4.1 Atmospheric entry model

First, atmospheric drag decelerates meteoroids from their initial velocity (~20 km/s on Earth) to a lower limit of terminal velocity ranging

from several centimetres to hundreds of metres per second, depending on the meteoroid size:

$$m\frac{dv}{dt} = -C_d\rho_a v^2 A + mg. \quad (76)$$

In this drag equation, m, v, A are mass, velocity, and cross-section of the meteoroid, respectively, ρ_a is the atmospheric density, and g is the gravitational acceleration. The drag coefficient C_d can be calculated by numerical models, measured in experiments, or deduced from observations. In a high-velocity continuum flow, this coefficient depends mainly on the meteoroid's shape and varies between 0.3 and 1.

Second, atmospheric shock waves heat the air surrounding the meteoroid and make it visible as a bolide or fireball. Moreover, the thermal radiation produced by shock-heated air evaporates the meteoroid and, as a consequence, it may lose more than 95% of its initial mass:

$$Q\frac{dm}{dt} = -C_h\rho_a v^3 A. \quad (77)$$

Here Q is the amount of heat required for vaporization of solid materials (2-10 kJ/g), and C_h is the heat transfer coefficient, which has to be deduced from observations or calculated by methods of radiative hydrodynamics. Typically its value depends on the altitude, velocity, and meteoroid size and varies over a much wider range than the drag coefficient C_d (Nemtchinov et al. 1997). Instead of C_h and Q we use the ablation coefficient $\sigma_a = \frac{C_h}{QC_d}$ with a typical value for stony meteoroids of 0.014 s^2/km^2 (e.g. Bland and Artemieva 2006).

Generally, one more important process has to be taken into account, namely the fragmentation of the meteoroid (Chyba et al. 1993; Artemieva and Shuvalov 2001). However, in this study we deal with small fragments of the Chelyabinsk meteorite, which decelerate quickly after the catastrophic fragmentation (Borovička et al. 2013; Popova et al. 2013) and most likely are not subject to further disruption.

7.4.2 Heat transfer with mass loss

To calculate the temperature distribution $T(r,t)$ within a spherical fragment, we solve the heat transfer equation:

$$\rho C_p \frac{\partial T}{\partial t} = \frac{1}{r^2}\frac{\partial}{\partial r}\left(kr^2 \frac{\partial T}{\partial r}\right), \quad (78)$$

where ρ is meteoroid density, C_p is specific heat capacity, and k is thermal conductivity. Typical values of these parameters used in this study are: ρ=3.32·10^3 kg/m^3, C_p= 500-700 J/kg/K, k=4.1-4.5 W/m/K (Szurgot 2014). We distinguish three stages of flight with different boundary conditions. In the first stage, at velocities exceeding 2-4 km/s, the heat flux q to the surface is defined by radiation emitted by atmospheric shock waves and by hot meteoroid's surface. Assuming that the air and the vapor at temperatures T_a and T_v radiate as black bodies and absorption by vapor is negligible, q is given by $q=\sigma_B(T_a^4-T_v^4)$. The given radiation from highly compressed air heats, melts, and vaporizes the external layer of the fragment. If the thickness of the molten layer (known as the fusion crust) exceeds 2 mm, we change the fragment radius to keep the fusion crust thickness constant. By varying the T_a and T_v in a reasonable range, we can fit the final fragment size to the results obtained by solving eqs. (76)-(77). The second stage begins when the velocity drops below 2 km/s and ablation ceases. Now, the external flux is defined mainly by conduction from hot vapour (T_v=3000K) surrounding the fragment. We do not know for how long fragments move together within a hot vapour cloud and when they enter the cold atmosphere as individuals. Thus, we continue calculations until the thickness of the outer molten layer exceeds 2 mm (the criterion is similar to the high-velocity regime). This restriction gives us the longest time (and hence, maximum heating of the fragment's interior) the fragment of a certain size may spend within the cloud. At the third stage, we solve the heat transfer equation (78) with a boundary temperature equal to atmospheric temperature (as fragments spend most of the time at low altitudes, we assume that this temperature is about 250 K or -23°C).

7.4.3 Impact into snow: numerical model

For the simulation of the penetration of fragments into the snow we use the Chicxulub version of the iSALE-2D Eulerian shock physics code (Wünnemann et al. 2006), which is based on the SALE hydrocode solution algorithm (Amsden et al. 1980). To simulate impact processes in solid materials SALE was modified to include an elasto-plastic constitutive model, fragmentation models, various equations of state (EoS), and multiple materials (Melosh et al. 1992; Ivanov et al. 1997). More recent improvements include a modified strength model (Collins et al. 2004) and the ε-α porosity compaction model (Wünnemann et al. 2006, 2006; Collins et al. 2011), which is of particular importance for this study. For natural materials like sandstone, the porosity compaction model has been tested and compared with mesoscale numerical models that explicitly resolve pore space with high resolution and experimental data (Collins et al. 2011; Kowitz et al. 2013; Güldemeister et al. 2015; Wünnemann et al. 2016).

We model the Chelyabinsk scenario using the Tillotson equations of state (EoS) for the basaltic fragments (projectile) and ice (target). The Tillotson Equations work well in the low pressure regime that is expected due to the low velocity impacts. In addition, we include porosity for the ice to represent the low-density snow layer. Unfortunately, the local undisturbed snow was not studied directly after the Chelyabinsk event in terms of strength and structure. Limited density tests were performed almost two months later (Gindilis and Shevelev 2014). Averaged over 50-cm depth, porosity (the ratio of the towed water volume to the collected snow volume) varies between 43% and 54% (Gindilis and Shevelev 2014). However, snow properties may change substantially on this time scale (Sturm and Holmgren 1998). We therefore adopt snow density values from the literature. Sturm et al. 1995) classify snow in the Chelyabinsk area as snow with tundric characteristics and give an average snow density of 260 kg/m³. In February (day 46), tundric snow varies in density from about 260 kg/m³ up to about 350 kg/m³ (e.g. Sturm and Holmgren 1998), therefore, we adopted an average porosity value of about 70% (density of 284 kg/m³).

In our study, we evaluated about 50 models to find the best fit to the observed snow funnels in terms of the final funnel depth and diameter, as well as on the compaction of the funnel walls. The yield strength of the projectile was set to 200 MPa with a constant Von Mises parameterisation, which corresponds to the average compressive strength of stony meteorites as measured in the laboratory (Petrovic 2001). In addition, thermal weakening was considered in most models (Ohnaka 1995). For the yield strength of the snow layer we use a Drucker-Prager rheology model. The strength model is described as:

$$Y = min(Y_0 + \beta\, P\, , Y_{max}) \tag{79}$$

with P being the pressure. We choose for Cohesion Y_0, Coefficient of friction β and maximum yield strength Y_{max} the following value ranges: of 1kPa-10 kPa, 0.185-0.415 and 10 kPa-100kPa, respectively (Haehnel and Shoop 2004; Arakawa and Yasui 2011; Lee and Huang 2014).

In addition to this macroscopic yield strength of the snow, we also account for the strength properties of snow crystals that define the resistance of snow against compaction and the crush-out of pore space. According to the ε-α model that we used in our models the crushing strength is described by the critical volumetric strain ε_e at which the elastic compaction regime is separated from the plastic compaction regime. For a volumetric strain smaller than ε_e (in absolute value) a decrease of pore space due to compaction is not permanent and the snow returns to its initial porosity after unloading. At larger volumetric strains permanent pore space compaction occurs. Mechanical work required for compaction consumes energy that is not available for crater formation or ejection of matter. Note, the unloading of a completely compacted volume of snow generally results in a minimum porosity due to elastic portion of the unloading path. Note further, that the volumetric strain is negative for compaction and positive for tension. More details about the porosity compaction model and how the reduced speed of sound (described by the speed of sound ratio χ that is the speed of sound in porous material relative to the speed of sound in solid material) in porous

media affects the penetration and compaction processes are given in the Appendix.

We study the penetration process for fragments with a mass of 150 g and an initial velocity of 60 m/s as constrained by the atmospheric entry model (see the Results section). We model a spherical projectile with resolution of 35 cells per projectile radius (CPPR). Previous studies using the same porosity compaction model used resolutions of 12 CPPR (Güldemeister et al. 2015) so that we consider our resolution of the projectile sufficient and at the same time still in an acceptable range in terms of computational costs. For the given resolution we set up a grid with 1600 vertical cells that covers at least the expected snow funnel depth of about one metre. The number of horizontal cells (350 cells in high resolution) was set small enough to reduce the computation time of the models and large enough to avoid artefacts such as shock wave reflection from the outer boundaries of the mesh. In addition, we included 50 cells of increasing size at the bottom, the side, and the top of our grid to avoid disturbances near the mesh boundaries.

7.4.4 Impact into snow: analytical model

As numerical models are computationally expensive, we also try to find an analytical solution for different fragment masses (4 g, 50 g, and 1 kg) assuming that gravity is not involved and the penetration is equivalent to a viscous flow around the fragment, i.e. the decelerating force G within the snow layer can be described by Stokes drag:

$$G = 6\pi r \eta_S v \quad , \tag{80}$$

where r is the projectile radius, η_S is snow viscosity, and v is the fragment velocity. Assuming that all parameters (except of velocity) are constant, the evolution of the projectile velocity and depth through time t can be described as:

$$v(t) = v_0 \, e^{-\frac{6\pi r \eta_S t}{m}} \quad , \tag{81}$$

$$d(t) = v_0 \, \frac{m}{6\pi r \eta_S t}\left(1 - e^{-\frac{6\pi r \eta_S t}{m}}\right) \quad , \tag{82}$$

where v_0 is the initial (prior to the contact with snow) velocity of the fragment. The value of viscosity is unknown but can be estimated by fitting our modelling results for a 150-g-weight fragment to equation (81) or (82).

7.5 Results

First, we present the results of the evolution of the fragments from the Chelyabinsk event from our atmospheric entry model. We obtain values for final velocities and masses of various fragments with the final mass smaller than 1 kg. We also study the thermal evolution of the fragments. In the second part, we present the results of the penetration model for a 150-g-weight fragment. We vary several model parameters to study their effect on the characteristics of snow funnels and present the best fit to observational constraints.

7.5.1 Atmospheric entry dynamics

We assume that after the catastrophic fragmentation at an altitude of ~30 km all fragments move independently and their masses vary from 10 g to 10 kg (point CF in Figure 7-2). Smaller fragments could be formed but their final mass is too small to be identified on the surface; larger fragments have not been observed to form "snow carrots". Immediately after fragmentation, all fragments have the same velocity as registered prior to fragmentation, i.e. 19 km/s at 17° to the horizon (Borovicka et al. 2013). Solving equations (1-2) we find that after 1-4 sec (depending on mass), individual fragments lose ~90% of their initial mass, are decelerated to velocities below 2 km/s, and ablation ceases (this part is marked by black diamonds in Figure 7-2). Then, within twenty seconds from the disruption,

the fragments reach a free-fall terminal velocity corresponding to equilibrium between gravity and drag (note change in the curves' slope in Figure 7-2). This free-fall velocity slowly decreases due to increasing atmospheric density. The final velocities near the surface vary from 32 m/s for the smallest 4-g-weight meteorite to 84 m/s for the largest 1-kg-weight meteorite. The atmospheric descent lasts 161s and 420s for the largest and the smallest fragments, respectively. All numbers above assume spherical fragments; change in shape, i.e. another drag coefficient, may increase or decrease final velocities (and hence, the total time in flight) slightly.

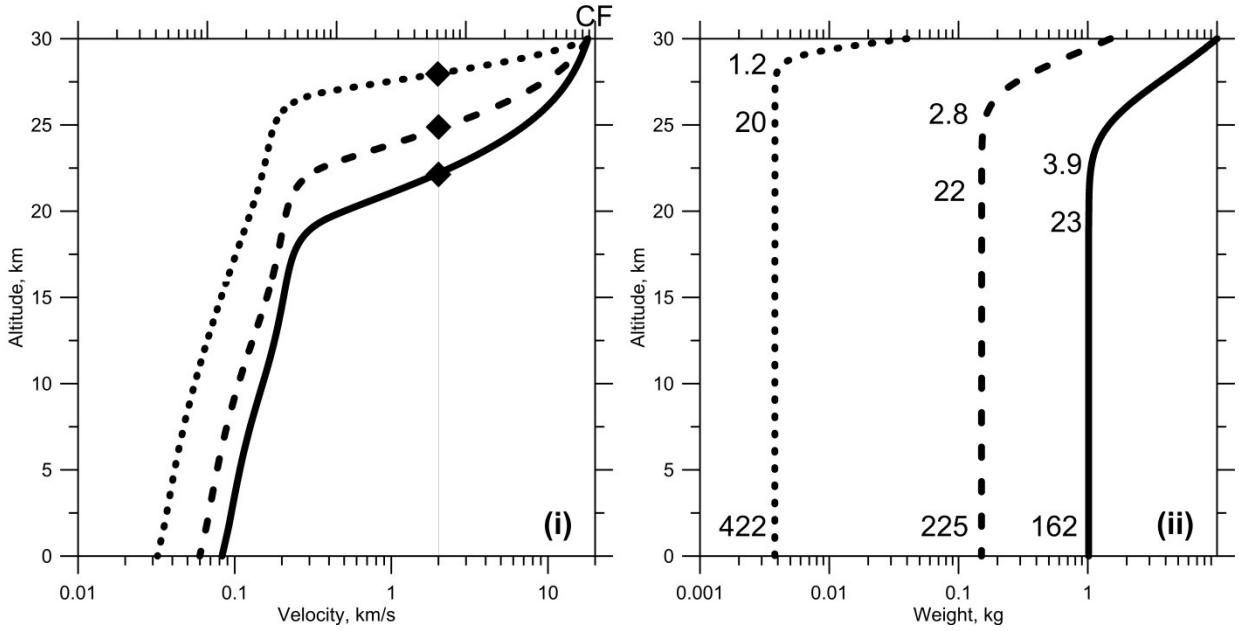

Figure 7-2: Fragment velocities (i) and masses (ii) as a function of altitude. Initial masses of fragments are 0.04 kg (dotted lines), 1.5 kg (dashed lines), and 10 kg (solid lines). i) CF – catastrophic fragmentation, beginning of fragments' flight; black diamonds - deceleration to 2 km/s, end of ablation; change in the slope corresponds to the beginning of free-fall. ii) Numbers near the curves show the time in seconds (starting from CF) to the end of ablation (upper numbers); to the beginning of free-fall (numbers in the middle); to landing (numbers at the bottom). Final masses are ~10 times smaller than initial ones.

7.5.2 Heating and cooling during the entry

The radiation emitted by the shocked atmospheric gas efficiently heats the outer surface of meteoroids up to melting and vaporization. Incoming gas flow removes this heated layer from the surface and exposing deeper layers to the radiation. This process is known as ablation of

meteoroids. Although meteoroids lose 50-90% of their initial mass by ablation, the total thickness of the heated layer (known as the ablation crust) usually does not exceed a couple of mm. This 'dynamically' formed layer of melt and vapour does not allow for substantial heating of the meteoroid interior, i.e. meteoroids remain cold below the ablation crust (Figure 7-3, grey lines). Heating could propagate inside when ablation ceases but the ablation crust remains hot due to surrounding vapor or hot air (or their mixture), i.e. the meteoroid stops losing mass but is still within a vapor cloud in close proximity to other fragments. It is difficult to estimate the timing of this stage, but it is certainly shorter than the timing for total deceleration (20 sec). If heating by a hot (~3000 K) external layer continues longer than 2-3 seconds, then the outer part of the meteoroid begins to melt, increasing the ablation crust thickness. Assuming a 2-mm-thick external molten layer we find that during this stage, small fragments could be heated above 0°C up to half of their final radius whereas the largest fragments remain cold (Figure 7-3, black dotted lines).

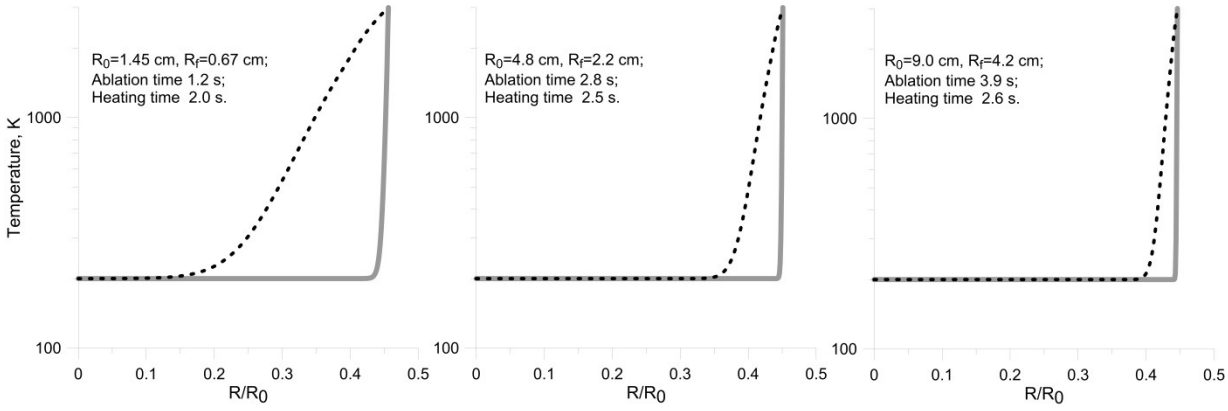

Figure 7-3: Heating of meteoroids of various masses (same as in Figure 7-2) in the vapor cloud after the end of ablation. Grey lines show the temperature profiles at the end of ablation; black dotted lines show the temperature profiles prior to cooling during free fall in the cold atmosphere.

As our estimates of heating are not precise, we use three different temperature profiles at the beginning of the free fall stage: 1) cold meteoroid surrounded by a 2-mm-thick melt layer; 2) calculated T-profile as in Figure 7-3; 3) totally molten meteoroid with $T=T_{melt}$. The latter case certainly overestimates heating during the entry and may be considered as the upper limit in our calculations of the cooling time and the upper limit of meteoroid

temperature after landing. During the free fall, meteorites cool quickly as the temperature outside is equal to the atmospheric temperature. The situation is different from cooling of hot rocks surrounded by immobile air. Finally, we can compare the cooling time of various meteorites with their free fall time (see Figure 7-4). In all but two cases, the cooling time is substantially shorter than the free fall time. The two exceptions are the totally molten meteorites with a mass of 150 g and 1 kg. As this temperature profile is unrealistic and large fragments are rare, we may conclude that all carrot-forming fragments reach the surface being as cold as the surrounded atmosphere, i.e. their temperature was below freezing.

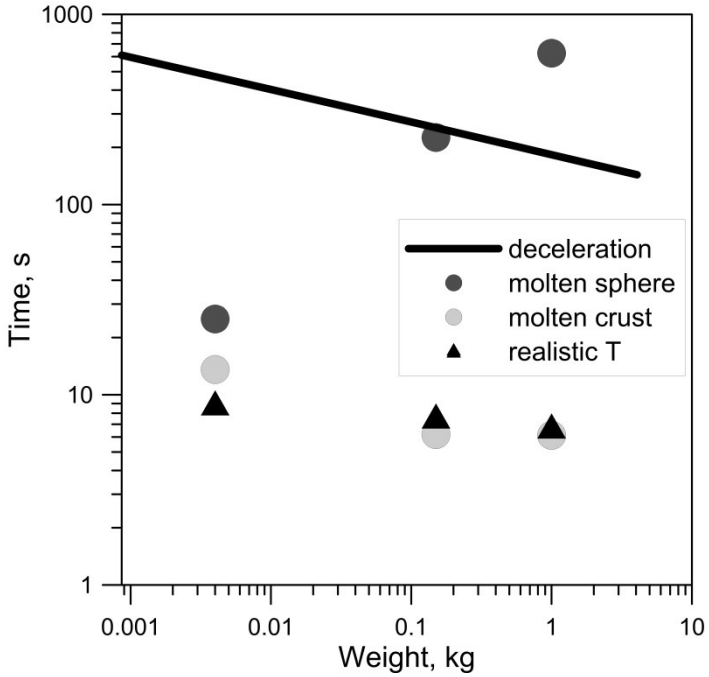

Figure 7-4: Comparison of the free-fall time (solid line) with the cooling time as a function of meteorite mass for various temperature profiles.

Final velocities and final masses of meteorites presented in Table 1 are used as initial conditions to model penetration of fragments into snow.

Table 7-1**:** Results for four initial fragment sizes. Case III is studied in detail using the iSALE model.

	Case I	**Case II**	**Case III**	**Case IV**
Initial fragment mass in kg	0.04	0.5	1.5	10
Final fragment mass in kg	0.004	0.05	0.15	1.04
Free fall time in s	420	271	224	161
Surface velocity (vertically) in m/s	32	50	60	84
Final fragment diameter in cm	1.34	3.14	4.8	8.6
Funnel depth in cm (model)	-	-	62	-
Funnel depth in cm (calculated)	4	31	-	394
Observed funnel depth in cm	~ 10	~ 35	~ 65	~ 70 (max. depth of snow layer)

7.5.3 Snow Penetration

7.5.3.1 Best fit model

Based on the range of possible impact parameters, we vary target properties (yield strength; parameters of the ε-α porosity compaction model) in order to reproduce the observed snow funnel length as well as the characteristic density features of the funnel walls. First, we present details of our best-fit model. The choice of strength parameters and the elastic volumetric strain threshold is discussed below according to their influence on funnel depth and funnel wall characteristics. In Figure 7-5, three snapshots of the penetration process are shown. The snapshots display the material (snow or projectile) on the left half of the image, and the density on the right half. First, the meteorite fragment compacts the snow underneath the first contact point (i). After ~1/10 of the whole penetration time, the projectile reaches a depth of ~12 cm, corresponding to about 1/5 of the maximum depth of the funnel. During the penetration process, the snow is pushed aside, the fragment decelerates, and the funnel wall of denser snow forms (ii). After ~8.5 ms, the fragment has lost about half of its initial velocity and reaches a depth of ~35 cm. The formation of the funnel wall continues until the fragment stops at the final funnel depth of ~62 cm (iii). Details on the evolution of velocity and depth are shown in Figure 7-5. The

temperatures in the funnel walls do not vary significantly from the pre-impact temperature. Note that the propagating denser precursor underneath the projectile is a known numerical artefact related to the symmetry axis and high porosity. However, this precursor has a minor influence on the results (see Appendix for more details). All snapshots show little ejected snow during the funnel formation.

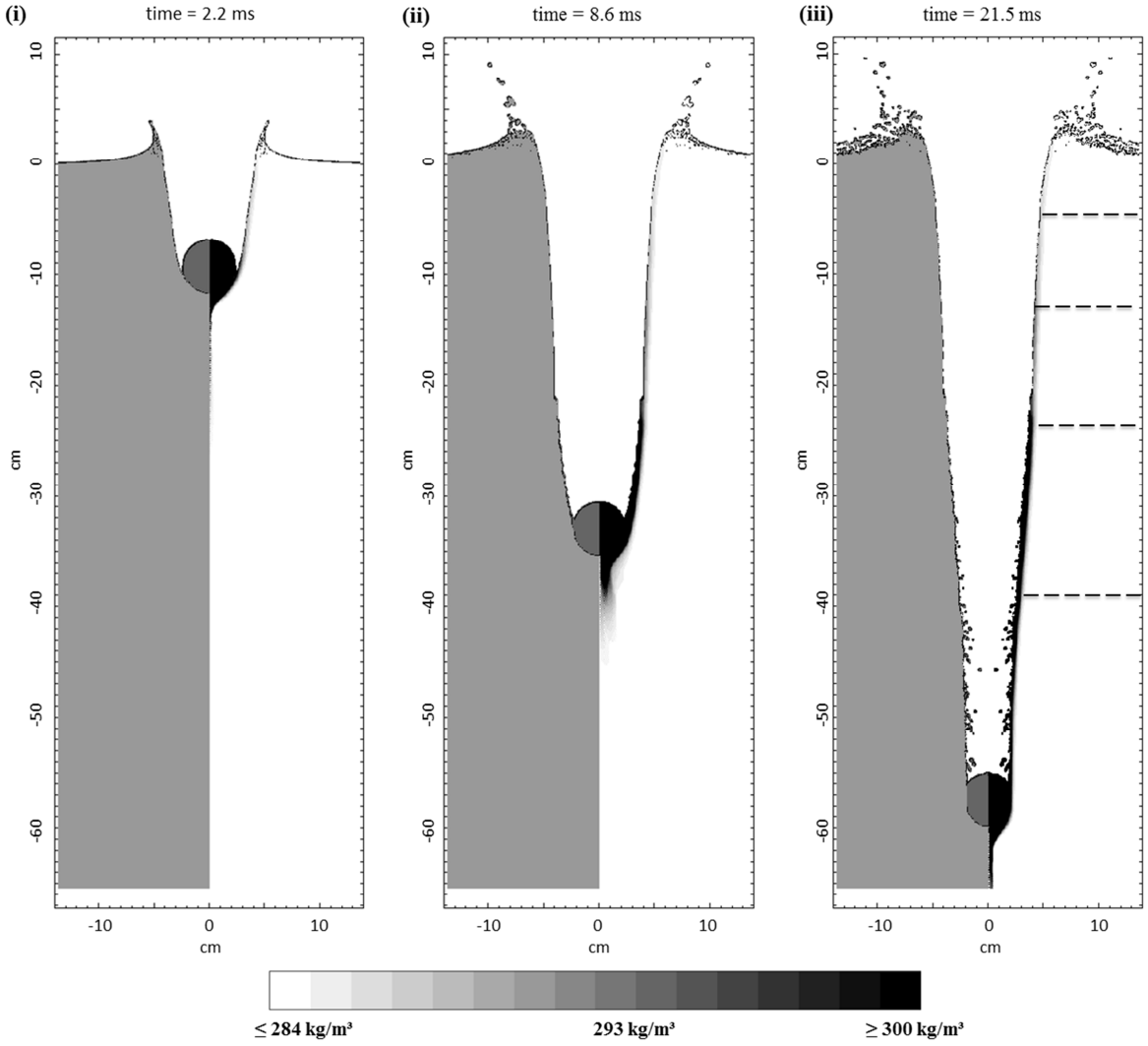

Figure 7-5: Snapshots of the funnel formation. The snapshots show the following time steps from (i) to (iii): 2.2 ms, 8.6 ms, and 21.5 ms (stop of funnel growth). For each image, the right side shows the density and the left side the material (dark grey for the fragment and light grey for the snow). A denser (black) funnel wall is created. On the right side in image (iii), dashed horizontal lines are included to show where the density profiles in Figure 7-8 have been taken. Small accumulations of material in the funnel above the fragment (image iii) mostly consist of projectile material and are numeric artefacts. The dense precursors underneath the projectile in snapshot (ii) as well as in snapshot (iii) are modelling artefacts caused by the symmetry axis.

For the first half of the penetration process, we fit the velocity evolution derived from the numerical model to eq. (81) – see Figure 7-6 (i). The best fit corresponds to the effective snow viscosity of 27.4 Pa s. To achieve a good fit for the late stage, a higher viscosity of 76.4 Pa s was required. Keeping the snow viscosity equal to 27.4 Pa s and using eq. (7) we estimate the penetration depth of three fragments (4 g, 50 g and 1 kg in weight) that have not been modelled with iSALE explicitly. The expected funnel depths are 4, 31 and 394 cm respectively (Table 7-1). At a depth of ~70 cm (boundary between the snow cover and soil), the largest fragment still moves with a velocity of about 69 m/s.

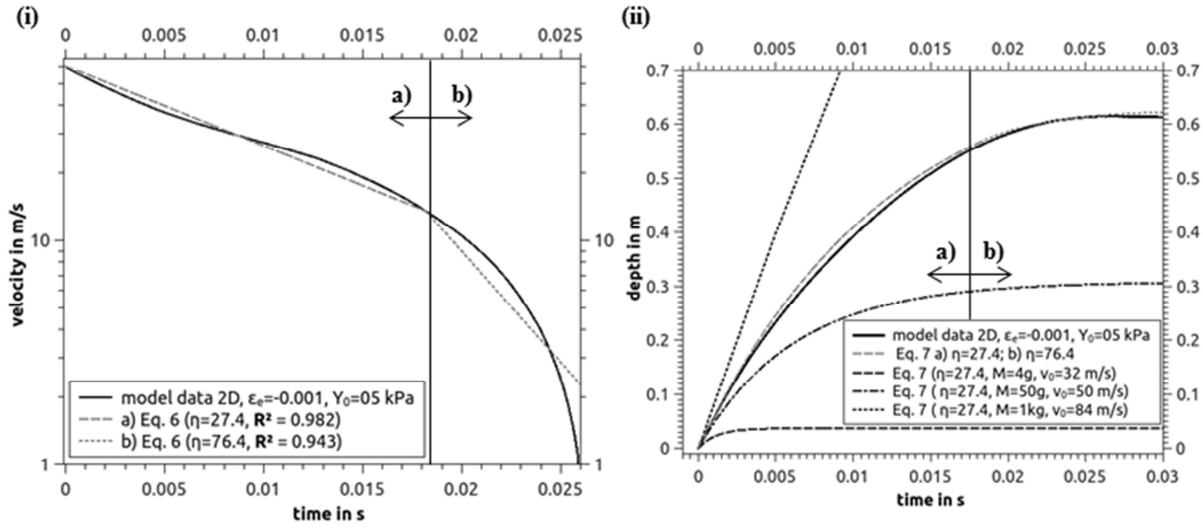

Figure 7-6: Fragment deceleration (i) and funnel depth evolution (ii). Eq. (81) is fitted against the velocity evolution of the preferred model with 5 kPa cohesion (i, solid black line) and gives a snow viscosity of 27.4 Pa s for a fit in regime (a), ranging until ~18.2 ms (i, dashed grey line), and a viscosity of 76.4 Pa s for a fit in regime (b), ranging from ~18.2 ms until the fragment stops (i, dotted grey line). Using the same two viscosity regimes, we plot eq. (82) in panel (ii). The other three fragment sizes of 4 g, 50 g, and 1 kg give a depth of 0.04 m, 0.31 m and 3. 94 m, respectively, for the same viscosity as in regime (a) (ii, thin dashed, dash-dotted and dotted lines).

7.5.3.2 Influence of strength parameters on a funnel depth

The funnel depth is influenced by a) macroscopic strength (cohesion, maximum yield strength and friction – see eq.(79)); and b) snow porosity and the microscopic strength represented by the parameter ε_e of the compaction model. The effects of different snow strength have been studied

by changing either the cohesion or the maximum yield strength, each for two different coefficients of friction (β=0.185 and β=0.415) and with and without elastic pore compaction (ε_e = 0 and ε_e = -0.01, corresponding to a strength of 0 kPa and 50 kPa, respectively, assuming the Young's modulus of 5 MPa, $\sigma = -\varepsilon E$). For varying the cohesion, the maximum yield strength was set to 1 MPa. When the cohesion increases from 1 kPa to 10 kPa (Figure 7-7 (i)), the resulting funnel depths decrease by 20-30% for the models with ε_e = 0. Two further models with an unrealistic high cohesion of 100 kPa have been evaluated and show a strong decrease in funnel depth by about 85% relative to the funnel depth for cohesion of 1 kPa (Figure 7-9). Furthermore, the models with elastic pore compaction show a stronger, 51-63%, decrease in funnel depth for an increase of cohesion from 1 kPa to 10 kPa. For all tested values of cohesion, the higher coefficient of friction leads to shorter funnels. The same behaviour in terms of coefficient of friction as well as elastic pore crushing holds true also for the models with varying maximum yield strength from 10 kPa to 100 kPa and fixed cohesion of 1 kPa. When the maximum yield strength increases from 100 kPa to 1 MPa, the funnel depth does not change significantly. The pressure and, thus, the strength of the snow remains below 100 kPa for most of the time so that the maximum value of yield strength has little effect except for the initial contact phase, when the highest pressures occur. Accordingly, it is clear that in the case of 10 kPa maximum strength, the resulting funnel depths scatter less (~1 m) and are mostly governed by this maximum strength value.

We compared the effect of different elastic volumetric strain thresholds ε_e of the porosity compaction model on the final funnel depth for a speed of sound ratio χ=*0.5* for ε_e - values of -0.0001, -0.001 and -0.01. In addition, we set up two models with a lower porosity of 50%, using the ε_e value of 0 and -0.01. Increasing the absolute value of the elastic threshold of the model results in a ~20% smaller depth of the final funnels for both values of porosity (Figure 7-7 ii). However, we do not see any significant difference in depth when decreasing the threshold from -0.001 to -0.01. Furthermore, funnels formed in the denser snow (Φ=0.5) are ~10-15% less deep than those formed in the more porous snow (Φ=0.7).

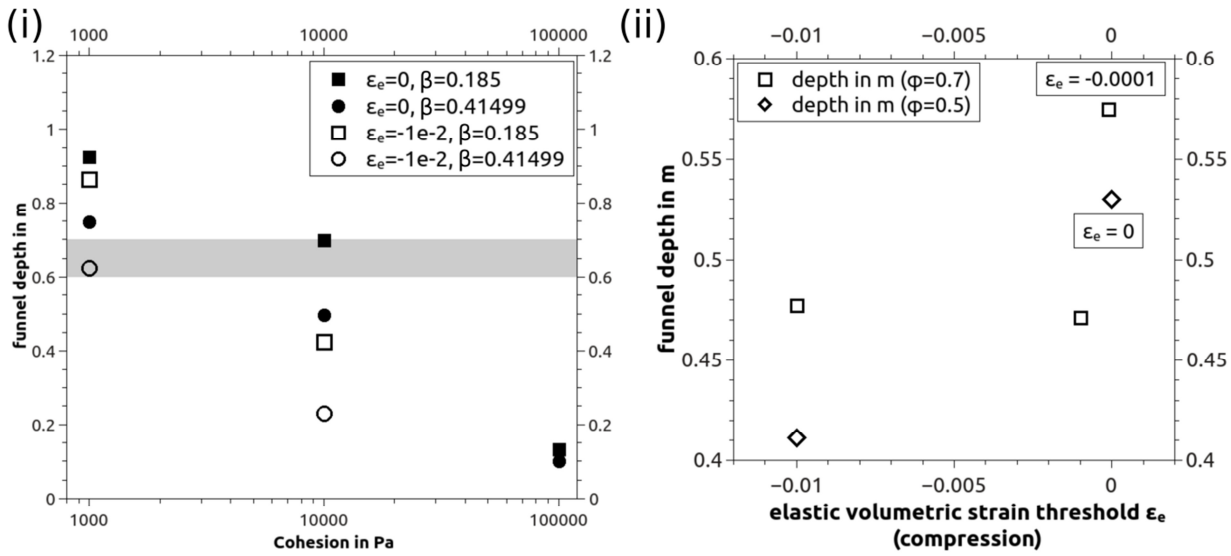

Figure 7-7: Influence of snow rheology on funnel depth. On the left (i) the funnel depth is shown as a function of cohesion Y_0 for two different coefficients of friction (square: β=0.185, circle: β=0.415) and two different thresholds of elastic volumetric strain (filled symbol: ε_e= 0, empty symbol: ε_e = -1e-2) at the same time of 28 ms (i). The funnels reach their final depth at this time if cohesion is > 10 kPa On the right (ii)the funnel depth is shown as a function of the elastic volumetric strain ε_e for two porosities (square: Φ=0.7, diamond: Φ=0.5). The speed of sound ratio is χ = 0.5 in both cases. The grey area shows the expected funnel depth of 0.6-0.7 m (large fragments penetrated through the snow cover to the surface).

7.5.3.3 Funnel walls

Besides the funnel depth, we also studied characteristics of the funnel walls as they represent a further constraint from the observations. In particular, we investigated horizontal density profiles of the funnel walls at different moments in time representing the same penetration depth relative to the final depth (Figure 7-8). Comparing three models with ε_e values of -0.01, -0.001 and -0.0001 (Φ=0.7), we see an increase of the maximum density of the snow in the funnel walls up to 330 kg/m³, 460 kg/m³ and 560 kg/m³ as well as of their thickness in terms of HWHM (half width at half maximum) from ~3 mm to ~8 mm. Hence, for the model with ε_e = -0.0001 the snow density in the wall can become twice as big as its initial value. Furthermore, we compare the effect of reducing the macroscopic strength from a cohesion of 10 kPa to 5kPa (ε_e= -0.001, Φ=0.7, Y_{max}=1MPa). The maximum density decreases by up to 20% for the lower cohesion. However,

the HWHM remains nearly unchanged. For all four cases, the uppermost snow layer is not as dense as the deeper snow layers (Figure 7-8 i). The compaction is negligible (less than about 5% increase in density: ~300 kg/m³) up to a depth of about 23 cm, 9 cm and 6 cm for the three cases of different compaction strength, respectively, and 22 cm for the case of different macroscopic strength. Such behaviour corresponds to the natural observed snow funnels that do not show an increase in snow density in the upper layers. In all four models the most compressed funnel walls can be found in the deepest parts of the funnel (Figure 7-8 iv). However, the thickness of the funnel wall is the greatest at intermediate depths (Figure 7-8 iii).

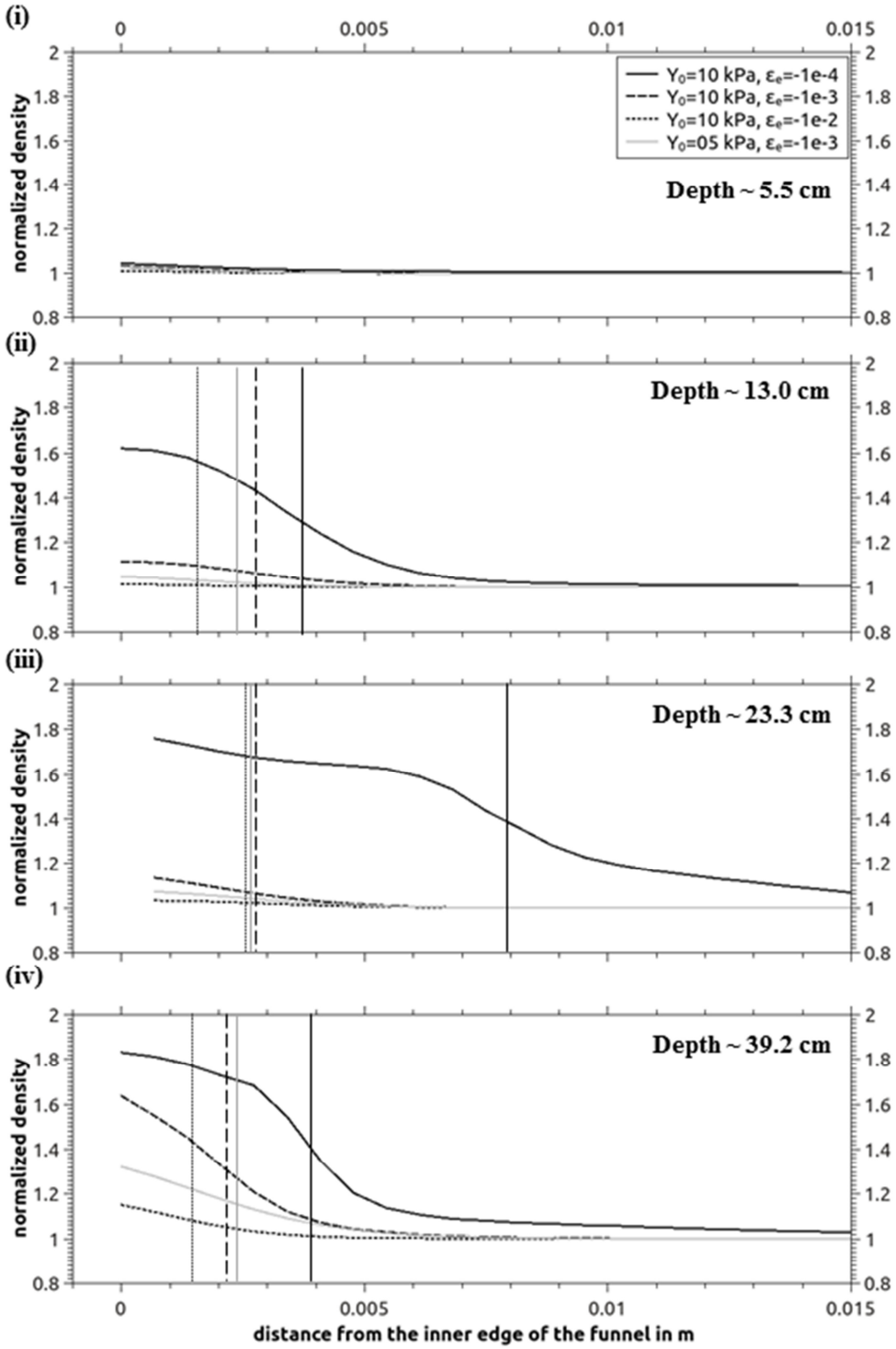

Figure 7-8: Density profiles for four different models at different times that correspond to the same depth relative to the final depth: (i) 1 ms, (ii) 2.5 ms, (iii) 5 ms and (iv) 10 ms; three models with an elastic volumetric strain ε_e thresholds of -0.0001 (solid line), -0.001 (dashed line), and -0.01 (dotted line) and the best fit model (solid grey line). For the best fit model the absolute depth is given in the figure. The profiles are taken through horizontal lines at four different relative depths (see Figure 7-5 for detailed positions of the best fit model). The vertical thin lines show the HWHM for the four corresponding models (solid, dashed, dotted and solid grey line, respectively). The density is normalized to the density of the undisturbed snow.

7.6 Discussion

Two hypotheses for the formation of "snow carrots" have been suggested in the framework of our study. The first scenario relies on the heating of fragments during the atmospheric entry: warm fragments fall onto the snow, cause its melting, and then sink into the mixture of water with snow; as the local temperature is below zero, later this mixture freezes forming crystals which may be different in size and color from the surrounding snow as it was observed by the expedition. However, the atmospheric entry model rules out this scenario by showing that fragments are in thermal equilibrium with the atmosphere upon landing. In the second scenario cold fragments fall onto the fluffy snow and compact it mechanically. In this section, we discuss the sensitivity of the model to various input parameters, possible mechanisms of funnels post-impact modification, uniqueness of the Chelyabinsk snow carrots, and applications of the model to other impacts in the Solar System.

7.6.1 Sensitivity to input parameters

Snow compaction and funnel formation in the penetration model depend on the snow properties. We compare our results with observational constraints: final funnel depth and estimates for thickness of the funnel walls are shown in Figure 7-1 (v) for fragment masses larger than 50 g. However, the observational constraints cannot be taken too strictly. There might be some differences between observations and models, e.g. in fragment geometry and, hence, in impact velocity. In several models the funnel depth is between 60 cm and 70 cm, which we consider as a sufficiently accurate approximation of the observed funnel depth of about 65 cm. Our best-fit model that is based on parameters that are in accordance with published properties of comparable snow (70% porosity, 5 kPa cohesion, and a coefficient of friction of 0.2) fits into this range (62 cm). Furthermore, its microscopic strength given with an elastic threshold ε_e = -0.001 produces the right HWHM and the maximum density of the funnel

walls. A further constraint can be derived using Young's modulus $E_Y = -\sigma/\varepsilon$. Dividing the cohesion of our best-fit model by the elastic threshold yields a Young's modulus of 5 MPa which lies between the values of 1.379 MPa and of 13.79 MPa given by Haehnel and Shoop 2004) for soft and age-hardened snow of comparable density. However, how the macroscopic yield strength of snow is related to the microscopic crushing strength of individual crystals, which controls the compaction of porosity, is not totally understood. We can only speculate whether the similarity of these two material parameters describing the strength behaviour of snow on very different spatial scale is a convincing argument. Systematic studies using controlled laboratory experiments are required to clarify the problem.

Our results show that final funnel depth depends on both macroscopic as well as microscopic strength (Figure 7-7). Macroscopic strength directly influences the amount of energy used for plastic work and higher strength reduces the funnel depth. Microscopic strength influences the pressure in the target and thus also affects macroscopic strength due to the friction term in equation (79). Higher microscopic strength (larger ε_e in absolute value) leads to less pore compaction and pressure attenuation is slower than for models without microscopic strength. Consequently, funnels in snow with a higher microscopic strength are smaller than those in models with the ε_e value set to zero. Note that the amount of elastic pore compaction is also influenced by the speed of sound ratio χ and increases with decreasing χ (see Appendix). Furthermore, an increase of the elastic thresholds (larger in absolute value) reduces the wall thickness up the point where no significant change in density can be observed. On the other hand, too low values of the elastic threshold result in too thick walls. We expect that snow compaction within the walls increases their strength by creating more bonds between snow grains as the observed funnel walls were stronger than the surrounding snow.

7.6.2 Analytical solutions for smaller and larger fragments

Comparison of our best-fit numerical model with analytical solutions (6-7) enables an estimate of the viscosity of snow during the penetration of a fragment of a given size. We found the best correlation for a snow viscosity of 27.4 Pa s during the first 18.2 ms and for a snow viscosity of 76.4 Pa s during the later stage. These viscosities are different from literature values (Maeno et al. 1980; Fellin 2013). Literature data for snow vary over many orders of magnitude and tend to be either much larger (100 MPa s – 10^9 MPa s) or much smaller (0.1 mPa s – 100 mPa s) than our estimates, and refer to long-term creep processes or to fluidized snow. In the present case of a fast impact process in snow, we consider our viscosity value in the right range and we see an increase in viscosity for decreasing velocity of the fragment (corresponding to smaller strain rate). Based on the parameters above, we calculate the funnel depth of 4 g, 50 g and 1 kg fragments (Table 7-1). For the fragment with the highest mass, the funnel depth cannot be compared with observations because the snow layer of ~70 cm is thinner than the calculated depth. Penetration into the soil underneath the snow layer differs substantially from funnel formation due to the different material properties and is not the subject of our study. For the 50 g fragment, we found a good agreement between observed and analytical funnel depth. The penetration depth of the smallest fragment (4 cm) agrees roughly with observations. However, we found that the calculated funnel depth from eq. (82) for small fragments is very sensitive to small changes in initial velocity and/or snow viscosity. Assuming that small fragments have specific orientation with their minimal cross section being perpendicular to the flight direction during a descent, initial impact velocities might easily be higher and the analytical funnel depth would agree better with observations.

7.6.3 Tagish Lake Meteorite Fall

To further stress the importance of impact conditions (mass and velocity) and target properties, we shortly discuss another well-studied atmospheric entry event, the Tagish Lake fall. On January 18, 2000, a fireball with a kinetic energy of 1.7-1.8 kT TNT was observed in the area of the Tagish Lake, Canada (Hildebrand et al. 2006). The pre-atmospheric radius of the body was estimated as 2.1–2.4 m. The recovered C2 carbonaceous chondritic fragments have an average bulk density of 1640 kg/m³ (~ 40% porosity). The initial recovery of fragments (870 g) was conducted by local resident Jim Brook on January 25-26. Fragments lay on the snow or were partly buried up to 1 cm and snow carrots were not reported. The largest fragment was 5 x 6 cm in size (~100–200 g). At the time of the meteorite fall, temperatures were approx. -30°C. Therefore, the snow characteristics, such as grain size and, thus, the viscosity of snow, would differ from the snow layer in the Chelyabinsk area. Unfortunately, the properties of the snow have not been measured at the time of the fall, but the snow has been described as “crusty, styrofoam-like” (Hildebrand et al. 2006).

We estimate the equilibrium fall velocity of a 100g fragment with the same high-velocity drag coefficient of 0.5 to be about 28 m/s. The lower density in comparison with the Chelyabinsk fragments and, hence, the ~60% larger cross section area of the fragment with the same mass results in substantially lower impact velocities. As the yield strength of the “crusty”, very cold snow layer is probably higher (corresponding to higher viscosity), the absence of significant snow penetration and thus snow carrot formation seems reasonable. For comparison, we also modeled the impact of a Chelyabinsk fragment into snow with a high cohesion of 100 kPa (Figure 7-9). The final depth of ~10 cm is about 16% of the depth of the best-fit model; and the depth of ~5 cm to the top of the projectile is only 9% of it.

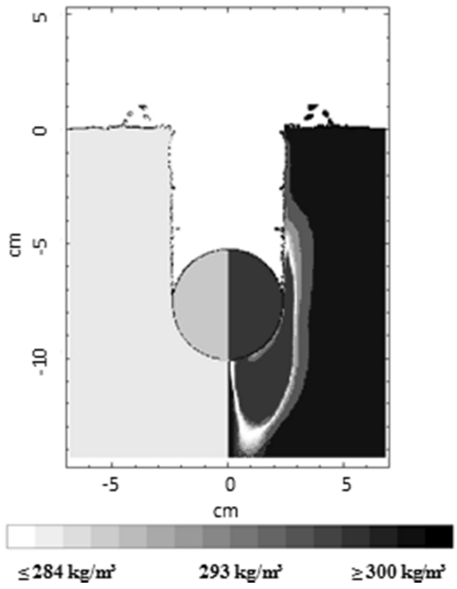

Figure 7-9: Snapshot of a fragment at its final depth in a snow target with a cohesion of 100 kPa. Density is shown on the right half. On the left half, the material is shown (darker grey for the fragment and light grey for the snow).

7.6.4 Post-Impact Processes

The results of our penetration model match the observed characteristics of snow funnels and, hence, support the cold compaction scenario in which an additional heat source (heat-up of the meteoritic fragments by atmospheric drag) is not required. Our current models end up with a fragment that is stuck at the end of the hollow funnel; the funnel walls are compacted and do not collapse to fill the funnel. Thus, an additional post-impact process (or a chain of late stage modification processes) is needed to explain the formation of "snow carrots".

Popova et al. 2013) suggest a combination of snow sintering of freshly fallen snow at temperatures below freezing that increases snow strength, formation of an icy crust (funnel walls) under temperature fluctuations due to sunlight, wind transportation of powdery snow, which fills the funnels. However, "snow carrots" have been found in different locations with different exposure to wind and sun; the weather was "perfect" (sunny with very gentle winds) during the expedition. Below we discuss an alternative mechanism, the temperature gradient metamorphism of snow due to thermal transpiration of water vapour in pores.

Thermal transpiration is a process of material movement that is fostered by thermal gradients. Already more than a century ago thermal transpiration was described by Knudsen (1910) for two communicating chambers at different temperatures that are connected by one or more thin pipes. Resulting differences in pressure depend on the temperature difference, pressure, gas parameters, and pipes diameter. So called Knudsen pumps are nowadays also used in micro-scale On-Chip experiments, a technique of miniaturized standard laboratory procedures for e.g. wet chemical processes (McNamara and Gianchandani 2005). Channel lengths in these systems control the thermal gradient and thus the flow rates of the medium. Knudsen's results also show that the pump mechanism (build-up of a pressure difference) becomes inefficient at ambient pressures. Still, he describes a gas flow on the surface of the pipe (or in our case the surface of snow crystals). Water vapour can interact with snow crystals (e.g. freezing or melting) leading to metamorphism of their structure. Recent findings by Staron et al. 2014) indicate that the rate of metamorphism is controlled primarily by the snow temperature under the presence of strong temperature gradients, but not by the temperature gradient itself. On the other hand, the results from tomography scans of two comparable snow samples with the same average temperature of -8°C and different temperature gradients show strong differences for growth of pore and grain sizes (Schneebeli and Sokratov 2004). Here, we compare their samples 2 and 3 with similar initial grain diameters of 93 μm and 105 μm and initial pore diameters of 240 μm and 220 μm, respectively. With a 4 times higher temperature gradient (100 °C/m versus 25 °C/m), the growth rate is 5-6 times higher for sample 2 than for sample 3 for a period of only a few days. Thus, we conclude that for the formation of snow carrots the absolute value of the thermal gradient is a driving factor for metamorphism rates. A critical minimum gradient for the occurrence of the metamorphism of snow is about 25 °C /m (Sturm and Benson 1997).

The thermal gradient within the snow layer in Chelyabinsk area can be estimated to be about 30 °C /m, assuming the local temperature of air of about -20°C and the warmer ground at 0°C that is isolated by the ca. 70-cm-

thick snow layer. The temperature gradient strongly increases after the penetration of the Chelyabinsk fragments into the snow layer. Immediately after formation the funnels are filled by cold air (Figure 7-10). Assuming a depth of the remaining snow layer of ca. 30 cm (see Figure 7-1 v), the vertical temperature gradient has more than doubled. Furthermore, a new horizontal temperature gradient is introduced to the system and perturbs pre-impact conditions. The temperature in the snow layer around the fragment must be roughly about -10°C (similar to experiments by Schneebeli and Sokratov 2004 mentioned above). Thus, the horizontal temperature contrast ranges only over a very short distance of a few cm and thus the temperature gradient is of on order of 100 - 1000 °C/m. Then the water vapour flux can be calculated by using the equation of thermal transpiration (e.g. Eq. 78 given by Mason et al. 1967) or by metamorphism models as presented by Staron et al. 2014). Due to the lack of experiments to characterize the snow, including the measurement of parameters describing gas kinetics, such efforts and are beyond the scope of this study. Qualitatively, it appears that this effect is stronger in the case of "snow funnels" than in any other natural snow phenomena. The growth of large snow crystals that is typical for temperature gradient metamorphism correlates with the presence of large snow crystal within "snow carrots" (see number 3, Figure 7-1 v).

In addition, different studies show that thermal metamorphism reduces the snow strength (Sturm and Benson 1997; Schneebeli et al. 1999) and increases the risk for avalanches. Thus, in conclusion it is reasonable to suggest that after the penetration the funnel walls lost their strength and partially collapsed filling the funnels with ice crystals originating from the veneer of compacted and metamorphed snow that lined the funnel wall. A comparison of the volume of "snow carrots" with the volume of funnel walls supports this idea as both volumes can be set equal under a realistic estimate that ~0.5-1 cm of walls collapsed. Furthermore, the diameters of the entry holes in the field were found to be 1.5-2 times larger than the diameters of spheres with equal mass to the corresponding fragment supporting this conclusion.

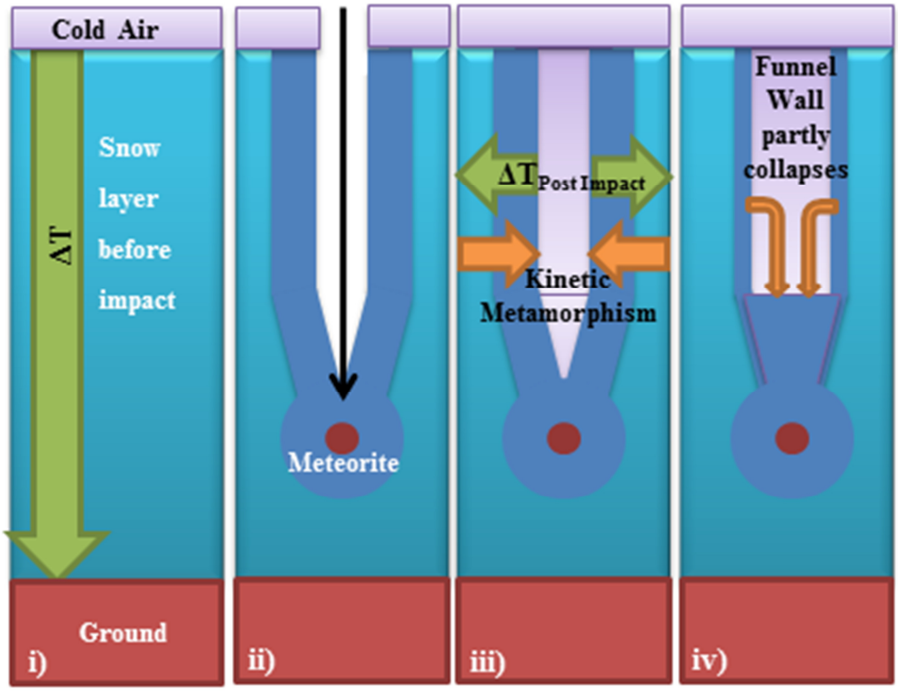

Figure 7-10: Post-impact filling of snow funnels due to thermal transpiration. i) The pre-impact temperature gradient in the layer. On the top, the snow layer is in contact with cold air and both are in thermal equilibrium with a temperature of about -20°C. The ground is much warmer as it is isolated by the snow layer. ii) The impact creates a snow funnel which is immediately filled by cold air. iii) The imposed strong temperature gradient between the warmer snow that was isolated from air before the impact and the cold air in the funnel fosters thermal transpiration and changes the snow structure towards larger snow grains with weak bonds. iv) This weakened snow collapses on top of the fragment to form a "snow carrot".

7.6.5 Applications to other impacts in the Solar System

In this study we describe impacts into materials with very high porosity and low strength. Such material properties are common for many objects in the Solar System including highly porous asteroids and comets, icy moons and minor planets, polar cups on Mars. Using our findings for the Chelyabinsk "snow carrots", we would like to discuss some applications of our model to impacts into highly porous objects.

The snow funnels, formed after the Chelyabinsk event, show a large depth-diameter ratio ranging from 2 for higher cohesion of 100 kPa up to 10 for lower cohesions. These ratios are rather uncommon for impact craters observed on terrestrial planets and on the Moon. However, our findings suggest that a crater on highly porous icy bodies could be different and

could resemble a funnel-like structure that hardly shows any ejected materials (see e.g. Kadono (1999) for a detailed study of funnel formation in porous targets in laboratory experiments with dense projectiles). Larger yield strength (e.g. due to the colder environment or different material composition) or lower porosities could also lead to ratios as observed for pits on the surface of the 67P/Churyumov-Gerasimenko comet. It is worth to mention that cometary material strength may vary over several orders of magnitude, from a few Pa to 4 MPa (Spohn et al. 2015; Thomas et al. 2015) and, hence, a variety of crater morphologies are possible.

In our study, we focus on very small objects on the order of some grams in mass. However, similar processes take place for larger objects if the material strength, porosity, and impact velocity are similar: the projectile compresses material in an area that is only slightly larger than the projectile itself while it penetrates deep into the target (Figure 7-11 i). The impact velocity is the most important parameter that deviates significantly from our study in most other impact scenarios in Solar System. In our case, meteorites strike the surface at approximately free-fall velocity while more typical hypervelocity impact scenarios happen at multiples of the speed of sound. At such high velocities shock waves are generated that affect a much larger target area than the projectile; fragmentation, melting and vaporization occurs and plays an important role in the crater excavation process. To demonstrate these effects we set up three model runs using the same material parameters as described above in a low-gravity environment (0.001 m/s² acceleration). A 20-m-diameter projectile (with 15 CPPR resolution) strikes vertically at 1, 5, and 10 km/s – see Fig. 12. At 0.3 s after the impact the projectile is still moving and all craters shown in the Figure are far from their final shape. Still, we can see strong compaction of the porous target material and funnel formation within the target with a narrow “entrance hole” in its upper part. The projectile is severely damaged at velocities > 1 km/s, but not molten; the projectile material survives and might be buried later by slumping of target material adjacent to the crater wall. Such processes seem to be relevant for early solar system accretion, material mixing, and compaction of early solar system objects.

A parameter we did not investigate explicitly is the effect of the impact angle: We expect that for an oblique impact a funnel would form at an angle according to the impact angle (cf. Fig. 33, Schultz et al. 2007). In this scenario more ejecta would be expelled from the target in downrange than siderange and even less in uprange direction. However, ejection is a very inefficient process in highly porous targets with relatively low ejection-velocities in comparison to nonporous matter. Nevertheless, the vast majority of the ejected material may escape the low-gravity field of the comet and would not be deposited on the surface of the comet. The final distribution of the material inside the funnel depends on strength, gravity, and the physical state of the involved materials (melting and vaporization may occur at higher impact velocities). Some of the material might flow inwards and cover the bottom of the funnel, depending on the direction of gravity. However, gravity is tricky on a comet with an irregular shape and potentially inhomogeneous mass distribution in the interior. It has to be considered that gravity vectors do not show necessarily to the centre (cf., Massironi et al. 2015) so if any collapse occurs, despite the low gravity, the material flow is very difficult to predict. In our model, we cannot investigate the collapse processes itself as it occurs on a totally different timescale in comparison to the impact. We can only speculate whether, and if so, then how the funnel may be modified by gravity-driven collapse.

Our findings can also be connected to the study of the Stardust aerogel catchers with porosity of 99.9%. Impact velocities of about 6.1 km/s have been much larger than in our study. Nevertheless, our test model with a velocity of 10 km/s (Figure 7-11 iii) resembles the Stardust track 163 as seen in (Greenberg and Ebel 2012). First, most of the energy (projectile velocity) is consumed while forming a growing cavity. Then, a penetration funnel is formed at the bottom of the cavity by the low-velocity remnants of the projectile. As the target material properties of the Stardust gel are very well constrained, simulations of impacts with different projectile masses and properties should be able to reproduce some of the Stardust funnels to allow for constraining cometary dust properties. Our findings also support the

principle of linking the entrance diameter with the projectile (dust) size as funnel compression in this area is lowest.

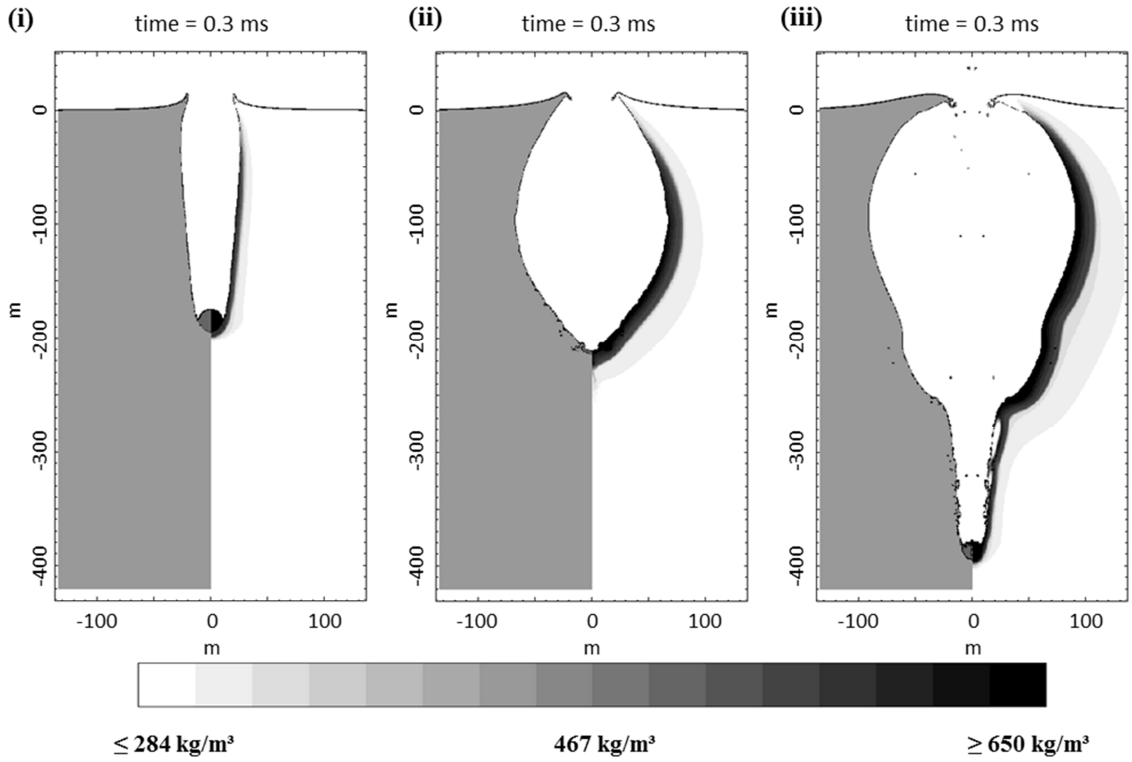

Figure 7-11: Snapshots of larger scale funnel formation. Snapshots are taken at 0.3 s and show the funnels for impacts with similar parameters as chosen for the snapshots in Figure 7-5 (Y_0=5 kPa, β=0.2, Φ=0.7), except for the size of projectile diameter (20 m), the impact velocity of 1 km/s (i), 5 km/s (ii) and 10 km/s (iii) and the gravity (0.001 m/s²). For each image, the right side shows the density and the left side the material (dark grey for the projectile and light grey for the snow). A denser (black) funnel wall is created. Although the projectile seems to be intact (a perfect sphere) on the right plate, it's not the case – the projectile is totally damaged and its remnants merge at the axis of symmetry.

7.7 Conclusions

1. We simulated the thermal and mass evolution of small meteoroid fragments of three different sizes during their descent in the atmosphere. During the first stage of the fall, ablation is the dominant process and fragments heat up to melting and vaporisation of the outermost (dynamic) layer, whereas the meteoroid interior is not affected. During the second stage of the fall, when ablation ceases, the fragments heating depends on their size but is still

minimal. Then fragments move through the atmosphere with free-fall velocity and cool down. We find that the cooling time is one to two orders of magnitude shorter than the free fall time. Thus, we argue that all recovered fragments were in equilibrium with the atmospheric temperature of ~265 K prior to contact with snow.

2. Crushing of pore space and friction during fragments penetration through snow could be another source of heating and melting. However, we do not see a significant temperature increase in any of the examined models. For example, the temperature increase does not exceed ~0.5 K and is highly localized in our best-fit model.
3. We rule out the scenario of snow melting and favour the scenario of funnel formation by cold compaction.
4. The funnel depth depends on pre-impact mass and velocity of fragments, which are constrained by the atmospheric model. In addition, the results are sensitive to poorly known properties of the local snow cover. However, the best-fit model utilizes the parameters in accordance with published values: snow porosity of 70%, the cohesion of 5 kPa, and the friction coefficient of 0.2.
5. Our models show that: a) the funnel depth increases with increasing fragment mass; b) funnel wall density increases at some depth but not at the top of the funnel; c) the ejecta are minimal if any. These results are in a reasonable agreement with field observations: large fragments were found in deeper funnels, top snow layers could easily be removed, and surrounding snow had no signs of ejecta deposition.
6. Formation of snow carrots requires an additional post-impact process. Thermal metamorphism is a good candidate.
7. The penetration model can be used for a wide range of impacts into highly porous targets including Stardust catchers, comets, and snowy surfaces of planets. Depending on impact velocity and target porosity, morphological features of the resulting crater may vary in a wide range.

7.8 Acknowledgements

We thank two anonymous reviewers for their constructive comments for improving this article. R.L. is funded by the DFG-grant # WU 355/6-2. We gratefully acknowledge the developers of iSALE-2D, including Gareth Collins, Kai Wünnemann, Dirk Elbeshausen, Boris Ivanov and Jay Melosh. We also acknowledge the developer of the pySALEPlot tool Tom Davison. iSALE –Website: **www.isale-code.de**

7.9 Appendix

7.9.1 Details on the ε-α porosity compaction model

In this study, we vary parameters of the ε-α porosity compaction model (Wünnemann et al. 2006, 2006; Collins et al. 2011), namely the elastic limit of the volumetric strain ε_e (by definition, strain is negative during the compaction). If the volumetric strain is below this limit, then porosity compaction behaves elastically. Presence of the elastic regime decreases the final depth of snow funnels (Figure 7-7). In addition, the compaction rate in the elastic regime depends on the speed of sound ratio χ defined as the speed of sound in the porous material c_0 divided by the speed of sound c_{s0} in the similar material without porosity (compare with eq. 6 and 7. in Collins et al. 2011):

$$\frac{d\alpha_d}{d\varepsilon} = \alpha_d \left[1 - \left(1 + \frac{\alpha_d - 1}{\alpha_{d,0} - 1} (\chi - 1) \right)^2 \right] \quad . \qquad (83)$$

where α_d is a distension that can be calculated by the porosity Φ: $\alpha_d = 1/(1-\Phi)$.

For χ =1, porosity does not change during the elastic compaction. If χ is different from one, then compaction takes place and porosity decreases already at the elastic stage: the smaller the χ-value, the higher the

compaction rate. During pressure release, the porosity again increases due to the elastic component. Note, that outside the elastic regime the slope for the release is different from the slope for the compaction (see also Figure 7-12). Furthermore, the speed of sound ratio affects the bulk modulus K of the material; $K = \rho\ c^2 = \rho\ (\chi\ c_{s0})^2$. Thus, the bulk modulus decreases strongly with decreasing χ and the compressibility $1/K$ increases.

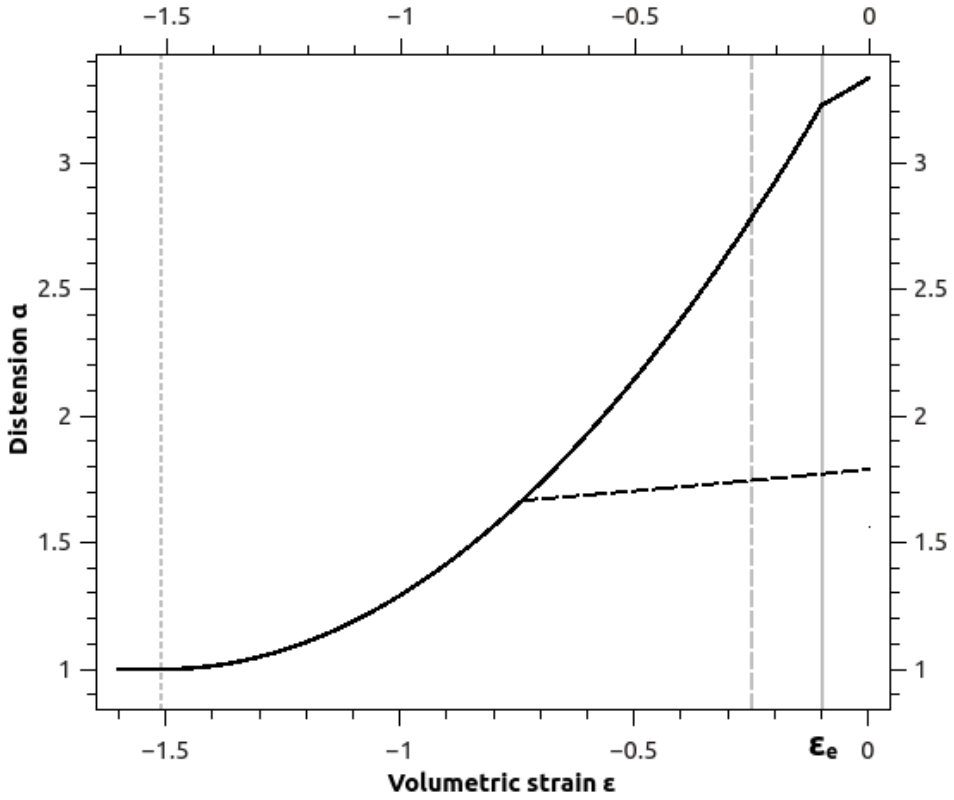

Figure 7-12: Pore compaction versus volumetric strain for the case of χ = 0.5 during the compression (black solid line) and during the release after reaching half of the initial distension (black dashed line). Note the differences in slope for elastic compaction and release for equal differences in distension. The thin vertical lines represent the transitions from the elastic to the exponential regime according to the ε-α porous compaction model (grey solid line), from the exponential to the power law regime (grey dashed line) and to the fully compacted regime (grey dotted line). If χ = 1, the distension remains constant during the elastic compaction and the elastic release.

7.9.2 Numerical resolution and artefacts

Results of numerical models depend on their resolution and will converge against some solution when the resolution is high enough. In order to show that our resolution of 35 CPPR is good enough to model the scenario of "snow carrots", we ran simulations with resolutions between 10 and 35 CPPR and show the results of final funnel depth (Figure 7-13 i) and of the density increase in the funnel walls (Figure 7-13 ii) for one example depth of ~33 cm (0.01 s after impact). Our test case has a cohesion of 5 kPa, a coefficient of friction of 0.2 and a maximum strength of 1 MPa. The elastic volumetric strain is set to -0.001. The funnel depth stabilizes for the highest shown resolutions. In addition, also the funnel wall density converges against a maximum funnel density. Thus, our test series supports our choice of a resolution of 35 CPPR.

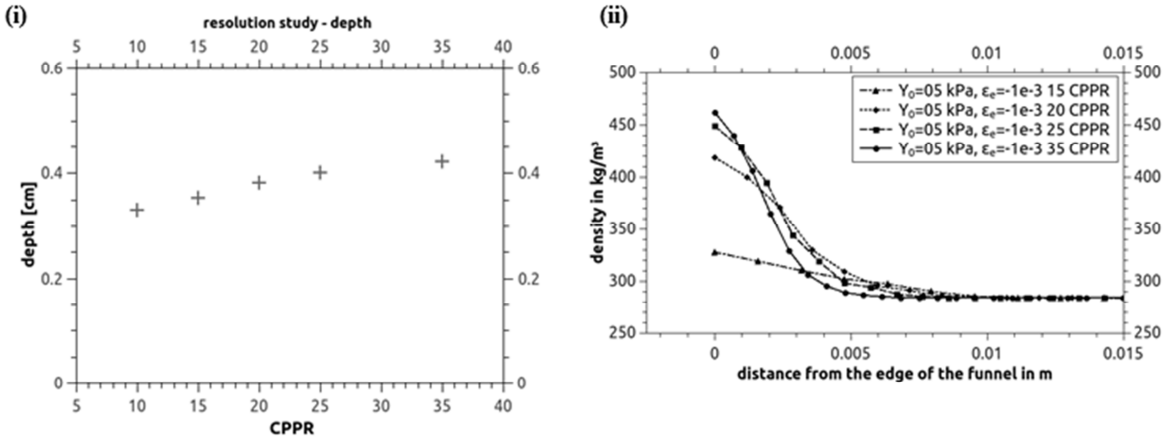

Figure 7-13: Resolution study. Funnel depth (i) and funnel wall density (ii) converge for the highest resolutions.

It's important to mention that some models are affected by numeric diffusion that smears the projectile material over computational cells and leads to artificial projectile deformations although the pressure reached during the penetration is more than an order of magnitude below the yield strength of basalt. Numerical diffusion affects those models with lower snow strength because in this case the fragment penetrates deeper into the snow and the number of computational time steps increases. A higher resolution helps to reduce this problem. We used a resolution of 35 CPPR

that we consider high enough for our study and at the same time still affordable in the sense of computational time required. We control the projectile mass evolution in our models and consider models with a mass of ~70% or more of the initial mass to be sufficient regarding mass conservation of the fragments.

The artefacts near the axis of symmetry (in particular, a precursor of snow with higher density beneath the projectile, see Figure 6) are another issue. To enhance the reliability of our study, we set up a three dimensional model without cylindrical symmetry and with an equal set up to one of the two-dimensional models. Due to higher computational costs of 3D calculations, we reduce the resolution to 15 CPPR and compare only the first ~ 6 ms when most of the funnel growth takes place (Figure 7-14). The evolution of the velocity as well as the penetration depth of the 2D- and the 3D-models agree very well, i.e. the artificial precursor does not affect our main results.

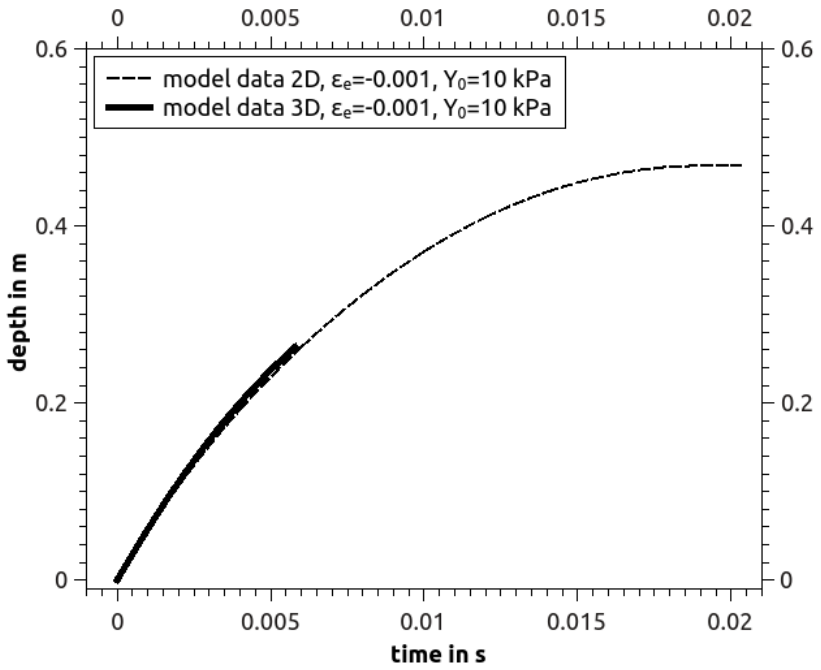

Figure 7-14: Funnel depth evolution for a 2D and a 3D model (in 3D with a lower resolution of 15 CPPR, run until ~6 ms) of a cohesion of 10 kPa.

7.9.3 Model Parameters

Table 7-2**:** Model Parameters of our best fit model.

General parameters	**basalt**	**snow**
Poisson ratio (basalt)	0.25	0.3
Specific heat capacity	1000 J/(kg K)	1960 J/(kg K)
Strength parameters		
Von Mises strength (basalt)	200 MPa	
Drucker Prager strength (snow):		
Cohesion Y_0		5 kPa
Coefficient of friction β		0.2
Maximum strength Y_{max}		1 MPa
Thermal Softening (Ohnaka)*		
Softening constant	1.2	
Melt temperate	1673 K	
Simon approximation:		
Simon constant	$6 \cdot 10^9$	
Simon exponent	3	
Porosity parameters		
Initial distension $\alpha_{d,0}$		3.2
Elastic volumetric threshold ε_e		-0.001
Transition distension $\alpha_{d,x}$		2.61
Compaction efficiency κ		0.99
Speed of sound ratio χ		0.5

* Thermal Softening was used only for the basalt and not for all models.

8 The Effect of Target Properties on Ejection Dynamics and Ejecta Deposition

This chapter has been published as the following peer-reviewed article:
Robert Luther, Meng-Hua Zhu, Gareth S. Collins, Kai Wünnemann (2018). *The Effect of Target Properties on Ejection Dynamics and Ejecta Deposition*. Meteoritics & Planetary Science 53 (8), 1705-1732, https://doi.org/10.1111/maps.13143.

In the previous chapters, the material models used in iSALE have been applied to reproduce laboratory craters and natural observations in porous targets, answering my objective *M I – Material Models*. Based on the tested material models, the following chapter is dedicated to some of the core questions of this thesis about the correlation of target properties and the resulting ejection dynamics for cratering events (key question *S I – Ejecta and Target Properties*). This chapter includes a parameter study of target materials with different strength properties, porosities, and increasing impact velocity (the latter for constant crater size). The ejection behaviour (ejection velocity and angle versus launch position) is derived from these model series. The results are used to derive scaling parameters that allow for scaling from small laboratory-sized impacts up to large natural cratering events. The theoretical background is explained within the chapter. Finally, based on the assumption of parabolic trajectories, ejecta deposits have been calculated and are presented in the last part of the chapter. Modifications to the ejecta blanket were not considered.

I set up and evaluated all models that were used in this study, and I wrote this article. The evaluation approach is based on the concept used by Meng-Hua Zhu, but I expanded the ejection criterion to read out the data at a certain altitude (as discussed in the manuscript). The ejection data is based on a calculation that includes two time steps, one before and one after fulfilling the ejection criterion (in contrast to three data points as in the approach by Meng-Hua Zhu). I validated the approach by comparison with experimental data, and, as such, I answer my objective *M II – Ejecta Analysis* in this chapter. The approach works as post-processing of a

calculated model, but calculations are more precise when the tracers are evaluated directly within the model calculations, using the much finer iteration time step than the model-saving time step from post-processing. Gareth S. Collins and Kai Wünnemann have both worked on ejection dynamics, so I was able to discuss the whole manuscript and problems in the numerical approach with them.

8.1 Abstract

Impact craters are formed by the displacement and ejection of target material. Ejection angles and speeds during the excavation process depend on specific target properties. In order to quantify the influence of the constitutive properties of the target and impact velocity on ejection trajectories we present the results of a systematic numerical parameter study. We have carried out a suite of numerical simulations of impact scenarios with different coefficients of friction (0.0 – 1.0), porosities (0% - 42%) and cohesions (0 MPa – 150 MPa). Furthermore, simulations with varying pairs of impact velocity (1-20 km/s) and projectile mass yielding craters of approximately equal volume are examined. We record ejection speed, ejection angle, and the mass of ejected material to determine parameters in scaling relationships, and to calculate the thickness of deposited ejecta by assuming analytical parabolic trajectories under Earth gravity. For the resulting deposits we parameterise the thickness as a function of radial distance by a power law. We find that strength—that is, the coefficient of friction and target cohesion—has the strongest effect on the distribution of ejecta. In contrast, ejecta thickness as a function of distance is very similar for different target porosities and for varying impact velocities larger than ~6 km/s. We compare the derived ejecta deposits with observations from natural craters and experiments.

8.2 Introduction

Crater formation is one of the most ubiquitous processes in our solar system. Most planetary surfaces are dominated by impact craters and their surrounding ejecta blankets. As long ago as the end of the 18th century, the astronomer Johann Hieronymus Schröter observed crater rims ("Ringgebirge") and crater cavities ("Wallebene") on the Moon and, after comparing their masses, proposed a common explosive process that may have caused the excavation of material (Schröter 1791).

During the cratering process, energy and momentum are transferred from the projectile onto the target, causing material movement (e.g. Wegener 1921; Schmidt 1980). Parts of the material are displaced into the expanding cavity, while other parts are ejected out of the cavity on ballistic trajectories. Most of the debris ejected from a crater is deposited within two crater radii as a more-or-less continuous ejecta blanket whose characteristics depend on the distance from the point of impact, target properties, and the presence or absence of an atmosphere.

The study of ejected material is important for the understanding of the evolution of the solar system: impact cratering and the formation of ejecta deposits are a dominant resurfacing process on most objects in the solar system. Near-rim ejecta deposits are a morphological unit where impactites and shock metamorphosed rocks can be found (e.g. Stöffler et al., (1975), and reveal valuable information for studying crater formation mechanics. Fast ejecta can escape the gravitational field of its parent body and can collide with other bodies, transporting material to them (Head et al. 2002; Artemieva and Ivanov 2004; Alvarellos et al. 2008). Thus, ejection dynamics have consequences for early planetary accretion, and collisional evolution of asteroids (e.g. Farinella and Davis 1992; Campo Bagatin et al. 1994). In contrast, ejected material that does not escape the gravity field of its parent body can cause a series of secondary impacts producing a regolith layer on the surface by fracturing of local material and mixture with the ejected material (e.g. Oberbeck 1975).

The study of ejecta dynamics has been conducted in laboratory experiments for different target and projectile materials, and for different

impact velocities. In some of the earliest work ejection speed was measured indirectly, by tagging target material prior to impact (or explosion) and locating its post-impact/explosion position (Stöffler et al. 1975; Piekutowski 1980). By necessity, this procedure assumes a constant ejection angle and that ejected material follows a simple ballistic parabola from the launch position to the landing site, with no subsequent outward flow, sliding, or rolling. The experiments by Stöffler et al. (1975) also investigated shock loading of ejecta in order to derive the relative amount of shocked material in the final ejecta distribution. A similar approach was followed by recent impact experiments into competent rock, reconstructing ejecta trajectories from ejecta catchers mounted opposite the target parallel to the surface (Sommer et al. 2013). More recently, both ejection angle and speed were measured directly, in a novel suite of experiments using systems of lasers and cameras to illuminate the ejecta and track its movement in time (Cintala et al. 1999; Anderson and Schultz 2003; Anderson et al. 2004; Anderson and Schultz 2006; Hermalyn and Schultz 2010, 2011; Hermalyn et al. 2012; Tsujido et al. 2015; Gulde et al. 2018). Some studies are able to track individual particles or give at least a particle size distribution for their total detected ejected material (Buhl et al. 2014b; Gulde et al. 2018). These experiments provide empirical relationships between ejection speed and angle and launch position within the crater for a number of different target materials (Housen et al. 1983; Housen and Holsapple 2011); however, as it is difficult to isolate the effect of individual target properties on ejection characteristics in experiments, the dominant controls on ejecta behaviour remain unclear.

Numerical impact simulations permit the investigation of the effect of individual material properties (such as porosity, cohesion and friction coefficient) on the cratering process thereby allowing a very wide variation in material behaviour to be studied. Such simulations also allow the use of impact velocities and impactor sizes that are much larger than is possible in laboratory experiments. Previous numerical studies analysed the ejection behaviour in models for specific impact set-ups (Wada et al. 2006; Hermalyn and Schultz 2011; Zhu et al. 2015; Wünnemann et al. 2016). In

this study that was conducted in the framework of the Multidisciplinary Experimental and Modeling Impact Research Network (MEMIN, e.g. **Kenkmann et al. 2018**), we use numerical modelling to systematically investigate the effect of several important target material properties on the ejection velocity vector (speed and angle) as a function of launch position within the growing crater. The results are used to predict the amount of ejecta landing on the surface as a function of distance assuming ballistic trajectories in the absence of an atmosphere.

8.3 Theoretical Background

Impact cratering has been studied at a variety of scales in both laboratory and numerical experiments. Scaling relationships (e.g. Housen et al. 1983) relating impactor and target parameters, such as projectile radius a, impact velocity v_i or target gravity g on the one hand side, to crater characteristics, such as the transient crater radius R or volume V on the other side, have been developed to allow for direct comparison of laboratory experiments with natural craters. With all impact parameters known, the outcome (crater size and ejecta distribution) of an impact scenario can be approximated with such scaling relationships. In the following, we introduce some of the concepts from literature that we will use later on. Note that we only consider vertical impacts.

In the early stage of an impact, the projectile transfers energy and momentum onto the target. In scaling theory, this transfer is parameterized by a single coupling parameter Θ (Holsapple 1981):

$$\Theta = a\, v_i^{\mu}\, \delta^{\nu} \quad , \tag{84}$$

where μ is a material dependent parameter with theoretical upper and lower limits of 2/3 (energy scaling) and 1/3 (momentum scaling), respectively, ν is an exponent that is typically set to 1/3, and δ is the projectile density.

At the contact between the projectile and target, a shock wave is generated and propagates through the target (and projectile), causing also an

increase in particle velocity within the material as a consequence. Close to the impact point, the material moves approximately in a radial direction from the centre (Figure 8-1). The shock wave is followed by a rarefaction wave originating from the free surface, which causes an upward pressure gradient and adds an upward component to the velocity field (Gault et al. 1968; Thomsen et al. 1979; Melosh 1989). As a result, during the excavation flow material moves along streamlines that curve upward toward the target surface. Material moving along streamlines that intersect the free surface inside the crater is 'ejected'—is called ejecta—and subsequently follows a ballistic trajectory. The contour of ejected material which intersects the target surface at the edge of the growing cavity, separates ejecta above from material displaced by the subterranean excavation flow (Figure 8-1). This latter material forms the floor, walls and uplifted rim of the transient crater. The size of the transient crater, i.e. radius R or volume V, can be estimated by scaling relationships and depends on parameters as described by Housen et al. (1983):

$$R = R\left(\Theta, \rho, Y_{eff}, \Phi, g\right) \quad , \qquad V = V\left(\Theta, \rho, Y_{eff}, \Phi, g\right) \quad , \tag{85}$$

with the target density ρ, an effective measure of the target strength Y_{eff} and the target porosity Φ. Combining Eq. (84) and (85) in a dimensional analysis yields a non-dimensional equation of the following type as described by e.g. Holsapple (1993). Here, we give a form that is valid in the gravity dominated regime:

$$\pi_V = K_1 \, \pi_2{}^{-\frac{3\mu}{2+\mu}} \left(\frac{\rho}{\delta}\right)^{-\frac{6\nu-2-\mu}{2+\mu}} \quad , \tag{86}$$

where K_1 is a constant, and Π_V and Π_2 dimensionless parameters:

$$\pi_V = \frac{\rho \, V}{\delta \, V_{pr}} \quad , \tag{87}$$

$$\pi_2 = 1.61 \frac{2a\,g}{v_i^2} \ ,$$

with the projectile volume V_{pr}.

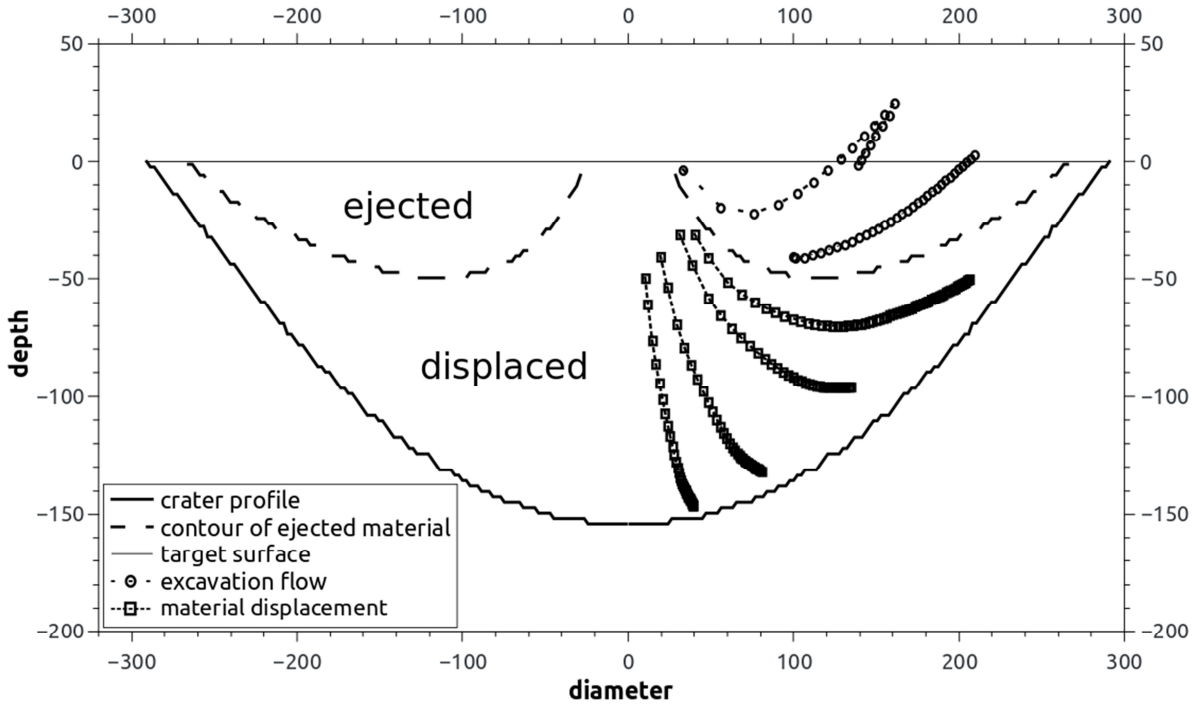

Figure 8-1: Excavation and material displacement. Trajectories are shown for some exemplary material trajectories within the excavation flow. Material above the dashed line is ejected from the growing cavity, whereas material underneath is displaced within the crater. Note that depending on the target properties material at similar launch positions can experience slightly different ejection angles, as the trajectories indicate. The figure was created from a model described in the results section (coefficient of friction of 0.6, no porosity, no cohesion, impact velocity 6 km/s). The impact site is at the centre.

Assuming a constant gravity field and the absence of an atmosphere or vapour plume, and neglecting any interaction between the ejected particles that might occur due to similar direction of movement of particles, the ejected material will follow parabolic trajectories that are defined by an initial ejection speed and ejection angle at a certain launch position. Note that we use both term “ejection” and “launch” interchangeably. These characteristics are closely connected with the material flow within the target prior to ejection and as such are subject to specific material properties that we focus on in this study. Ejection velocities v_{ej} relate to other parameters as follows:

$$v_{ej} = v_{ej}\left(\Theta, \rho, Y_{eff}, \Phi, g, x\right) \quad , \tag{88}$$

with the launch position *x*. At sufficient distance inward from the crater rim (x/R<1), the kinetic energy of the ejecta is large compared to what is needed to lift it above the surface and, thus, strength and gravity can be neglected (Housen et al. 1983). Using this simplification, and by combining Eq. (84) and (88) with dimensional analysis, it can be assumed that:

$$x\, v_{ej}^{\mu}\, \rho^{\nu} \;\sim\; \Theta = a\, v_i^{\mu}\, \delta^{\nu} \quad . \tag{89}$$

Eq. (6) accounts for the density contrast between target and impactor. Rewriting of this relationship as equation gives (Housen and Holsapple 2011):

$$\frac{v_{ej}}{v_i} = K_2 \left(\frac{x}{a}\left(\frac{\rho}{\delta}\right)^{\upsilon}\right)^{-\frac{1}{\mu}} \quad , \tag{90}$$

where K_2 is a fitting constant. This relationship holds true for most of the range of launch positions (approximately 1.2 a ≤ x < R, Housen and Holsapple 2011). However, close to the impact point, the assumption of a point source and the single coupling parameter *C* does not hold true. On the other hand, at positions close to the crater rim, ejection velocities are overestimated by this scaling relationship and are better described by adding a factor to the equation above (Housen and Holsapple 2011):

$$\frac{v_{ej}}{v_i} = K_2 \left(\frac{x}{a}\left(\frac{\rho}{\delta}\right)^{\upsilon}\right)^{-\frac{1}{\mu}} \left(1 - \frac{x}{a}\,\frac{a}{\omega_n\, R}\right)^{\omega_p} \quad , \tag{91}$$

with the transient crater radius *R* and the fitting parameters *p* and *n*. Note, that *a*/*R* in the last position gives an inverse measure of cratering efficiency; Eq. (87) states: $\pi_V \sim (R/a)^3$.

The previous expressions used impactor parameters to normalise the physical parameters. This approach is useful to predict the cratering results from known impact parameters. However, the inverse is sometimes required. Instead of using impactor parameters, ejection velocities can also be expressed relative to transient crater radius and gravity by combining Eqs. (85) and (88) in a non-dimensional expression:

$$x\, v_{ej}^{\mu} \;\sim\; R\sqrt{gR}^{\,\mu} \quad . \tag{92}$$

Rewriting of this relation as equation gives (Housen et al. 1983):

$$\frac{v_{ej}}{\sqrt{gR}} = K_3 \left(\frac{x}{R}\right)^{-\frac{1}{\mu}} \quad , \tag{93}$$

with the constant K_3 that relates to K_2 as:

$$K_3 = K_2 \frac{v_i}{\sqrt{gR}} \left(\frac{R}{a}\right)^{-\frac{1}{\mu}} \quad . \tag{94}$$

Based on scaling relationships, a theoretical expression for the thickness T_e of the deposited ejecta as a function of landing distance can be derived. Following the old idea of relating the cavity volume with the volume of material around the crater (Schröter 1791), the volume of ejected material can be related to the integral over the thickness of the blanket (i.e. volume of blanket material) as was done by Housen et al. (1983). Note that only a fraction of the cavity volume is ejected. Using the relationship of ballistic trajectories for flat surfaces and an approximation for a far-field solution, Housen et al. (1983) obtain the following relationship for the thickness of the deposited ejecta over distance in the gravity regime:

$$\frac{T_e}{R} = K_4 \frac{3\mu}{4\pi} (\sin 2\alpha)^{\frac{3\mu}{2}} \left(\frac{x}{R}\right)^{-\frac{3\mu+4}{2}} \quad , \tag{95}$$

with the constant K_4 and the launch angle α (relative to the horizontal). This simple power-law approximation assumes that all ejecta emanates from the centre of the crater and, thus, is strictly valid only beyond some distance from the crater (approximately 2-3 crater radii, depending on crater size). A simple power-law expression based on observations was formulated by McGetchin et al. (1973) and modified by Pike (1974):

$$T_e(r) = T_0 \left(\frac{x}{R}\right)^{-B} \quad , \tag{96}$$

where T_0 is the thickness at the crater rim ($T_0 \sim R$) and B is an exponent. Comparing both Eqs. (95) and (96) gives a correlation between the exponent B and the scaling parameter μ:

$$B = \frac{3\mu + 4}{2} \quad <=> \quad \mu = \frac{2\,B - 4}{3} \quad . \tag{97}$$

However, we again note that a simple power-law ejecta thickness distribution is not expected close to the crater rim.

The set of consistent equation Eqs. (84) - (95) relates different observables like ejection velocity or crater size with projectile parameters such as a and v_i or crater parameters such as R and $\sqrt{gR}$. They are based on a number of idealised assumptions, the most fundamental of which is the assumption of a single coupling parameter as shown in Eq. (84) that combines the three projectile parameters a, v_i and δ (Housen et al. 1983). From the set of scaling relationships, the scaling coefficient μ can be derived from various measurements (e.g. crater size, Eq. (84); ejection velocity, Eqs. (90), (91) & (93); or ejecta deposits, Eq. (95)). However, previous studies (Cintala et al. 1999; Yamamoto et al. 2017) have shown that the determined value of μ from different observational approaches may not be consistent, hinting at a limitation of the idealised concept of scaling relationships.

Scaling relationships suggest that the impact process at different scales and different gravities are directly comparable. However, care is required when applying these equations to large-scale craters on planetary

surfaces. The crater diameter (or volume) scaling equations are underpinned by measurements of the final crater diameter in small-scale laboratory experiments, often measured at the preimpact surface, whereas the diameters of natural craters are typically measured at the topographic rim. More significantly, crater enlargement by collapse of the crater rim becomes increasingly important with increasing crater size. At the laboratory scale the difference between final (post-collapse) and transient (pre-collapse) crater radius (at the preimpact level) is typically <10% (e.g. Ormö et al. 2015; Wünnemann et al. 2016). For natural simple craters the difference is estimated to be ~20% (e.g. Melosh 1989). For complex craters different relationships to estimate the ratio between final crater radius R_{final} and transient crater radius R have been suggested by different authors (e.g. Croft 1985; Holsapple 1993; Krüger et al. 2017). They all assume that the gravity driven enlargement of the transient crater results in a much larger ratio between final crater and transient crater radius in the case of complex crater formation. In the present study we do not model any crater modification processes; our simulations are stopped at the end of the excavation stage and crater dimensions used in the ejecta scaling relationships refer to those of the transient crater. For explicit comparison with experimental results where the final rim-to-rim diameter has been measured we estimate the apparent crater diameter by assuming a 10% reduction in diameter from the rim-to-rim diameter.

8.4 Methods

In this study, we use the iSALE-2D Eulerian shock physics code (Wünnemann et al. 2006), which is based on the SALE hydrocode solution algorithm (Amsden et al. 1980). To simulate impact processes in solid materials, SALE was modified to include an elasto-plastic constitutive model, fragmentation models, various equations of state (EoS), and multiple materials (Melosh et al. 1992; Ivanov et al. 1997). More recent improvements include a modified strength model (Collins et al. 2004) and the ε-α porosity compaction model (Wünnemann et al. 2006; Collins et al.

2011). For natural materials like sand or sandstone, the porosity compaction model has been tested and compared to mesoscale numerical models that explicitly resolve pore space with high resolution, and to experimental data (Collins et al. 2011; Kowitz et al. 2013; Güldemeister et al. 2015; Wünnemann et al. 2016). At the macroscale, the compaction model has been shown to give reasonable results in crater (funnel) morphology and pore compaction (compacted funnel walls) up to very high porosities (Luther et al. 2017a)[6].

Detailed comparison between model outputs and NASA Ames experimental data for impacts into quartz sand from the 1970s have shown that the iSALE shock physics code can accurately simulate the ejection process (Wünnemann et al. 2016). Also in large-scale cratering processes, iSALE is capable of producing ejection data that agrees with observable constraints as shown for the Orientale basin on the Moon, where the simulated ejecta deposit (for different lunar thermal conditions) was compared with LOLA observations (Zhu et al. 2015; Zhu et al. 2017).

To study the effect of material properties on ejection characteristics, we use a single impact scenario with invariant impactor parameters and Earth gravity. The spherical projectile, 25 m in radius resolved by 20 cells, impacts with a velocity of 5 km/s, which corresponds to Π_2 of 3.2e-5. The pairs of Π_2 and Π_V in this study are given in Table A2.

For the simulation of the thermodynamic material behaviour, we use an analytic equation of state (ANEOS) of quartzite for both projectile and target (Melosh 2007). The yield strength of the projectile is neglected. For the strength of the target we use a Drucker-Prager rheology model. The strength model is described as:

$$Y = min(Y_0 + \beta\, P\, , Y_{max}) \tag{98}$$

with P being the pressure, Y_0 the cohesion, β the coefficient of friction, and Y_{max} maximum yield strength. Most of the models in this study consider a

[6] See chapter 5.

cohesionless (granular) material behaviour. We assume a range of the coefficient of friction from 0.0-1.0 for nonporous material as well as for a moderate porosity Φ=0.42. In addition, we investigate the effect of cohesion Y_0 in a range from 0-150 MPa, which shall mimic the behaviour of competent rock instead of granular material. However, we do not account for the fact that dynamic fracturing of the material will result in a significant weakening of (Collins et al. 2004). The limiting yield strength Y_{max} is set to 1 GPa. Thermal weakening was considered in the simulations using typical parameters for rock (Ohnaka 1995; Collins et al. 2004).

Besides strength, common target materials also differ in porosity. We therefore conducted a series of numerical experiments with cohesionless targets and porosity ranging from Φ=0 to Φ=0.42. For all those models where porosity was varied the coefficient of friction was set to 0.6. Apart from porosity itself, the parameters describing the porosity compaction behaviour were kept constant. Detailed values are given in the appendix. Note, some combinations of material properties do not reflect the behaviour of real materials. For example, a nonporous (Φ=0), cohesionless (Y_0=0) material is unrealistic as granular material always contain some porosity. Noncohesive (Y_0=0) and frictionless (β=0) material implies fluid behaviour of a dense rock, which also does not exist in nature without extreme heating. However, for a systematic study on the effect of material properties there is illustrative value in including such hypothetical end-member cases.

Ejection dynamics are expected to depend on the impact velocity. In general, faster projectiles are able to produce ejecta that are faster than for slower projectiles. To study this scenario, we run models with velocities between 1 km/s and 20 km/s and adapt the projectile size according to crater scaling relationships as shown in Eq. (86), yielding approximately the same crater volume for the different scenarios. We use a cohesionless, non-porous material with a coefficient of friction of 0.6 for these simulations (for both target and impactor). The scaling exponent μ that is required to estimate the projectile size for a given impact velocity that results in the same crater size was taken from Prieur et al. (2017) and corresponds to 0.44.

We use a grid with 750 horizontal and 700 vertical cells. On the top, at the bottom, and on the side, 120 cells where the space increment increases gradually by 3% are added to ensure that the domain boundaries do not influence ejecta behaviour.

Previous studies have shown that iSALE and the material models above are suitable for modelling impact craters with a continuum approach where the material is advected in an Eulerian grid. However, to track the trajectory of ejected material requires knowledge of the history of each material parcel, which is not naturally recorded by an Eulerian code. Furthermore, accurate simulation of the ejecta curtain as it thins requires very high spatial resolution. Therefore, we use about 1000-10000 Lagrangian tracers that are distributed equally in the centre of each computational cell initially and that are moved with the velocity field of the material flow during the simulation. We record the horizontal and vertical velocity components (i.e. speed and ejection angle), launch position and launch time of the tracers at the point of time they are considered to be ejected. We define the time of ejection as the time when the tracer reaches the altitude of one projectile radius above the surface. This approach is simplistic, because it assumes that at this altitude the material represented by the tracer is moving ballistically (i.e. only influenced by gravity) and yet also travelling fast enough that gravity has had insufficient time to deflect its trajectory. An ejection altitude of one projectile radius is a compromise. If the criterion is set to a lower altitude, closer to the target surface, large variations in angle and velocity occur because pressure gradients are still influencing material motion; the ejecta is not yet moving ballistically. On the other hand, an ejection altitude criterion that is too high will lead to an underestimate of ejection angles (and potentially not capturing the ejecta entirely) for slow ejecta, expelled near the crater rim.

Although the simple criterion that we adopt excludes a small amount of material that does not reach a height of one projectile radius, which occurs near the rim towards the end of crater excavation, we find that it gives a relatively robust measurement of ejection speed and angle. We compared ejection statistics for several altitudes for this criterion and found

a general consistency in the average ejection speed and angle for altitudes greater than about one projectile radius. While the spread in ejection angles is reduced at higher ejection altitudes, this also excludes more of the slower ejecta (see Appendix for more details). To derive the launch position for the ejecta at the surface level, we interpolate the launch position linearly to the target surface, based on the determined velocity vector. The mass of the ejected material is assumed to equal the mass of material within the cell where each tracer originally is located before the impact.

In order to account for precise time stepping, which is crucial for a correct interpretation especially of the fastest ejecta close to the impact point, we use the described method above that has been recently implemented into iSALE to detect ejected tracers and record their ejection parameters. This implementation is not included in the standard iSALE Dellen distribution.

Based on the ejection characteristics, we calculate the final distribution of the ejected material under Earth gravity by analytically calculated parabolic trajectories. Hereby, we assume a flat target. From the mass of each tracer and a reference density of the ejected material as the initial density of the material, we calculate the volume of deposited ejecta. By radially binning the location of ejecta, we can calculate the surface area of each bin and thus, we can derive the thickness of the deposited ejecta in each bin. Typically, we use ~100 bins and consider ejecta up to a distance of ~200 projectile radii. Note, we neglect any ejecta sliding or modification to the target material by the falling ejecta (i.e. ballistic sedimentation or secondary mass wasting, Hörz et al. 1983). Early ejected material is fast and deposited at the largest radial distance. It can cause an outward material sliding and mixing of ejecta with local target material that alters the theoretical ejecta thickness to some extent. In addition, the formation of final craters by inward slumping material will change the ejecta deposit close to the transient crater rim. By assuming parabolic trajectories, we furthermore neglect effects of interaction with an atmosphere or vapour plume (Schultz 1992; Barnouin-Jha and Schultz 1996; Artemieva et al. 2013) and the effects of spatially varying gravity. This study focuses on

effects caused by target properties only, and atmosphere induced changes in the ejecta distribution are subject to a future study. Hence, our results are directly applicable to small craters on planetary bodies without an atmosphere. For larger (i.e. complex) craters or basins with diameters of several hundred kilometres, care must be taken about the relation of transient to final crater radius when comparing to observational data and the planetary curvature. Large craters on Earth might be compared as long as ejecta masses are dense enough to show little perturbation by the atmosphere (valid for rather proximal ejecta).

8.5 Comparison to experimental data and scaling models

In addition to previous validation studies (Wünnemann et al. 2016) we explicitly test our approach to determine the ejection characteristics against laboratory data. We compare two of our models that approximately reproduce the target properties of the materials used by Cintala et al. (1999), Anderson et al. (2004), and Housen and Holsapple (2011) in order to show that our model results fall into the same range, despite the very different impact scenarios (impactor mass and speed) considered. We use a coefficient of friction of 0.6 and a porosity between 30% and 42%, which we consider to be typical for the material (sand) used in the experiments. The real coefficient of friction was not stated in these studies. For comparison, we also show predicted behaviour from scaling relationships (Eq. (93)) for several target materials using parameters given by Housen and Holsapple (2011). The comparison is shown in Figure 8-2, where we plot launch velocity and ejection angles as a function of launch distance. Note that launch velocity and distance are normalised by the term $\sqrt{g\,R}$ and crater radius (Figure 8-2 (i) and (ii)), respectively. We use a different size-scale to the experimental data in our model because simulations of real experimental sizes are computationally expensive due to the high cratering efficiency (cf., Pierazzo et al. 2008). However, following the concept of scaling relationships, our comparison is justified as long as the scaling relationships hold true. The comparison shows that the model results are

consistent with the predicted ejection velocity from Eq. (93): the velocity data plot in the expected range for the sand scaling relationship, especially for $x/R>0.5$. Even more pronounced is the agreement of our model data for velocity (Figure 8-2 (i)) and the experimental data from Cintala et al. (1999), Anderson et al. (2004), and Housen and Holsapple (2011).

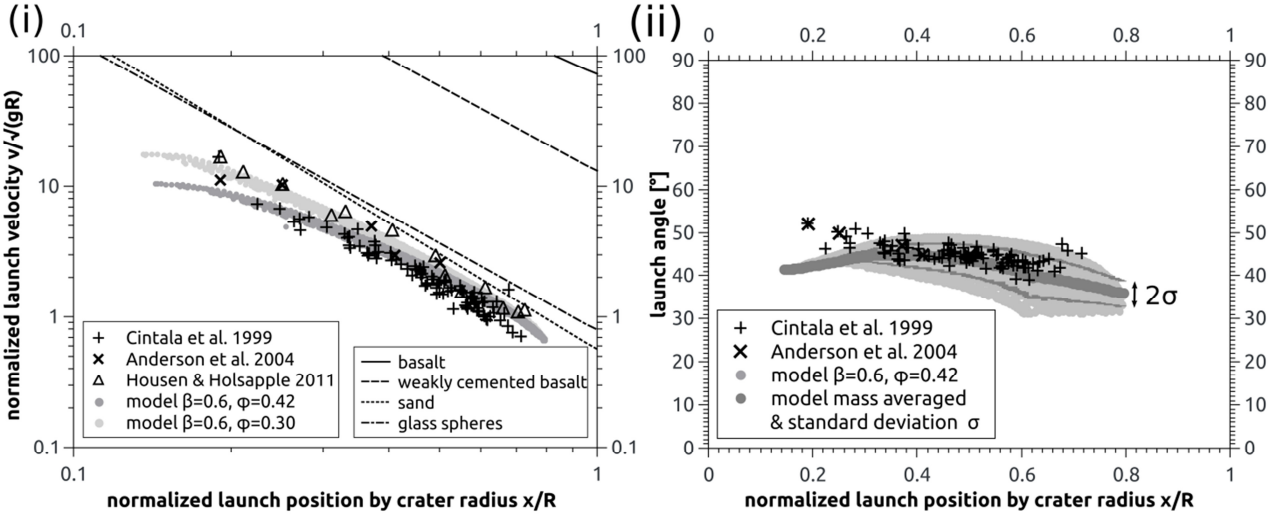

Figure 8-2: Ejection behaviour of cohesionless target materials with a coefficient of friction of 0.6 and a porosity of 30% (light grey symbols in (i); model represents dense sand as given by Housen and Holsapple 2011) and 42% (grey symbols; model represents coarse sand as given by Cintala et al. 1999). The porosity of the sand used by Anderson et al. (2004) is not further specified, but falls into the same range of porosity as for the other two experiments. The launch velocity is normalised by the term $\sqrt{g\,R}$ (i), ejection angles are given in degree (ii), and the distance is normalised by crater radius. In addition to our model data, we plot experimental data (cross symbols; Cintala et al. 1999 and Anderson et al. 2004; and triangles; Housen and Holsapple 2011) and the scaling relationships (Eq. (91) and (93)) for competent basalt, weakly cemented basalt, sand and glass spheres (solid, dashed, dotted and dash-dotted lines, respectively; see Housen and Holsapple (2011) and references therein). The crater size given by Cintala et al. (1999) was measured as rim-to-rim diameter and we estimated 10% difference to the apparent crater diameter. For basalt we arbitrarily assume R/a~20. The modelled impact velocity is 5 km/s. The simulated projectile radius is 25 m. Ejection angles are averaged with a mass weighted moving average with 100 data points. Cintala et al. (1999) used projectiles with a=2.38 mm and v_i=1.4 km/s, Anderson et al. (2004) used a=3.18 mm and v_i~1 km/s, and Housen and Holsapple (2011) used aluminium cylinders with a=6 mm and a height of 12 mm, and v_i=1.4 km/s.

The ejection angle taken from our model varies by about ~12° for a given launch distance for a sand-like target (light grey circles, Figure 8-2 (ii)). This is comparable to, but somewhat greater than, the ~8° spread in the experimentally determined ejection angle. This discrepancy might be

because some fraction of ejected material might not have been captured by the experimental technique used, as acknowledged by Cintala et al. (1999). The experiments were designed to detect a wide range of ejection speeds, but had to exclude very fast or slow ejecta. Furthermore, it was difficult to detect very small particles (Cintala et al., (1999), state an optimum detection size range of ~1-3 mm). On the other hand the simplified criterion used to determine ejection angles in our models might exaggerate the ejection angle spread in the model data (see Appendix). As ejection angle distributions have not been determined experimentally for many materials, it is possible that some of this enhanced spread is real. For example, a certain spread may be expected to some extent because of the physics behind the ejection process. The detailed interaction between the shock wave and the free surface implies that material ejected from near the surface will experience a different combination of acceleration and deceleration vectors from the shock and release waves compared to material that is ejected from deeper within the target (e.g. Melosh 1985, cf. Figure 8-1). On the other hand, the spread might be exaggerated in the models compared with reality. One possible influencing factor is spatial resolution. At the time of ejection (when a tracer satisfies the criteria defined above) the ejecta curtain is typically only resolved by a couple of cells. While the nodal velocity vectors across the curtain show a relatively consistent speed, the angle of the vectors varies, which may result in the observed spread in the angle data. Another factor is mass-weighting of the tracer data. In Figure 8-2 (ii) we show modelling results in which each tracer (light grey circles) is treated equally. However, each tracer actually represents a different mass depending on its radial position of origin. Very proximal tracers represent a smaller mass than those that originate further away from the symmetry axis due to the cylindrical geometry. To correct for this effect, we process our simulated angle data in order to give some uncertainty range and to enable a mass-weighted comparison between experimental and modelling data for the ejection angles. Given the fact that different model data points represent a different mass, we show our results for ejection angles as a moving mass weighted average with a mass weighted standard deviation. This method

allows for the determination of the range of angles where most of the material is ejected. Figure 8-2 (ii, dark grey circles and lines) shows that the observed variations in ejection angles fall into the envelop given by the standard deviation (~ $\pm$4°) from the mass-weighted average. Also for targets with a large range of ejection angles for a given launch distance we can reduce the spread in the raw data significantly. A deviation of speed and angle between model and laboratory data for small launch positions x/R<0.2 might be related to the smaller cratering efficiency of our scenario: a similar initial pattern of rising ejection angles at early stages (close to the projectile) has been shown at least in some experiments by Hermalyn and Schultz (2010).

8.6 Results

In this section, we present our model results for the effect of the coefficient of friction, porosity, and cohesion on ejection velocity and angle. We normalise our results of ejection velocity and launch position by impact velocity and projectile radius, respectively.

8.6.1 Coefficient of friction

In Figure 8-3 we show ejection velocities (i and iii) and ejection angles (ii and iv) for models with coefficient of frictions between 0 and 1 for a non-porous case and a 42%-porosity case, respectively. An increase of the coefficient of friction does not change the onset of material ejection or the velocity of the first ejected material for a given porosity. However, farther away from the impact point, the material with the higher coefficient of friction shows lower velocities and ejection ceases at shorter launch positions due to reduced crater growth. This corresponds to a steepening of the slope in the double logarithmic representation: e.g. at the relative launch position of 10 the velocities for the materials with the largest and lowest coefficient of friction differ by a factor of four.

For the smallest launch position, the angle of ejection depends on the coefficient of friction (Figure 8-3 (ii) and (iv)). After a short regime of steepening of the ejection angle for the lowest launch positions, a maximum quasi-plateau is reached. This plateau is most pronounced for the lowest coefficient of friction (~5° lower angles for $3<x/a<10$) and reduces to a small peak for the largest coefficients in the non-porous case that is followed by a quick decrease in ejection angle. Furthermore, the ejection angle spreads most for the lowest coefficient of friction (~48-70° at launch position 10 for the nonporous material) while the range narrows for larger coefficients of friction (~5° at launch position 5 for the non-porous material). As shown in Figure 8-1, material that originates from a position close to the surface experiences a larger ejection angle than the material that followed the excavation path within the growing cavity. Consequently, and due to the 2D cylindrically symmetric geometry of the setup, the tracer of the material originating from shallow depth and larger distance from the impact point corresponds to a larger mass. In addition, this figure also shows the earlier cessation of ejection for larger coefficients of friction, which is due to smaller crater sizes. Interestingly, we see a small increase in launch angles for larger launch positions ($x/a>10$) for material with a coefficient of friction of 0.0 – 0.2 and no porosity. However, this increase of launch angle occurs at launch positions between about $0.7R$ and $1.3R$, where R is the radius of the transient crater measured at the preimpact level. Launch positions outside the transient crater radius occur if material in the crater rim reaches the height of the ejection altitude criterion (one projectile radius). Although this material reaches the prerequisite height, our analysis does not ensure that it is moving ballistically and therefore this material may not represent ejected material. Fortunately, its effect on the distribution of ejecta landing on the surface as a function of distance is small, as shown in section “Ejecta deposits” further down.

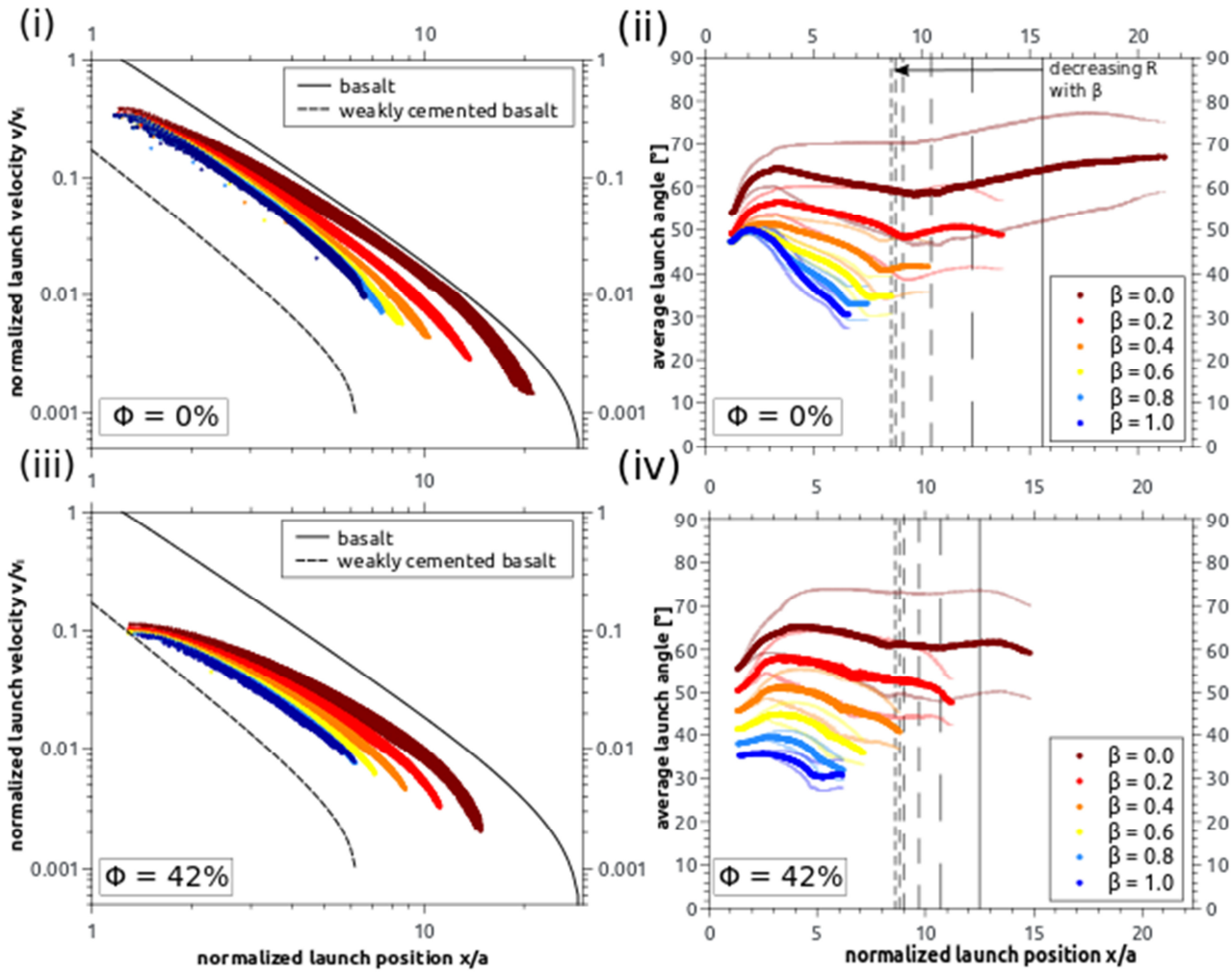

Figure 8-3: Launch velocity (i, iii) and launch angle (ii, iv) versus launch positions on the target surface. Target materials are cohesionless, nonporous (i, ii) or porous (iii, iv, Φ=0.42) and have different coefficients of friction. Velocity and launch position are normalised to the impact velocity and the projectile radius, respectively. The colour-scale corresponds to an increase in the coefficient of friction from dark-red to blue. In addition to our model data, we plot the scaling relationships (Eq. (91)) for competent basalt (equal scaling parameters as water) and weakly cemented basalt (solid and dashed lines, respectively; see Housen and Holsapple (2011) and references therein). For basalt we arbitrarily assume R/a~20. Note, that the velocity data for the highest coefficient of friction in (i) and (iii) overlaps with the other data. Ejection angles are averaged with a mass weighted moving average with 500 data points (ii, all β and iv, β = 0.0) and 100 data points (iv, all β > 0.0), respectively. The crater size is shown by the grey lines ((ii & iv), bold line to finely dashed line correspond to the scenarios with coefficients of friction of 0.0 to 1.0, respectively).

8.6.2 Porosity

Figure 8-4 shows ejection velocities (i) and ejection angles (ii) for models with porosity between 0% and 42% and a coefficient of friction of

0.6. An increase of the porosity substantially affects the velocity of the fastest ejecta at the same launch position (Figure 8-4 (i)). The fastest ejecta from the non-porous target material are ~3.5 times faster than the ones from the material with 42% porosity. For more distal launch positions, the ejection velocities of the ejecta from the different materials align and ejection ceases at about the same distance. This corresponds to a flattening of the slope in the double logarithmic representation.

Ejection angles range from ~40° to ~50° for the different target porosities. However, the general slopes for the ejection angles of the different materials align well, including maximum angles that are reached for each model. Although visible only to some small extent, there seems to be a tendency for steepening of the ejection angle towards the highest porosities of 30% and 42%, while for 20% the average angle was the lowest for all materials.

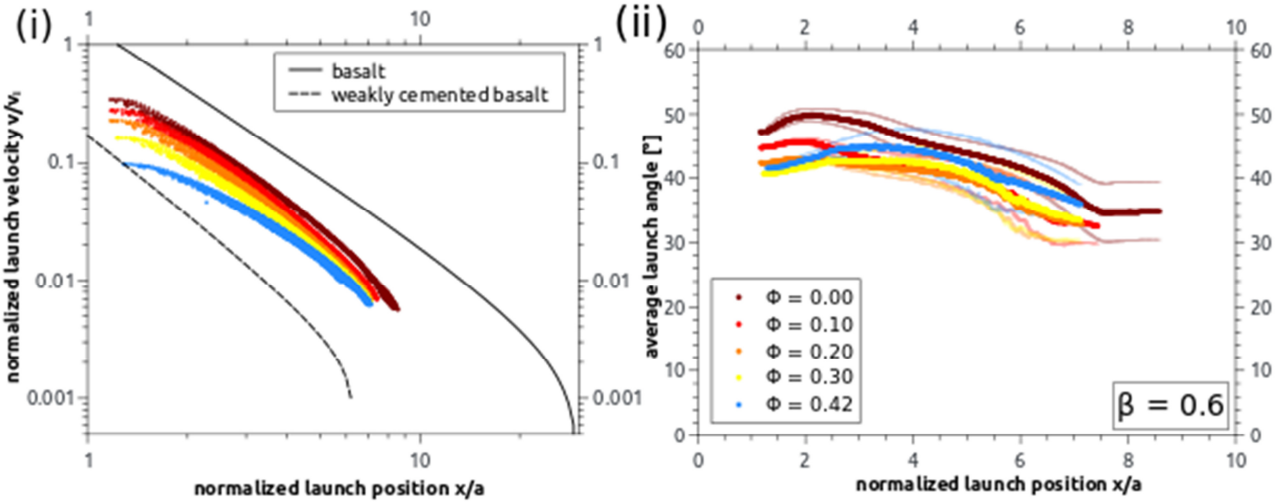

Figure 8-4: Launch velocity (i) and the launch angle (ii) versus launch positions on the target surface. Target materials are cohesionless, have a coefficient of friction of 0.6 and different target porosities. Velocity and launch position are normalised to the impact velocity and the projectile radius, respectively. The colour-scale corresponds to an increase in the coefficient of friction from dark-red to blue. In addition to our model data, we plot the scaling relationships (Eq. (91)) for competent basalt (equal scaling parameters as water) and weakly cemented basalt (solid and dashed lines, respectively; see Housen and Holsapple (2011) and references therein). For basalt we arbitrarily assume R/a~20. Note, that the data of ejection angles partly overlap. Ejection angles are averaged with a mass weighted moving average with 100 data points (ii).

8.6.3 Cohesion

In Figure 8-5 we show ejection velocities (i) and ejection angles (ii) for models with a non-porous material with a cohesion of 0-150 MPa and a coefficient of friction of 0.6. An increase of the cohesion of a material neither changes the velocity of the fastest ejecta at the early launch positions nor the slope in the double logarithmic representation (Figure 8-5 (i)). However, the cohesion affects the final size of the crater and thus the final launch positions of the ejecta. An increase of cohesion leads to ejection velocities ceasing towards zero at smaller launch positions, which may correspond already to the rim.

Ejection angles for different cohesive material align well until the crater rim of each scenario, where ejection ceases. Increasing the cohesion does reduce the crater size and maximum launch positions. The early onset and the maximum ejection angle match for the different materials. The general range of angles agrees with the range resulting from different target porosities. However, material with the highest cohesion values is ejected at a narrow range of angles between 45°-50° and does not show the decline of ejection angle down to ~30° at the largest launch positions that seems to be typical for material with a substantial coefficient of friction.

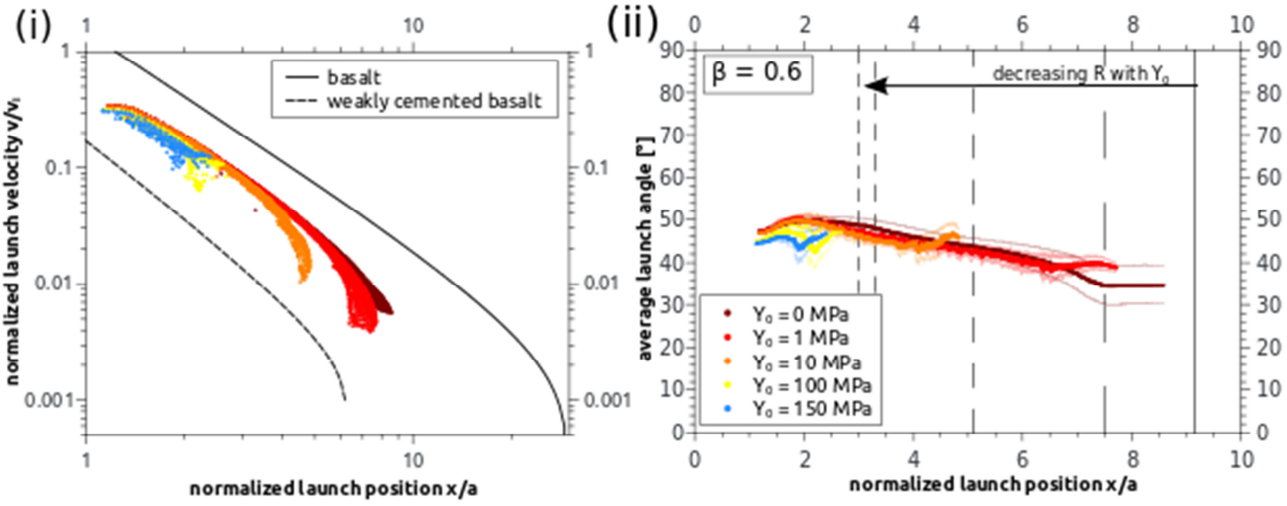

Figure 8-5: Launch velocity (i) and the launch angle (ii) versus launch positions on the target surface. Target materials are non-porous with different target cohesions Y_0 and a coefficient of friction of 0.6. Velocity and launch position are normalised to the impact velocity and the projectile radius, respectively. The colour-scale corresponds to an increase in the coefficient of friction from dark-red to blue. In

addition to our model data, we plot the scaling relationships (Eq. (91)) for competent basalt (equal scaling parameters as water) and weakly cemented basalt (solid and dashed lines, respectively; see Housen and Holsapple (2011) and references therein). For basalt we arbitrarily assume R/a~20. Note, that the data of ejection angles partly overlap. Ejection angles for Y_0>0 Pa are averaged with a mass weighted moving average with 25 data points (ii); and for Y_0=0 Pa with 500 data points. The crater size is shown by the grey lines ((ii), bold line to finely dashed line correspond to the scenarios with 0 MPa to 150 MPa cohesion, respectively).

The common representation of ejection velocities and angles against launch positions normalised to projectile radii does not take into account the final crater size. As stated above, some differences we observe for ejection velocities are due to differences in transient crater radii. Therefore, we also present the ejection velocity as a function of normalised launch positions relative to crater radius x/R (Figure 8-6). For different coefficients of friction, we see an overlap of ejection velocities close to the crater rim for both non-porous and 42%-porous material (Figure 8-6 (i) and (ii)). Some slight differences occur in the non-porous case for very small launch positions. However, these differences (30-40 for x ~0.1) are smaller than differences that occur for varying target porosity (10-40 for x ~0.1, Figure 8-6 (iii)). Further differences can be found for velocity plots of different cohesion (Figure 8-6 (iv)). Here, we see an offset between the different scenarios that overlap in projectile normalisation. The cohesionless case plots in the range of the scaling relationship for sand, whereas the case with highest cohesion plots close to the scaling relationship of weakly cemented basalt that has a compressive strength of 680 kPa (Housen 1992). Note, that the normalisation used is typical for the gravity dominated regime. Larger cohesions will shift the scenario into the strength regime.

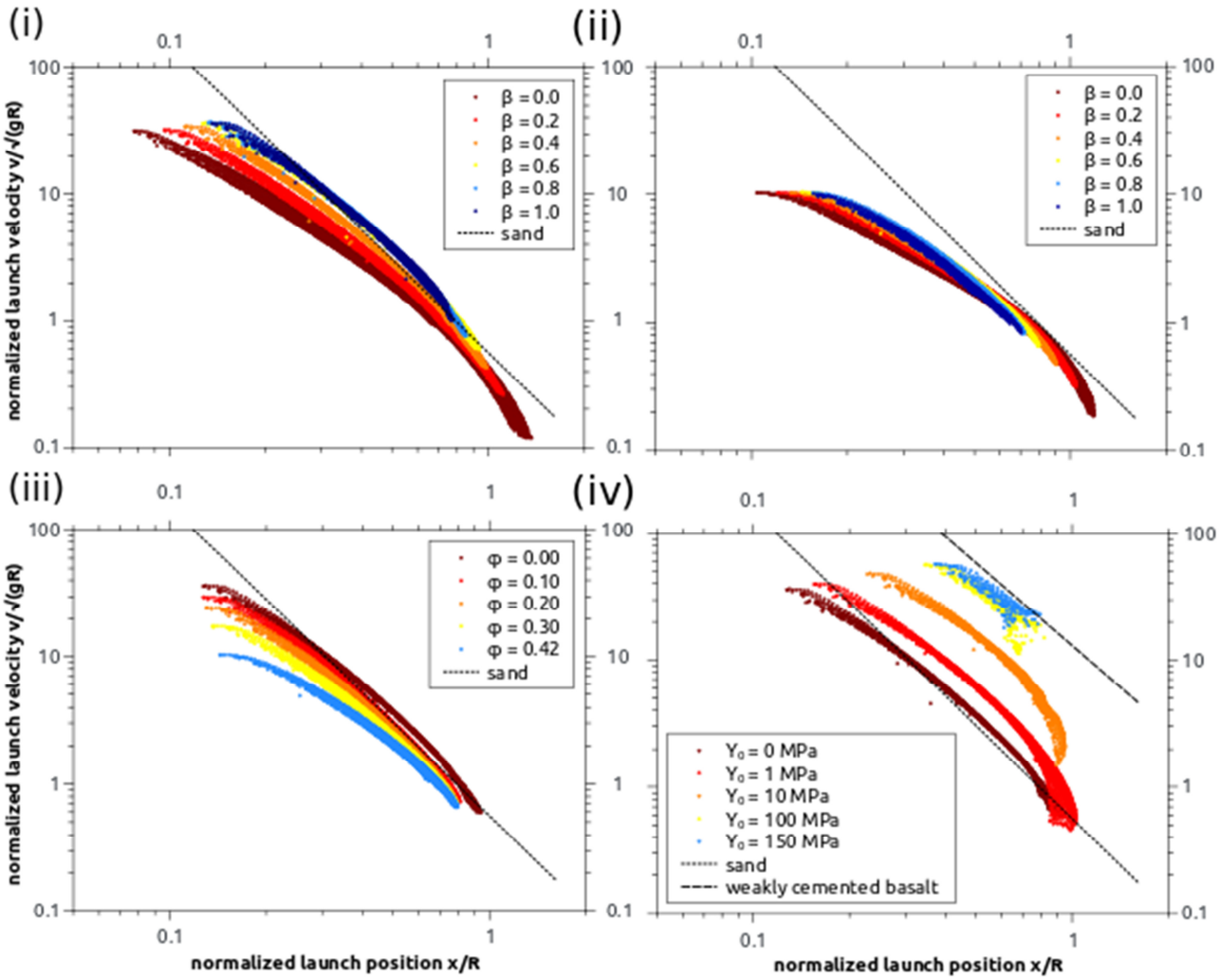

Figure 8-6: Ejection velocity for the same cases as shown in Figure 8-3 - Figure 8-5 ((i)-(iv), respectively). The distance is normalised to crater radius and the launch velocity to $\sqrt{g\,R}$. In addition to our model data, we plot the scaling relationships (Eq. (93)) for weakly cemented basalt and sand (dashed and dotted lines, respectively; see Housen and Holsapple (2011) and references therein). In (i)-(iii), there is no cohesion. In (iii) and (iv), the coefficient of friction is 0.6.

8.6.4 Effects of impact velocity

In our study, we compare models with different impact velocities that result in the same crater size, as described in the method section (Table A2). In Figure 8-7, we show ejection velocities (i) and ejection angles (ii) for models with a non-porous material and a coefficient of friction of 0.6 for impact velocities in the range from 1 – 20 km/s. A comparison of these models shows that ejected material behaves similar for different impact velocities in terms of absolute launch velocities, but not in terms of ejection

angles (Figure 8-7). In terms of ejection velocities, all models fall on the same line which is a consequence of the different projectile radii. The proximal ejecta of the slowest impact (= largest projectile) is launched at larger launch distance than in the scenario with 20 km/s impact velocity.

Differences are more pronounced for ejection angles: Keeping in mind the uncertainties in the measurement of ejection angles as discussed in the chapter "Comparison to experimental data and scaling models", lower impact velocities appear to result in lower ejection angles for our non-porous target. Thus, a larger fraction of the total momentum of ejected material goes in horizontal direction for lower impact velocities. Maximum ejection angles differ by a factor of about two comparing the fastest and the slowest impact. The most significant differences can be observed for locations close to the impact point (Figure 8-7 (ii)). Furthermore, we see that ejection angles for one launch position can vary more in the case of a fast impact than in the slower case. In contrast to the previous figures, we show the data in absolute values as the craters are about equal in size (< 8% difference of radius to reference value). Normalised plots are shown in the discussion section.

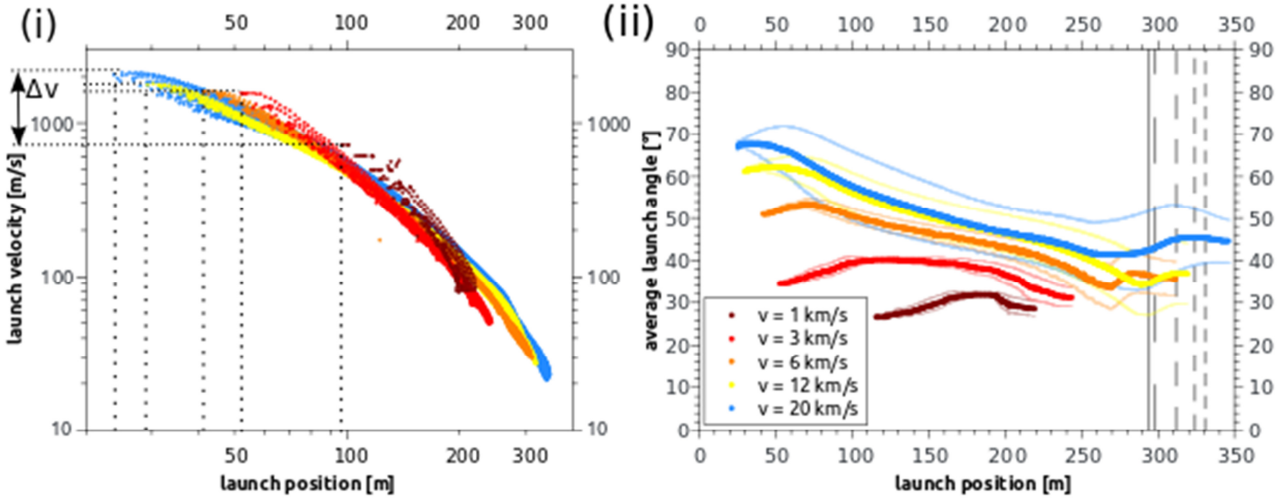

Figure 8-7: Absolute launch velocity (i) and the launch angle (ii) versus absolute launch positions on the target surface for different impact velocities. The target material is non-porous, cohesionless and has a coefficient of friction of 0.6. The colour-scale corresponds to an increase in impact velocity from dark-red to blue. Dashed and dotted lines show the projectile radii of the different models and the corresponding maximum ejection velocities, respectively. Ejection angles are averaged with a mass weighted moving average with 50, 100 and 500 data points

for impact velocities of 1 km/s, 3-6 km/s, and 12-20 km/s, respectively (ii). The crater size is shown by the grey lines ((ii), bold line to finely dashed line correspond to the scenarios with an impact velocity of 1 km/s to 20 km/s, respectively).

8.7 Discussion

8.7.1 Effects of different impact velocities for constant crater size

In the previous results section, we show a comparison of ejection dynamics for different target properties, followed by a comparison of scenarios with different impact velocities. For a better understanding we begin our discussion with aspects for the latter cases as these serve as the best starting point of our argumentation. The results show that absolute ejection velocities for craters with similar volume follow the same trend for all impact velocities (Figure 8-7). For the averaged ejection angles, we see increasing launch angles at positions close to the impact point that agree with patterns described in previous studies of early excavation at similar launch positions to ours (Hermalyn and Schultz 2010, 2011; Hermalyn et al. 2012; Gulde et al. 2018). For slower impacts, ejection angles are shallower. These findings are not seen by Hermalyn and Schultz (2010) with 1.63 km/s as slowest impact velocity, but are in agreement with the trend observed by Hartmann (1985) for powdered basalt (5 m/s – 2.3 km/s). However, both studies used a different target material to the one we used for the velocity study, indicating that the effect is depending on the target material used. The scenarios with an impact velocity of 6, 12 and 20 km/s are more similar to each other than the slower scenarios of 1 and 3 km/s impact velocity. The latter two velocities are smaller, or about equal, respectively, to the bulk sound speed in the target material (3684 m/s as derived by ANEOS for quartzite) and as such are not or only just in the hypervelocity regime and a shockwave-induced excavation flow may have not been fully established. Note that the speed of sound of the target material in the studies from Hartmann (1985) and Hermalyn and Schultz (2010) is substantially lower than for the non-porous target material we used for this velocity studies and, thus, the effects for low-velocity impacts that we see might occur at

different velocities for other target materials. For such low-velocity impact scenarios crater formation and ejection of material mostly occurs in the nearfield, where the point source approximation to describe the excavation flow in the farfield is not applicable. Therefore, the scaling relation Eq. (86) used for the determination of the projectile parameters yielding the same crater volume does not hold true and crater mass and volume do not agree with the mass and volume of the faster scenarios (Figure 8-15). The ratio of maximum excavation depth to transient (maximum volume) crater radius (~0.2) is equal for all scenarios apart from the lowest impact velocity.

Although the ejection velocities for the scenarios with different impact velocities follow the same trend in absolute numbers, their trend diverges in the non-dimensional representation normalised to impact velocity and projectile radius (Figure 8-8 (i)) for launch positions $x/a \leq 3$. The maximum values at the smallest launch positions vary by about an order of magnitude between the 1 km/s and the 20 km/s scenario. The proximal slope is different for all models with different impact velocities. Only for larger distances the decay of the different models may agree. As the absolute velocities appear to be equal, the difference in the decay in the normalised representation is no surprise. Faster impacts correlate with smaller projectile radii if the same crater volume is reached (Figure 8-7). As such, the slope must flatten for faster impacts. Better agreement between the ejection velocities of the scenarios with different impact velocities can be achieved when plotting in crater parameter normalisation (Figure 8-8 (iii)). Apart from very early ejecta ($x/R < 0.2$), the different models roughly plot on the same line, which corresponds to the line from sand scaling relationship (μ = 0.41). We will address this topic later on.

Larger differences appear in the ejection angles of the impacts with different impact velocity (Figure 8-8 (ii) and (iv)). The mass weighted average of the angles that we use suggests that for the fastest impacts, a larger fraction of the ejection velocity goes in a vertical direction whereas it is more in a horizontal component for the slower impacts. As mentioned before, the excavation flow that is transferred onto the material by the shock wave initially has a radial direction away from the source of the shock

wave. The onset of the rarefaction wave causes a pressure gradient, and thus adds an upward component to the excavation flow (Gault et al. 1968; Thomsen et al. 1979; Melosh 1989). In our scenario with different impact velocities, peak pressures will increase with impact velocity whereas the isobaric core will be smaller and probably shaped differently as the projectiles are smaller. We argue that the increase in peak pressure with increasing impact velocity causes a larger pressure gradient that, consequently, will add a larger upward component to the velocity field. Note that the effect of varying impact velocities is less pronounced in more porous targets. For targets with a porosity of Φ=0.42, ejection angles reach ~38° and ~45° for impact velocities of 1 km/s and 5 km/s, respectively, and as such differ less than in a non-porous target where ejection angles reach ~30° and ~53° for impact velocities of 1 km/s and 6 km/s, respectively. Target properties will be discussed further in the next chapter. Note further, that in early ejection times an effect of projectile parameters (e.g. density) on initial launch angles was shown; resulting in higher launch angles for denser projectiles (Hermalyn and Schultz 2011). This is in agreement with the explanation of larger shock pressures above: A larger impedance contrast between projectile and target due to the density increase in the projectile causes higher shock pressures (cf. e.g. with a steeper Hugoniot in Fig. 10 from Ebert et al. 2017), and presumably also affects the geometry of the isobaric core and, hence, radial directions to the isobaric core.

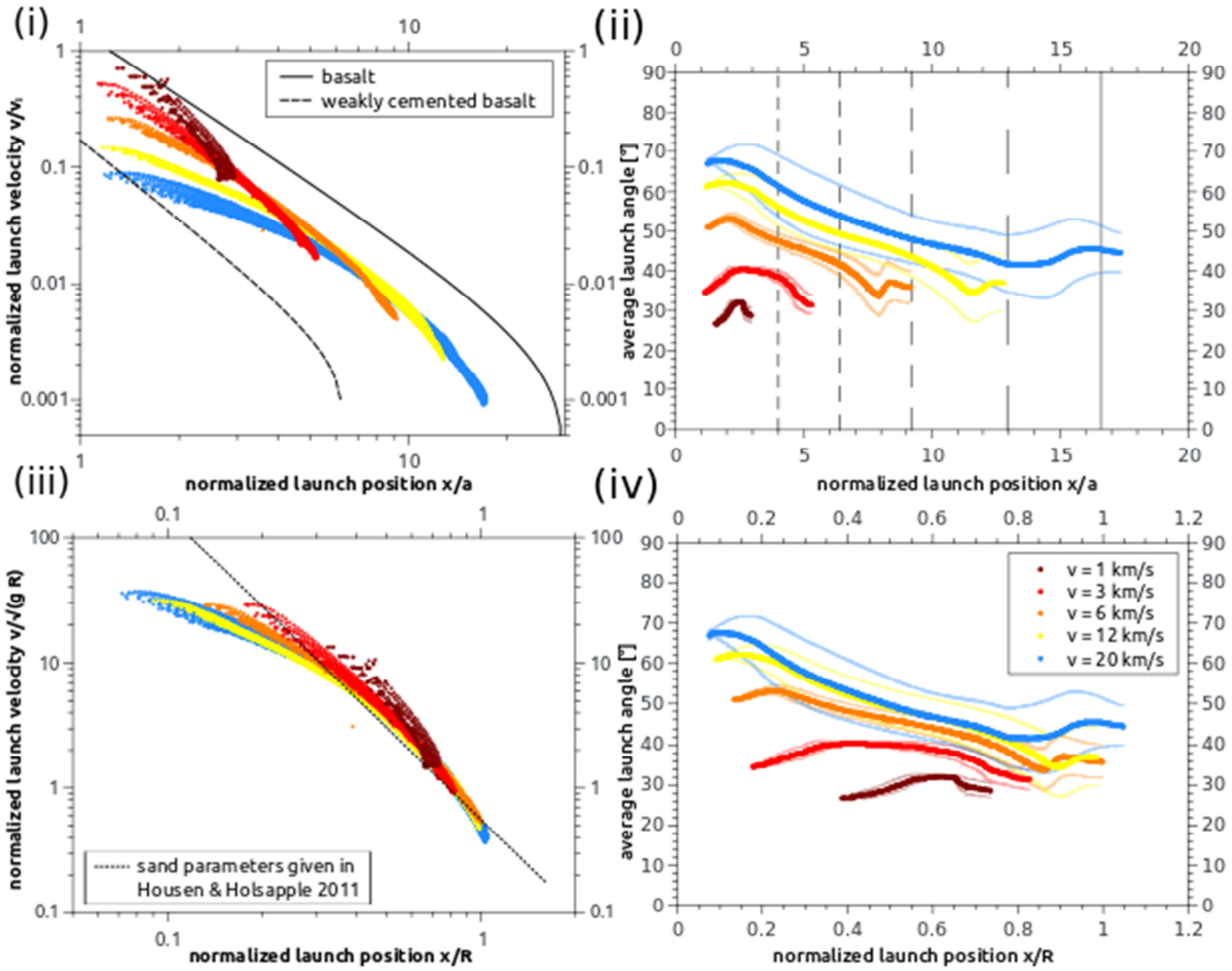

Figure 8-8: Ejection velocity and angle for the same cases as shown in Figure 8-7. The launch velocity is normalised to impact velocity (i) and $\sqrt{g\,R}$ (iii), respectively. The launch positions on the target surface are normalised to projectile radius (i & ii) or crater radius (iii & iv). In addition to our model data, we plot the scaling relationships (Eq. (91) and (93)) for competent basalt (equal scaling parameters as water), weakly cemented basalt, and sand (solid, dashed, and dotted lines, respectively; see Housen and Holsapple (2011) and references therein). For basalt we arbitrarily assume R/a~20. The colour-scale corresponds to an increase in impact velocity from dark-red to blue. Note, that the data of ejection angles partly overlap. Ejection angles are averaged with a mass weighted moving average with 50, 100 and 500 data points for impact velocities of 1 km/s, 3-6 km/s, and 12-20 km/s, respectively (ii & iv).

8.7.2 Target properties and excavation flow

In the following, we discuss the mechanism that causes the different ejection characteristics that we observe for different target properties. In the previous section, we discussed pressure gradients that differ due to the increased peak pressures with impact velocity, and different isobaric cores

due to different projectile size. In our impact cases with varying target properties, we use equal impact conditions. Hence, the peak pressure and the size of the isobaric core are similar (Figure 8-9), and peak pressures exceed the material strength, causing similar proximal $\left(\frac{x}{a} \leq 2\right)$ ejection velocities and ejection angles for different coefficients of friction in the non-porous case (Figure 8-3 (i) and (ii)). However, with increasing distance from the impact point we see more pronounced differences in the ejection characteristics that are caused by differences in the attenuation of the shock wave as a consequence of material properties such as strength and porosity (cf. decrease of peak pressure in Figure 8-10). In either case shock wave attenuation is enhanced because of energy dissipation by plastic work. Hence, the greater attenuation in pressure with distance in the target (Figure 8-9), leads to smaller pressure gradients in upwards direction. In addition, peak pressure isobars are shaped differently and the pressure gradient vector at shallow depths and at a given normalised radius points less-steeply towards the surface in the simulation with a larger coefficient of friction (Figure 8-9). Consequently, as friction coefficient is increased, the upward-directed acceleration is less and ejection angles shallower for launch positions $\frac{x}{a} \geq 2$ (Figure 8-3 (ii)). Experimental results for ejection angles for pumice and sand (the coefficient of friction of pumice is larger than for sand) support our conclusion (Hermalyn and Schultz 2014).

When porosity is added to the target material, the behaviour of ejected material again changes (Figure 8-4). Very proximal ejection velocities are very different and converge only towards the crater rim, whereas ejection angles do not differ much between the different scenarios (10° for the smallest launch positions). The decrease of maximum ejection velocities correlates with lower peak pressures in the target material with increasing porosity (Figure 8-10). As a result, the pressure gradients and acceleration from the shock wave decrease as well, causing the slight decrease in proximal ejection angles. However, for larger ejection distances, differences between the models disappear; so the same must hold true for pressure gradients in the target. Different processes due to the presence of porosity acting towards an increase (+) or decrease (-) of the ejection angle

((I) faster attenuation (-) and lower peak pressure (-) of the shock wave (Figure 8-10), (II) longer duration of the unloading path (+), (Güldemeister and Wünnemann 2017); and (III) enhanced thermal weakening due to pore space crushing (+), Wünnemann et al. 2008), respectively, balance out each other so that for different porosities the ejection angles remain constant. Note, that ejection angles for the largest porosity in parts are slightly larger than all other porosities, and especially larger than the nonporous scenario. Note further, that we discuss only porosities up to 42%. Cratering in very porous targets can lead to an almost complete suppression of the ejection of matter for large craters (above a threshold size) due to the dominant mechanism of pore compaction and when cratering is dominated by the crushing strength (e.g. Housen and Holsapple 2012).

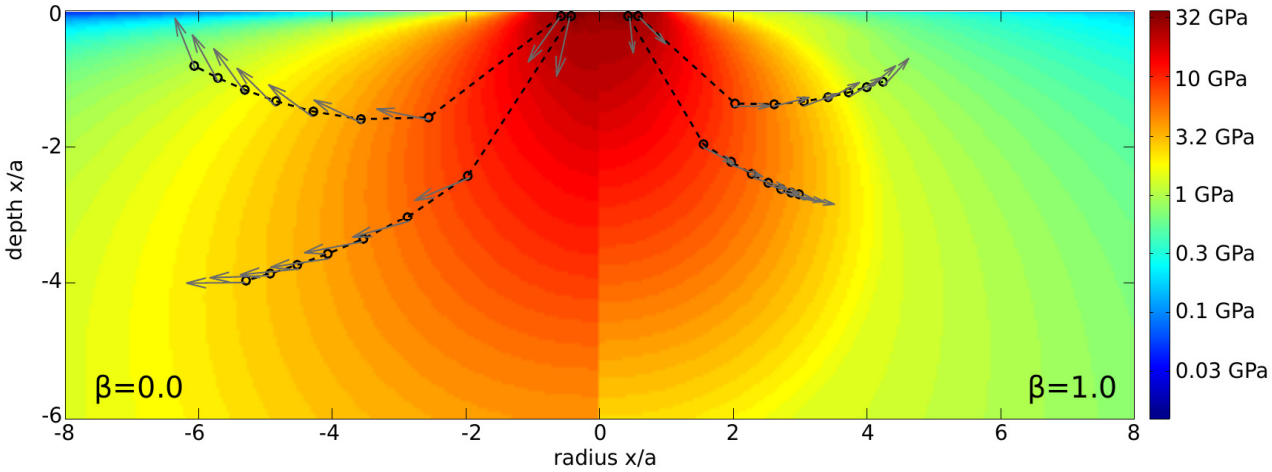

Figure 8-9: Peak pressure contours and gradients for two different coefficients of friction. The colour scale shows the peak pressure that was reached at the given location within the target for cohesionless, nonporous materials with coefficients of friction β=0.0 (left side) and β=1.0 (right side). Dashed lines indicate two exemplary tracer trajectories for equal initial positions. Grey arrows depict the direction of the gradient of peak pressures at the given locations.

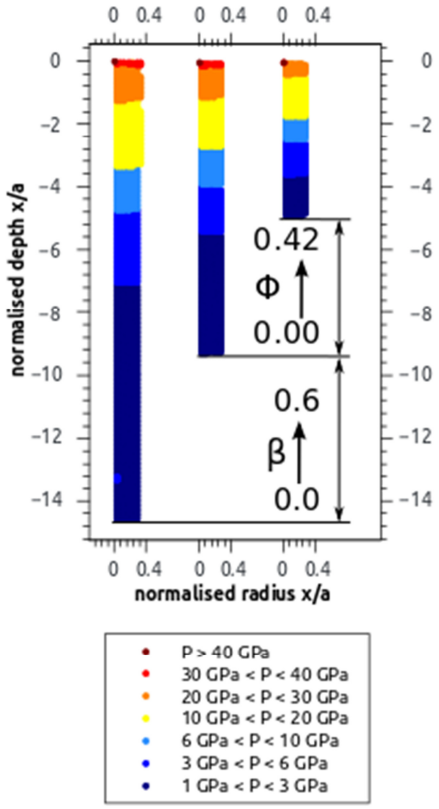

Figure 8-10: Peak pressure contours for three different materials. The colour scale shows the peak pressure range that was reached at the given depth within the target underneath the impact point. All materials are cohesionless. From left to right, first the coefficient of friction increases from 0.0 to 0.6, and second porosity increases from 0% to 42%.

8.7.3 Implications for ejecta scaling

In this section, we discuss our results in the context of the scaling relationships shown in the chapter "Theoretical Background". One approach is to fit Eq. (90) to the model data in the normalisation to projectile size and impact velocity. However, for models with equal crater volume but different impactor parameters it was not possible to adopt a consistent range in launch position when normalised by impactor radius for fitting Eq. (90) to the data (Figure 8-8 (i)). The slope in the range $\frac{x}{a} \leq 3$ differs a lot for the different impact velocites. Therefore, we fit Eq. (93) to the model results in the normalisation to crater radius (cf. Figure 8-6 and Figure 8-8).

For fitting Eq. (93), we adopted a fixed criterion for the maximum launch position for the fitting range in order to achieve consistency in our

results (given in Table A2). We define the maximum fitting range by a common minimum velocity of ~80 m/s for all models. Defining the maximum range in this way avoids including data too close to the rim, which may be affected by our ejecta selection criterion. For non-porous, cohesionless material, we find a nearly constant scaling exponent of μ = 0.46 - 0.49 and an increasing constant K_3 from 0.43 to 0.82 for coefficients of friction between 0 and 1 (Figure 8-11 (i)). The same trend of μ is observed for a material with 42% porosity. When increasing porosity from 0 to 42% for a constant coefficient of friction of 0.6, we find an increase in μ from 0.46 to 0.62, whereas K_3 first decreases from 0.77 to 0.60, before it rises again to 0.70 (Figure 8-11 (ii)). Increasing the cohesion for a non-porous material strongly increases μ as well as K_3 (Figure 8-11 (iii)). For increasing impact velocity from 1 km/s to 6 km/s for a cohesionless, non-porous target with a coefficient of friction of 0.6, we find an increase of μ and K_3 from 0.32 to 0.48 and from 0.59 to 0.85, respectively (Figure 8-11 (iv)). For larger velocities, these values remain constant. Note that this trend is inverse to the trend found by Yamamoto et al. (2017) for porous sand targets. However, this trend is similar to the one shown by Schultz (1988).

Literature values for sand like targets give a value for the scaling exponent of μ =0.41 (Housen and Holsapple 2011). Our closest results to these values have been achieved for non-porous, cohesionless materials with a coefficient of friction of 0.6 at an impact velocity of 3 km/s. However, sand has a significant amount of porosity, so that the corresponding simulated material should have porosity, as well. If we increase porosity, μ increases up to 0.62 for 42% porosity. This value is a bit larger than the value for rock like material or water (rock and water: μ=0.55, Housen and Holsapple 2011), and much larger than the literature value for sand of 0.41 that is based on crater size scaling. However, experimental measurements of ejection dynamics for sand-like materials have shown the same discrepancy between μ-values derived from crater scaling and ejecta scaling that we observed: Cintala et al. (1999) fitted scaling relationships (Eq. (93)) to their ejecta velocity data and found values between 0.5 and 0.66. They attributed the discrepancy to the coarseness of their particulate target material relative

to the projectile size used. However, similar results were derived for finer-grained sand targets in more recent experiments using the same technique for measuring ejection velocity (Anderson et al. 2007). Similarly, Tsujido et al. (2015) find some deviation of μ derived from crater scaling and from ejecta scaling with a scatter in the range of the data from Cintala et al. (1999) in a study with different projectile densities at an impact velocity of ~200 m/s. Anderson et al. (2007) also mention some (partly unpublished) results where both scaling results agree with each other. More recently, (Yamamoto et al. 2017) described a different study that compared μ-values estimated from measurements of crater growth as a function of time and crater size measurements that revealed a similar discrepancy in the scaling exponent derived from both measurements. These studies of crater growth, excavation and material ejection show differences in scaling relations for dynamic aspects of the cratering process that involve both intermediate- and far-field phenomena versus singular, far-field observations (e.g. crater size). One interpretation of such discrepancies is that the point source assumption is valid for crater size, which is a metric dominated by far-field phenomena, but is not satisfied for the dynamic aspects of cratering. Anderson et al. (2004) introduced the concept of a moving flow field centre and argued that a stationary point source is not adequate for the dynamic aspects of cratering. An implication of this result is that a scaling exponent derived from crater sizes may predict incorrect ejecta behaviour when used in an ejecta scaling relationship. It is therefore prudent to use scaling exponents derived for the process of interest. It is likely that for impacts with large cratering efficiencies (i.e. small π_2), the point source approximation might be more applicable also for describing dynamic aspects because most of the excavation occurs more distant from the impact centre. Our findings for our fastest impact velocities (12 km/s and 20 km/s, π_2=5.5 10^{-6} and 1.6 10^{-6} , respectively) show a constant scaling exponent of μ =0.52, a value that is close to predicted values for non-porous targets (rock and water: μ=0.55, Housen and Holsapple 2011), but still deviates somewhat from crater size scaling results for similar numerical materials (μ=0.45, Prieur et al. 2017).

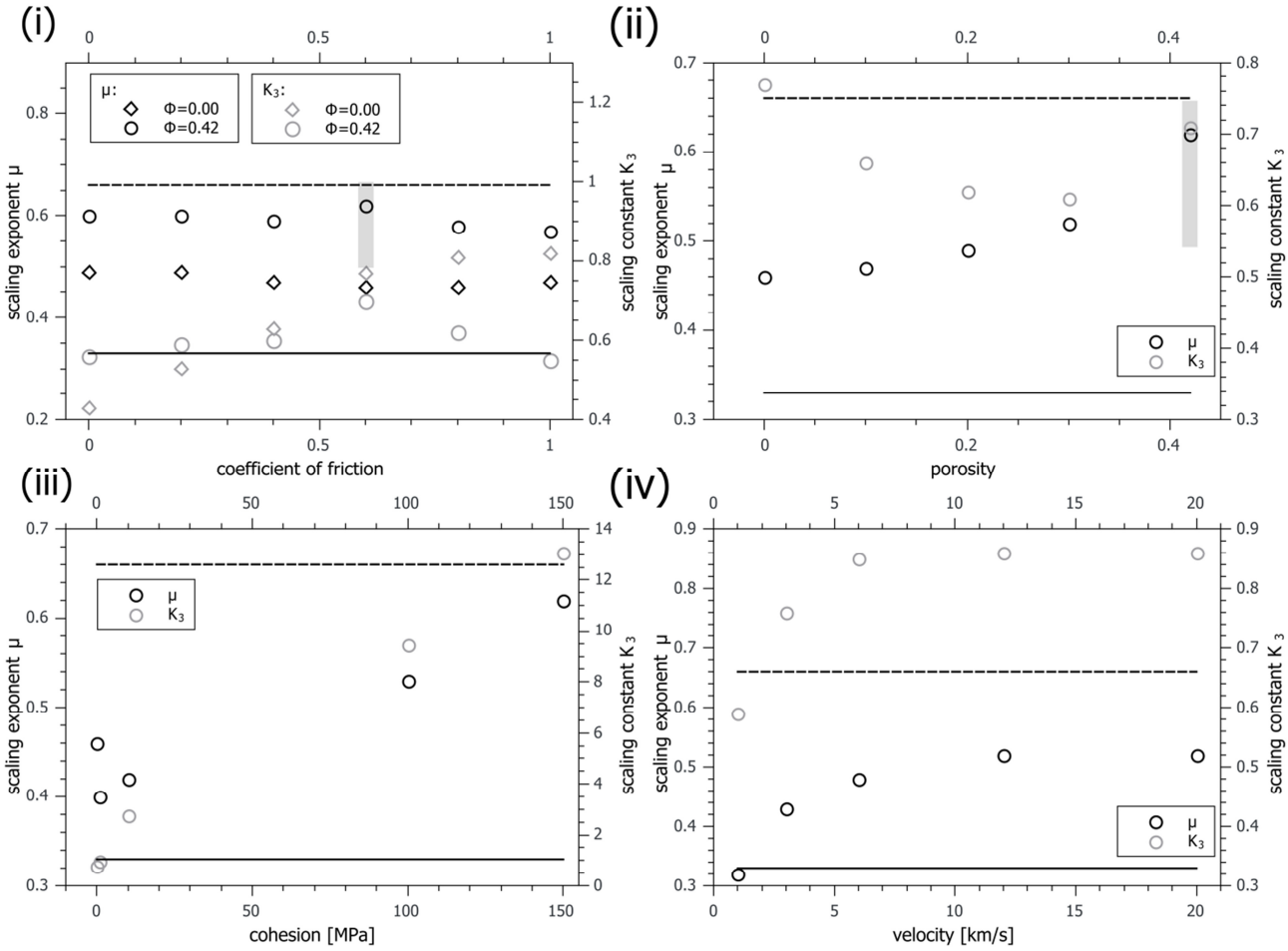

Figure 8-11: Ejecta velocity fitting results. Black symbols denote the scaling exponent, grey symbols the scaling constant. The results are given for the models shown in Table A2: (i) cohesionless target with Φ=0.00 (◊) and Φ=0.42 (o), (ii) cohesionless target with β=0.6, (iii) non-porous target with β=0.6, and (iv) a cohesionless, non-porous target with β=0.6. The black solid and dashed lines represent the momentum and energy scaling limits, respectively. The grey area depicts the range for the scaling exponent μ as derived by (Cintala et al. 1999) and most of the range from (Tsujido et al. 2015).

8.7.4 Ejecta deposits

We calculate the deposition of the ejected material based on the assumption of parabolic trajectories for the cases of different target materials mentioned so far. We do not consider any late stage modification processes, but show the amount of material that lands at a given radial distance. Our calculation takes into account the launch position of ejecta within the crater when calculating its deposition position. As a result, unlike the simple scaling model (Eq. (95)) the model-derived ejecta thickness distributions do not suffer from inaccuracies near the crater rim. We plot the

thickness of the deposited ejecta against the radial distance normalised by the transient crater radius (Figure 8-12). For the scenario of a non-porous material (Figure 8-12 (i)) we see a decrease in the slope of the thickness of the deposited ejecta for increasing coefficients of friction. The difference in ejecta thickness is most prominent in the proximal range $\left(\frac{x}{R} \leq \sim 2\right)$. For the same coefficients of friction, this effect is even more pronounced for the porous material with a porosity of 42% in a range until x< ~6 (Figure 8-12 (ii)). In contrast, little variation in the slope of the ejecta thickness is found for different target porosities with a constant coefficient of friction of 0.6 and ejecta thickness are nearly identical (Figure 8-12 (iii)). Only the nonporous case shows a thicker ejecta thickness that is about twice as thick as those of the porous materials for equal normalised distance x/R. The differences that result from cohesion are more prominent. Increasing cohesion results in a decrease of the slope of the ejecta thickness and in a reduction of its thickness. For the two largest values of a cohesion of 100 MPa and 150 MPa, only small thicknesses of the deposited ejecta are observed.

Our results for different targets show that the effect of material properties on the ejection characteristics results in deviating ejecta trajectories and, thus, in different deposition thickness as a function of distance. Especially, the coefficient of friction affects the decay exponent of the ejecta deposit due to increasing ejection angles for lower friction values. Ejection angle close to 45° result in the furthest distances that the ejected material can reach. For the nonporous material that is the case for a coefficient of friction between 0.4 and 0.6. Lower coefficients of friction yield angles >45° resulting in ejecta accumulation close to the crater rim, as shown in Figure 8-12 (i). In contrast, for different material porosities ejection angles lie between 40° and 50° for a large range of launch positions. As such, the resulting ejecta deposits are similar in terms of decay exponent and ejecta thickness if distance is normalised by the transient crater radius (Figure 8-12 (ii)). The difference in ejection velocities that is affecting ejecta deposition is accounted for by the normalisation to the crater radius (that itself depends on the various porosities).

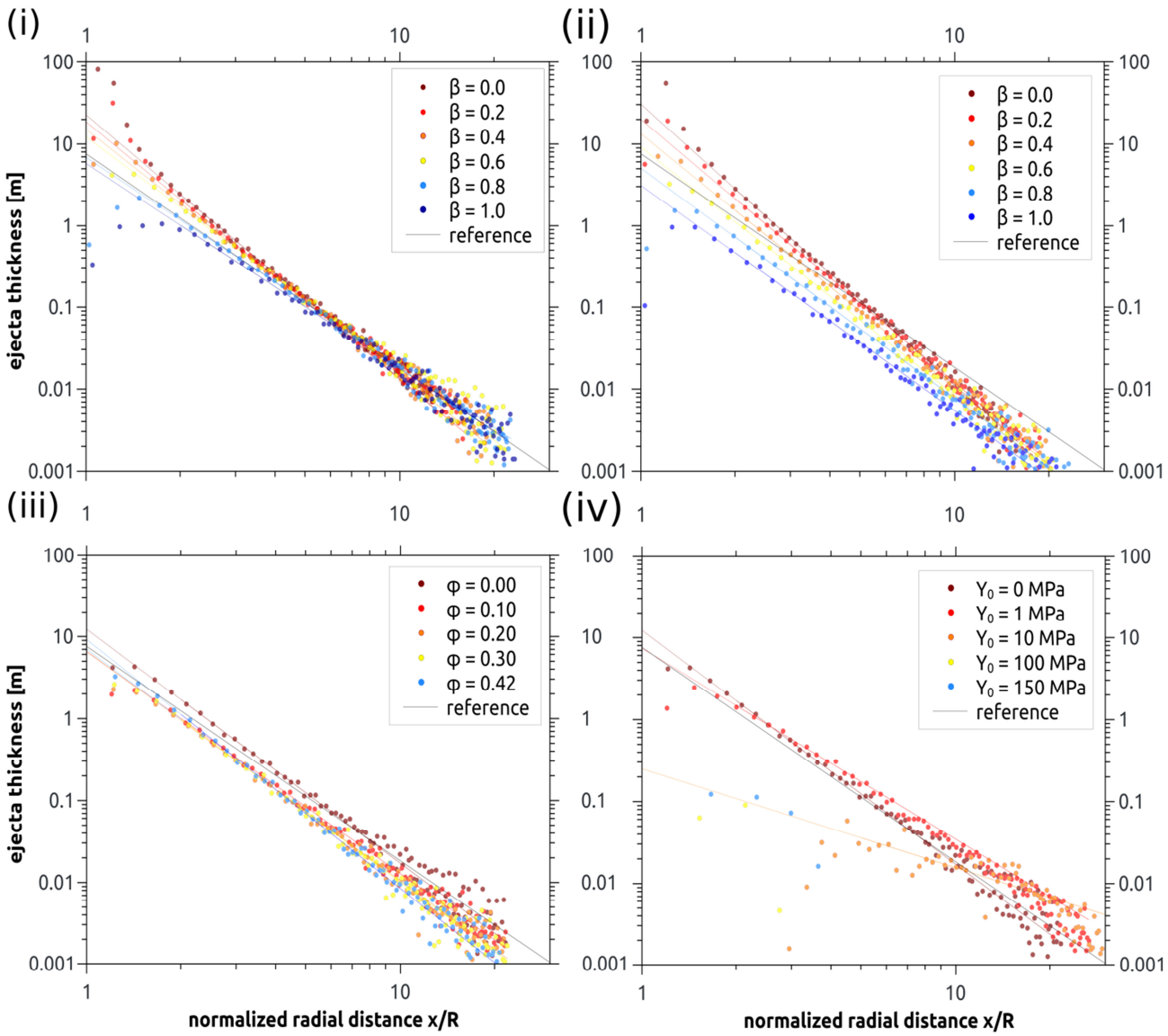

Figure 8-12: Distribution of the ejecta thickness for different target properties. The cases shown refer to: i and ii) different coefficients of friction in a nonporous and a porous (Φ=0.42) material, respectively (cf. Figure 8-3), iii) different porosities (cf. Figure 8-4), and iv) different values of cohesion (cf. Figure 8-5). The distance is normalised to transient crater radii. For comparison with our results, we also show scaling data using Eq. (95) as a reference. We use a constant K_4 = 0.32 as given by Housen et al. (1983) and a sand like value of μ=0.41. We use a typical constant value of 45° as ejection angle. As reference crater radius we use the transient radius R=242.5 m of our model with 42% porosity and a coefficient of friction of 0.4. Note that the reference line assumes all ejecta emanates from the crater centre and, thus, is not expected to hold in the vicinity of the crater rim. In (i)-(iii), there is no cohesion. In (iii) and (iv), the coefficient of friction is 0.6.

To support our previous statements, we fit the thickness of ejecta deposits over the radial distance with Eq. (96). We exclude data in the range $1 < x/R < 2$ from the fitting as a simple power law relationship is not expected this close to the crater rim, as evidenced by the simulation results.

The different parameters for different target properties are given in Table A2, and are shown in Figure 8-13. The relationship between ejection angle and ejecta deposition mentioned above is shown e.g. by the larger T_0 for targets with low coefficient of friction (Figure 8-13 (i)). Furthermore, parameters for different porous materials remain nearly constant (Figure 8-13 (ii)). The smallest and largest exponents that we found give a range for B between 2.52 and 3.43 for the cohesionless targets. We also calculated the scaling parameter μ according to Eq. (97). However, we find that these values partly exceed the theoretical limit of energy scaling (0.66) and all models with porosity do not fall into the typical range of μ~0.4. One explanation for these results can be seen in too strong assumptions made for deriving Eq. (95), including one ejection angle instead of a range of angles, and the negligence of exact launch positions. Furthermore, as indicated in the previous chapter, the static point source seems to have limitations for describing the dynamic aspects of cratering (e.g. material ejection). For deriving Eq. (95), dynamic and static aspects are combined, but only one scaling exponent (which has been shown to be not identical for both aspects of cratering in the previous chapter, or e.g. by Cintala et al., (1999)) is present in Eq. (95). Hence, the resulting scaling exponents from ejecta deposits should be considered with care. Consequently, comparing the derived scaling exponents based on the ejecta deposit with those derived by the velocity data, we find large differences in μ for 11 of 21 cases and only 6 cases where both results agree (Table A2). For the usage of scaling relations for ejection processes, we prefer the usage of the results based on the velocity plots instead of the deposits. For the μ derived from deposit data, we see a trend to smaller μ for increasing β. This seems to be so far reasonable as the scaling parameter for water is larger than the one for sand (0.55 and 0.41, respectively, Housen and Holsapple 2011).

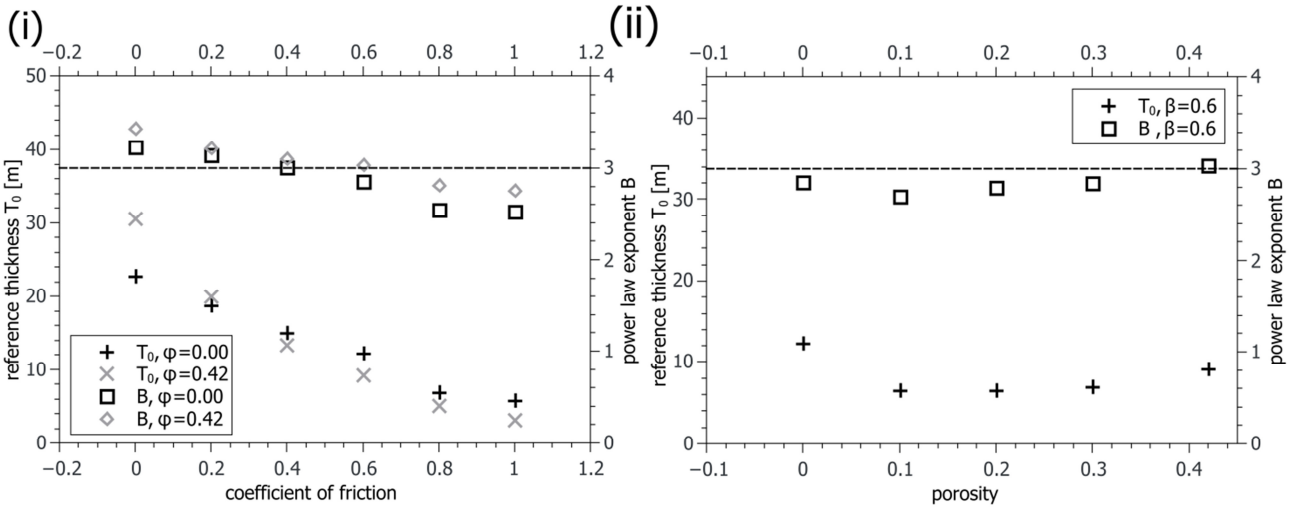

Figure 8-13: Ejecta deposit fitting results. In panel i), fit parameters are shown for different coefficients of friction for nonporous (black symbols) and 42% porous (grey symbols) targets. In panel ii), the same parameters are shown for different target porosities and a coefficient of friction of 0.6. All targets are cohesionless. The black dashed line shows the estimate of B=3 for large lunar craters (McGetchin et al. 1973).

Finally, we also studied different values of material cohesion for nonporous targets. We find that cohesion strongly reduces the amount of ejected material. Increasing the cohesion does not only reduce crater size, it also hinders ejection of lower velocity material by dominating the material strength after the passage of the shock and rarefaction waves (compare Eq. (79)). Accordingly, T_0 decreases. In addition, also B decreases with increasing cohesion.

We also modelled the ejecta thickness as a function of range for the scenario of different impact velocities (Figure 8-14) and a nonporous, cohesionless target with a coefficient of friction of 0.6. In this case, we observe a similar slope for all the ejecta thicknesses of different impact velocities, apart for the slowest case with 1 km/s that shows a somewhat flattened ejecta thickness. For the scenario with 3 km/s impact velocity, the slope is slightly lower than for the faster cases. The ejecta thickness in the proximal range $\left(\frac{x}{R} \leq 3\right)$ is equal for the cases with 6 km/s, 12 km/s and 20 km/s impact velocity. Those three scenarios also agree well in the total amount of ejected material as well as the total crater material (Figure 8-15). We calculated the crater mass based on the volume and the quartzite density of 2650 kg/m³. The slowest case of 1 km/s impact velocity shows a large deviation in both

ejected and crater mass. The ratio of ejected to crater mass is ~0.37 and equal for the four fastest impacts. Only the 1 km/s shows a deviation also in this value (0.25).

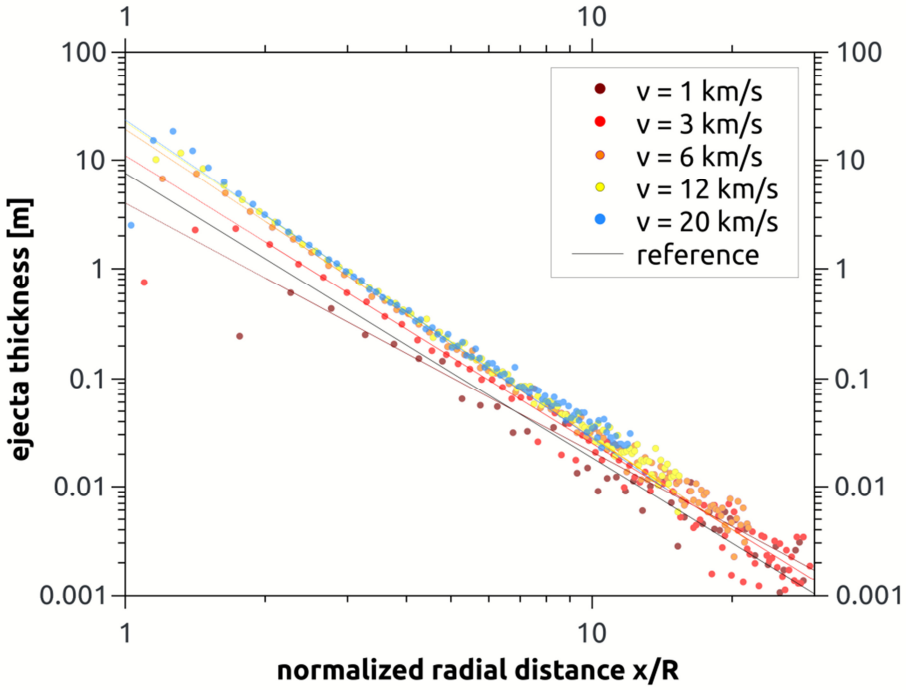

Figure 8-14: Distribution of the ejecta thickness for a nonporous, cohesionless target with different impact velocities. The cases shown refer to the ones in Figure 8-7. The colour-scale corresponds to an increase in impact velocity from dark-red to blue. For comparison with our results, we also show scaling data using Eq. (95) as a reference. We use a constant $K_4 = 0.32$ as given by Housen et al. (1983) and a sand like value of μ=0.41. We use a typical constant value of 45° as ejection angle. As reference crater radius we use the transient radius R=242.5 m of our model with 42% porosity and a coefficient of friction of 0.4. Note that the reference line assumes all ejecta emanates from the crater centre and, thus, is not expected to hold in the vicinity of the crater rim.

For planetary applications it is interesting to see if there is a correlation between impact velocity and the distribution of the ejecta thickness. Again, we fit Eq. (96) to the data shown in Figure 8-14 for impact velocities between 1 – 20 km/s. The fitting parameters T_0 and B are plotted against velocity in Figure 8-16 and are listed in Table A2. The decay exponent of the ejecta thickness varies only slightly for all impact velocities. Only for the lowest impact velocity of 1 km/s we found a somewhat smaller decay exponent, which could be explained by the fact that such a low velocity does not represent hypervelocity-regime anymore. In general, the decay exponent does not allow for a distinction of (especially higher) impact

velocities. Furthermore, no trend towards different thickness T_0 at the rim with increasing velocity can be observed. From 6 km/s to 20 km/s T_0 remains nearly constant. Also the ejected mass is nearly constant for these cases (Figure 8-15) as crater size was kept constant. Neglecting any post-deposition changes, it appears to be impossible to derive information on the projectile velocity by the ejecta thickness. Similar findings for the decay exponent have been shown for simulations of Orientale-sized impacts on the Moon by Zhu et al. (2015) for a projectile with 80 km diameter and impact velocities between 15 and 19 km/s. However, their ejecta thickness at the rim shows a slight increase with increasing impact velocity, i.e. larger coupling parameter (see Eq. (84)).

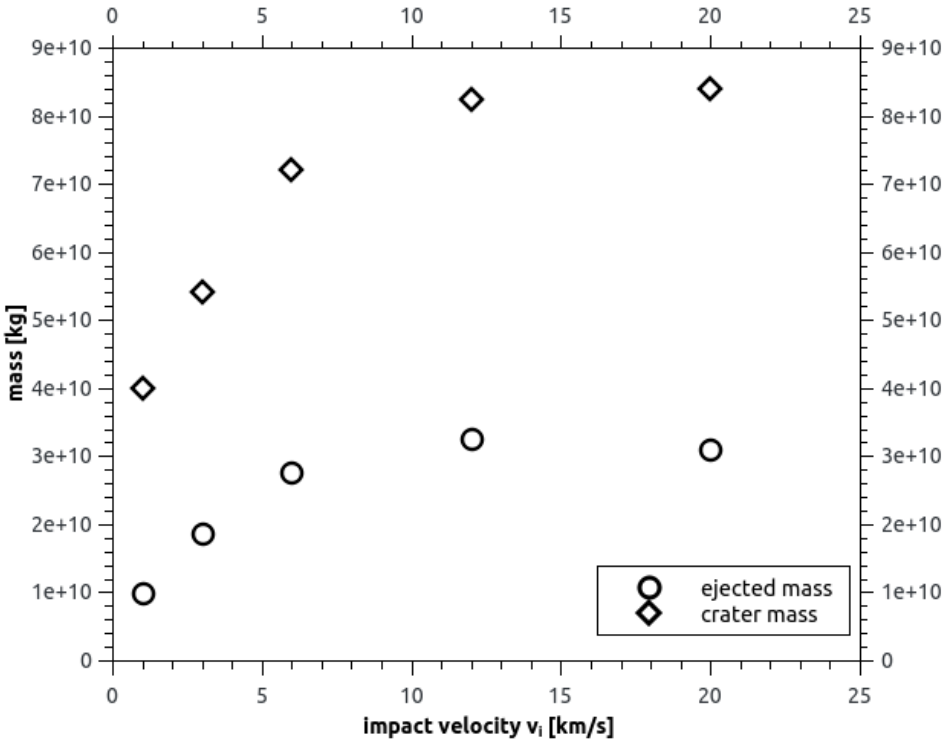

Figure 8-15: Crater and ejected mass for the cases of different impact velocities. For comparison, we considered only ejected masses with a velocity of at least 50 m/s. The ratio of both masses is ~0.37, excluding only the slowest impact with a ratio of 0.25.

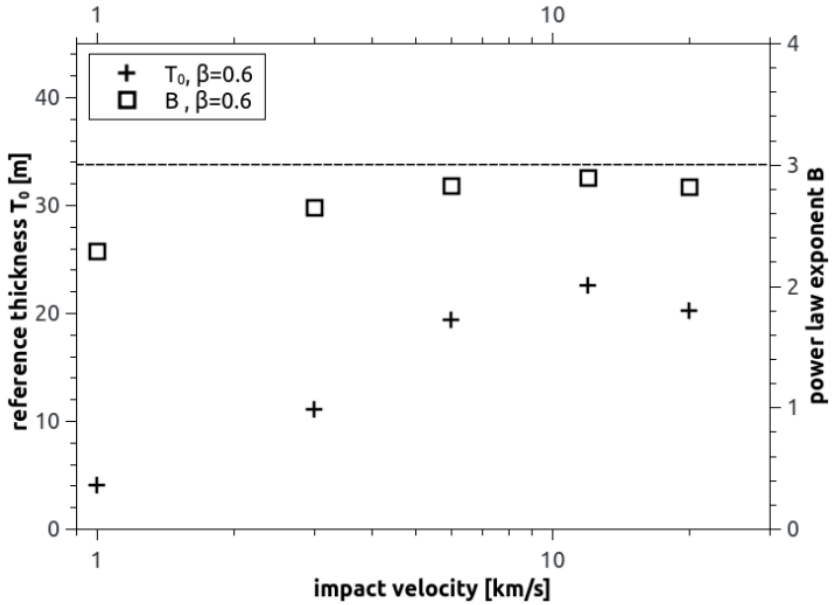

Figure 8-16: Ejecta deposit fitting results. The fit parameters are shown for scenarios with different impact velocity for non-porous targets with a coefficient of friction of 0.6. The target is cohesionless. The black dashed line shows the estimate of B=3 for large lunar craters (McGetchin et al. 1973).

8.7.5 Ejecta deposits at natural impact craters

According to our models the power law decrease of the ejecta thickness with distance, parameterised by the decay exponent B in Eq. (96) only depends on the coefficient of friction and cohesion, and is independent from porosity or impact velocity. From the study of lunar ejecta blankets, McGetchin et al. (1973) determined an exponent B = 3, and we find similar values of B for Earth gravity. Eq. (95) shows that the thickness of the deposited ejecta for gravity dominated craters does not depend on gravity. Hence, ejecta blankets on different planetary bodies have been found to be geometrically similar (Housen et al. 1983; Melosh 1989), and we can compare our results with ejecta blankets on bodies with different gravity.

The assumption that the scaling decay exponent μ depends only on material properties may allow for an inverse approach to determine material properties of the target from a given ejecta distribution. Fassett et al. (2011) determined the ejecta distribution of the Orientale crater and found a decay exponent of 2.8 ± 0.5. According to our models, this average value would correspond to e.g. a coefficient of friction of about 0.6 assuming a low

porosity. Zhu et al. (2015), who use the ejecta distribution as a model constraint, use a similar coefficient of friction for the strength parametrisation of their heavily damaged material (note that they employ a more complex strength model). The ejecta distribution from their best fit model follows a decay exponent of 3.2; a value that we derive using a coefficient of friction of ~ 0.2. However, Zhu et al. (2015) account for thermal weakening of material due to a significant temperature increase with depth for the given scale of the basin structure, which would explain the relative low strength (low coefficient of friction, low cohesion, Table A2) as our study predicts.

On Earth, a comparison is possible to e.g. the Ries crater. Hörz et al. (1983) gave a detailed description on the ejecta blanket (Bunte Breccia) and analyse possible ejection flows. They give a decay exponent between 2.5 and 4, with 3 as a reasonable value. This range, of course, is too large to distinguish between target properties. However, Hörz et al. (1983) state that most of the material in the ejecta blanket originates from shallow target areas and, thus, can show very similar target properties. Assuming that the simplistic approach of a Drucker-Prager yield strength does describe this shallow material, we find an decay exponent of 4 to be unrealistically high based on target properties, as it is an even larger value than for a 42% porous, low coefficient of friction material. Lower values seem more realistic, with B=3 corresponding to a friction between 0.4 and 0.6 for a nonporous, noncohesive target and B=2.5 corresponding to either an even larger friction up to 1.0 or additional cohesion. Note that the range of coefficient of friction from 0.4-0.6 is in excellent agreement with the coefficient of friction for sediments and basement material used by Collins et al. (2008) for modelling the Ries crater. However, a comparison with the Ries crater is difficult and we expect a deviation from our results from the parabolic trajectories due to the presence of an atmosphere. Numerical results for ejection from small craters with the presence of an atmosphere have shown differences in the thickness of deposited ejecta and show a reduced range of the blanket (Shuvalov and Dypvik 2013). Furthermore, different authors (e.g. Hüttner 1969; Oberbeck 1975; Hörz et al. 1983)

demonstrated the importance of the contribution from local material during the ejecta emplacement.

In very small scale, we can compare our results to laboratory data. Stöffler et al. (1975) conducted impact experiments into sand and measured the ejecta distribution thereafter. They find a decay exponent of 3.2. This value corresponds to a coefficient of friction between 0.2 and 0.4 for the given porosity of 42%. Even though Stöffler et al. (1975) did not determine the coefficient of friction of the sand used, 0.4 seems a reasonable value.
Based on the previous discussions, it is possible that detailed measurement of ejecta blankets from observations and laboratory experiments might reveal properties of the target material or even the thermal structure of the target at the time of the impact (cf. Zhu et al. 2017). However, further laboratory and modelling studies on this topic are needed to test this hypothesis including varying thermal profiles and using more complex rheological target setups. There are certainly several limitations of our analysis that may hinder attempts to derive information about the target at the time of impact from ejecta deposits. In addition, the comparisons made so far by this approach do not include modification processes. We do not account for crater modification in the case of complex craters. In this case, modification of the transient crater would cause slumping of material into the crater, resulting in a final crater that is larger than the transient crater (summarised recently e.g. by Krüger et al. 2017). Zhu et al. (2015) show a reduction of the thickness of the ejecta blanket by 5-15% by material sliding within 1.2 transient crater radii. However, we already excluded this range from our fitting results.

In our approach, we also neglected effect of ballistic sedimentation or secondary mass wasting as described by Hörz et al. (1983). Early ejected material is fast and deposited at large radial distance. It will impact the target with an equal large velocity as during ejection, causing secondary cratering and material mixture of local target material and ejecta. Furthermore, radial momentum will cause material sliding. Both effects will change the thickness of the deposited ejecta at a given radial distance, modifying the decay behaviour of the ejecta deposit over distance. These

processes depend on the velocity and mass of the ejecta that re-impacts the target and as such are size-scale depending.

Finally, our assumption of parabolic trajectories neglects effects of the interaction with an atmosphere or impact plume or possible effects of spatially varying gravity for large impact scenarios. To include such effects it is necessary to calculate trajectories within a realistic gravity field that depends on radial distance from the central body, or to model ejecta trajectories in a consistent model set-up including the interaction with the atmosphere. This interaction is size-dependent and can cause sorting of ejecta by its particle size in radial or vertical direction of the ejecta deposit, and causes deviations from the results derived by ballistic parabolas. Hence, deriving information from final ejecta blankets is a challenging task as many processes are involved in their formation, and the required measurement precision of observed ejecta blankets may prove too difficult to achieve for natural craters.

8.8 Conclusion

We performed a suite of numerical impact simulations to investigate the influence of impact velocity and target properties on ejection velocities and angles, as well as the thickness distribution of ejecta deposits. The main conclusions from our simulations are:

1. Our simulations with increasing coefficient of friction (0.0 – 1.0) show a steeper reduction in ejection velocity with launch position, consistent with the formation of smaller craters. Ejection angles also decrease, and show a decreasing spread, with distance. This affects the ejecta deposit thickness as a function of distance: increasing the coefficient of friction leads to smaller thickness at the rim T_0 and smaller decay exponents.
2. Our simulations with increasing porosity (0% – 42%) show a reduction in proximal ejection velocities, consistent with a decrease in peak pressure owing to compaction of target porosity. Ejection

angles remain similar for all porosities. The ejecta thickness is characterised by similar T_0 and decay exponent for all porosities.

3. Our simulations with increasing cohesion (0 MPa – 150 MPa) show that the craters are smaller, but ejection velocities follow the same trend with launch position until the near-rim region where ejection velocities decrease much more steeply than for the simulations with increasing coefficient of friction. The same behaviour holds true for the ejection angle that focus at ~ 45°-50°. The ejecta thickness is characterised by smaller T_0 and decay exponent.
4. Our simulations with increasing impact velocity (but approximately equal crater volumes) show that proximal ejection velocities increase. However, the ejection velocities as a function of distance follow similar trends at large launch positions. Ejection angles increase with impact velocity for our non-porous target. The ejecta thickness is characterised by similar T_0 and decay exponent for all impact velocities in the hypervelocity regime.
5. Scaling exponents μ were derived for all model data. Comparing the results for sand-like material, we see a discrepancy between the μ-value derived from ejecta distributions and from crater size. However, for sand-like material the μ-value that we derive for the ejecta distribution from numerical simulations is consistent with that measured in experiments by Cintala et al. (1999). The static point source assumption should be considered with care when applying scaling relationships for dynamic cratering phenomena, such as ejecta distributions.
6. According to our study, it appears to be possible to derive information on the target material properties based on sufficiently accurate measurements of the ejecta thickness over distance. However, sufficiently accurate measurements are difficult to achieve and modifications processes need to be considered.

8.9 Acknowledgements

This project is part of the MEMIN FOR887 and the SFB-TRR170 funded by the German Research Foundation: DFG-grants # WU 355/6-2 and A4, respectively. M. Z. is partly supported by the Science and Technology Development Fund of Macau (075/2014/A2). We thank J. L. B. Anderson and P. H. Schultz for their very constructive reviews, and Jeff Plescia for editing this article. We gratefully acknowledge the developers of iSALE-2D, including Dirk Elbeshausen, Boris Ivanov and Jay Melosh. We also acknowledge the developer of the pySALEPlot tool (who also implemented the code version of ejecta determination that we used into the iSALE source code) Tom Davison, and the developer of the VIMoD software Dirk Elbeshausen. iSALE –Website: **www.isale-code.de.**

8.10 Appendix

8.10.1 Ejection criterion

In this study we define the time of ejection as the time when ejected material reaches an altitude above the target surface of one projectile diameter. Using this criterion we allow pressure, which occasionally is present within the evolving ejecta curtain, to decrease. At this time, ejection characteristics can still be influenced by pressure gradients. We also avoid including large volumes of material from the rim area in the ejected material. At the same time the criterion is close enough to the surface that the ejecta curtain is well resolved (the curtain is resolved by fewer cells with increasing altitude) and little ejected material is neglected because it does not reach that cut-off altitude. We use a linear interpolation to derive launch positions and launch times of ejecta that correspond to the surface level. This interpolation is necessary to allow for comparison with other numerical or laboratory results. However, it can cause interpolation artefacts that affect ejection speeds and angles at the rim. Linear interpolation fails due to changing trajectory angles of material moving within the transition volume

of ejecta curtain and crater rim, causing a shift of the interpolated launch distance of the ejecta relative to the real launch position.

The altitude of the ejection criterion can influence the results for ejection angles to some extent. In the section "Comparison to experimental data and scaling models" we discuss the issue of determining ejection angles. For increasing altitudes of the criterion, the resulting spread in ejection angles decreases to some extent at smaller launch positions (x/a~<4, Figure 8-17 i). Nevertheless, some spread does remain. The question of whether this decrease in angular spread with increasing altitude improves the accuracy of the results, or whether this behaviour is caused by numerical material transport with poorer resolution of the ejecta curtain in larger altitudes for several model iterations is difficult to answer. However, the mean angle that we derive by using a mass weighted moving average is nearly consistent for all altitudes applied (Figure 8-17 ii). Most of the mass is ejected with this angle. We therefore adopt the mass weighted running average to most robustly characterise the effect of material properties on ejection angles.

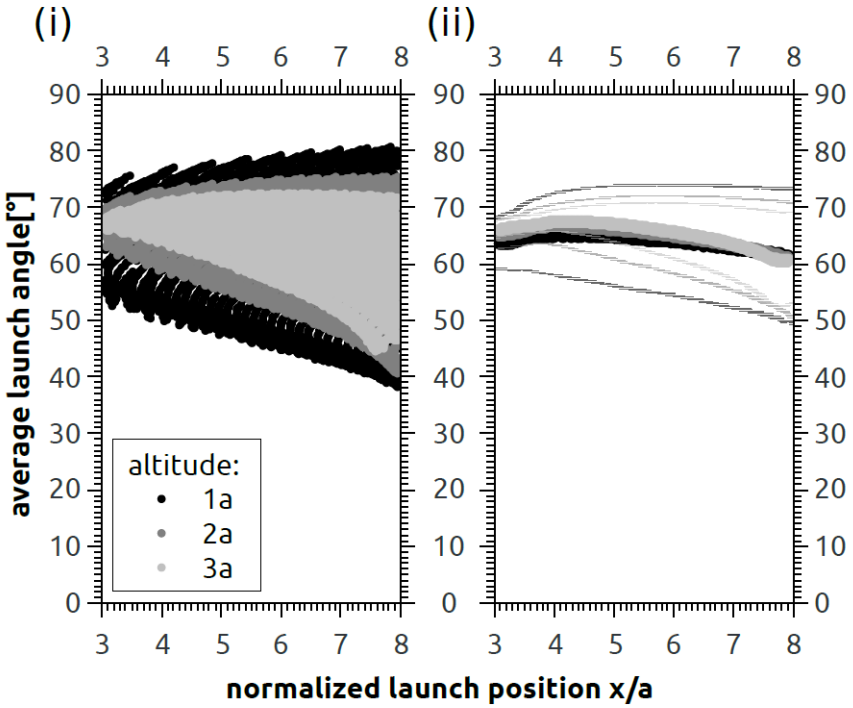

Figure 8-17: Launch angles (i) and mass weighted averages of launch angles (ii) for different ejection criteria. Brightening of the grey scale represents the increasing altitude of the ejection criterion. The average is shown with a mass weighted standard deviation for the data.

8.10.2 Resolution

We tested the sensitivity of ejection results against model resolution using 4 different resolutions between 5 and 20 CPPR for one impact scenario (Figure 8-18). Ejection velocities follow the same trend for all resolutions. However, the largest ejection velocities of the 5 CPPR model deviate from the velocities of the other models. Increasing the resolution from 5 to 20 CPPR shows that maximum ejection velocities seem to converge against a common value. For ejection angles, we see a similar behaviour. Ejection angles overlap for all model resolutions towards the larger launch positions. However, for the proximal range the ejection angle of the 5 CPPR model (~40°) deviates from the converging value of the 20 CPPR model (~50°). Note that increasing the model resolution includes more tracers per volume of the target material and allows for more precise assessment of material movement.

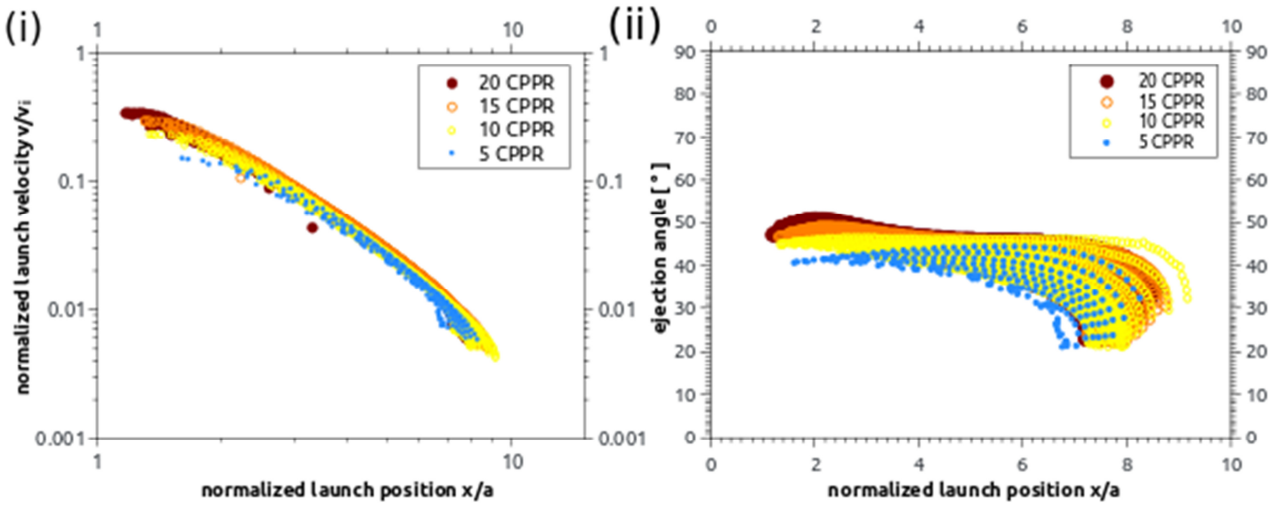

Figure 8-18: Launch velocity (i) and the launch angle (ii) versus launch positions on the target surface. The ejection behaviour is derived for different model resolution for equal impact scenarios. Velocity and launch position are normalised to the impact velocity and the projectile radius, respectively. Note that ejection angles are not averaged. The colour-scale corresponds to an increase in resolution from 5 CPPR to 20 CPPR.

8.10.3 Model Parameters

Table 8-1**:** Model parameters for all 50 models.

General parameters	
Poisson ratio (basalt)	0.3
Specific heat capacity [J/(kg K)]	800
Strength parameters	
Drucker Prager strength:	
Cohesion Y_0 [MPa]	0, 1, 10, 100, 150
Coefficient of friction μ	0.0, 0.2, 0.4, 0.6, 0.8, 1.0
Maximum strength Y_{max} [GPa]	1
Thermal Softening (Ohnaka)	
Softening constant	1.2
Melt temperate [K]**	1327
Simon approximation:	
Simon constant	$6 \cdot 10^9$
Simon exponent	3
Porosity parameters*	
Initial porosity Φ [%]	0, 10, 20, 42
Elastic volumetric threshold ε_e	-0.001
Transition distension α_x	1.1
Compaction efficiency κ	0.9
Speed of sound ratio χ	0.3

* The same porosity model parameters were used for all porosities.

**Typical range of melting temperature for rocky material (Wünnemann et al. 2008).

8.10.4 Unprocessed model launch angles

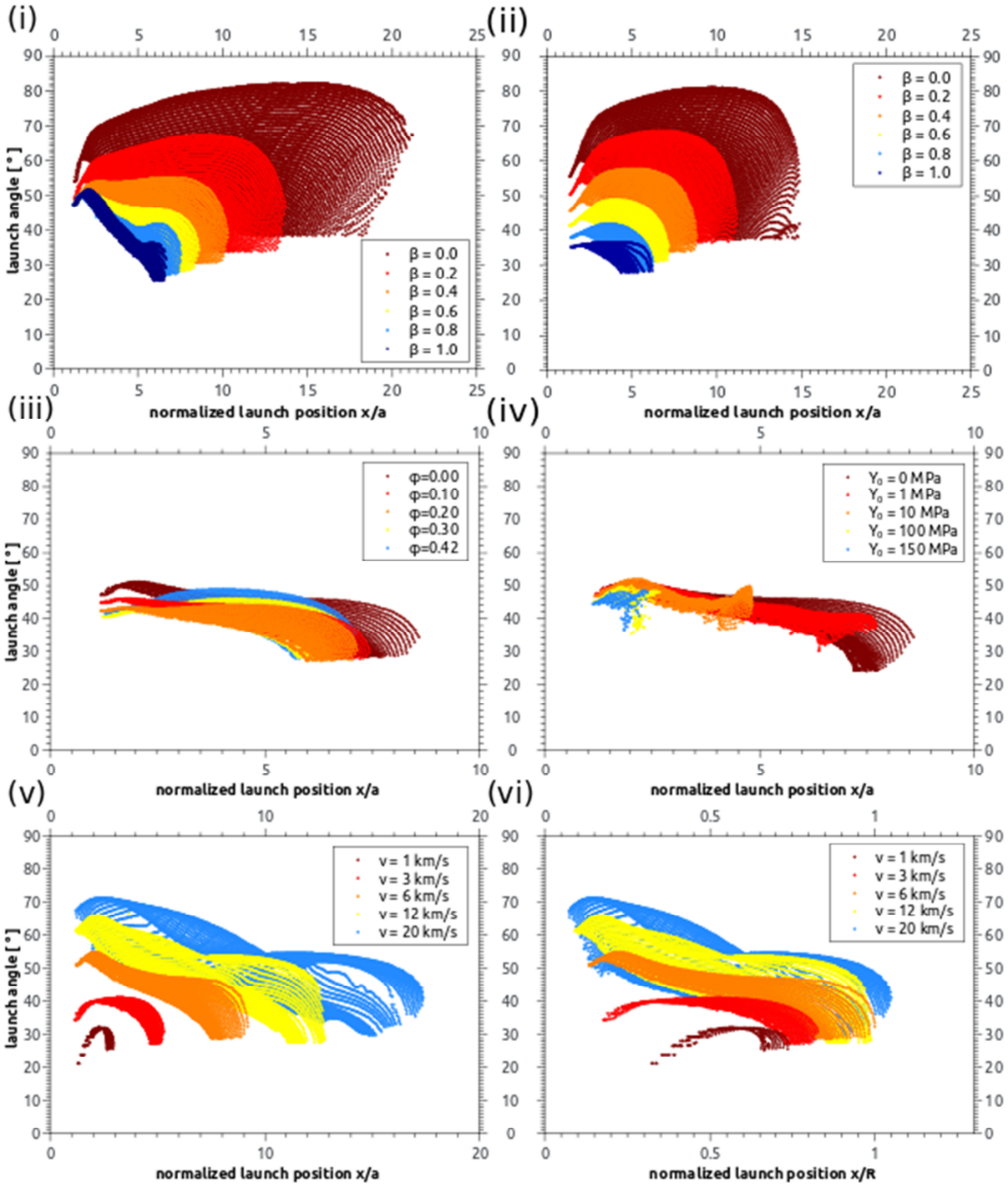

Figure 8-19: Unprocessed model launch angles for all scenarios from this study. (i) cohesionless, unporous target material with coefficients of friction from 0.0-1.0. (ii) cohesionless, porous (42%) target material with coefficients of friction from 0.0 – 1.0. (iii) cohesionless target material with a coefficients of friction of 0.6 and porosities from 0-42%. (iv) non-porous target material with a coefficients of friction of 0.6 and cohesions from 0-150 MPa. (v) and (vi) cohesionless, unporous target material with a coefficient of friction of 0.6 with increasing impact velocity and decreasing projectile size, yielding equal crater volumes, shown in a normalisation for projectile size and crater radius, respectively.

8.10.5 Model Results - Overview

Table 8-2**:** Overview of target materials and dimensionless parameters of the models used in this study and fitting results from Eqs. (93), and (96) & (97).

Cohesion	Coefficient	Porosity	Impact	Projectile	π_2 [10^{-5}]	π_V	Fit data:							
							ejection velocity, Eq. (10)				ejecta deposit, Eqs. (13) & (14)			
[MPa]	of friction β	Φ	velocity [km/s]	radius [m]			x-range x/R	K_3	μ		μ		B	T_0 [m]
0	0.0	0	5	25	3.159	1465.3	0.08 - 0.53	0.43	0.49	<<	0.82		3.23	22.8
0	0.2	0	5	25	3.159	458.9	0.10 - 0.56	0.53	0.49	<<	0.77		3.15	18.8
0	0.4	0	5	25	3.159	234.8	0.11 - 0.68	0.63	0.47	<<	0.67		3.01	15.1
0	0.6	0	5	25	3.159	147.4	0.13 - 0.70	0.77	0.46	<<	0.57		2.85	12.3
0	0.8	0	5	25	3.159	113.7	0.13 - 0.66	0.81	0.46	>>	0.36		2.54	6.9
0	1.0	0	5	25	3.159	99.7	0.14 - 0.64	0.82	0.47	>>	0.35		2.52	5.8
0	0.0	42%	5	25	3.159	754.9	0.10 - 0.54	0.56	0.60	<<	0.96		3.43	30.7
0	0.2	42%	5	25	3.159	335.0	0.12 - 0.55	0.59	0.60	<<	0.81		3.22	20.0
0	0.4	42%	5	25	3.159	190.6	0.13 - 0.51	0.60	0.59	<<	0.74		3.11	13.3
0	0.6	42%	5	25	3.159	128.7	0.20 - 0.53	0.70	0.62	<	0.69		3.04	9.2
0	0.8	42%	5	25	3.159	100.2	0.16 - 0.51	0.62	0.58	~	0.55		2.82	5.1
0	1.0	42%	5	25	3.159	85.8	0.16 - 0.48	0.55	0.57	>	0.51		2.76	3.1
0	0.6	10%	5	25	3.159	175.1	0.13 – 0.60	0.66	0.47	=	0.47		2.71	6.5
0	0.6	20%	5	25	3.159	157.5	0.13 - 0.56	0.62	0.49	~	0.53		2.80	6.6
0	0.6	30%	5	25	3.159	143.5	0.14 - 0.54	0.61	0.52	~	0.56		2.84	7.0
1	0.6	0	5	25	3.159	105.6	0.16 - 0.75	0.97	0.40	>>	0.22		2.33	7.4
10	0.6	0	5	25	3.159	42.8	0.23 – 0.95	2.75	0.42		-*		1.21	0.3
100	0.6	0	5	25	3.159	12.9	0.34 – 0.81	9.46	0.53		-		-	-
150	0.6	0	5	25	3.159	10.6	0.37 – 0.79	13.07	0.62		-		-	-
0	0.6	0	1	75	235.670	8.7	0.32 - 0.74	0.59	0.32	>>	0.19		2.29	4.0
0	0.6	0	3	46	16.148	50.1	0.25 - 0.70	0.76	0.43	=	0.43		2.65	11.1
0	0.6	0	6	34	2.976	166.5	0.25 - 0.73	0.85	0.48	<	0.55		2.83	19.4
0	0.6	0	12	25	0.548	474.8	0.25 - 0.69	0.86	0.52	<	0.59		2.89	22.6
0	0.6	0	20	20	0.158	949.5	0.25 - 0.70	0.86	0.52	~	0.55		2.82	20.2

* Value would be negative and is excluded. The scenario is strength dominated.

9 The Effect of Atmospheric Interaction on Impact Ejecta Dynamics and Deposition

This chapter has been published as the following peer-reviewed article:

Robert Luther, Natasha A. Artemieva, Kai Wünnemann (2019). *The Effect of Atmospheric Interaction on Impact Ejecta Dynamics and Deposition*. ICARUS 333, 71-86, https://doi.org/10.1016/j.icarus.2019.05.007.

In the previous chapter, I discussed the excavation process and the ejection behaviour for different target properties. However, some planetary bodies like Venus, Mars, Titan, or Earth possess a significant amount of atmosphere, which cannot be neglected in crater simulations. Ejecta blankets will deviate from crater deposits in a vacuum as a fraction of the ejected dust will not be deposited on parabolic trajectories. Instead, these grains will be subject to atmospheric turbulence and wind patterns, causing a separation of ejecta depending on its size (vertically and horizontally). The interaction of ejecta with an atmosphere is the topic of the following chapter.

My work in this chapter, which answers my objective *M III – Representative Particles* and my key question *S II – Ejecta and Atmosphere*, included implementing the representative particle approach, which is also used in the SOVA code (Shuvalov 1999), into iSALE. Natasha Artemieva supported me with fruitful discussions and her important advice and experience in programming the necessary new routines, and in writing this chapter. The coding of these routines required intensive testing for each step of improvement: the testing started with separate routines to calculate the interaction, then it involved coupling these routines into the iSALE main routines, and finally finished with setting up the different model scenarios (scaling relationship input, or direct modelling input). Apart from programming the routines, several analysis routines are required to read the data, which I also programmed.

9.1 Abstract

Fine dust from impact ejecta settles slowly in an atmosphere, whereas large chunks of ejecta easily traverse the surrounding gas on nearly parabolic trajectories. In order to study the effects of the interaction of impact ejecta with an atmosphere, we implemented a "representative particle" approach into the iSALE-2D shock physics code. We verify the modelling approach using analytical equilibrium sedimentation velocities, and successfully benchmark the results against simulations with the shock physics code SOVA. We study vertical dust settling scenarios of different initial mass and dust size (100 μm – 10 cm), and find three different regimes of settling – sedimentation, formation of density currents, and the free-fall. Based on this, we model ejecta curtains for craters from 200 m – 4 km in radius, and in the laboratory for different atmospheric pressure from 1 kPa – 6 MPa. We assess the range of ballistic ejecta deposition within an atmosphere in terms of ejecta thickness and deposition velocity.

9.2 Introduction

Upon impact of cosmic bodies on planetary surfaces material is ejected during crater excavation. Under vacuum conditions (or at low atmospheric pressure), ejected solid and molten fragments move along ballistic trajectories and form an ejecta curtain as observed in laboratory experiments, numerical models, and in nature (e.g. Gault 1973; Oberbeck 1975; Stöffler et al. 1975; Wünnemann et al. 2016). In addition, the impact- and shock-wave induced vaporisation of matter creates a hemisphere of hot gases above a target plane that approximately expands isotropically (Melosh 1989, p. 211). As a consequence, the material that is expelled during crater excavation is composed of a mixture of solid and molten particles with vapour. For this reason, or if additionally an atmosphere is present, the trajectories of some material may be affected by gas-particle interaction such that its final resting place may significantly deviate from purely ballistic estimates. Table 9-1 summarises a variety of impact conditions in the Solar System where ejecta deposits could be substantially influenced by ejecta interaction with the atmosphere or vapour.

Table 9-1: Impacts and Planetary & Lunar atmospheres.

	Atmospheric/ Earth pressure	**Surface density [kg/m³]**	**Target volatiles**	**Typical projectile type and velocity**	**Non-ballistic ejecta deposits**
Venus	92	67	No	Asteroid, ~20 km/s	Parabolas, melt flows
Earth	1	1.3	Various	Asteroid, 20 km/s	Double ejecta layers
Mars	0.006	0.02	Rich	Asteroid, 7-10 km/s	Double ejecta layers, ramparts
Titan	1.47	5.7	Various	Comet, ~15 km/s	Parabolas

Macroscopic observations of terrestrial ejecta layers are rare because of their pure preservation whereas microscopic observations (particles' structure, chemical composition, etc.) are quite common (Hörz et al. 1989; Hamann et al. 2013; Fazio et al. 2016). The situation is opposite on other planets: numerous macroscopic observations (asymmetric ejecta and parabolas on Venus and Titan, or double ejecta layers on Mars; e.g. Vervack et al. 1992; Barlow 1994; Wood et al. 2010) allow us to speculate about planet's subsurface and its past whereas chemical and petrological analysis of samples are still restricted to returned lunar samples, lunar and Martian

meteorites, and first in situ analysis of Martial soils (e.g. Wänke et al. 2001; Fernandes et al. 2013; Borg et al. 2016; Snape et al. 2018).

In general, modelling the formation of ejecta during a high-velocity impact is approached in terms of four successive (albeit overlapping) stages:

1. Compression of the projectile and the target with formation of early ejecta (called sometimes 'jetting') and an impact plume;
2. Excavation and formation of an ejecta curtain;
3. Propagation of two types:
    a. Ballistic flight on airless planets (the single active force being gravity), and/or
    b. Non-ballistic flight via interactions between the plume, the ejecta curtain, and the atmosphere;
4. Deposition via two modes:
    a. Ballistic sedimentation (involving secondary cratering ground-hugging flows) and/or
    b. Re-entry into the atmosphere (involving re-heating, deceleration, slower sedimentation)

Stages 1 and 2 are closely connected to crater-forming models as they require a proper treatment of strong shock waves, equations of state (EOSs) of the involved materials in a wide range of pressures and temperatures, and proper constitutive models (e.g. Collins et al. 2013). Stages 3 and 4 (except for a purely ballistic flight) require a different approach, the so-called two- (or multi-) phase hydrodynamics.

In the standard two-phase hydrodynamics method (Harlow and Amsden 1975; Valentine and Wohletz 1989), the two 'phases' (one representing the particles, the other the surrounding gas or liquid) traveling at different speeds are treated as fluids with separate equations of state. The governing equations include additional terms for describing the interphase exchange of heat, mass (via evaporation/condensation), and momentum (via drag). Multi-phase models also exist that can account for several phases and hence a suite of particle sizes (e.g. Neri et al. 2003). The original two-phase code KFIX (Rivard and Torrey 1978) was modified by Goldin and Melosh (2008, 2009) to model impact ejecta, but as it allows only the treatment of

two phases it is restricted to a single ejecta particle size (one phase represents the gas the other the ejecta with uniform properties).

An alternative multiphase approach is the so-called “dusty flow” approach (Boothroyd 1971). This method was implemented into the SOVA code by Shuvalov (1999) for impact applications. On the one hand, the dusty flow model easily allows treating particles of various sizes, which is a more realistic approximation of the particulate ejecta. On the other hand, direct particle-particle collisions are not considered (this assumption is correct, if the dust/gas volume ratio is <0.1, Artemieva et al. 2013). As it is numerically impossible to track each individual ejected dust particle in a model, so-called representative particle (RP) are introduced in the dusty flow model. Each RP usually describes the movement of 10^4-10^6 real particles, all of which have the same size, velocity and trajectory. Each RP is subject to gravity, drag, and, optionally, to heat exchange with surrounding gas. The equations of motion describing such conditions are solved simultaneously and explicitly for all particles within one computational cell allowing for the “collective” behaviour of the particles to be accounted for.

The “dusty-flow” approach can be implemented into any standard shock physics code as an additional routine keeping the code structure. In this paper we use a similar implementation of this approach into the iSALE code as described by Shuvalov (1999) and test its performance using simple sets of initial conditions.

In a first set of models, we analyse the behaviour of dust to grains sized RP (100 μm – 10 cm) that settle vertically in an atmosphere, in order to find out about different regimes of settling. Therefore, we also change the initial mass of the RP layer in air. We expect equilibrium settling for small masses, and a free fall approximation for large initial masses. However, the outer limits of the range of this obvious behaviour are not clear. Furthermore, the behaviour will change according to the initial velocity of the RP – and ejected particles from a crater exhibit a significant velocity of 100s of m/s to some km/s. Based on the understanding of such settling regimes, we model the behaviour of a complete ejecta curtain and derive the

radial range where material is deposited approximately undisturbed as ballistic ejecta.

9.3 Methods and Useful Analytical Solutions

We use the iSALE and SOVA shock physics codes in this paper. The basic concepts of these codes can be found in Supplementary Material and in previously published papers (Amsden et al. 1980; Shuvalov 1999; Collins et al. 2004; Wünnemann et al. 2006). The description of the "dusty flow" approach as implemented in SOVA is given by Shuvalov (1999). The implementation into iSALE is similar to the SOVA implementation and is given by Luther (2019)[7]. We use an atmosphere in litostatic equilibrium (barometric formula) and the ideal gas equation of state in all iSALE models (specific heat ratio γ =1.4) whereas in SOVA runs we use the CIRA atmospheric stratification and more realistic EOS (Kuznetsov 1965). The difference between two EOSs is minor as we do not have extremely hot or rarefied gases in our simulations. All models were run in 2D with a cylindrical symmetry, restricting the simulations to vertical impacts. As we do not model crater formation, we use rather coarse resolution in all runs. The model set-up in terms of resolution and number of cells is chosen to exclude reflections of shock waves from the mesh boundaries. Details on the models are stated in the Appendix. In the supplementary material, we also study an influence of RP resolution on our results (number of real particles in one RP) in addition to the standard spatial resolution problem. Our resolution test showed that increasing the number of representative particles affects only slightly the average behaviour of the dust, but widens the range of observed values (like e.g. maximum and minimum velocities).

In any impact process, ejecta are characterized by a specific size-frequency distribution (SFD) of ejected fragments, which depends on many factors (ejection velocity, physical state, maximum strain rate, etc.) and may

[7] This reference refers to this thesis, chapter 4.3.

vary in a wide range. For simplicity, in most runs presented in this paper, all fragments have the same size, except when stated differently.

9.3.1 Analytical solutions

9.3.1.1 Sedimentation and free fall

The free-fall velocity v_{ff} of any object falling from an altitude s with initial velocity v_0 is defined by the equation:

$$v_{ff} = \sqrt{{v_0}^2 + 2sg} \quad , \qquad (99)$$

where g is gravity. The equation reduces to the simple expression of $v_{ff} = \sqrt{2\ s\ g}$ when particles are initially at rest. If a particle falls within an atmosphere, it is decelerated by the drag forces and accelerated by gravity. In the iSALE and SOVA routines describing gas/particle interaction we use two components of drag:

$$F_D = 6\pi\ r\ \eta\left(\vec{\boldsymbol{v}}_g - \vec{\boldsymbol{v}}_{\boldsymbol{d}}\right) + C_D\pi\ r^2\rho_g\left|\vec{\boldsymbol{v}}_g - \vec{\boldsymbol{v}}_{\boldsymbol{d}}\right|\left(\vec{\boldsymbol{v}}_g - \vec{\boldsymbol{v}}_{\boldsymbol{d}}\right) \quad , \qquad (100)$$

with the first term being the Stoke's drag typical for laminar low-velocity flows and the second term a high velocity drag typical for turbulent high-velocity flows (v_g is the gas velocity and v_d the velocity of the dust, r is a particle radius, ρ_d is the density of the dust grain, ρ_g is the atmospheric density, η is gas viscosity, and C_D is a high-velocity drag coefficient). An equilibrium (i.e, drag forces are equal the gravitation force) sedimentation velocity v_{sed} can be written as:

$$v_{sed} = -\frac{3\eta}{C_D\ r\rho_g} + \sqrt{\left(\frac{3\eta}{C_D\ r\rho_g}\right)^2 + \frac{4\ r\rho_d\ g}{3C_D\ \rho_g}} \quad . \qquad (101)$$

In this study, we assume spherical particles (C_D=0.5), a viscosity of 17.1 10^{-6} Pa s and a particle density of 2650 kg/m³. In many studies a unified drag coefficient C_D' is used so that the drag force could be written as $F_D = C_D' \rho_a v^2 \pi r^2$. It is easy to show that C_D' is a function of μ and C_D. Studies on the drag coefficient have been conducted since long ago and are, not surprisingly, of military interest (see e.g. Korschelt et al. 1913, p. 560), but also of highest interest for space vehicle returns (Muylaert and Berry 1998). Melosh and Goldin (2008) presented a complex behaviour of C_D' for a wide range of Reynold (*Re*) and Mach (*M*) numbers. Our approach in Eq. (101) may deviate from C_D' in some transitional regimes, but gives a reasonable representation of the drag forces in both, high *Re* and *M* regimes and low *Re* and *M*, regimes.

9.3.1.2 Scaling of ejecta

In this paper we use scaling laws (Housen et al. 1983; Holsapple 1993) to estimate the initial (near the surface) ejection conditions in our tests. Recent discussion on values of scaling parameters can be found in the literature (**Raducan et al. (submitted)**; Housen and Holsapple 2011, 2012; Tsujido et al. 2015; Prieur et al. 2017; Yamamoto et al. 2017; Luther et al. 2018). Ejection velocities v_{ej} as function of radial distance x are described as:

$$\frac{v_{ej}}{\sqrt{gR}} = K_1 \left(\frac{x}{R}\right)^{-\frac{1}{\mu}} , \qquad (102)$$

with the constant K_1, crater radius R, and fitting parameter μ. The cumulative ejected mass m_{ej} as a function of ejection velocity can be derived by:

$$\frac{m_{ej}(v_{ej})}{\rho R^3} = K_2 \left(\frac{v_{ej}}{\sqrt{gR}}\right)^{-3\mu} , \qquad (103)$$

with the constant K_2, and crater density ρ.

The timing of ejection is inferred from the velocity derived by Eq. (93) and the ejection angle. The horizontal velocity component v_h yields the time when crater growth (i.e., material ejection) reaches the ejection distance x_{ej}:

$$x_{ej}(t) = \int_0^t v_h(t')\, dt' \quad . \tag{104}$$

The vertical velocity component v_v is used to derive the ejected mass at a given position during each time step

$$dm_{ej}(x) = A\, v_v(x)\, \rho_d\, dt, \tag{105}$$

where A is the surface area segment from where the mass dm_{ej} is ejected in the time dt.

In the dusty flow approach, direct inter-particle collisions are neglected (particles interact indirectly through gaseous medium). Although particles are produced close to each other initially (the density of the particles in the flow is only slightly smaller than solid body density), they all move in the same direction as defined by the ejection conditions above. Hence, inter-particle collisions are of minor importance.

9.4 Verification, Validation, and Benchmarks

9.4.1 Sedimentation of individual particles in undisturbed atmosphere.

This simple problem allows us, first, to validate our mathematical model (Eqs. (47) or (100)), and, second, to verify the code performance. We set up a simple scenario to calculate sedimentation of individual dust particles from an initial altitude of ~5 km; particles are initially at rest or have a vertical velocity of 1 km/s. Particle radii vary from 1 mm to 1 m.

Each representative particle contains exactly one dust particle, and the mass of each representative particle is much smaller than the mass of the gas in the corresponding cell. A few representative particles are located with large distances between each other to study their individual behaviour. In Figure 9-1 we show vertical velocities of particles versus altitude. Black lines show the analytical equilibrium solution derived from Eq. (101). Particles of all sizes except of the largest ones reach their equilibrium sedimentation velocity (Eq. (101)); however, smallest particles reach this equilibrium much faster than large ones (Figure 9-1). Vertical velocities of particles initially at rest also converge quickly with the analytical solutions.

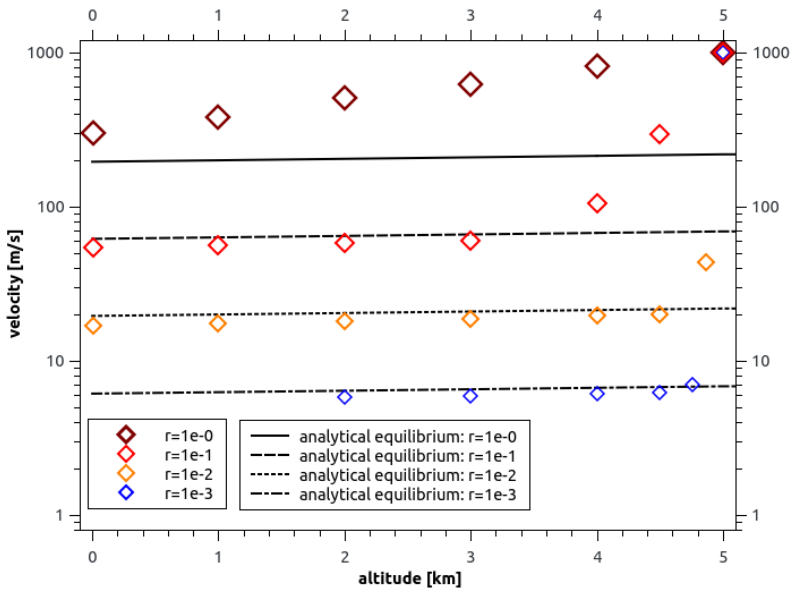

Figure 9-1: Sedimentation velocities for particles of different sizes as a function of altitude. The modelling results have been generated with iSALE and are shown in colour. The analytical equilibrium solutions are indicated by black lines. All particles start at the initial altitude of 5 km. The relaxation length for reaching the sedimentation velocity is estimated to be 7.1 km, 1.47 km and 0.4 km for particles with a radius of 1m, 10 cm, and 1 cm, respectively (yielding ratios of relaxation length to radius of the order of ~10000). Note that the time evolution is from the right side (high altitude, large velocity) to the left side (low altitude).

9.4.2 Settling of dust-laden layers

In this section, we study the settling of dusty layers with various initial properties (particle size, particle concentration, total mass of dust per unit area) in Earth's atmosphere. We evaluate the behaviour of layers with

the total mass per unit area from 2.65 kg/m² to 26500 kg/m² which would correspond to a final deposition thickness of dust on the surface, *h,* from 1 mm to 10 m, consisting of particles with radius from 100 µm to 1 m. We use a similar initial setup as in the previous section and particles are initially at rest or have an initial vertical velocity of 1 km/s. Representative particles (1 – 100 particles per cell) are distributed over a radius of 5 km to simulate a dusty layer. Within 20 seconds density currents are formed and the layer settles faster than individual 1-cm-radius particles (Figure 9-2).

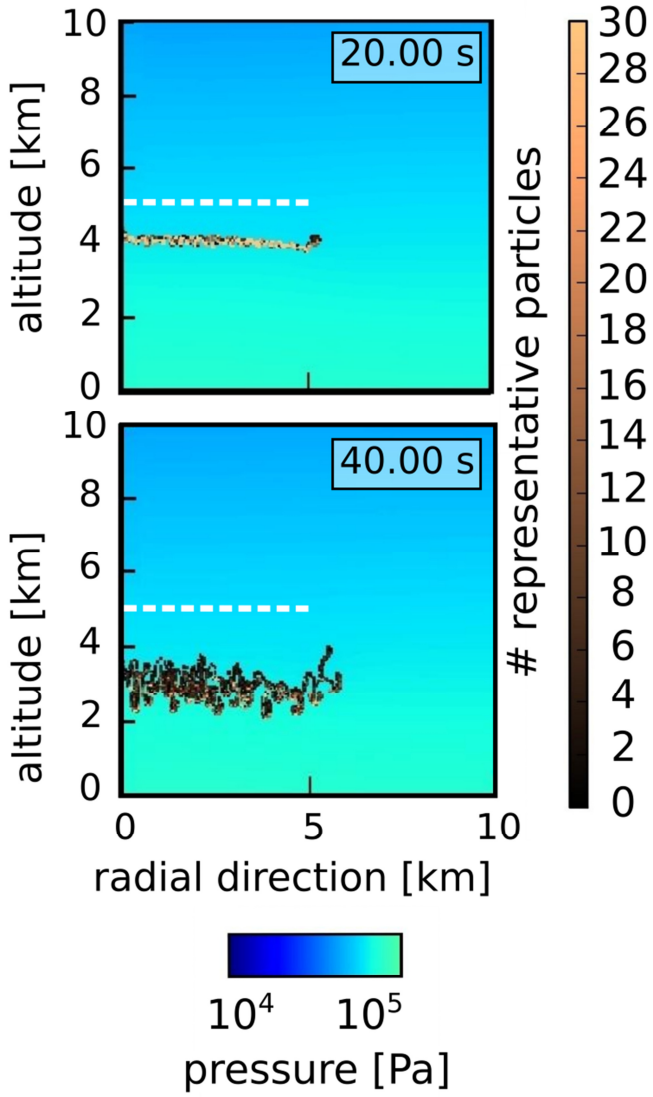

Figure 9-2: Model (iSALE) snapshots showing settling of a dusty layer in atmosphere. The layer consists of 1-cm-radius particles and its mass is equivalent to a 10-cm-thick deposit on the surface. All RP are distributed evenly in one cell at an altitude of 5 km and are at rest (white dashed lines show initial position of the layer). In this specific case, changes of pressure amplitudes are small and shock waves do not form.

Figure 9-3 shows particles' and gas velocities for a similar dusty layer descending with an initial velocity of 1 km/s. In this case shock waves are formed in the atmosphere, reach the surface, and while moving upward, interact with dust (peaks in velocities at an altitude of 2.5-3 km). In the Figure we compare modelling results of iSALE with SOVA simulations (Figure 9-3). Both modelling results agree and show: a) quick deceleration of particles during the first 2 km (deviation between two codes in velocities is up to~ 100 m/s); b) upward motion of the layer due to the arrival of the shock wave; c) slow motion near the surface with velocities of 38 m/s (iSALE) and 35 m/s (SOVA) and as such close to the sedimentation velocity of 23 m/s in equilibrium atmosphere according to Eq. (101), or matching sedimentation velocity for a reduced atmosphere of ρ_g=0.5 kg/m³.

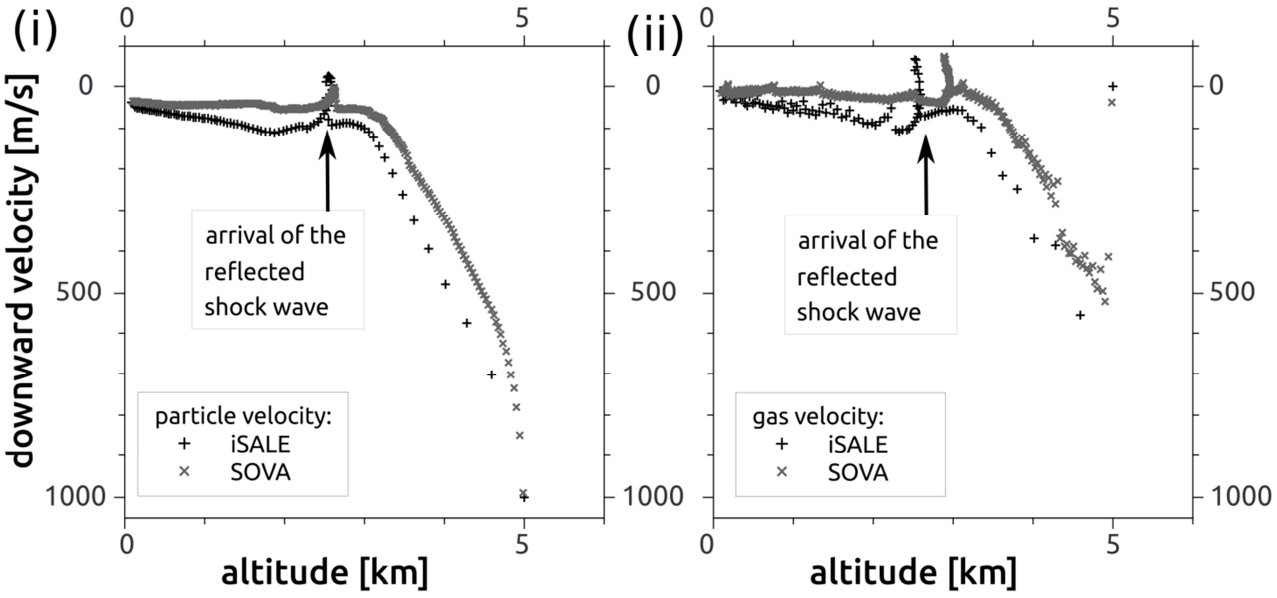

Figure 9-3: Deceleration of an individual particle (i) and surrounding gas velocity (ii). Absolute velocities are shown versus the particle position (altitude) for the same scenario modelled with iSALE (black +) and SOVA (grey x), (r_{dust} = 1 cm, h = 0.1 m). The initial downward velocity of the particle at 5 km altitude is 1 km/s, and the gas is at rest. The peaks in velocity at ~ 2.5 – 3 km altitude (arrows) are due to the arrival of the shock wave reflected from the ground.

9.4.2.1 Different Regimes of Settling

We analysed model setups for various combinations of particle size, initial mass distribution, and initial velocity. For each model, we track the trajectory of each representative particle. Representative particles that reach the lowermost cells are considered as deposited and are deleted from the model. In general, heavy dusty layers quickly penetrate through the atmosphere whereas thin layers settle with an equilibrium sedimentation velocity (Eq. (101)).

To analyse settling of dusty layers for various values of the total mass and various particle sizes, we plot horizontal velocities normalised to the total particle velocity versus the vertical velocity normalised to the sedimentation velocity (Figure 9-4).

Thin dust layers (h = 0.001 m) settle with approximately sedimentation velocity for all particle sizes tested and show fewer turbulences (small horizontal velocity component). Horizontal velocities are smaller for the larger particle size (~0.1 for particles with r_{dust} = 1 mm). This behaviour holds true for particles initially at rest and particles initially moving with velocities larger than the free fall velocity.

An increase of dusty layer thickness up to h = 0.1 m causes a shift to more turbulent behaviour. Horizontal velocities increase up to ~ 0.7, and particles settle with a velocity larger than the equilibrium sedimentation. In the model this can be seen by the formation of particle vortices and density currents. The increase in horizontal velocity depends on the particle size and is most enhanced for the smallest particles (~0.7 for particles with r_{dust} = 100 μm) compared to larger ones (~0.4 for particles with r_{dust} = 0.1 m). In models with high initial velocity shock waves are generated causing an additional increase of the horizontal velocity component.

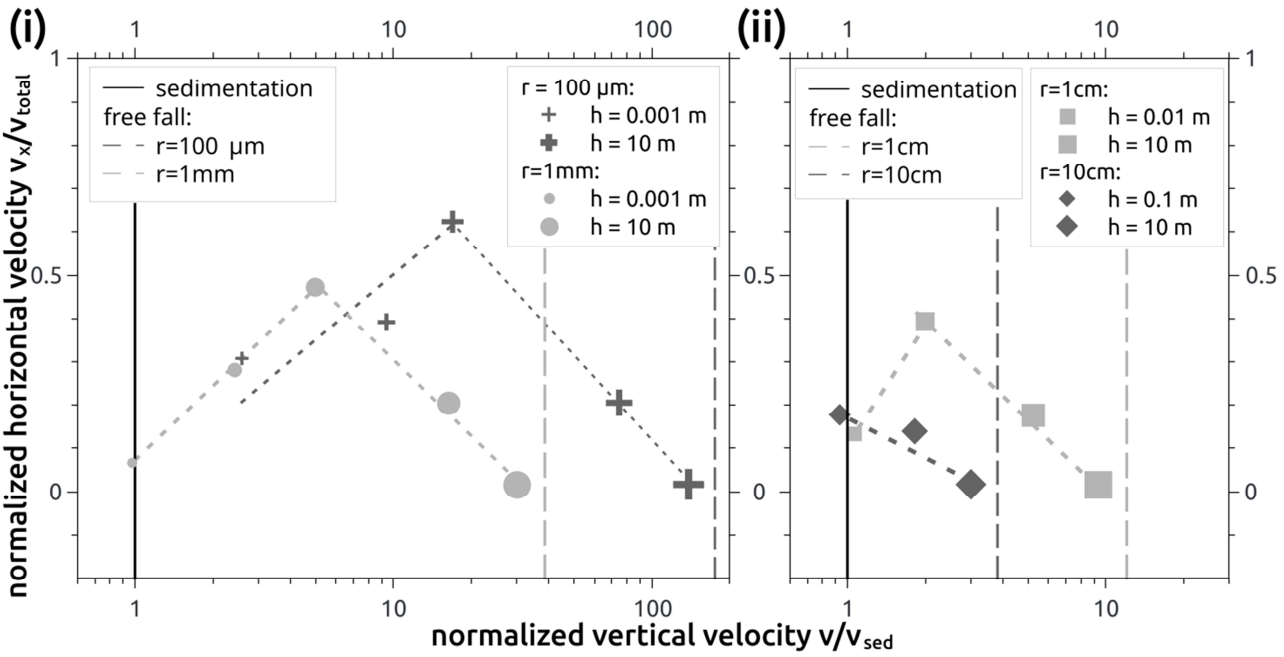

Figure 9-4: Normalised horizontal velocities versus normalized vertical velocities of particle: i) r_{dust} = 100 µm & r_{dust} = 1 mm; ii) r_{dust} = 1 cm & r_{dust} = 10 cm (determined with iSALE). Symbol type shows the particle size (see legend) whereas the symbol size increases with increasing layer thickness (minimal and maximal thicknesses area shown in the legend; thicknesses increase by a factor of 10). The dashed lines show normalised free fall velocities. The black solid line shows the normalised sedimentation velocity (=1). Dotted lines represent the velocity trend for increasing blanket thicknesses.

Even thicker dust layers (h > 0.1 m) represent the third regime of settling. For these layers, horizontal velocities are small compared to the total velocity and the settling velocity approaches the free fall limit (for the largest dust layer thickness of h = 10 m) regardless of the particle size. In scenarios with an initial downward velocity of 1 km/s particles are deposited at velocities higher than the free fall velocity.

In summary, we may distinguish three regimes of dust settling depending mainly on the layer thickness: sedimentation, turbulent regime, and free fall (Figure 9-5). Particles size plays a minor role, shifting boundaries between these regimes.

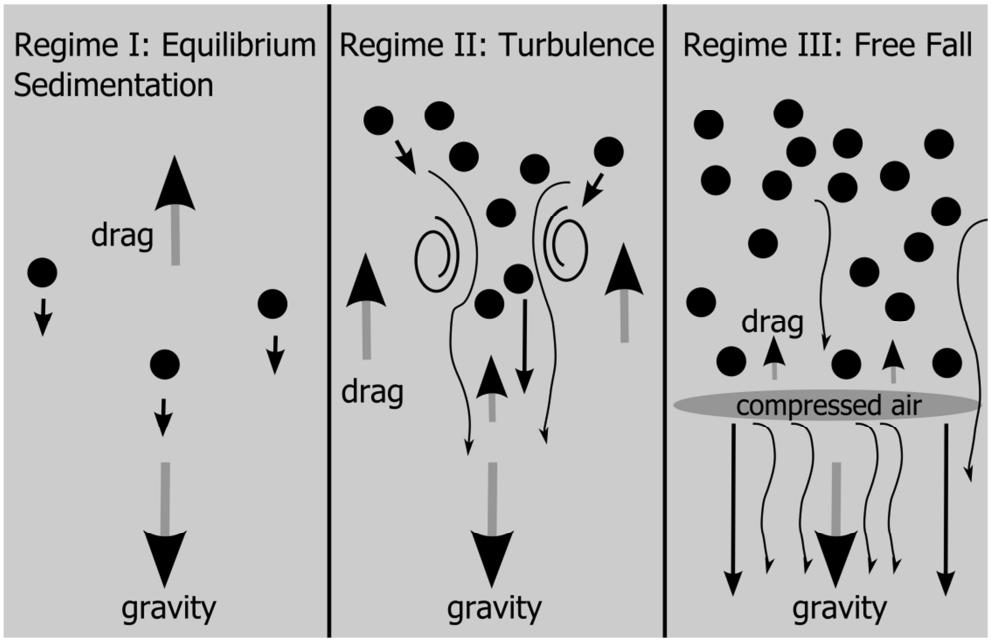

Figure 9-5: Three Regimes of settling. Regime I: gravity and drag are in equilibrium and particles settle with a constant velocity (black arrow). Regime II: The mass of dust is too large to allow for individual settling. Density currents form because dust momentum is transferred onto the gas (thin arrows indicate gas movement). The dust aligns, minimising the drag forces. Regime III: The mass of the dust is big enough to set the gas into motion and to compact gas in front of the dust. Drag forces are small.

We consider material as deposited when it enters the bottom two cells of the grid. Figure 9-6 shows the thickness and the extent of deposited layers. Note, that particles can be pushed upwards by a reflected shock wave only if they have not entered the bottom two cells above the ground. Material that is still in the air at the end of the simulation is interpolated to the ground vertically to reduce computational costs (in most cases, only a few representative particles are still in motion at the end of simulations). For all grain sizes ranging from r_{dust} = 100 µm – 0.1 m, we find similar material deposition patterns if particles are initially at rest (Figure 9-6, left panel). Dusty layers with final thickness between h = 0.001 m and 0.01 m are deposited close to their original location and the radial range of 5 km is exceeded by 1 km at maximum. Deposition thicknesses scatter around the initial value of h (Figure 9-6 i). Some mass concentration with neighbouring mass depletion can be caused by the formation of density currents. This behaviour is more pronounced for larger thicknesses of h = 0.1 m. Furthermore, material is transported to larger radial distances (up to ~ 8

km). An even thicker dusty layer (h = 1 m) causes significant lateral movement (>12 km for r_{dust} < 0.1m), producing spiralling vertices. The largest initial dust layer thickness of h = 10 m is mostly deposited in the proximal range of 5 km. Nevertheless, also at larger distances some material is observed that has been re-ejected due to atmosphere compression near the surface and finally settles nearly vertically. Metre-sized rocks are deposited only within the proximal range of 5 km regardless of the initial dust layer thickness. Deposition patterns for particles with an initial velocity of 1 km/s are similar to the presented scenarios but lateral spreading is more pronounced (Figure 9-6, right panel).

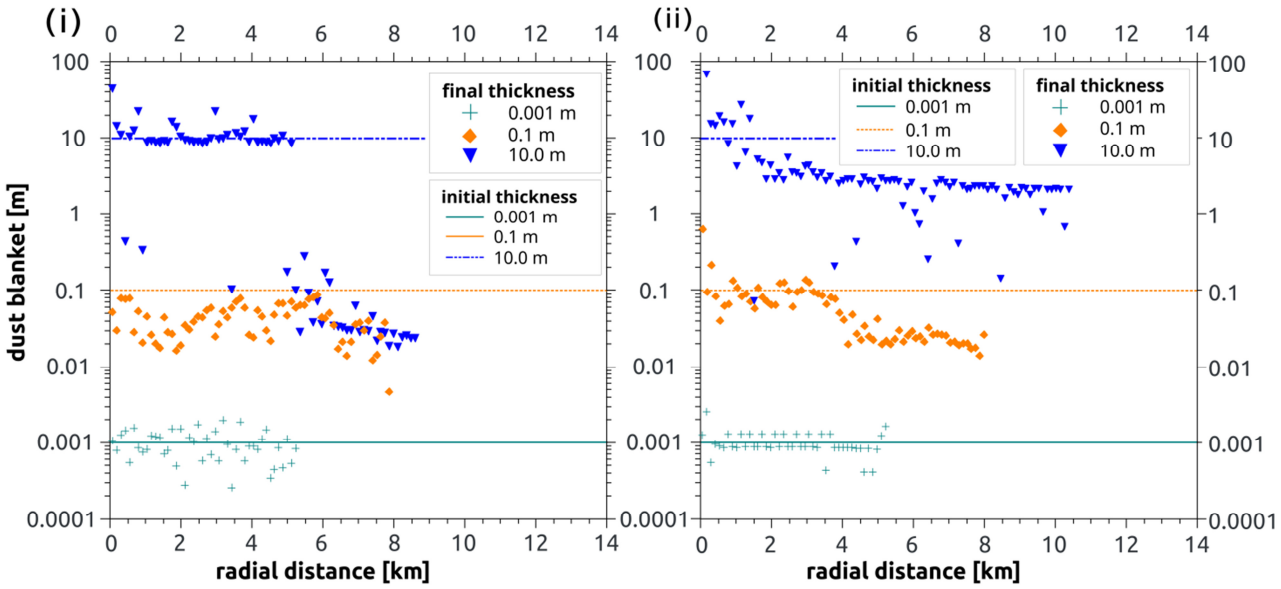

Figure 9-6: Deposition thickness (determined with iSALE) of material with r_{dust} = 100 µm over radial distance for no initial velocity (i), and 1 km/s initial velocity (ii). The lines show the initial dust layer thickness at t = 0s. Colours, line type and marker type correspond to these initial thicknesses as shown in the legend. For models shown in panel i), we used 100 representative particles per initial cell, and for models shown in panels ii), we used one representative particle per initial cell. For colours we refer to the online version.

9.5 Motion of ejecta curtains through the atmosphere

In the previous section we studied a simplified scenario of vertical dust settling keeping the initial dust mass per unit area constant for each scenario. In this section we discuss a scenario of an evolving ejecta curtain which is more complicated in several respects: the ejected mass within the curtain increases with radial distance from the centre of the crater towards the rim, and the mass flux at each distance varies with time. Based on the results from vertical settling, we study the trajectories of dust particles within the curtain in order to distinguish the range of ballistic settling of ejecta from turbulent deposition behaviour.

9.5.1 Curtain Evolution

In this section, we describe the evolution ejecta curtains corresponding to craters with transient crater radii of r = 200 m, 1 km, and ~4 km. As we do not model crater formation, we use the initial mass-velocity distributions from scaling laws (Housen and Holsapple 2011). We simulated four different scenarios each with a different size of particles within the ejecta curtain ranging from 100 μm to 0.1 m. The evolution of the ejecta curtain emanating from a 4-km-radius transient cavity is shown in Figure 9-7 and Figure 9-8. During the ejection (first 15 seconds) the ejecta curtain is still dense, its structure does not depend on ejected fragment size and resembles a “classic” ejecta curtain.

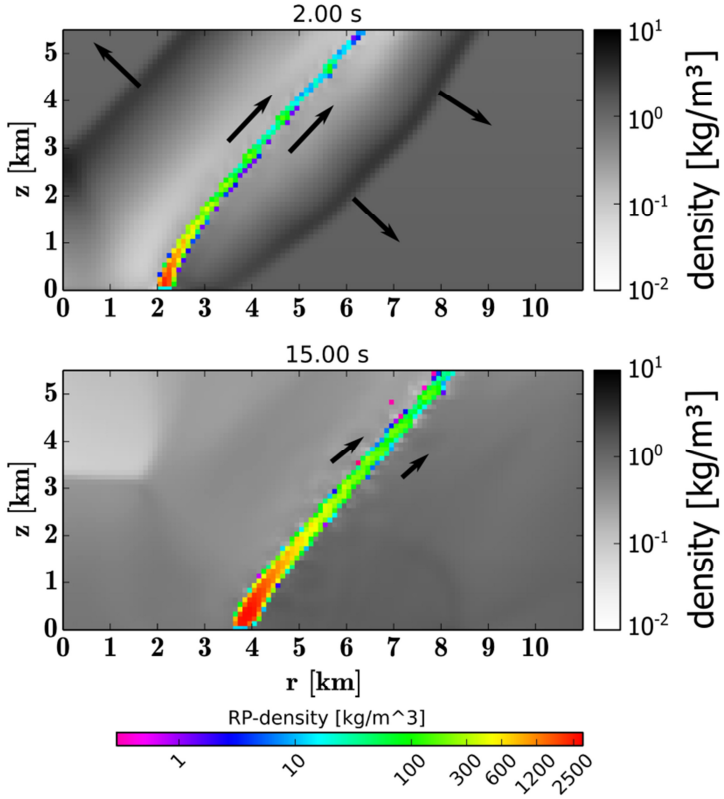

Figure 9-7: Formation of the ejecta curtain during 4-km-diameter crater formation (simulated with iSALE). The background grey scale represents the density of the air; colours represent the dust density within the curtain. Upper plate: fastest early ejecta generate shock waves in the atmosphere, Bottom plate: in 15 seconds the transient cavity reaches its maximum diameter and the ejection ceases; the ejecta curtain has a width of ~0.5 km near the surface and is still dense. Black arrows indicate the direction of air motion and are not to scale.

The late evolution of the curtain is substantially affected by the atmosphere especially in the case of smallest (100 μm) fragments (Figure 9-8, i) whereas the curtain with largest fragments (Figure 9-8, ii) keeps its classic shape for a longer time, but eventually, is also subject to atmospheric interaction.

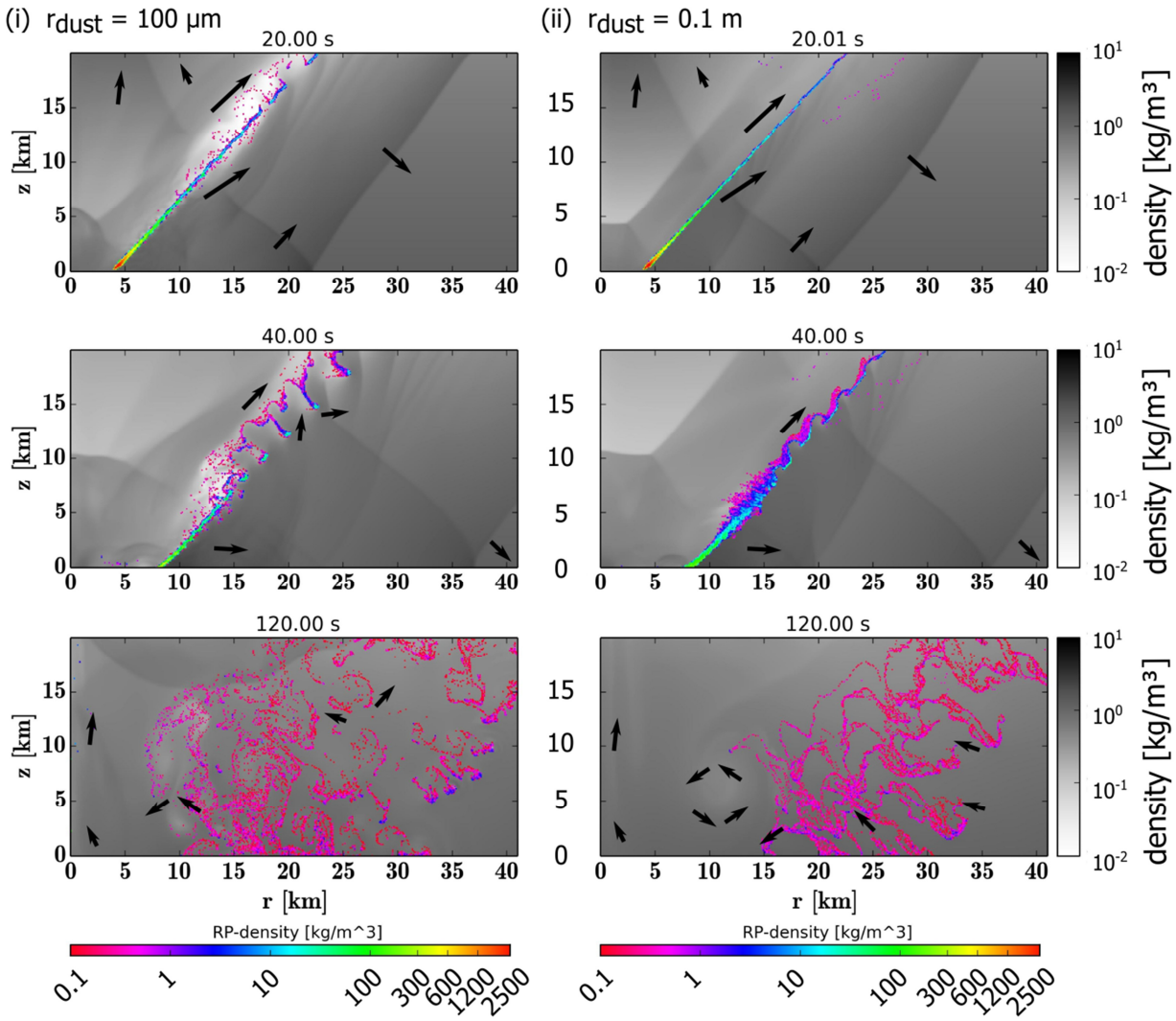

Figure 9-8: Ejecta curtain evolution from 20s to 120 s (simulated with iSALE). The snapshots show curtains consisting of 100 µm particles (left), and 10-cm-radius particles (right). The background grey scale represents the density of the air; colours represent dust flow density. The lowest part of the curtain keeps its high density and move mainly ballistically, whereas the upper, low-density, part of the curtain is subject to substantial mixing with the atmosphere and density currents are formed (earlier for small fragments, later for larger fragments). To the end of simulations (2 mins after crater formation) ejecta are mainly deposited up to a distance of 15 km, but some particles move still in a highly turbulent atmosphere. Black arrows indicate the direction of air motion and are not to scale.

9.5.2 Thickness of deposited Ejecta

At the end of each run (200 seconds) we calculate the resulting thickness for all four simulated particle sizes (if particles are still in the atmosphere, we assume their vertical descent to the ground, usually an input of these particles is minor – see below) and normalise it to the ballistic

thickness (Figure 9-9 i & ii). The ballistic thickness, which we will refer to as "reference" in the following, can be calculated analytically based on the parabolic trajectories of ejected material, but can be also calculated by our model if drag forces are switched off. For the 4 km crater scenario that we have shown in the previous section, we find that the resulting ejecta thickness agrees with pure ballistic solution within 3 crater radii independently on the particle size. At larger distances we have thicker than ballistic deposits up to a distance of 8, and then, for larger distances, much thinner deposits. Ejecta thicknesses at larger distance of $x/R > 9$ at 200 s after the model start are size dependent, with increasing thickness with particle size. For the largest simulated particle size, the blanket is thicker by one order of magnitude relative to the mm-sizes particles, representing the slower settling of smaller particles. Only the very smallest particles show a thickness similar to the largest particles. However, this is caused by an atmospheric dust flow close to the surface that transports dust to larger distances (see Figure 9-8 i at 120 s, near the surface). This mechanism is absent or less pronounced for larger particle sizes.

Assuming vertical settling of ejecta that are still in the atmosphere at the end of our simulations, we calculate the thickness of the ejecta blanket. For the largest particle size of 10 cm we find an increase in the thickness of the deposit (relative to the deposition in vacuum) for $\sim 3 < x/R < \sim 7$ (up to ~200%), and a decrease for $x/R > \sim 9$ (~60%; decreasing to ~30% at x/R=20). For the smallest simulated dust with r_{dust} = 100 μm, we find no continuous increase at the range of $\sim 3 < x/R < \sim 5$. Instead, the thickness changes between the norm and 140% of the norm. In the range of $\sim 6 < x/R < \sim 10$, the thickness first increases to 160% and then to 220% of the norm. At x/R>10, the thickness decreases sharply to about 30% of the reference (Figure 9-9 i). Ejecta at larger x/R are still in flow-like motion with substantial horizontal velocity. Hence, vertical interpolation to the surface illustrate a snap-shot of the mass in the moving flow at these distances (i.e. spikes represent the position of flow at the end of the model, e.g. at $x/R = 18$ Figure 9-9 i).

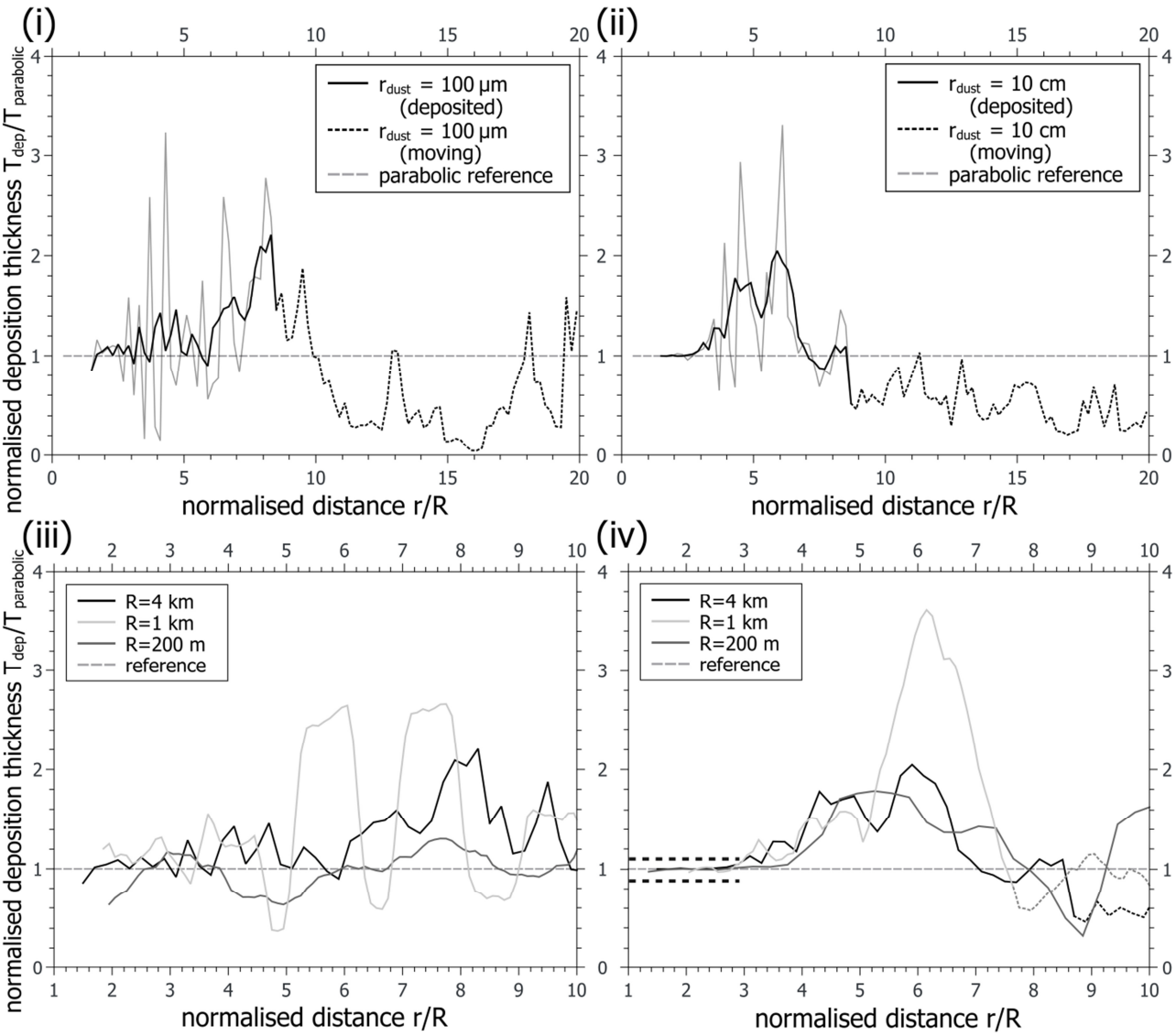

Figure 9-9: Ejecta deposits for a 4-km-radius transient cavity and two particle sizes ((i): 100 µm; (ii): 0.1 m) normalised to the ballistic reference thickness (determined with iSALE). Black lines for x/R<8.5 show the averaged ejecta deposited within 200 seconds (total time of this run) whereas black dotted lines show the sum of already deposited ejecta and ejecta that are still in atmosphere. Grey solid lines show the model data before averaging with a moving average of width 5. For small particles, the horizontal velocity is larger than the vertical velocity and further radial movement has to be assumed. For 10 cm-sized particles; the thicknesses beyond x/R~10 is smaller than the particle size and must be interpreted as an average value of a patchy blanket. In panels (iii) and (iv), the deposits of the 4-km-radius crater as shown in (i) and (ii), respectively, are compared to results for a 200-m-radius crater and a 1-km-radius crater for the same dust sizes. The black dashed lines in (iv) indicate the range of +/-10% from the reference that we consider as ballistic deposition.

For smaller crater sizes of 200 m and 1 km we find similar characteristics of the ejecta thicknesses: small dust particles (100 µm) settle slowly and therefore have more time to move in dust clouds in horizontal

direction up to large distances ($x/R > 20$). Large particles (10 cm) cluster in air and are deposited sub-vertically. Hence, several peaks of ejecta thickness form due to the formation of individual dust clusters as described in section 9.4. For a crater size of 1 km radius, we find a more pronounced, but thinner peak, where ejected material accumulated ($x/R \sim 6$).

9.5.3 Deposition Velocity of Ejecta

In impact events in vacuum conditions, the deposition velocity of ejecta increases with the distance from the crater due to the inverse order of ejection and deposition, i.e. the earliest ejected material is the fastest ejecta and reaches the farthest distance. In contrast, ejecta deposition within an atmosphere causes a decrease in deposition velocity. To further study the behaviour of ejecta upon landing, we track the velocity of the dust for all scenarios. For largest particles, as expected, landing velocities increase with increasing distance and are equal to the ejection velocities. With decreasing particle size to 10 cm and 1 cm, the dust gets more affected by atmospheric interaction, and final velocities decrease in comparison with ejection velocities approaching sedimentation velocities. However, final velocities for very small particles ($r_{dust} < 1$ mm) are always higher than sedimentation velocities and still have a substantial horizontal component. In Figure 9-10 we normalise the velocity data by the ballistic velocity and compare them with the equilibrium sedimentation velocities in undisturbed atmosphere. Small particles with $r_{dust} = 100$ µm quickly deviate from normal ballistic reference deposition at $x/R \sim 2$ and the vertical velocity component decelerates to sedimentation velocity at $x/R \sim 5$, while the horizontal velocity is larger (Figure 9-10 i). The velocity of large particles with $r_{dust} = 10$ cm equilibrate to vertical sedimentation for $x/R > 5$, but show some undulations around equilibrium where clusters of ejected particles have landed (Figure 9-10 ii). For different crater sizes, the distance where equilibrium velocity is reached, depends on the interplay of the radially growing excavated mass of ejecta, larger excavation mass for the larger crater sizes, and the radial increase of encountered atmospheric mass.

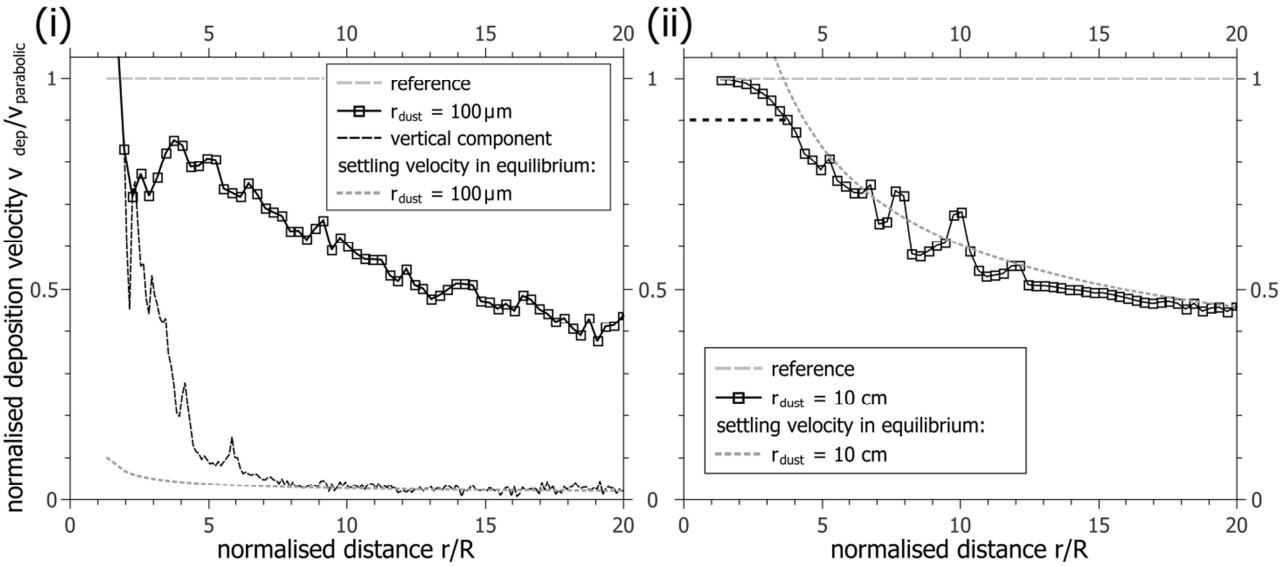

Figure 9-10: Normalised total deposition velocities (determined with iSALE) for a crater with R = 200m for (i) 100 µm and (ii) 10 cm (black lines and squares). Grey dashed lines show the landing velocity for parabolic trajectories as norming reference, grey dotted lines show equilibrium sedimentation velocities according to Eq. (101). The black dashed line in (i) shows the vertical velocity component from the model. The black dashed line in (ii) depicts the range of 10% deviation from the reference that we consider as ballistic deposition range.

9.5.4 Ballistic Range

Based on the normalised plots of ejecta thickness and deposition velocity, we analysed the range of ballistic deposition as a function of crater size and particle size. We consider ejecta as deposited with ballistic velocity if their deposition velocity differs by less than 10% from the reference (c.f. black dashed line in Figure 9-10 ii) within two neighbouring data bins (i.e. *r/R* positions). Similarly, the thickness is "ballistic" if a running average of width 5 deviates less than 10% from the vacuum reference (cf. black dashed line in Figure 9-9 iv).

In case of 0.2 – 1 km-radius craters, we find a decrease of the ballistic range with decreasing dust size for both criteria (ejecta thickness and deposition velocity). Only for the smallest dust size for R = 200 m, we could not assign any ballistic range for the deposition velocity. For a crater of 4 km radius, the described general trend of the smaller craters could not be observed. The ballistic range for the ejecta thickness as well as the

deposition velocity remains about equal for all dust sizes. In general, there is a good agreement between two different "ballistic range" criteria except of the smallest, 100 µm, ejecta: flow features as described above have been observed and influence the results on the ballistic range (deposition velocity has a substantial horizontal component).

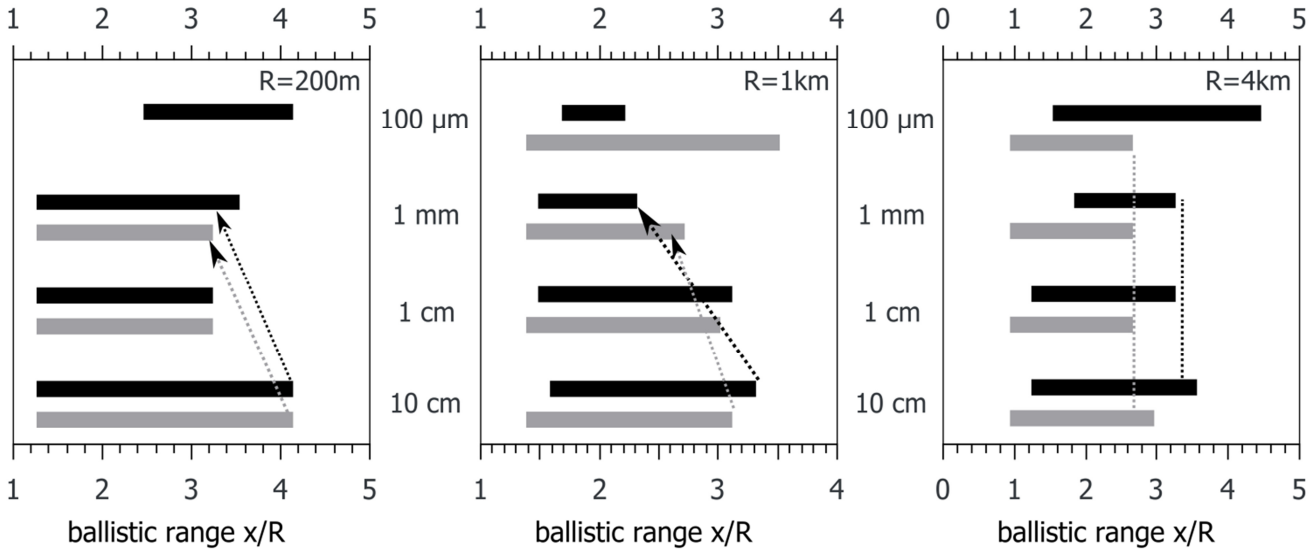

Figure 9-11: Ballistic range of ejecta deposition in terms of ejecta thickness (black) and deposition velocity (grey) for the three crater sizes: 200 m (left), 1 km (centre), and 4 km (right). The results have been determined with iSALE. Particle sizes are given from top to down: 100 µm, 1 mm, 1 cm, and 10 cm. Dotted lines and arrows support the visualisation of trends (black and grey for thickness and velocity, respectively).

9.5.5 Crater Fall Back

For cratering scenarios in vacuum, all ejecta are expelled from the crater on trajectories to be deposited outside the transient crater. Ejecta occasionally found within the crater might occur due to the final crater modification (e.g. slumping), ejecta from secondary craters, or so-called plume ejecta. In our models of ejecta curtain interaction with atmosphere we see that some ejecta move inward and are deposited inside the transient crater ($x/R < 1$). We found that the fallback thickness depends on both, the crater size and the fragment size (Figure 9-12): Smaller craters (200-m-diameter) are more sensitive to the presence of atmosphere and the fallback

thickness decreases from ~2 m in case of the finest ejecta to ~20 cm for ejected particles 1 mm in radius. For 10 cm sized particles the fallback was too little to form a deposit within the crater and only a sporadic occurrence of these particle sizes is expected. We analysed and averaged the thickness of ejecta deposition h/R in the range of $0.1 < x/R < 1$ in our models for all scenarios at the final stage of the model (Figure 9-12).

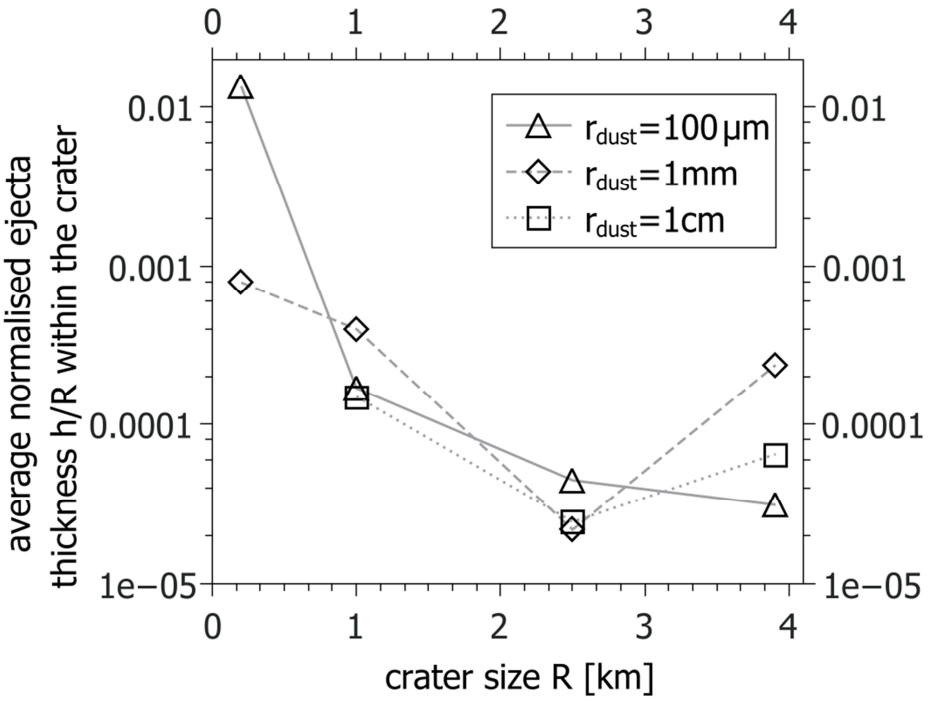

Figure 9-12: Average crater fall back for our simulated crater sizes from 200 m – 4 km (determined with iSALE). We analyse the ejecta thickness h/R in the range of $0.1 < x/R < 1$. Results are shown for three sizes of particles (see legend).

9.5.6 Influence of different particle sizes

In previous sections we described idealised cases with one particle size to understand the underlying principles of particle-gas interaction. Here we present the first model with a size frequency distribution of ejected particles described by the power law $N_{cum}(> r) = C\, r^{-D}$, where N is the number of particles with a radius larger than r, C is a constant defined by the total ejected mass, and D is the power law exponent. The actual (local) size-frequency distribution is not known and cannot be derived directly from our model. We use the power law exponent of 2.66 from Buhl et al.

(2014b), which remains constant during the ejection process. Figure 9-13 shows three snapshots of an ejecta curtain consisting of 5 classes of particles with radii from 100 μm to 1 m. The curtain starts sorting according to the size of the dust (100 μm, 1 mm, and larger sized dust). This separation into individual sub-curtains is partly caused by the discrete choice of particle classes; in nature, the particle size-frequency distribution is more continuous and the ejecta curtain would continuously widen due to particle/gas interaction. Our implementation does not support a continuous range of dust sizes for a given launch position. Many real dust grains are represented by one numerical particle, which is characterised by equal properties for all of the represented dust grains. In Figure 9-13 we used 5 size bins. However, in principle, an individual dust size could be assigned to each representative particle based on a fragmentation model, which is desirable for future studies.

Although the curtain separates into individual sub-curtains of different particle sizes, particles have moved on similar trajectories before this separation. In the dusty flow approximation particles show a collective behaviour due to coupling through the atmospheric gas. Instead of being immediately decelerated like an individual particle, which would cause dust collisions within the curtain, smallest dust grains move in the wake of larger particles, or a swarm of small particles moves with a higher velocity than isolated particles (as shown in section 9.4.2), because in this way atmospheric drag on the finest dust is minimised and the separation of the curtain occurs to a later time. Indeed, cm-sized particles still move along with the largest size classes within the main curtain in Figure 9-13.

We analyse the data similarly to the previous cases shown (Figure 9-14). In agreement to Figure 9-11, we find a ballistic range for this scenario for $1.7 < x/R < 3.1$ for the ejecta thickness. The crater fallback with h/R = 8.4e-5 for this scenario is slightly lower than the values for the pure 100 μm and 1cm scenarios.

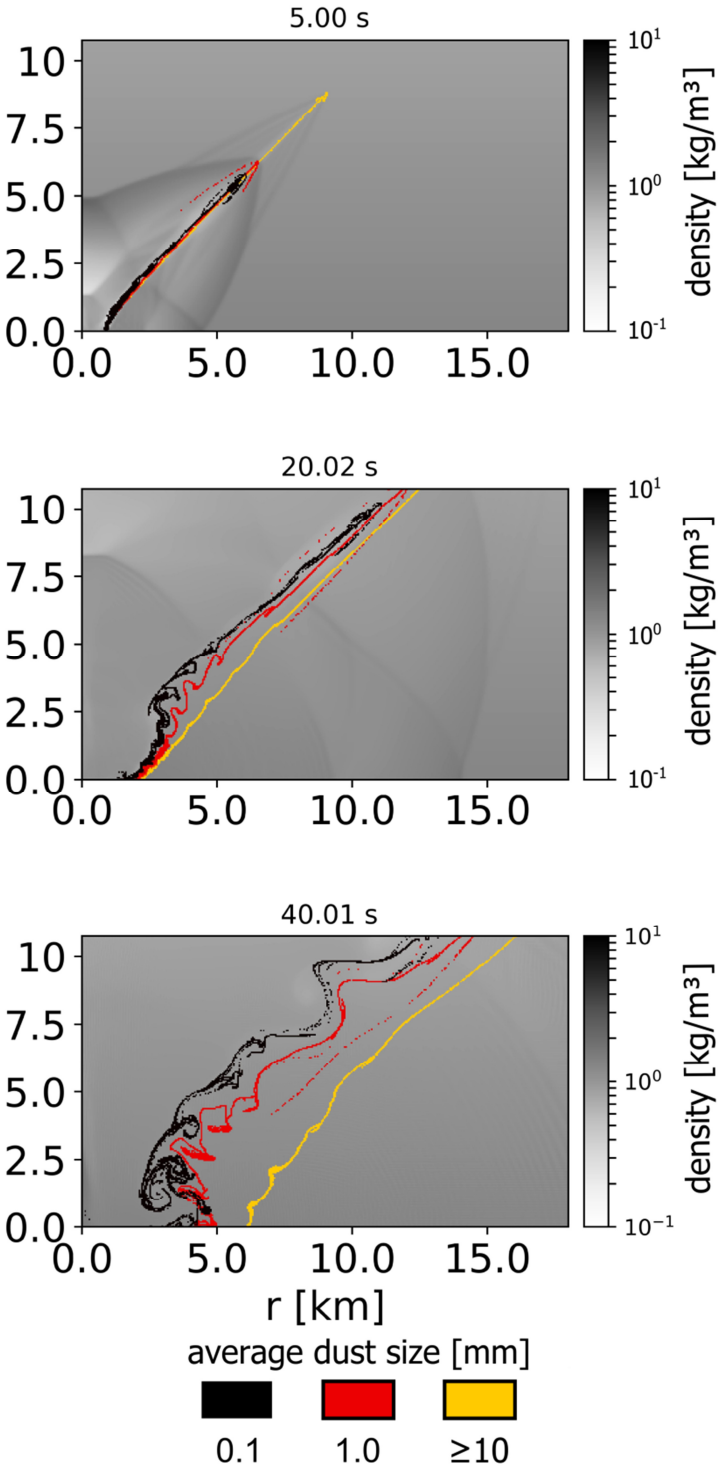

Figure 9-13: Ejecta curtain for a 1 km sized crater after 5, 20 and 40 s (simulated with iSALE). The snapshot shows a curtain consisting of 100 µm – 1m particles that separate according to their size (cf. separate lines and colour). The background grey scale represents the density of the air. The lowest part of the curtain keeps high density and moves mainly ballistically (cf. curtain at 20 s up to ~ 2 km altitude). Also, upper parts of the curtain consisting of larger fragments move ballistically (yellow), whereas the part of the curtain with smaller particles shows initial mixing with the atmosphere and turbulent patterns are formed (inner curtain boundary, black and red colour). Note that particles of a size of 10 cm and larger move within a common curtain.

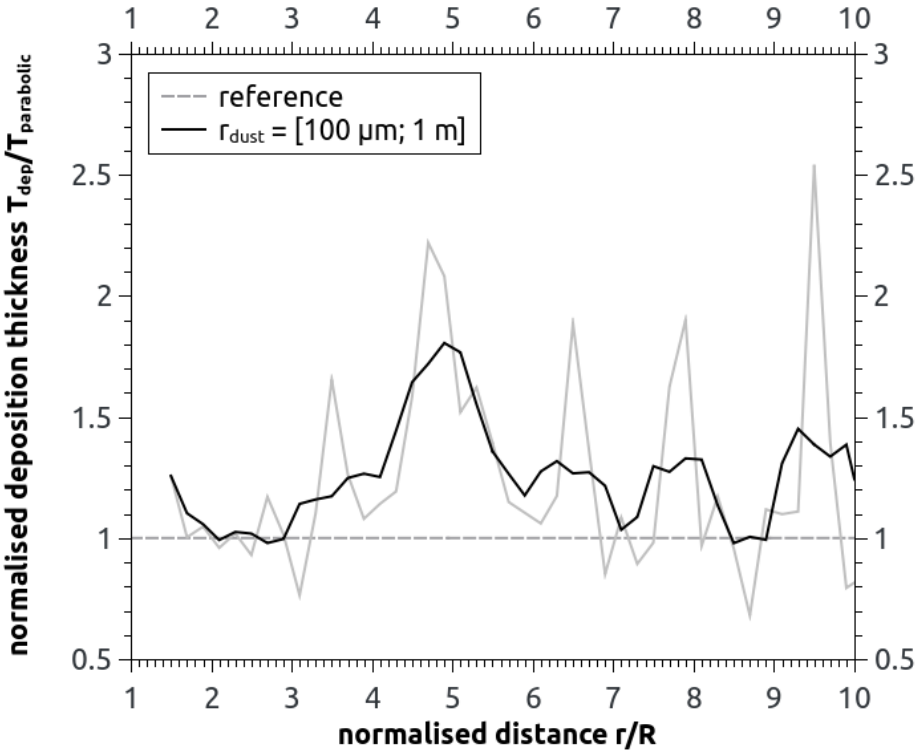

Figure 9-14: Ejecta deposits (determined with iSALE) for a 1-km-radius transient cavity and five particle sizes from 100 µm to 1 m (in each class particle size increases is by a factor of ten) normalised to the ballistic reference thickness. Black lines show the averaged deposited ejecta. The determined ballistic range according to our criteria ranges from 1.7 to 3.1. Grey lines show the model data before averaging with a moving average of width 5.

9.6 Laboratory Scale Impacts

Typically, the pressure in the target chamber in a laboratory experiment is reduced to some 1-10 mbar in order to avoid atmospheric effects (Stöffler et al. 1975; Cintala et al. 1999; Anderson et al. 2004). In this section we study the influence of higher gas pressure on ejecta deposition using ambient pressures of 1 kPa, 10 kPa, 100 kPa, and 6 MPa. In contrast to the previous section, we constructed a new set of scaling parameters to fit modelling (Wünnemann et al. 2016) and experimental results (Stöffler et al. 1975). We found that $C_1 = 0.232$ and $\mu = 0.48$ fit the published data best. To produce the same mass as in the experiments, we used $k = 0.37$, which is slightly larger than the value from Housen and Holsapple (2011). In this section all ejected particles have the same size of 100 µm in line with the experimental setup (Stöffler et al. 1975), except when stated differently.

Obviously, the influence of the atmosphere increases with increasing gas pressure: an ejecta curtain becomes unstable at an earlier point in time, a turbulent component is enhanced, and the thickness of ejecta deposit deviates stronger from the ballistic approximation (Figure 9-15, Figure 9-16, and Figure 9-17).

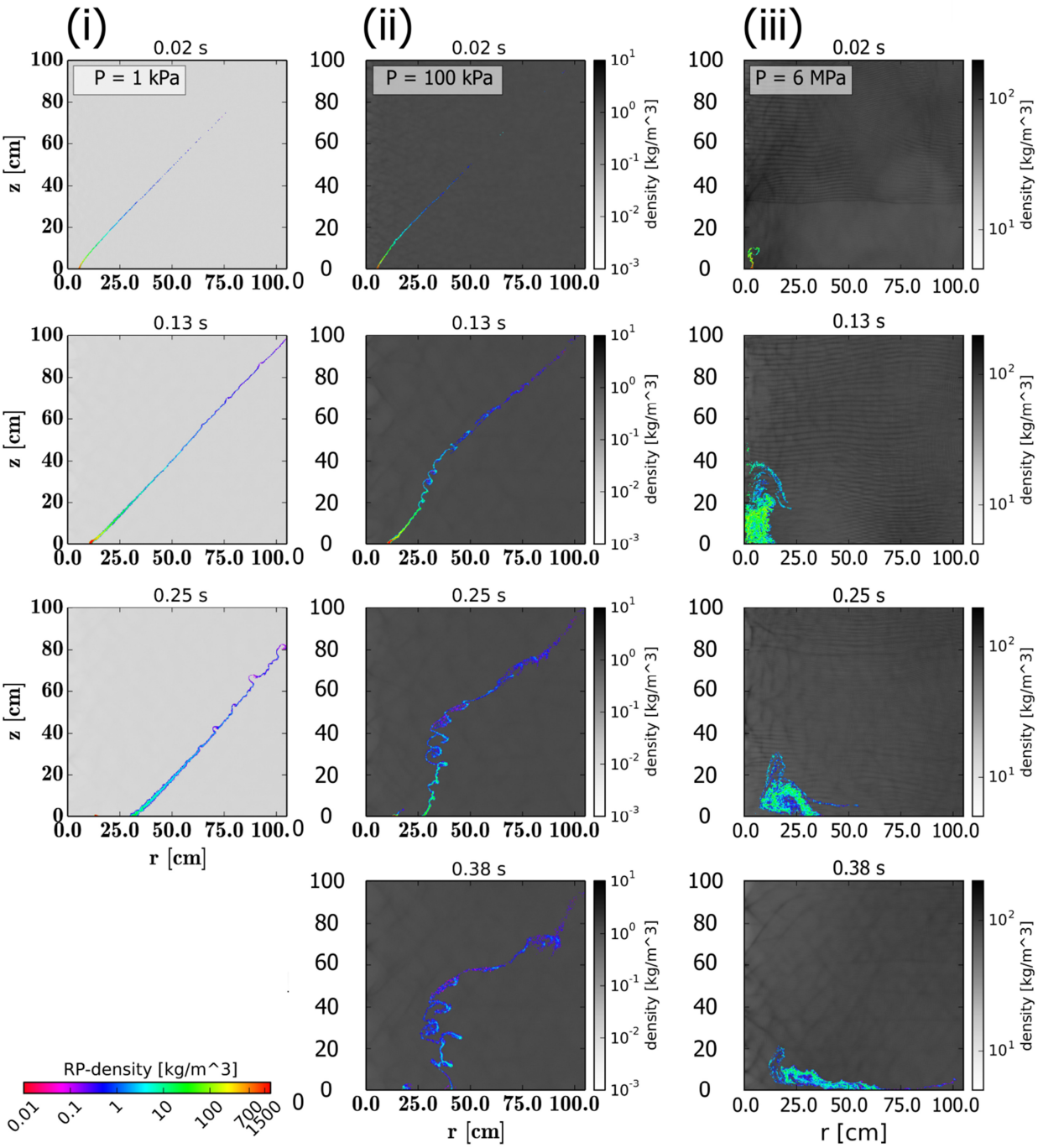

Figure 9-15: Laboratory-scale ejecta curtains (simulated with iSALE). The three columns of snapshots show simulations with a set-up corresponding to the set-up from Stöffler et al. (1975) and target chamber pressures of i) 1kPa, ii) 100 kPa, and iii) ~6 MPa. The background grey scale represents the density of the air; colour represents the density of ejected dust.

9.6.1 Thickness of deposited Ejecta

We calculated the thickness of the ejecta blanket for all scenarios up to a 1 m radial distance and also for vertical ejecta catchers as in experiments (Stöffler et al. 1975). Ejecta in a target chamber with pressure of 1 kPa do reproduce the trend observed in experiments by Stöffler et al. (1975): some deviations occur at larger distances of $x > 80$ cm (diamonds in Figure 9-16 i). The material at these distances has been longer affected by the atmosphere than the proximal ejecta and some clustering of ejected particles can be expected (cf. Figure 9-2), causing fluctuations in deposited mass. In addition, the experimental ejecta thickness close to the vertical ejecta catchers can be slightly exaggerated due to reflected material from the vertical catchers. The fluctuations in thickness get stronger (by one order of magnitude) and occur at smaller distances ($x > 55$ cm) if pressure increases to 10 kPa. At 100 kPa pressure deviations from pure ballistic results are obvious at all radial distances: there are two maxima at distances from 40 to 53 cm, and at ~63 cm, whereas at distances >68 cm the deposits are substantially (order of magnitude) thinner than in experiments. At the highest pressure of 6 MPa we find complete absence of ballistic behaviour. There is a substantial amount of crater fall back, whereas outside of the crater the ejecta thickness is strongly reduced (two orders of magnitude for about $1 < x/R < 3$, otherwise still one order of magnitude, Figure 9-17). Dust is transported to large horizontal distances while being dissolved in the thick atmosphere, and the transport mechanism can be compared to transport in a fluid (Figure 9-15 iii).

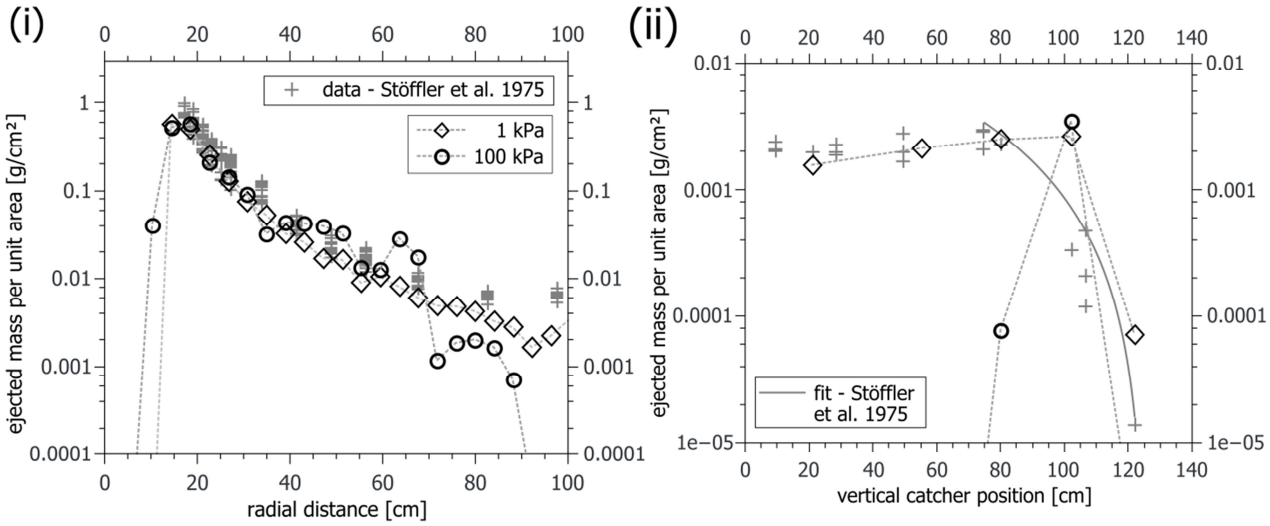

Figure 9-16: Ejecta deposits from numerical simulations for a target chamber pressure of 1 kPa and 100 kPa (determined with iSALE). Horizontal (i) and vertical ejecta deposition (ii) are derived from the model (black symbols) and compared to the data (grey symbols) from Stöffler et al. (1975). The function (grey line, ii) for altitudes above 80 cm is approximated from Stöffler et al. (1975), Figure 7. The model data in vertical direction is binned between: 0, 42, 68, 92, 112, and 132 cm.

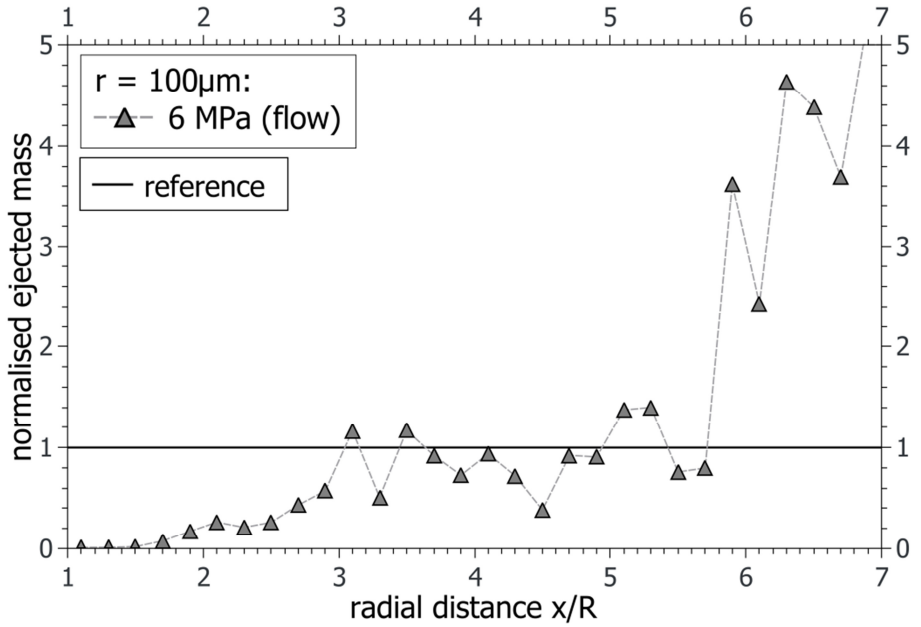

Figure 9-17: Normalised (to parabolic deposition) ejecta deposits from numerical simulations with iSALE for a target chamber pressure of 6 MPa with a high atmospheric density (~84 kg/m³). Due to the high density of air, the dust cloud remains stable for a long time before it collapses as a dust flow. The crater is filled by material. However, only a small fraction is deposited in the near range outside of the crater. Once, the dust cloud collapses and a horizontal flow establishes, a large amount of mass is transported to larger distances. As this flow lasts longer than the model run-time, we show the mass distribution at the end of the model to give an impression of the importance of the mass movement.

For vertical catchers, our simulation with a target chamber pressure of 1 kPa reproduces the observed mass distribution from Stöffler et al. (1975) for altitudes up to 80 cm (Figure 9-16 ii), which additionally confirms the applicability of our dust cloud approach. We also reproduce a decay of mass per unit area for an altitude of 1.2 m as observed by Stöffler et al. (1975). In our scenarios with larger target chamber pressures, we see strong deviations from the experimental results in vacuum. Especially for the largest pressure of 100 kPa, most vertical ejecta catchers do not contain any ejecta as horizontal motion of the dust has been stopped by the atmosphere before the catchers could be reached. Consequently, future experiments need to place vertical catchers closer to the centre of impact in order to derive a vertical ejecta distribution. However, for the very dense atmosphere with a pressure of 6 MPa, we see a significant horizontal movement as a ground hugging flow. The mass detection in a vertical catcher would occur up to an altitude of ~5 cm, while the top catchers would stay empty. Thus, the trend from 1 kPa to 100 kPa is inverse to the trend from 100 kPa to 6 MPa because of different deposition mechanisms.

9.6.2 Ejecta curtain angle

As an additional comparison to experimental data, we measure the ejecta curtain angle in our models (Figure 9-18). Curtain angles have been studied by Schultz (1992) for various combinations of gas and target chamber pressure for sand (~62.5 µm) and pumice (bimodal distribution with sizes of ~12.5 µm and ~40.5 µm). More recent studies discussed the increase of the ejecta curtain angle during the evolution of the ejecta curtain and the role of atmospheric turbulence (Sommer et al. 2013). However, measuring the ejecta curtain angle within the model is not straight forward, because turbulent dust clouds hamper the determination of a sharp boundary of the curtain. Therefore, we assessed the curtain angle based on the highest density distribution within the curtain, assuming that this is the best approach comparable to experiments in which the visibility and measurement of the angle of the curtain correlates with the optical thickness

of the ejecta cloud, which itself depends on the dust density in air. Therefore, we chose to measure the angle of one or more fitting lines through the areas with the highest dust densities. In the following we discuss only simulations with an ejection angle of 45°, whereas ejection angles in laboratory experiences deviate from this angle depending on the target material as well as the time and location of ejection (e.g. Hermalyn and Schultz 2014; Gulde et al. 2018; Luther et al. 2018).

In Figure 9-18 we plot the measured curtain angles at atmospheric pressures of 1 kPa, 10 kPa and 100 kPa, corresponding to a density of ρ/ρ_0 = 0.01, 0.1, and 1 relative to normal density (ρ_0 = 1.3 kg/m³) for sand with a particle size of 100 µm (Figure 9-18 i), and for $\rho/\rho_0 = 1$ for pumice-like dust with a size of 10 µm (Figure 9-18 ii). For $\rho/\rho_0 = 0.01$ and $\rho/\rho_0 = 0.1$ we find an ejecta curtain angle that nearly agrees with the ejection angle of 45° itself for more than 150 ms. For $\rho/\rho_0 = 0.1$, the ejecta curtain angle for the sand model slightly increases after 150 ms and reaches a value of 55° after 250 ms. This similar behaviour between the cases of $\rho/\rho_0 = 0.01$ and $\rho/\rho_0 = 0.1$ agrees with the observed values for sand from Schultz (1992). The observed ejecta curtain angles also fall into the range that was observed by Tsujido et al. (2015), who studied the formation of ejecta curtains by conducting impact experiments into quartz sands using different projectile materials. In contrast to the lower atmospheric density cases, the ejecta curtain angle increases faster for $\rho/\rho_0 = 1$ for both pumice-like and sand materials. The ejecta curtain angle for sand increases to ~80° after 250 ms (cf. wall-like shape in Figure 9-15 ii). Also Schultz (1992) observed a larger curtain angle for sand with the highest atmospheric density of $\rho/\rho_0 = 1$ (up to ~68°). For the 10-times smaller pumice-like dust we observe a much faster increase of the ejecta curtain angle for the initial (top) part of the curtain, which steepens to ~74° within 25 ms and agrees to the value observed by Schultz (1992) who measured ~70° at 20 ms. The fast increase of the curtain angle for the small pumice-like dust is related to the small grain size of pumice compared to sand that causes a faster deceleration to the ambient gas velocity. However, in the same time the lower more mass rich part of the ejecta curtain in our pumice-like model does not steepen to more than 50°.

The high angles are reached at a later time (76° after 80 ms), but relax to smaller ~60° later on. In summary, we are confident that our modelling approach represents the observed experimental tendencies.

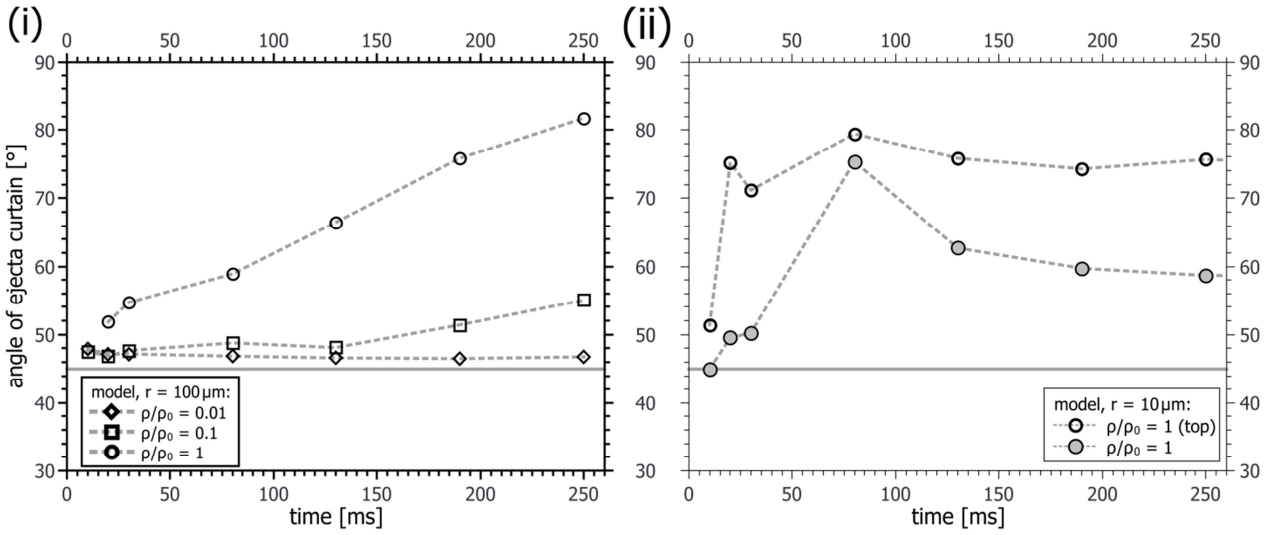

Figure 9-18: Evolution of angle of ejecta curtain for different chamber pressures expressed by the density ratio relative to ambient air density ρ_0 (determined with iSALE). Target materials are quartz sand (i) and pumice (ii). The solid grey line shows the 45° ejection angle.

The movement of ejecta within the curtain, and the agglomeration of dust clouds, depends on the dust size and density ratio between dust and gas. Different areas within the ejecta curtain have different dust densities. E.g. the surface-near regime of the curtain shows the highest density (up to some 100 kg/m³) and a curtain angle of 50° (close to ballistic behaviour) evolves (Figure 9-18 i). Material in this lower curtain moves almost parabolic. Material with a density of >10 kg/m³ as it occurs in the intermediate part of the curtain corresponds to a vertical settling scenario from section 3 (based on the density criterion) with an initial thickness of $h = 0.1$-1 m with a large horizontal velocity component of up to $v_{horizontal}/v_{absolute} \sim 0.6$ (Figure 9-4). Curtain evolution and the ejecta movement in these intermediate altitudes (e.g. at ~20-50 cm altitude 0.25 s after the impact) are affected by the development of Kelvin-Helmholtz instabilities, which cause the formation of vortices due to differences in dust velocity in neighbouring areas, even if in each area horizontal and vertical velocity components point into the same

direction. The low mass fraction at the top of the curtain (<1 kg/m³) initially shows an angle of ~45°, but starts to collapse due to dust deceleration and the acting gravity, and the curtain angle decreases to < 30° at ~300 ms.

9.7 Discussion and Perspectives

Natural cratering events produce ejecta with a size-frequency-distribution that stretches over several orders of magnitude from smallest dust to blocks of 100's of metre in size (depending on the crater dimensions). In our study, we mostly analyse the behaviour of individual dust or particle sizes to avoid further complexity and to isolate the physical behaviour of individual size classes. However, we note that ejecta with a set of different sizes can behave differently to single-sized ejecta. Larger fragments or big blocks of material are less affected by atmospheric deceleration. In contrast, they accelerate the atmosphere and cause the formation of shock waves. In the wake of such large fragments, small dust grains can reach larger distances than without the presence of these large fragments as discussed in section 9.5.6. In general, large fragments occur in areas of low shock pressure (in particular, in the so-called spallation zone), whereas small dust grains are typical for a wide range of shock pressures and ejection velocities.

Late low-velocity massive ejecta are less subjected to atmospheric influence and move mainly ballistically. The range of our largest particle size of 10 cm gives a rough maximum range of ballistic behaviour in terrestrial atmosphere (Figure 9-11).

In natural cratering events, the projectile produces disturbances in the atmosphere. This effect was included in the study of Shuvalov and Dypvik (2013). In our approach of producing ejecta with scaling relationships, we neglect such disturbances in the atmosphere in order to primarily focus on the variation of the parameters that are demonstrated above. However, we think that this is a feasible assumption because the intense interaction of the ejecta curtain with the atmosphere takes place at the later stage of ejecta deposition when strong winds generated by shock

waves are gone and the atmosphere is mostly relaxed to its standard conditions.

We demonstrated that atmospheric transport can cause the fall back of ejected material into the crater (Figure 9-12). However, this material is suspended in air for a relatively long time and possibly is subject to winds which are not included in our simulations. We can expect that exactly these "suspended" ejecta form dark parabolas on Titan (Wood et al. 2010) and on Venus (Vervack et al. 1992; Schaller and Melosh 1998).

On planets without substantial atmosphere (e.g. Moon, Mercury) ejecta are deposited mainly ballistically. However, with average impact velocities of ~19 km/s on the Moon (e.g. Jeffers et al. 2001) and 42 km/s on Mercury (Marchi et al. 2009), peak shock pressures may be as high as 300 – 1000 GPa. The release from these high pressures causes vaporisation of the target and projectile materials. This vapour expands quickly from the impact point: early solid/molten ejecta are entrained into the plume and later probably form double ejecta layers (Goldin and Melosh 2009). Moreover, specific thermal conditions within the plume can affect chemical processes by enforcing or inhibiting specific chemical reactions (Zahnle 1990).

The dusty flow approximation assumes non-collisional conditions, e.g. particles' volume (but not mass) should be substantially smaller than the gas volume. These conditions are satisfied in all simulations shown in the paper except of the early (adjacent to the surface) ejecta curtain. However, even in this case all particles are on similar trajectories with similar velocities and an influence of their inter-collisions is minimal.

The effect of different target rheologies has not been addressed in this study. Our reference ejecta blanket based on parabolic trajectories always refers to a case with constant ejection angles of 45°, which is typical for porous materials with a medium coefficient of friction like sand (Cintala et al. 1999). Different studies have shown that the ejection behaviour depends on target properties (e.g. Hermalyn and Schultz 2014; Luther et al. 2018). To show the influence of material properties, we have taken the ejection scaling parameters from Luther et al. (2018) for two non-porous

target materials (very low strength: μ = 0.49 & K_1 =v0.53, and very high strength: μ = 0.47 & K_1 = 0.82) and use these parameters to produce ejecta in our model (Figure 9-19). We assume a constant average ejection angle of 35° and 55° for the high and low strength materials, respectively (Luther et al. 2018). For a low strength material the deposition pattern appears smoother than for the other cases and deviations from the reference are smaller than 25%. The trend follows the pattern of the minima of the deposit of the scenario with 45° ejection angle. In contrast, the high material strength scenario shows an increase of the deviation from the reference with distance. At x/R~5 the difference increases to more than 25%. These differences in the deposition pattern require further detailed studies. They form due to interplay of dust size, ejection speed and ejection angles. Small particles are more sensitive to atmospheric drag. The deposition velocities are small, and as such the time that the dust remains in the atmosphere, where it can be transported, is longer. Ejection angles and ejection speeds affect the altitude to which material can be transported. Large angles allow for dust transportation to higher altitudes, which increases the time that the dust remains in the atmosphere. Smaller ejection angles lead to a more horizontal momentum transfer onto atmospheric gas, and influence the transport direction. Hence, the material rheology appears to be important for ejection models with atmospheric interaction, because they change the initial ejecta conditions like speed and angle. Such effects are important when comparing, e.g. basaltic lava areas with areas of rather lose sands, or areas which are depleted or rich in volatiles (like on Mars), and modelling the ejecta distribution requires initial conditions that fit to the target rheology (i.e. scaling parameter and ejection angle should represent the target properties, or ejection speed and angle are taken from shock-physics codes directly).

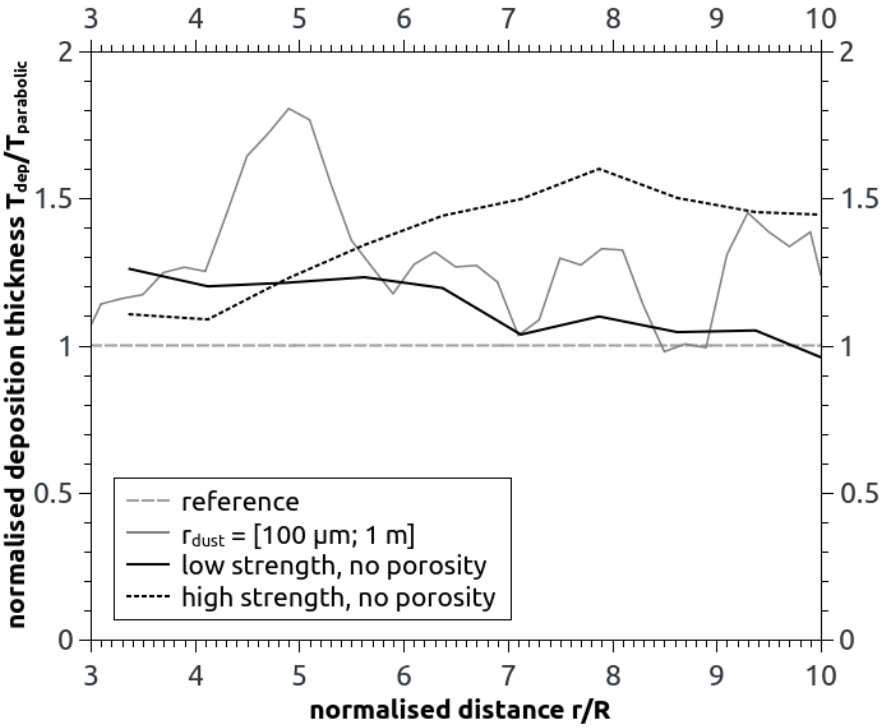

Figure 9-19: Ejecta deposits (determined with iSALE) as in Figure 9-14. In addition, similar model results are shown for a low strength material and a high strength material as described in the text (black solid and dotted lines, respectively).

9.8 Conclusions

1. The simplest test of particle sedimentation in undisturbed atmosphere may be considered as validation and verification of the dusty flow approximation. Although we use a simplified drag coefficient, we are able to accurately reproduce the settling velocities for different particle sizes and different regimes of sedimentation (from Stoke's law to Newtonian drag). Modelling of dusty layers in atmosphere reveal three different regimes of settling – sedimentation, formation of density currents, and the free-fall – depending on particle size within the layer and its dust loading (mass of dust per unit area).
2. We simulate the behaviour of ejecta that are expelled from a growing crater for different transient cavity sizes (200 m, 1 km, and 4 km) and for different fragment sizes (100 µm, 1mm, 1 cm, and 10 cm). For each scenario, we calculate the thickness of the ejecta

deposit, the deposition velocity, and a norm against results assuming pure parabolic trajectories. In general, we find that the dimensionless ballistic range (in terms of deposition velocities and thickness of ejecta layers) x/R decreases with increasing crater size and decreasing dust size.

3. We find that the amount of material that falls back into the crater depends on the particle size, and in general it is larger for smaller grain sizes. In addition, we find a scale dependency of the fall back with crater size.
4. We show that an ambient pressure in experimental setups could be an important factor influencing ejecta curtain angles and the decay of ejecta deposit thickness with distance. In experiments with sand (particle size 100 μm) substantial deviation from ballistic deposits (Stöffler et al. 1975; Wünnemann et al. 2016) is observed at a pressure of ~10 kPa. In general, we demonstrate that ejecta/atmosphere interaction is an important physical process, which we can model using the dusty flow approximation coupled with the iSALE code.
5. Examples presented in this paper are idealised, but of theoretical interest. Assuming mono-sized ejecta is still far from realistic scenarios. However, they have to be considered as preliminary tests that constrain the theoretical range of outcomes, and serve as the basis for future development of the iSALE code.

9.9 Acknowledgements

This project is part of the MEMIN FOR887 funded by the German Research Foundation: DFG-grants # WU 355/6-2. We thank Dr. Tom Davison and an anonymous reviewer for their comments which helped us to improve the manuscript with their comments. We gratefully acknowledge the developers of iSALE-2D, including Gareth Collins, Dirk Elbeshausen, Boris Ivanov and Jay Melosh. We also acknowledge the developer of the

pySALEPlot tool Tom Davison, and the developer of the VIMoD software Dirk Elbeshausen. iSALE –Website: **www.isale-code.de**

9.10 Appendix

9.10.1 Model Parameters

Table 9-2: Model parameters for vertical settling.

General parameters	
CPDR*	50
Grid spacing [m/cell]	100
Vertical high resolution cells	320
Vertical extension cells (top)	40
Horizontal high resolution cells	700
Horizontal extension cells	80
Representative Particle parameters	
Initial number of representative particles per cell	1 / 100

* cells per initial RP-disk radius.

Table 9-3: Model parameters for ejecta curtain.

Crater radius [m]	0.1365	200	1000	3908
General parameters				
CPCR*	27 / 55	16	20	39
Grid spacing [m/cell]	0.0025 / 0.005	12.5	50	100
Vertical high resolution cells	500 **/** 250	800	640	500
Vertical extension cells (top)	0 / 0	80	40	50
Horizontal high resolution cells	500 / 250	700	1000	600
Horizontal extension cells	0 / 0	100	80	100
Representative Particle parameters				
Number of created representative particles per iteration	16 / 20	10	100	20
maximum density at ejection [kg/m³] (governs RP production)	1580	2500	2500	2500

* cells per crater radius, values are rounded to full numbers.

10 Discussion and Conclusion

The objective of this thesis is to expand the knowledge and understanding of the formation of impact ejecta blankets, which are a consequence of impact cratering events. More specifically, I focus on the ejection dynamics of material with different target properties and the material deposition in vacuum, and I also focus on what happens when the ejecta interacts with an atmosphere or a vapour plume. First, I summarise my results in light of the key questions and objectives as stated in chapter 1.2, then I discuss the limitations of the methodological approach, and, finally, I draw conclusions from the results with respect to a more general context beyond the key questions that I raised in chapter 1.2. I also provide some further applications of my work and show future prospects.

10.1 Objectives & Key Questions

In this thesis, I raised three objectives and two key questions, which I briefly summarise, respectively, as:

M I. Material Models
M II. Ejecta Analysis
M III. Representative Particles

and:

S I. Ejecta and Target Properties
S II. Ejecta and Atmosphere

The answers to the key questions *S I* & *II* rely on findings of the objectives *M I*, *II*, & *III*, and consequently, I start by summarising the objectives before the key questions.

***M I* - Material Models:** Ejection processes are affected by the material behaviour, which is described by material models and parameterisations. Therefore, the first objective *M I* aims at testing the

material models used in iSALE in order to prepare to address key question *S I*. Rheology models are important to describe the material resistance against impact-induced stresses. Often, these rheology models are applied to and compared with natural-scale cratering events. However, comparing modelling results with laboratory experiments gives a better constraint on the validity of the material models. Furthermore, I use experimental results in chapter 8 for validating the ejection simulation results. Hence, in chapter 6, I compare laboratory-scale simulation results with experimental results for cratering events in quartzite and marble targets. The experiments were performed using a two-stage light gas gun. Both targets are competent rocks, and I used a rheology model that includes material damage and a yield envelope for each intact and damaged material, respectively, as described in chapter 3.2.3. The simulated craters and the laboratory craters agree in depth and diameter. The replication of the experimental craters by applying the strength models that are included in iSALE is an important step to answer objective *M I*: For the given study, I found that the rheology models are sufficient to reproduce experimental results. Hence, it can be assumed that the rheology models are sufficient to describe the material behaviour in complex impact scenarios, which is important for addressing the first key question *S I*. Consequently, the rheology models allow for conducting parameter studies where individual parameters are varied in order to study the consequences of different material rheology characteristics.

Having addressed the rheology model, I also discuss the applicability of the porosity-compaction model. Porosity affects the ejection behaviour by energy consumption due to pore compaction, density variations, and the reduction of the speed of sound in the target material. To show the validity of the ε-α porosity-compaction model that is included in iSALE, I chose an end-member testing scenario of a very porous target that nearly completely suppresses material ejection. In chapter 7, I compare observed funnels in snow, which formed after the Chelyabinsk event, with modelling results. With initial impact conditions that had been derived by atmospheric entry modelling by N. Artemieva, the “snow carrots” serve as a natural

experiment in a target with 70% porosity. Consequently, the deceleration of the dense basaltic projectile is small and computation times are long. Still, results from iSALE show a good correlation to observed characteristics of the penetration funnels in snow in terms of funnel length, density increase in the funnel walls, and repression of material ejection.

The length of the snow funnels for a given snow porosity depends on the chosen strength parameters for the Drucker-Prager rheology model. The chosen cohesion as well as the coefficient of friction strongly affect the funnel length. However, the parameters of the porosity-compaction model also influence the funnel length. Here, the most obvious parameter is the porosity itself, but also other parameters such as the elastic volumetric strain threshold, which defines the limit of elastic compaction, cannot be neglected. For example, it is the latter parameter that has a big effect on the density increase in the snow funnel walls.

For the given study in chapter 7, the ε-α-compaction model of iSALE has shown to reproduce observed natural funnels in snow, and, consequently, can be assumed to be sufficient for describing the compaction of porosity in impact scenarios. Parameter studies where individual parameters of the ε-α-compaction model are varied are expected to give reliable results for studying the consequences of different material characteristics.

***M II* – Ejecta Analysis:** The second objective is addressed in several chapters of this thesis. In chapter 4, I describe the difficulties in studying ejecta. The material continuum as described in the numerical grid does not yield correct results when ejecta trajectories and the ejecta curtain are simulated through to deposition. One major problem is the reduced resolution of the ejecta curtain. The ejecta curtain thins out with increasing altitude and distance, and empty cells occur within the curtain between cells that contain clumps of accumulated ejected material. A more reliable assessment of ejection data is reached when the data is analysed shortly after ejection with the help of massless tracer particles that follow the continuum material flow. The method is described, validated and applied in

chapters 4 and 8. Comparisons of the model data to laboratory experiments show agreement in ejection velocities and the average ejection angle, and, thus, they support the approach.

***M III* – Representative Particles:** The representative particle approach that is used for simulating the interaction of ejected material with an atmosphere and/or a vapour plume is described in detail in chapter 5. Representative particles represent a given amount of real dust particles of one size and with a given material density on similar trajectories. Each representative particle exchanges momentum and energy with the surrounding atmosphere. Validation tests and resolution tests are shown in chapters 5 and 9. These tests have shown that the approach implemented into iSALE is capable of reproducing analytical solutions for equilibrium sedimentation. Benchmarking results derived for vertical settling of many representative particles agree with results of the SOVA shock physics code. Furthermore, comparisons of numerical and laboratory experiments using particles of two different sizes (10 µm and 100 µm) show similar results for ejecta curtain angles. Having gone through intensive testing, the code appears to yield reasonable results and can be applied to in-depth parameter studies.

***S I* – Ejecta and Target Properties:** Target properties affect the ejection properties and, in extreme cases, can even cause the suppression of material ejection as shown in chapter 7. Having addressed objectives *M I* and *M II* as described above, the material models and ejecta analysis approaches available in iSALE are sufficient to tackle this first key question *S I*. In chapter 8, I analyse ejection behaviour under equal impact conditions. To simulate the different target materials, I use a Drucker-Prager rheology with a varying coefficient of friction, and for some models I also include cohesion. Different porosities are modelled with the porosity-compaction model. Ejection characteristics, like the ejection velocity and the ejection angle, are different for liquids, granular materials, and competent rocks. Craters in competent rock tend to be smaller than those in soft granular

materials, and consequently, ejection velocities in competent rocks decrease closer to the impact point than for granular materials. In contrast, granular materials often are more porous than competent rocks, and ejection velocities close to the impact point tend to be smaller. The ejection angles tend to be largest for hydrodynamic materials, and they decrease with increasing material strength. This compares well with experimental observations that show a decrease in ejecta curtain angles for different target materials with increasing strength (Koschny, personal communication). The glass beads targets, sand targets, and regolith simulant targets are characterised by increasing angles of repose.

Based on the ejection velocities, I derive the scaling parameters for the different target materials. These findings are important for future studies that use scaling relationships to study aspects of the ejection process on different planetary bodies and/or different geologic units with different target properties. Such studies could focus, e.g. on the formation of secondary craters, or the material transport of shocked material due to repeated cratering events. Highly shocked lunar melt rocks are used for age determinations, whereby the derived ages can be used to calibrate the age of the geological unit where the rock originates. Therefore, it is important to correlate melt rocks with an area of origin, which is not necessarily the location of its discovery. Ejection processes play a major role in this, and the new scaling parameters allow for including the effect of target properties in future studies.

Based on the ejection behaviour, I calculated the deposition thickness of the ejecta under the assumption of parabolic trajectories in a vacuum. Depending on the internal friction of a granular material (e.g. sand, or fractured rocks that behave as a granular medium on a larger scale), the thickness of the ejecta blanket decreases faster or slower with increasing distance from the crater rim. A change in porosity (e.g. resembling different grain shapes and void spaces) does not seem to affect the decay of the thickness, but it does affect the total ejecta volume. Changing the impact velocity results mostly in a change of the deposit thickness close to the rim, especially for low-velocity impacts. The results shown in chapter 8 raise the

question of whether it is possible to derive information about the impact velocity for a specific natural crater or information about the target properties of a geological unit on a planetary body by accurately measuring the ejecta blanket. However, the calculated deposits neglect any post-deposition modifications. Furthermore, the calculated deposits do not account for atmospheric interaction with the ejecta, and, as such, are valid for planetary bodies with very low atmospheric pressure or vacuum conditions.

***S II* – Ejecta and Atmosphere:** The emplacement of ejected material is affected by the presence of an atmosphere or an impact vapour plume. To quantify the effect of atmospheric interaction on the distribution of ejecta, I applied the representative particle approach, which is described in chapter 4. As little published data and even fewer systematic studies on the topic of atmospheric interaction of ejected dust are available, I first tested the sensitivity of different particle sizes on atmospheric interaction in a vertical settling scenario. Second, I analysed the ejecta distribution of crater ejecta scenarios ranging from a laboratory to a natural scale. I focused on determining the effect of atmospheric interaction for different individual particle sizes and different crater sizes (chapter 9).

The vertical settling scenario showed that small masses of ejecta in air will quickly decelerate to the sedimentation velocity, which depends on the dust grain size. In contrast, a large initial mass of material in air will fall at free fall velocity as if no atmosphere was present; atmospheric effects are small in this case. The dust behaviour between these two end-member cases depends on the initial dust loading (mass of material that is distributed in the atmosphere) and the particle size. Dust in the intermediate regime forms density currents with a settling velocity larger than the sedimentation velocity, and the dust shows a significant horizontal velocity component. This means that the dust survival time in the atmosphere, which is relevant for analysing climatic effects due to the reduction of solar irradiance, depends not only on the particle size but also on the mass of dust that is deposited in the atmosphere.

In the second scenario of ejecta curtain evolution, I test the influence of particle size and crater size on the ejecta deposition in an atmosphere. Smaller dust grains are affected more easily by gas interaction. Both an increase in particle size and a decrease in crater size result in a larger relative range (x/R) of ballistic deposition. In contrast, smaller particle sizes increase the rate that material falls back into the crater. This implies that a good understanding of the size-frequency distribution of the ejected material is crucial for a reliable simulation of ejecta deposition.

Results from answering both key questions *S I & II* have shown that it is important to consider both target properties and atmospheric interaction when discussing ejecta deposits. In this thesis, both aspects have been studied independently from each other so far, and neither of them can be neglected because they both influence the shape of the final ejecta blanket. Target properties affect the ejection characteristics, which define the starting conditions for ejecta motion in an atmosphere. A low material strength correlates with high ejection angles, and the material is ejected to larger altitudes in the atmosphere than for harder materials. Hence, the material is affected for a longer time via atmospheric interaction and can be transported in lateral directions during this time. In contrast, ejecta masses with low ejection angles, which are typical for harder materials, are decelerated by atmospheric interaction and are immediately deposited at shorter distances due to the low altitudes reached. It is difficult to judge which of the two aspects – target properties or atmospheric interaction – is more important when simulating the ejecta distribution of a crater. Atmospheric interaction depends on the particle size and the size-frequency distribution of ejected material, as fine dust can survive for a longer time in the atmosphere. As shown before, atmospheric interaction depends also on the amount of ejected material and, as such, on the size scale of the impact, what makes it difficult to weigh both aspects against each other. However, there are aspects that can be described only when accounting for atmospheric interaction, such as the occurrence of crater fall-back material. Further aspects that can indicate atmospheric interaction are a size sorting, due to

the small deposition velocities of fine dust compared to larger fragments, or an irregular appearance of the deposit due to material agglomeration during flight.

10.2 Discussion and Limitations

Material properties of natural materials span strong competent rocks with low porosity (e.g. solid rocks, solidified lava, etc.) to soft granular materials with a significant amount of porosity (e.g. sand, regolith). In my approach, I use a Drucker-Prager parameterisation in order to describe the material rheology. The Drucker-Prager parameterisation describes the behaviour of a granular material. Granular materials were used in numerous studies on impact ejection (e.g. Cintala et al. 1999; Anderson and Schultz 2003; Hermalyn and Schultz 2010), and validating the simulation results against such experimental observations yields accurate results. Even though no complex failure model is included, the Drucker-Prager rheology in combination with the ε-α porosity-compaction model allows for varying parameters over a wide range and for setting up a parameter study. Many natural materials on various objects in space (e.g. regolith surfaces, or planetary deserts, just to mention a few) should fall into the range of parameters covered. I expanded the range of materials to very cohesive materials that serve to mimic the material behaviour of competent rock. A more realistic description of a competent rock, e.g. in geologic units with solidified lava, could be reached by using a more complex rheology model as discussed in chapter 6, which allows for materials to fail and, eventually, allows for a reduction of strength in the damaged state. However, on a larger scale, competent rocks show fractures, so their material behaviour might again be able to be approximated by a granular rheology model, and the results of this thesis should be applicable. Furthermore, the occurrence of fractures or pore spaces on a larger scale reduces the bulk material strength, and the material will fail first at these weak points. In contrast, on laboratory scale, the strength of a competent rock must be assumed to be much harder than on a natural scale.

Natural materials behave differently according to their thermal state (temperature, inner energy). Impacts into ice will cause significant vaporisation and melting, which affects the ejection characteristics. Similar thermal effects can be expected to occur when studying the ejecta at early times in the history of the solar system, when planetary interiors were hotter than today. In my study, I did not focus on such thermal aspects. Hence, when icy surfaces, such as on the Moons of the gas giants or planetary polar regions, are of interest, the study of ejection behaviour should be expanded to include a thermal dimension. For example, Senft and Stewart (2008) derived ejection angles and speeds for targets on Mars with i) no ice, ii) a surface with an ice layer, and iii) a buried ice layer. They observe a significant increase of ejection angles for scenario ii) and even more for scenario iii), which can partly be attributed to differences in the target rheology (including an earlier onset of thermal softening for ice), and also partly to the equation of state of ice that is used. Approximating the trend based on my results, I would expect that an increase of the melt fraction/temperature of the target material would reduce the total strength of the target and change its ejection properties in a similar way as shown for weaker targets with a lower coefficient of friction (i.e. larger ejection angles, slower decrease of ejection velocities with distance). However, for a quantitative analysis of such thermal aspects, thermal profiles and reliable equations of state have to be used in order to conduct detailed modelling studies.

Impact events occur on scales that range from small micro-impacts to large or giant impacts. Early in the history of the solar system, large cratering events occurred much more often than today. On the scale of large impacts, the target shows some curvature that needs to be taken into account for the analysis of ejecta deposition. Furthermore, the assumption of a constant vertical gravity field might not hold true anymore, and a realistic radial gravity field with dependence on the radial distance from the centre needs to be applied. To answer my first key question *S I*, I developed an ejecta analysis routine focusing on events on a small scale below complex crater formation. Using the dimensionless representation of the ejection

characteristics, the results derived in this study can also be applied to large cratering events. However, for analysing ejection dynamics in large-scale models directly, the ejection routine used so far needs to be further developed to include the surface curvature during ejection from spherical targets to guarantee a correct interpolation of ejecta to its launch position. This issue becomes even more important for an accurate determination of the deposition position of the ejecta, which may reach to large distances of hundreds to thousands of kilometres, where the effect of planetary curvature on the deposition location becomes more important. Furthermore, gravitational (vertical) deceleration of ejected material needs to be accounted for when using the interpolation algorithm for deriving the ejecta launch position for large-scale impacts. In the scenario shown to answer the first key question *S I* (chapter 8), these effects are negligible. However, when the ejection criterion is set at an altitude of one projectile radius for a projectile that itself is on the order of several hundred kilometres, the vertical component of the ejection velocity at this altitude is smaller than at the surface level, and gravitational deceleration needs to be accounted for. In addition, large-scale impacts will produce a significant amount of ejecta on trajectories that leave the proximal range where the constant gravity approximation does not hold true anymore. In such a case, trajectories need to be calculated with more effort using the radial symmetric gravity field.

Once the ejected material lands back on the ground, it interacts with the target and transforms it. Ejected rocks form individual secondary craters. Fast ejected material modifies the target, and the ejecta blanket is characterised by local admixture of target material (Hüttner 1969; Oberbeck 1975; Hörz et al. 1983). As deposition velocities increase with increasing distance from the crater (inverse order with respect to launch velocities), this effect, called ballistic sedimentation, is more pronounced at larger distances (note, though, that the ejecta thickness decreases with distance). A further modification process occurs due to complex crater formation. Close to the crater rim, crater modification can cause sliding of ejected material and modify the ejecta blanket, as the crater grows in the radial direction. Such effects need to be discussed to answer the key questions *S I* & *S II*

(chapter 8 & 9). In my study, I discuss ejecta deposits but neglect any modification effects to the ejecta blanket. Thus, the approach does not consider material transformation or further movement after the ejected material is deposited, and slumping of the transient crater walls and the whole crater formation are not included in the calculation. However, for materials that fall into a typical range of parameters for planetary materials, recent studies have shown a good correlation between simulations and laboratory experiments, or simulations and observations of natural craters even when ejecta-related material modification is not accounted for (Zhu et al. 2015; Wünnemann et al. 2016). Furthermore, Zhu et al. (2015) assessed the effect of material sliding close to the crater rim: the ejecta thickness decreases by 5-15% only close to the crater rim (within a distance of 1.2 transient crater radii) for large lunar craters. Furthermore, when answering the second key question *S II – Ejecta and Atmosphere*, modification processes are less important because atmospheric interaction effectively reduces the deposition velocities. The area of deposition with velocities close to the vacuum deposition velocities is limited to a proximal range close to the crater rim where ejecta deposition velocities are low. However, for blanket modifications, high deposition velocities are required; this means that atmospheric interaction reduces the amount of modification. For future studies, the modelling results shown above can provide initial conditions (e.g. deposition velocities) that can be used as input for further modelling work that accounts for blanket modifications. Nevertheless, the derived thicknesses of ejecta blankets for granular and rocky materials are expected to be reliable as shown by experimental/observational comparisons from previous studies (Zhu et al. 2015; Wünnemann et al. 2016; Zhu et al. 2017). The results give an indication of the importance of target properties and atmosphere for the shape of the ejecta blankets.

There are materials for which modification processes might be more important. It can be assumed that modification processes themselves depend on the target properties that I have used as initial set-up for the study of ejection dynamics. For example, a more rigid target with a high coefficient of friction and some cohesion can be expected to show less modification

and less material sliding into the crater than a weaker target. The same can be assumed for the resistance against ballistic sedimentation. In contrast, very soft materials with a low coefficient of friction might be unstable over the long term when deposited as an ejecta blanket, and post-deposition modification can be expected to be more important for these materials. However, such materials do not represent nowadays geologic (rocky) materials on planetary bodies and moons. A discussion on modification processes is rather important when ejecta deposits are discussed on icy moons, polar caps, or for ancient hot rocks in early times of the solar system. These materials are less strong, and their resistance against deformation is smaller. Long-term effects of relaxation should be considered for such materials. However, such systems were not the focus of my study, but are very interesting topics for future studies.

Natural impact events occur at all impact angles from 0° to 90°, and the most probable impact angle is 45°. The impact angle has an effect on the ejection dynamics and the deposition of the material: With a decreasing impact angle, oblique impacts show a transition from circular ejecta patterns towards a butterfly pattern (Shuvalov 2011). Early ejecta in the downrange direction is characterised by a larger ejection velocity and lower ejection angles relative to the vertical impact scenario (Anderson and Schultz 2003; Anderson et al. 2004; Shuvalov 2011). However, deviations are scale dependent: whereas an impact angle of 45° has little effect in a scenario with a projectile smaller than 100 m in diameter, the same impact angle causes a significant difference in the ejecta blanket pattern of a 10-km-diameter projectile impact scenario (Shuvalov 2011). Strictly speaking, the answers to key questions *S I* & *S II* on ejecta deposition apply only for vertical impact scenarios due to the 2D-cylindrical symmetry that was used in the simulation. However, the studies to answer *S I* & *S II* are parameter studies, which aim to discuss the effect of target properties and atmospheric interactions in general. Even though differences in the quantitative result for a given impact angle might deviate from the results for a vertical scenario, I expect qualitatively similar results for the variation of the parameters that have been addressed by the two studies (e.g. target strength, particle size

distribution of ejecta) for one fixed impact angle. Determining the effect of impact angles in conjunction with the other effects is an important next step for better understanding the processes of ejecta blanket formation in nature. However, the study of full three-dimensional scenarios requires further improvements to the iSALE-3D code, including expanding the representative particle code to three dimensions. In principle, the code can be easily expanded to 3D. In vacuum, the ejecta analysis script needs to be extended to 3D by accounting for ejecta trajectories into each radial direction independently. Consequently, the ejecta blanket would require the analysis of deposited ejecta for individual circular sectors on the surface around the crater. Instead of the rotational symmetry along the vertical axis (cylindrical symmetry), the impactor trajectory acts as a symmetry axis (line symmetry). In particular, studying individual craters and their ejecta deposits requires the implementation of the tools used in this study into 3D. Nonetheless, for parameter studies, 2D simulations are still preferable due to the large computational costs of 3D models. Based on the results for 100 m-sized projectiles from Shuvalov (2011), the results for the 2D-cylindrical symmetric scenarios are expected to give accurate results or at least good approximations to the results for impacts with impact angles larger than 45° (which would cover already about 50% of the impact events based on the probability of impact angles, c.f. Pierazzo and Melosh 2000).

In nature, target properties and the presence of an atmosphere both affect ejection dynamics and deposition. To answer my key questions *S I* & *S II*, I focused on each of these effects individually. But, to study an individual impact structure, both effects need to be combined. This can be done by using the scaling parameters derived for different target materials in order to produce ejected material in the atmospheric interaction models that shows the ejection characteristics of the corresponding target material. Another more sophisticated step for combining both aspects (target properties and atmospheric interaction) is to directly produce representative particles from real impact models instead of scaling relationships. This approach is more complex and more accurate than using scaling laws. I implemented the translation from solid continuum material to representative

particles into iSALE, but to determine the effect of dust sizes, I used the simpler but computationally cheaper approach of injecting representative particles by scaling laws. Especially when shock waves have decayed, the larger sound speed in solid materials can increase the computation time because more iterations are required by the Courant criterion relative to a model with only atmospheric gases to cover the same absolute time. For a parameter study, such simplifications work well. However, especially when aiming at simulating a specific crater, a fully coupled approach seems more appropriate to tackle the objective of such a study.

Material that is expelled from a forming crater has been subject to a range of shock pressures, and material that has seen high shock pressures is severely damaged; a few of the consequences are fracturing and grain disruption. Hence, ejected material shows a variety of grain sizes. The grain size is an important factor when discussing ejecta trajectories in an atmosphere, as shown in my study focussing on key question *S II*. However, in this study, I only show results for model runs with equal grain sizes (with one exception). An important improvement is to use a whole set of different grain sizes within one model run. In addition, the determination of the grains sizes should be coupled to the pressure history of the ejected material based on a physical model. Modelling different grain sizes within one simulation allows small grains to travel to farther distances within the wake of bigger chunks. Nonetheless, the qualitative trends derived for models with individual particle sizes are expected to hold true.

Although there are limitations to the results shown in this thesis, the approximations and assumptions were chosen carefully, and the results are expected to be applicable in many scenarios, as discussed in the previous paragraphs. The Drucker-Prager rheology model in combination with the ε-α porosity-compaction model can be applied to study the ejection characteristics for many planetary materials. The deposition of the ejected material depends on the presence of an atmosphere. In such cases, the size of dust particles plays an important role for the deposition. Although the size-frequency distribution of dust particles in general is unknown, I was able to provide results for individual size classes of dust, which improve the

understanding of ejection and deposition processes. The derived deposits for both vacuum and non-vacuum cases are cylindrically symmetric. Although the impact angle is an important variable that influences the final deposition, especially for early ejected material, the deposition pattern of the proximal, continuous ejecta blanket is affected less by impact angles down to intermediate values of the angle, as shown above.

Hence, the results of this study are expected to be applicable to a wide range of scenarios; some of which I will address in the next section.

10.3 Conclusions & Outlook

In this thesis, I provide results for parameter studies on ejection processes in vacuum or in cases where an atmosphere is present. The key questions of this thesis are of a more general nature. However, the results can be applied to more specific questions and are relevant in several respects.

Studying the ejection behaviour for different target properties is crucial for assessing the possibility of deflecting a hazardous asteroid. Different techniques of asteroid deflection are discussed in the literature, including e.g. impacts (e.g. Eggl et al. 2015), nearby nuclear explosions (Ahrens and Harris 1992) or gravity traction.

Kinetic impactors work by transferring momentum onto the target asteroid in order to change its trajectory. Momentum transfer is imparted of course, by the impacting spacecraft, but it is also, and more importantly, caused via the momentum carried away by ejected material (e.g. Jutzi and Michel 2014). The momentum that is carried by the ejected material depends on the mass, the angle and velocity with which the material is expelled from the crater. These values depend on the target properties. Asteroids can show a variety of different properties (e.g. porosity/density) even for the same body, as e.g. in the case of Itokawa (Lowry et al. 2014). The results for answering my key question *S I – Ejecta and Target Properties* can be used to calculate the momentum transfer onto an asteroid once the target properties are known.

Recently, a kinetic impactor mission called AIDA was proposed (e.g. Cheng et al. 2016). The mission is run by both NASA (the impactor mission itself, called DART, planned lift off in 2021) and ESA (a mission to study the outcome of the impact, called HERA, planned lift off 2023). One of the aims of this mission is to observe the momentum transfer onto the small moon of the asteroid Didymos and the subsequent change of its orbit around the parent body. By studying the crater morphology, the target properties shall be derived by comparison with experimental and numerical results.

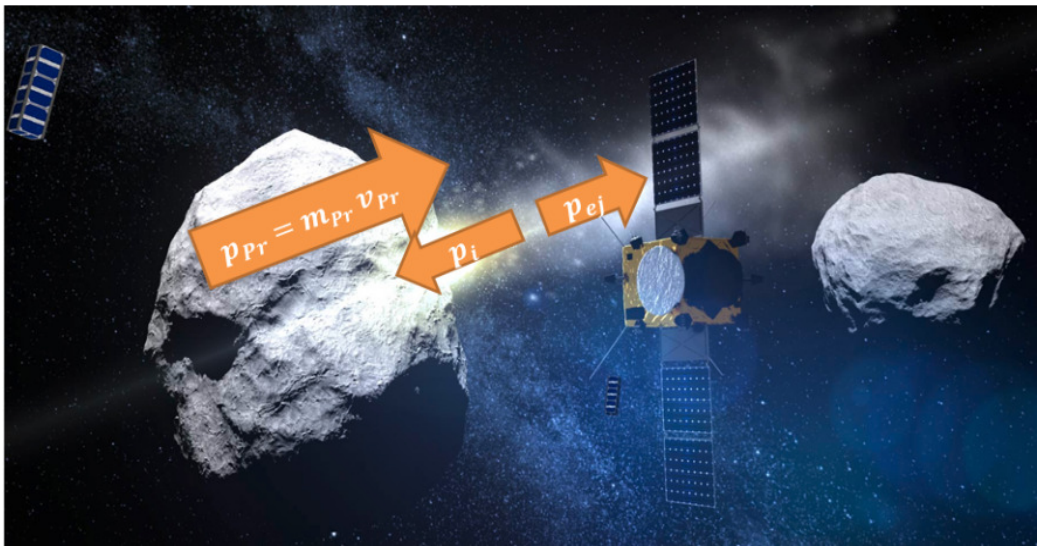

Figure 10-1: Representation of momentum multiplication factor. The asteroid momentum p_{Pr} changes due to the momentum transmitted from an impactor. But, in addition, momentum is carried away from the asteroid by the ejected material. Image credit: ESA/ Science Office.

The momentum transfer enhancement by ejecta is described with the momentum multiplication factor β_p (cf. Figure 10-1):

$$\beta_p = 1 + \frac{p_{ej}}{m_{Pr} v_{Pr}} \quad , \tag{106}$$

where p_{ej} is the momentum carried by the ejecta in the direction opposite of the impactor, and m_{Pr} and v_{Pr} are the mass and velocity of the impactor, respectively. If there is no ejecta, β_p = 1 and only the momentum of the impactor is transferred to the target body. The momentum of the ejecta, p_{ej},

strongly depends on the flight direction of the ejecta. For the 2D simulations of vertical impacts that I conducted to answer the key question *S I* (chapter 8), p_{ej} is directed upwards from the target and depends only on the vertical velocity component of the ejecta velocity vector (i.e. on the ejection angle). As such, target properties strongly influence the success of an asteroid deflection mission. I showed that an increase in material strength of granular materials causes i) a reduction of ejected mass, ii) a reduction of ejection speeds at intermediate to distant launch positions, and iii) a decrease of ejection angles. All three findings lead to a decrease of the momentum carried by the ejected material and, consequently, reduce the momentum multiplication factor. Furthermore, my findings for increasing target porosity show i) a reduction of ejection speed between proximal and intermediate launch positions, and ii) roughly constant ejection angles at 45°. Hence, the momentum multiplication factor decreases with increasing porosity.

In my study, I also assessed the effect of increasing the impact velocity for impacts with constant impact energy into equal targets. I find i) roughly similar ejection velocity distributions, ii) an increase of ejected mass (with larger ejection velocities) at very proximal launch positions, and iii) an increase of ejection angles. These findings lead to the conclusion that for a given impact energy, the momentum multiplication factor increases with impact velocity. This correlation might be important for future asteroid deflection missions. The momentum multiplication of the scenario with larger impact velocity could resemble a case of lower material strength and could be more effective than a low-velocity impactor.

For future asteroid deflection scenarios, the transfer of momentum and, consequently, the change of collisional trajectories of an asteroid could be improved if a kinetic impactor mission is accompanied by some precursor mission with the aim of actively changing the properties of the material at the impact point. Probably, it would be effective to have a double impact, where the first impactor, prior to the impact of the second impactor, modifies the target properties by, e.g. material melting, or target compaction and reduction of the target porosity. This scenario could be more effective

than a single-projectile scenario in which the single projectile weighs as much as the two individual impactors taken together; note that mass is one of the critical parameters for space missions in terms of transportation (or lift up) costs.

A different application for the findings of this thesis might be the analysis of lunar impact flashes, which aim to improve our understanding of the population of decimetre- to metre-sized objects that cross the Earth-Moon system and to investigate the potential threat posed by impact events and their ejecta on future lunar habitats. In the past two decades, scientific interest has arisen in observing impact flashes on the Moon via Earth-bound observing systems. One of the main driving interests is to use the Moon as a large detection area for relatively "cheap" observing systems. Impact flashes occur at hypervelocity impacts of meteoroids onto the atmosphereless lunar surface. Over 300 flashes were observed between 2006 and 2013 alone by the NASA Marshall Space Flight Center (Suggs et al. 2014). Most flashes are of short duration (some tens of milliseconds) and are thought to originate from hot impact plumes (Melosh et al. 1993; Ortiz et al. 2000; Artemieva et al. 2001). However, the observation of long-lasting flashes requires researchers to find different explanations for the origin of the radiated light. Yanagisawa and Kisaichi (2002) and later on Bouley et al. (2012) used a model of ejected, impact-generated, radiating melt droplets to explain the duration of longer-lasting flashes of several hundreds of milliseconds. Following their idea, the amount of generated melt can be calculated by numerical modelling via analysing the temperature distribution in ejected material (see Luther et al. 2017b for first attempts). Furthermore, trajectories of hot ejecta could be calculated to assess the size and evolution of the radiating impact plume. The evolution of the impact plume correlates with its optical properties, such as its optical thickness. The influence of a vapour phase on these trajectories can be simulated by the approach used to answer my second key question *S II – Ejecta and Atmosphere*. Future studies are needed to enhance our understanding of the processes that cause impact flash.

In principle, these topics can be studied with the numerical tools available. However, further development is required for studying the effect of the impact angle on ejection trajectories in a vacuum or in an atmosphere or vapour phase, as discussed in section 10.2.

Apart from the two applications of asteroid deflection and impact flash observations mentioned above, analysing the effects of target properties on ejection characteristics and material deposition is important for many other scenarios.

It is possible that such an analysis of an ejecta blanket would offer information about the properties of the geological unit on a planetary body in which an impact crater is located, by combining the analysis with remote sensing observations. Local material analysis and observations require a space mission with a landing unit that deploys some geophysical experiments. However, it is not feasible to undertake such missions for a large number of different landing locations.

The study of material transport, which plays an important role when local samples have to be correlated with a location of origin, requires knowledge of the ejection characteristics. Target properties influence the distance at which material is deposited by affecting the ejection angle and speed. Specifically, they could be used either to exclude potential source locations of an age-dated rock sample or to correlate the samples with a source location. In this way, the formation age of the source location can be estimated and used as a calibration for the relative ages determined by crater counting ages in a particular area.

Combining results for both key questions *S I & II*, *Ejecta and Target Properties* and *Ejecta and Atmosphere*, offers the opportunity to study the effects of large past impacts on Earth. Specific questions aim at estimating the amount of ejected dust, the time that the dust stayed in the atmosphere, and global consequences of the dust coverage, or ejecta re-entry into the atmosphere, which could have caused further consequences due to radiative heating or the formation of atmospheric blast waves. On Earth, such questions can be linked to the study of mass extinction events on a large

scale or to local events that affect life on smaller scales. Nevertheless, similar studies about ejecta and dust distributions on planetary bodies that possess an atmosphere would be interesting for Venus, (early) Mars, or Saturn's moon Titan, as large impact events could have also had global effects on these bodies.

Studying ejection processes and ejecta movement is a key to answer scientifically important questions that address the formation of individual impact structures, but also to answer questions that focus on more general processes that occur during the evolution of the planetary system. Besides pure scientific questions, the study of material ejection is also of practical interest for aspects of planetary defence and asteroid deflection scenarios.

11 Bibliography

Ahrens T. J. and Harris A. W. 1992. Deflection and fragmentation of near-Earth asteroids. *Nature* 360:429–433.

Ai H.-A. and Ahrens T. J. 2004. Dynamic tensile strength of terrestrial rocks and application to impact cratering. *Meteoritics & Planetary Science* 39(2):233–246. doi:10.1111/j.1945-5100.2004.tb00338.x.

Alvarellos J. L., Zahnle K. J., Dobrovolskis A. R., and Hamill P. 2008. Transfer of mass from Io to Europa and beyond due to cometary impacts. *Icarus* 194(2):636–646. doi:10.1016/j.icarus.2007.09.025.

Alvarez L. W., Alvarez W., Asaro F., and Michel H. V. 1980. Extraterrestrial Cause for the Cretaceous-Tertiary Extinction. *Science* 208(4448):1095–1108.

Amsden A., Ruppel H., and Hirt C. 1980. *SALE:: A simplified ALE computer program for fluid flow at all speeds*. Los Alamos National Laboratories Report LA-8095.

Anderson C. E. 1987. An Overview of the theory of Hydrocodes: f. *International Journal of Impact Engineering* 5:33–59.

Anderson J. L. B., Cintala M. J., Siebenaler S. A., and Barnouin-Jha O. S. 2007. Ejecta- and Size-Scaling Considerations from Impacts of Glass Projectiles into Sand. *Proceedings of the Lunar and Planetary Science Conference* 38:2266.

Anderson J. L. B. and Schultz P. H. 2003. Asymmetry of ejecta flow during oblique impacts using three-dimensional particle image velocimetry. *Journal of Geophysical Research* 108(E8):3987. doi:10.1029/2003JE002075.

Anderson J. L. B. and Schultz P. H. 2006. Flow-field center migration during vertical and oblique impacts. *International Journal of Impact Engineering* 33(1-12):35–44. doi:10.1016/j.ijimpeng.2006.09.022.

Anderson J. L. B., Schultz P. H., and Heineck J. T. 2004. Experimental ejection angles for oblique impacts: Implications for the subsurface

flow-field. *Meteoritics & Planetary Science* 39(2):303–320. doi:10.1111/j.1945-5100.2004.tb00342.x.

Arakawa M. and Yasui M. 2011. Impact crater formed on sintered snow surface simulating porous icy bodies. *Icarus* 216(1):1–9. doi:10.1016/j.icarus.2011.08.018.

Artemieva N. and Morgan J. 2017. Quantifying the Release of Climate-Active Gases by Large Meteorite Impacts With a Case Study of Chicxulub. *Geophysical Research Letters* 44(20):10,180-10,188. doi:10.1002/2017GL074879.

Artemieva N. A. and Ivanov B. A. 2004. Launch of martian meteorites in oblique impacts. *Icarus* 171(1):84–101. doi:10.1016/j.icarus.2004.05.003.

Artemieva N. A., Kosarev I. B., Nemtchinov I. V., Trubetskaya I. A., and Shuvalov V. V. 2001. Light Flashes Caused by Leonid Meteoroid Impacts on the Lunar Surface. *Solar System Research* 35(3):195–198.

Artemieva N. A. and Shuvalov V. V. 2001. Motion of a fragmented meteoroid through the planetary atmosphere. *Journal of Geophysical Research: Planets* 106(E2):3297–3309. doi:10.1029/2000JE001264.

Artemieva N. A., Wünnemann K., Krien F., Reimold W. U., and Stöffler D. 2013. Ries crater and suevite revisited-Observations and modeling Part II: Modeling. *Meteoritics & Planetary Science* 48(4):590–627. doi:10.1111/maps.12085.

Austin M. G., Thomsen J. M., Ruhl S. F., Orphal D. L., Borden W. F., Larson S. A., and Schultz P. H. 1981. Z-model analysis of impact cratering:: An overview. *Proceedings of the Lunar and Planetary Science Conference* 12:197–205.

Badyukov D. D. and Dudorov A. E. 2013. Fragments of the Chelyabinsk meteorite shower: Distribution of masses and sizes and constraints on the mass of the largest fragment. *Geochemistry International* 51(7):583–586. doi:10.1134/S0016702913070070.

Barber D. J. and Wenk H.-R. 1979. Deformation twinning in calcite, dolomite, and other rhombohedral carbonates. *Physics and Chemistry of Minerals* 5(2):141–165. doi:10.1007/BF00307550.

Barlow N. G. 1994. Sinuosity of Martian rampart ejecta deposits. *Journal of Geophysical Research* 99(E5):10927. doi:10.1029/94JE00636.

Barnouin-Jha O. S. and Schultz P. H. 1996. Ejecta entrainment by impact-generated ring vortices:: Theory and experiments. *Journal of Geophysical Research* 101(E9):21,099-21,115.

Bland P. A. and Artemieva N. A. 2006. The rate of small impacts on Earth. *Meteoritics & Planetary Science* 41(4):607–631.

Boothroyd R. G. 1971. *Flowing Gas-Solid Suspensions*. London: Chapman and Hall.

Borg L. E., Brennecka G. A., and Symes S. J.K. 2016. Accretion timescale and impact history of Mars deduced from the isotopic systematics of martian meteorites. *Geochimica et Cosmochimica Acta* 175:150–167. doi:10.1016/j.gca.2015.12.002.

Borovička J., Spurný P., Brown P. G., Wiegert P., Kalenda P., Clark D., and Shrbený L. 2013. The trajectory, structure and origin of the Chelyabinsk asteroidal impactor. *Nature* 503(7475):235–237.

Bouley S., Baratoux D., Vaubaillon J., Mocquet A., Le Feuvre M., Colas F., Benkhaldoun Z., Daassou A., Sabil M., and Lognonné P. 2012. Power and duration of impact flashes on the Moon: Implication for the cause of radiation. *Icarus* 218(1):115–124. doi:10.1016/j.icarus.2011.11.028.

Bronikowska M., Artemieva N. A., and Wünnemann K. 2017. Reconstruction of the Morasko meteoroid impact-Insight from numerical modeling. *Meteoritics & Planetary Science* 52(8):1704–1721. doi:10.1111/maps.12882.

Brugger J., Feulner G., and Petri S. 2017. Baby, it's cold outside: Climate model simulations of the effects of the asteroid impact at the end of the Cretaceous. *Geophysical Research Letters* 44(1):419–427. doi:10.1002/2016GL072241.

Buhl E., Poelchau M. H., Dresen G., and Kenkmann T. 2013. Deformation of dry and wet sandstone targets during hypervelocity impact experiments, as revealed from the MEMIN Program. *Meteoritics & Planetary Science* 48(1):71–86. doi:10.1111/j.1945-5100.2012.01431.x.

Buhl E., Poelchau M. H., Dresen G., and Kenkmann T. 2014a. Scaling of sub-surface deformation in hypervelocity impact experiments on porous sandstone. *Tectonophysics* 634:171–181. doi:10.1016/j.tecto.2014.07.030.

Buhl E., Sommer F., Poelchau M. H., Dresen G., and Kenkmann T. 2014b. Ejecta from experimental impact craters: Particle size distribution and fragmentation energy. *Icarus* 237:131–142. doi:10.1016/j.icarus.2014.04.039.

Burchell M. J. and Whitehorn L. 2003. Oblique incidence hypervelocity impacts on rock. *Monthly Notices of the Royal Astronomical Society* 341(1):192–198. doi:10.1046/j.1365-8711.2003.06385.x.

Burkhard M. 1993. Calcite twins, their geometry, appearance and significance as stress-strain markers and indicators of tectonic regime: a review. *Journal of Structural Geology* 15(3-5):351–368. doi:10.1016/0191-8141(93)90132-T.

Campo Bagatin A., Farinella P., and Petit J.-M. 1994. Fragment ejection velocities and the collisional evolution of asteroids. *Planetary and Space Science* 42(12):1099–1107. doi:10.1016/0032-0633(94)90010-8.

Carroll M. M. and Holt A. C. 1972. Static and Dynamic Pore-Collapse Relations for Ductile Porous Materials. *Journal of Applied Physics* 43(4):1626–1636. doi:10.1063/1.1661372.

Cheng A. F., Michel P., Jutzi M., Rivkin A. S., Stickle A., Barnouin O. S., Ernst C. M., Atchison J., Pravec P., and Richardson D. C. 2016. Asteroid Impact & Deflection Assessment mission:: Kinetic impactor. *Planetary and Space Science* 121:27–35. doi:10.1016/j.pss.2015.12.004.

Chyba C. F., Thomas P. J., and Zahnle K. J. 1993. The 1908 Tunguska explosion:: Atmospheric disruption of a stony asteroid. *Nature* 361:40–44.

Cintala M. J., Berthoud L., and Hörz F. 1999. Ejection-velocity distributions from impacts into coarse-grained sand. *Meteoritics & Planetary Science* 34(4):605–623. doi:10.1111/j.1945-5100.1999.tb01367.x.

Collins G. S. 2014. Numerical simulations of impact crater formation with dilatancy. *Journal of Geophysical Research: Planets* 119(12):2600–2619. doi:10.1002/2014JE004708.

Collins G. S., Elbeshausen D., Davison T. M., Wünnemann K., Ivanov B. A., and Melosh H. J. 2017. *iSALE-Dellen manual*.

Collins G. S., Kenkmann T., Osinski G. R., and Wünnemann K. 2008. Mid-sized complex crater formation in mixed crystalline-sedimentary targets:: Insight from modeling and observation. *Meteoritics & Planetary Science* 43(12):1955–1977. doi:10.1111/j.1945-5100.2008.tb00655.x.

Collins G. S. and Melosh H. J. 2002. *SALES 2: A multi-material extension to the SALE hydrocode with improved equation of state and constitutive model*.

Collins G. S., Melosh H. J., and Ivanov B. A. 2004. Modeling damage and deformation in impact simulations. *Meteoritics & Planetary Science* 39(2):217–231.

Collins G. S., Melosh H. J., and Wünnemann K. 2011. Improvements to the ε-α porous compaction model for simulating impacts into high-porosity solar system objects. *International Journal of Impact Engineering* 38(6):434–439. doi:10.1016/j.ijimpeng.2010.10.013.

Collins G. S., Wünnemann K., Artemieva N., and Pierazzo E. 2013. Numerical Modelling of Impact Processes. In *Impact cratering: Processes and products*, edited by Osinski G. R. and Pierazzo E. Chichester, West Sussex: Wiley-Blackwell. pp. 254–270.

Colwell J. E., Batiste S., Horányi M., Robertson S., and Sture S. 2007. Lunar surface:: Dust dynamics and regolith mechanics. *Reviews of Geophysics* 45(2):7420. doi:10.1029/2005RG000184.

Croft S. K. 1980. Cratering flow fields:: Implications for excavation cavities, transient cavities, and depth of excavation. *(Abstract)* 11th Lunar and Planetary Science Conference. Lunar and Planetary Institute, LPI, Houston:180–183.

Croft S. K. 1985. The scaling of complex craters. *Journal of Geophysical Research* 90(S02):C828. doi:10.1029/JB090iS02p0C828.

Davison T. M., Collins G. S., and Bland P. A. 2016. Mesoscale Modeling of Impact Compaction of Primitive Solar System Solids. *The Astrophysical Journal* 821(1):68. doi:10.3847/0004-637X/821/1/68.

Davison T. M., Collins G. S., Elbeshausen D., Wünnemann K., and KEARSLEY A. 2011. Numerical modeling of oblique hypervelocity impacts on strong ductile targets. *Meteoritics & Planetary Science* 46(10):1510–1524. doi:10.1111/j.1945-5100.2011.01246.x.

Dufresne A., Poelchau M. H., Kenkmann T., Deutsch A., Hoerth T., Schäfer F., and Thoma K. 2013. Crater morphology in sandstone targets: The MEMIN impact parameter study. *Meteoritics & Planetary Science* 48(1):50–70. doi:10.1111/maps.12024.

Earth Impact Database. 2016. http://www.passc.net/EarthImpactDatabase/index.html (accessed Accessed April 13, 2016).

Ebert M., Hecht L., Deutsch A., Kenkmann T., Wirth R., and Berndt J. 2014. Geochemical processes between steel projectiles and silica-rich targets in hypervelocity impact experiments. *Geochimica et Cosmochimica Acta* 133:257–279. doi:10.1016/j.gca.2014.02.034.

Ebert M., Hecht L., Hamann C., and Luther R. 2017. Laser-induced melting experiments: Simulation of short-term high-temperature impact processes. *Meteoritics & Planetary Science* 52(7):1475–1494. doi:10.1111/maps.12809.

Eggl S., Hestroffer D., Thuillot W., Bancelin D., Cano J. L., and Cichocki F. 2015. Post mitigation impact risk analysis for asteroid deflection demonstration missions. *Advances in Space Research* 56(3):528–548. doi:10.1016/j.asr.2015.02.030.

Elbeshausen D., Wünnemann K., and Collins G. S. 2009. Scaling of oblique impacts in frictional targets: Implications for crater size and formation mechanisms. *Icarus* 204(2):716–731. doi:10.1016/j.icarus.2009.07.018.

Farinella P. and Davis D. R. 1992. Collision rates and impact velocities in the main asteroid belt. *Icarus* 97(1):111–123. doi:10.1016/0019-1035(92)90060-K.

Fassett C. I. 2016. Analysis of impact crater populations and the geochronology of planetary surfaces in the inner solar system. *Journal of Geophysical Research: Planets* 121(10):1900–1926. doi:10.1002/2016JE005094.

Fassett C. I., Head J. W., Smith D. E., Zuber M. T., and Neumann G. A. 2011. Thickness of proximal ejecta from the Orientale Basin from Lunar Orbiter Laser Altimeter (LOLA) data: Implications for multi-ring basin formation. *Geophysical Research Letters* 38(17):n/a-n/a. doi:10.1029/2011GL048502.

Fazio A., D'Orazio M., Cordier C., and Folco L. 2016. Target–projectile interaction during impact melting at Kamil Crater, Egypt. *Geochimica et Cosmochimica Acta* 180:33–50. doi:10.1016/j.gca.2016.02.003.

Fellin W. 2013. Schneemechanik. In *Einführung in Eis-, Schnee- und Lawinenmechanik*, edited by Fellin W. Berlin, Heidelberg: Springer Berlin Heidelberg. pp. 45–100.

Fernandes V. A., Fritz J., Weiss B. P., Garrick-Bethell I., and Shuster D. L. 2013. The bombardment history of the Moon as recorded by 40 Ar- 39 Ar chronology. *Meteoritics & Planetary Science* 48(2):241–269. doi:10.1111/maps.12054.

Ferziger J. H. and Perić M. 1997. *Computational Methods for Fluid Dynamics. Berlin etc., Springer-Verlag 1996. XIV, 356 pp., DM 74,00. ISBN 3-540-59434-5*. Berlin: Springer. XIV, 423.

Galimov E. M., Kolotov V. P., Nazarov M. A., Kostitsyn Y. A., Kubrakova I. V., Kononkova N. N., Roshchina I. A., Alexeev V. A., Kashkarov L. L., Badyukov D. D., and Sevast'yanov V. S. 2013. Analytical results for the material of the Chelyabinsk meteorite. *Geochemistry International* 51(7):522–539. doi:10.1134/S0016702913070100.

Gault D. E. 1973. Displaced mass, depth, diameter, and effects of oblique trajectories for impact craters formed in dense crystalline rocks. *The Moon* 6(1-2):32–44. doi:10.1007/BF02630651.

Gault D. E. and Heitowit E. D. 1963. The partition of energy for hypervelocity impact craters formed in rock. *Proceedings of the 6th Hypervelocity Impact Symposium* 6:419–456.

Gault D. E., Quaide W. L., and Oberbeck V. R. 1968. Impact Cratering Mechanics and Structures. In *Shock Metamorphism of Natural Materials: Proceedings of the First Conference held at NASA, Goddard Space Flight Center*, edited by French B. M. and Short N. M. Baltimore: Mono Book Corporation. pp. 87–100.

Gindilis L. M. and Shevelev G. N. 2014. Analysis of snow in Chelyabinsk area and search of its dust content (in Russian). *Proceedings of Chelyabinsk meteorite – one year on Earth:*266–278.

Gingold R. A. and Monaghan J. J. 1977. Smoothed particle hydrodynamics: Theory and application to non-spherical stars. *Monthly Notices of the Royal Astronomical Society* 181(3):375–389. doi:10.1093/mnras/181.3.375.

Goldin T. J. and Melosh H. J. 2008. Chicxulub Ejecta Distribution: Patchy or Continuous? *Proceedings of the Lunar and Planetary Science Conference* 39:LPI Contribution No. 1391., p.2469.

Goldin T. J. and Melosh H. J. 2009. Planet Earth set to broil:: Thermal Radiation from Chicxulub Ejecta Reentry. *Proceedings of the Lunar and Planetary Science Conference* 40:2342.

Greenberg M. and Ebel D. S. 2012. Properties of original impactors estimated from three-dimensional analysis of whole Stardust tracks. *Meteoritics & Planetary Science* 47(4):634–648. doi:10.1111/j.1945-5100.2012.01356.x.

Groshong R. H. 1972. Strain Calculated from Twinning in Calcite. *Geological Society of America Bulletin* 83(7):2025. doi:10.1130/0016-7606(1972)83[2025:SCFTIC]2.0.CO;2.

Gulde M., Kortmann L., Ebert M., Watson E., Wilk J., and Schäfer F. 2018. Robust Optical Tracking of Individual Ejecta Particles in hypervelocity Impact Experiments. *Meteoritics & Planetary Science*. doi:10.1111/maps.12958.

Güldemeister N. and Wünnemann K. 2017. Quantitative analysis of impact-induced seismis signals by numerical modeling. *Icarus* 296:15–27. doi:10.1016/j.icarus.2017.05.010.

Güldemeister N., Wünnemann K., Durr N., and Hiermaier S. 2013. Propagation of impact-induced shock waves in porous sandstone using mesoscale modeling. *Meteoritics & Planetary Science* 48(1):115–133. doi:10.1111/j.1945-5100.2012.01430.x.

Güldemeister N., Wünnemann K., and Poelchau M. H. 2015. Scaling impact crater dimensions in cohesive rock by numerical modeling and laboratory experiments. In *Large Meteorite Impacts and Planetary Evolution V: Geological Society of America Special Paper*, edited by Osinski G. R. and Kring D. A. pp. 17–29.

Haehnel R. B. and Shoop S. A. 2004. A macroscale model for low density snow subjected to rapid loading. *Cold Regions Science and Technology* 40(3):193–211. doi:10.1016/j.coldregions.2004.08.001.

Hamann C., Hecht L., Ebert M., and Wirth R. 2013. Chemical projectile–target interaction and liquid immiscibility in impact glass from the Wabar craters, Saudi Arabia. *Geochimica et Cosmochimica Acta* 121:291–310. doi:10.1016/j.gca.2013.07.030.

Hamann C., Luther R., Ebert M., Hecht L., Deutsch A., Wünnemann K., Schäffer S., Osterholz J., and Lexow B. 2016. Correlating laser-generated melts with impact-generated melts: An integrated thermodynamic-petrologic approach. *Geophysical Research Letters* 43(20):11. doi:10.1002/2016GL071050.

Harlow F. H. and Amsden A. A. 1975. Numerical calculation of multiphase fluid flow. *Journal of Computational Physics* 17(1):19–52. doi:10.1016/0021-9991(75)90061-3.

Hartmann W. K. 1985. Impact experiments. *Icarus* 63(1):69–98. doi:10.1016/0019-1035(85)90021-1.

Head J. N., Melosh H. J., and Ivanov B. A. 2002. Martian Meteorite Launch:: High-Speed Ejecta from Small Craters. *Science (New York, N.Y.)* 298(5599):1752–1756. doi:10.1126/science.1076469.

Hermalyn B. and Schultz P. H. 2010. Early-stage ejecta velocity distribution for vertical hypervelocity impacts into sand. *Icarus* 209(2):866–870. doi:10.1016/j.icarus.2010.05.025.

Hermalyn B. and Schultz P. H. 2011. Time-resolved studies of hypervelocity vertical impacts into porous particulate targets: Effects of projectile density on early-time coupling and crater growth. *Icarus* 216(1):269–279. doi:10.1016/j.icarus.2011.09.008.

Hermalyn B. and Schultz P. H. 2014. Effects of Target Properties on Impact Ejecta Distributions:: Time resolved Experiments and Computational Benchmarking. *Proceedings of the Lunar and Planetary Science Conference* 45:2791.

Hermalyn B., Schultz P. H., Shirley M., Ennico K., and Colaprete A. 2012. Scouring the surface: Ejecta dynamics and the LCROSS impact event. *Icarus* 218(1):654–665. doi:10.1016/j.icarus.2011.12.025.

Hildebrand A. R., McCausland P. J. A., Brown P. G., Longstaffe F. J., Russell S. D. J., Tagliaferri E., Wacker J. F., and Mazur M. J. 2006. The fall and recovery of the Tagish Lake meteorite. *Meteoritics & Planetary Science* 41(3):407–431. doi:10.1111/j.1945-5100.2006.tb00471.x.

Holsapple K. A. 1981. Coupling parameters in cratering. *Earth & Space Science News - Transactions American Geophysical Union* 62:949.

Holsapple K. A. 1993. The Scaling of Impact Processes in Planetary Sciences. *Annual Review of Earth and Planetary Sciences* 21(1):333–373. doi:10.1146/annurev.earth.21.1.333.

Holsapple K. A. and Schmidt R. M. 1982. On the scaling of crater dimensions: 2. Impact processes. *Journal of Geophysical Research* 87(B3):1849. doi:10.1029/JB087iB03p01849.

Hörz F. 1969. Structural and mineralogical evaluation of an experimentally produced impact crater in granite. *Contributions to Mineralogy and Petrology* 21(4):365–377. doi:10.1007/BF02672808.

Hörz F., Ostertag R., and Rainey D. A. 1983. Bunte Breccia of the Ries:: Continuous deposits of large impact craters. *Reviews of Geophysics and Space Physics* 21(8):1667–1725.

Hörz F., See T. H., Murali A. V., and Blanchard D. P. 1989. Heterogeneous Dissemination of Projectile Materials in the Impact Melts from Wabar Crater Saudi Arabia. *Proceedings of the Lunar and Planetary Science Conference* 19:697–709.

Housen K. R. 1992. Crater ejecta velocities for impacts on rocky bodies. *(Abstract)* 23th Lunar and Planetary Science Conference. Lunar and Planetary Institute, LPI, Houston:555–556.

Housen K. R. and Holsapple K. A. 2011. Ejecta from impact craters. *Icarus* 211(1):856–875. doi:10.1016/j.icarus.2010.09.017.

Housen K. R. and Holsapple K. A. 2012. Craters without ejecta. *Icarus* 219(1):297–306. doi:10.1016/j.icarus.2012.02.030.

Housen K. R., Schmidt R. M., and Holsapple K. A. 1983. Crater ejecta scaling laws:: Fundamental Forms based on Dimensional Analysis. *Journal of Geophysical Research* 88:2485–2499.

Hüttner R. 1969. Bunte Trümmermassen und Suevit. *Geologica Bavarica* (61):142–200.

Ivanov B. A., Deniem D., and Neukum G. 1997. Implementation of dynamic strength models into 2D hydrocodes: Applications for atmospheric breakup and impact cratering. *International Journal of Impact Engineering* 20(1-5):411–430. doi:10.1016/S0734-743X(97)87511-2.

Ivanova M. A., Badyukov D. D., Ryazantsev K. M., Lorenz C. A., Demidova S. I., Sadilenko D. A., Artemieva N. A., Korochantsev A. V., Skripnik A. Y., Ivanov A. V., and Nazarov M. A. 2013. Fall, searching and first study of the Chelyabinsk meteorite. *Meteoritics & Planetary Science* (76th-Annual Meteoritical Society Meeting, Edmonton, Canada (abstract #5366)):76:5366I.

Izidoro A. and Raymond S. N. 2018. *Formation of Terrestrial Planets*.

Jeffers S. V., Manley S. P., Bailey M. E., and Asher D. J. 2001. Near-Earth object velocity distributions and consequences for the Chicxulub impactor. *Monthly Notices of the Royal Astronomical Society* 327(1):126–132. doi:10.1046/j.1365-8711.2001.04747.x.

Jutzi M. and Michel P. 2014. Hypervelocity impacts on asteroids and momentum transfer I. Numerical simulations using porous targets. *Icarus* 229:247–253. doi:10.1016/j.icarus.2013.11.020.

Jutzi M., Michel P., Benz W., and Richardson D. C. 2010. Fragment properties at the catastrophic disruption threshold: The effect of the

parent body's internal structure. *Icarus* 207(1):54–65. doi:10.1016/j.icarus.2009.11.016.

Kadono T. 1999. Hypervelocity impact into low density material and cometary outburst. *Planetary and Space Science* 47:305–318.

Kenkmann T., Artemieva N. A., Wünnemann K., Poelchau M. H., Elbeshausen D., and Prado H. N. d. 2009. The Carancas meteorite impact crater, Peru:: Geologic surveying and modeling of crater formation and atmospheric passage. *Meteoritics & Planetary Science* 44(7):985–1000. doi:10.1111/j.1945-5100.2009.tb00783.x.

Kenkmann T., Collins G. S., and Wünnemann K. 2013. The Modification Stage of Crater Formation. In *Impact cratering: Processes and products*, edited by Osinski G. R. and Pierazzo E. Chichester, West Sussex: Wiley-Blackwell. pp. 60–75.

Kenkmann T., Deutsch A., Thoma K., Ebert M., Poelchau M. H., Buhl E., Carl E.-R., Danilewsky A. N., Dresen G., Dufresne A., Durr N., Ehm L., Große C. U., Gulde M., Güldemeister N., Hecht L., Hiermaier S., Hoerth T., Hamann C., Kowitz A., Langenhorst F., Lexow B., Liermann H.-P., Luther R., Mansfeld U., Moser D., Raith M., Reimold W. U., Sauer M., Schäfer F., Schmitt R. T., Sommer F., Wilk J., Winkler R., and Wünnemann K. 2018. Experimental impact cratering:: A summary of the major results of the MEMIN research unit. *Meteoritics & Planetary Science*. doi:10.1111/maps.13048.

Kenkmann T., Wünnemann K., Deutsch A., Poelchau M. H., Schäfer F., and Thoma K. 2011. Impact cratering in sandstone: The MEMIN pilot study on the effect of pore water. *Meteoritics & Planetary Science* 46(6):890–902. doi:10.1111/j.1945-5100.2011.01200.x.

Kenkmann T., Zwiessler R., Poelchau M. H., Hess S., and Nau S. 2017. Strain-Rate Dependent Brittle Deformation During Impact Cratering. *Meteoritics & Planetary Science* (79th-Annual Meteoritical Society Meeting, Berlin, Germany (abstract #6253)):LPI Contribution No. 1921, id.6253.

Knudsen M. 1910. Eine Revision der Gleichgewichtsbedingung der Gase: Thermische Molekularströmung. *Annalen der Physik* 31(4):205–229.

Korschelt E., Linck G. E., Oltmanns F., Schaum K., Simon H. T., Verworn M., and Teichmann E., editors. 1913. *Handwörterbuch der Naturwissenschaften*. Jena: Verlag von Gustav Fischer.

Kowitz A., Güldemeister N., Reimold W. U., Schmitt R. T., and Wünnemann K. 2013. Diaplectic quartz glass and SiO2 melt experimentally generated at only 5 GPa shock pressure in porous sandstone: Laboratory observations and meso-scale numerical modeling. *Earth and Planetary Science Letters* 384:17–26. doi:10.1016/j.epsl.2013.09.021.

Krüger T., Kenkmann T., and Hergarten S. 2017. Structural uplift and ejecta thickness of lunar mare craters: New insights into the formation of complex crater rims. *Meteoritics & Planetary Science* 52(10):2220–2240. doi:10.1111/maps.12925.

Kurosawa K., Ohno S., Sugita S., Mieno T., Matsui T., and Hasegawa S. 2012. The nature of shock-induced calcite (CaCO3) devolatilization in an open system investigated using a two-stage light gas gun. *Earth and Planetary Science Letters* 337-338:68–76. doi:10.1016/j.epsl.2012.05.022.

Kuznetsov N. M. 1965. *Thermodynamic functions and shock adiabats for air at high temperatures*. Moscow: Mashinostroyenie.

Lacombe O. and Laurent P. 1996. Determination of deviatoric stress tensors based on inversion of calcite twin data from experimentally deformed monophase samples: preliminary results. *Tectonophysics* 255(3-4):189–202. doi:10.1016/0040-1951(95)00136-0.

Lange M. A., Ahrens T. J., and Boslough M. B. 1984. Impact cratering and spall failure of gabbro. *Icarus* 58(3):383–395. doi:10.1016/0019-1035(84)90084-8.

Langenhorst F. 2002. Shock metamorphism of some minerals:: basic introduction and microstructural observations. *Bulletin of the Czech Geological Survey* 77(4):265–282.

Laurent P., Kern H., and Lacombe O. 2000. Determination of deviatoric stress tensors based on inversion of calcite twin data from experimentally deformed monophase samples. Part II. Axial and triaxial

stress experiments. *Tectonophysics* 327(1-2):131–148. doi:10.1016/S0040-1951(00)00165-7.

Lee J. H. and Huang D. 2014. Vehicle–snow interaction: Testing, modeling and validation for combined longitudinal and lateral slip. *Journal of Terramechanics* 55:1–16. doi:10.1016/j.jterra.2014.05.002.

Lindgren P., Lee M. R., Sofe M., and Burchell M. J. 2011. Microstructure of calcite in the CM2 carbonaceous chondrite LON 94101: Implications for deformation history during and/or after aqueous alteration. *Earth and Planetary Science Letters* 306(3-4):289–298. doi:10.1016/j.epsl.2011.04.022.

Lindgren P., Price M. C., Lee M. R., and Burchell M. J. 2013. Constraining the pressure threshold of impact induced calcite twinning: Implications for the deformation history of aqueously altered carbonaceous chondrite parent bodies. *Earth and Planetary Science Letters* 384:71–80. doi:10.1016/j.epsl.2013.10.002.

Lowry S. C., Weissman P. R., Duddy S. R., Rozitis B., Fitzsimmons A., Green S. F., Hicks M. D., Snodgrass C., Wolters S. D., Chesley S. R., Pittichová J., and van Oers P. 2014. The internal structure of asteroid (25143) Itokawa as revealed by detection of YORP spin-up. *Astronomy & Astrophysics* 562:1. doi:10.1051/0004-6361/201322602.

Lundborg N. 1968. Strength of rock-like materials. *International Journal of Rock Mechanics and Mining Sciences* 5:427–454.

Luther R., Artemieva N. A., Ivanova M. A., Lorenz C. A., and Wünnemann K. 2017a. Snow carrots after the Chelyabinsk event and model implications for highly porous solar system objects. *Meteoritics & Planetary Science*. doi:10.1111/maps.12831.

Luther R., Prieur N., Wünnemann K., and Werner S. 2017b. Crater formation and Shock Melt Production for the 17th March 2013 Lunar Impact Flash Event. *Proceedings of the Lunar and Planetary Science Conference* 48(LPI Contribution No. 1964):3012.

Luther R., Zhu M.-H., Collins G. S., and Wünnemann K. 2018. Effect of Target Properties and Impact Velocity on Ejection Dynamics and Ejecta Deposition. *Meteoritics & Planetary Science* 53(Special Issue).

Madiedo J. M., Ortiz J. L., Morales N., and Cabrera-Caño J. 2014. A large lunar impact blast on 2013 September 11. *Monthly Notices of the Royal Astronomical Society* 439(3):2364–2369. doi:10.1093/mnras/stu083.

Maeno N., Nishimura K., and Kaneda Y. 1980. Viscosity and heat transfer in fluidized snow. *Journal of Glaciology* 26(94):263–274. doi:10.3189/S0022143000010807.

Marchi S., Mottola S., Cremonese G., Massironi M., and Martellato E. 2009. A new Chronology for the Moon and Mercury. *The Astronomical Journal* 137(6):4936–4948. doi:10.1088/0004-6256/137/6/4936.

Mason E. A., Malinauskas A. P., and Evans R. B. III. 1967. Flow and Diffusion of Gases in Porous Media. *The Journal of Chemical Physics* 46(8):3199–3216. doi:10.1063/1.1841191.

Massironi M., Simioni E., Marzari F., Cremonese G., Giacomini L., Pajola M., Jorda L., Naletto G., Lowry S., El-Maarry M. R., Preusker F., Scholten F., Sierks H., Barbieri C., Lamy P. L., Rodrigo R., Koschny D., Rickman H., Keller H. U., A'Hearn M. F., Agarwal J., Auger A.-T., Barucci M. A., Bertaux J.-L., Bertini I., Besse S., Bodewits D., Capanna C., Da Deppo V., Davidsson B., Debei S., Cecco M. de, Ferri F., Fornasier S., Fulle M., Gaskell R., Groussin O., Gutiérrez P. J., Güttler C., Hviid S. F., Ip W.-H., Knollenberg J., Kovacs G., Kramm R., Kührt E., Küppers M., La Forgia F., Lara L. M., Lazzarin M., Lin Z.-Y., Lopez Moreno J. J., Magrin S., Michalik H., Mottola S., Oklay N., Pommerol A., Thomas N., Tubiana C., and Vincent J.-B. 2015. Two independent and primitive envelopes of the bilobate nucleus of comet 67P. *Nature* 526(7573):402–405. doi:10.1038/nature15511.

Maxwell D. E. 1977. Simple Z model of cratering, ejection, and the overturned flap. In *Impact and Explosion Cratering*, edited by Roddy D. J., Pepin R. O., and Merrill R. B. New York: Pergamon Press. pp. 1003–1008.

McGetchin T. R., Settle M., and Head J. W. 1973. Radial Thickness Variation in Impact Crater Ejecta:: Implications for Lunar Basin Deposits. *Earth and Planetary Science Letters* 20:226–236.

McNamara S. and Gianchandani Y. B. 2005. On-chip vacuum generated by a micromachined Knudsen pump. *Journal of Microelectromechanical Systems* 14(4):741–746. doi:10.1109/JMEMS.2005.850718.

Melosh H. J. 1984. Impact ejection, spallation, and the origin of meteorites. *Icarus* 59(2):234–260. doi:10.1016/0019-1035(84)90026-5.

Melosh H. J. 1985. Impact Cratering Mechanics:: Relationship between the Shock Wave and Excavation Flow. *Icarus* 62:339–343.

Melosh H. J. 1989. *Impact cratering:: a geologic process*. New York: Oxford Univ. Press. 245 p.

Melosh H. J. 2007. A hydrocode equation of state for SiO_2. *Meteoritics & Planetary Science* 42(12):2079–2098.

Melosh H. J., Artemieva N. A., Golub A. P., Nemtchinov I. V., Shuvalov V. V., and Trubetskaya I. A. 1993. Remote Visual Detection of Impacts on the Lunar Surface. *Proceedings of the Lunar and Planetary Science Conference* 24:975–976.

Melosh H. J. and Goldin T. J. 2008. Heat and drag coefficients for reentry of impact ejecta. *Proceedings of the Lunar and Planetary Science Conference* 49:2457.

Melosh H. J., Ryan E. V., and Asphaug E. 1992. Dynamic fragmentation in impacts: Hydrocode simulation of laboratory impacts. *Journal of Geophysical Research* 97(E9):14735. doi:10.1029/92JE01632.

Moore H. J. and Gault D. E. 1962. *Current tabulation of data from hypervelocity impact experiments*. Semiannual Progress Report February 25, 1961–August 24, 1961, pp. 106–112.

Moore H. J., Gault D. E., and Lugn R. V. 1963. Experimental impact craters in basalt.: Transactions of the American Institute of Mining. *Metallurgical and Petroleum Engineers* 229:258–262.

Moser D., Güldemeister N., Wünnemann K., and Große C. U. 2013. Acoustic Emission Analysis of Experimental Impact Processes in Comparison to Ultrasound Measurements and Numerical Modeling. *Journal of Acoustic Emission* 31:50–66.

Muylaert J. and Berry W. 1998. Aerothermodynamics for Space Vehicles - ESA's Activities and the Challenges. *ESA Bulletin* (96):1–10.

Nemtchinov I. V., Svetsov V. V., Kosarev I. B., Golub A. P., Popova O. P., Shuvalov V. V., Spalding R. E., Jacobs C., and Tagliaferri E. 1997. Assessment of Kinetic Energy of Meteoroids Detected by Satellite-Based Light Sensors. *Icarus* 130(2):259–274. doi:10.1006/icar.1997.5821.

Neri A., Esposti Ongaro T., Macedonio G., and Gidaspow D. 2003. Multiparticle simulation of collapsing volcanic columns and pyroclastic flow. *Journal of Geophysical Research* 108(B4):281. doi:10.1029/2001JB000508.

Neukum G. 1983. Meteoritenbombardement und Datierung Planetarer Oberflächen. Habilitation (Sektion Geophysik, Fakultät für Geowissenschaften), Ludwig-Maximilians Universität, München.

Oberbeck V. R. 1975. The Role of Ballistic Erosion and Sedimentation in Lunar Stratigraphy. *Reviews of Geophysics and Space Physics* 13(2):337–362. doi:10.1029/RG013i002p00337.

Ohnaka M. 1995. A shear failure strength law of rock in the brittle-plastic transition regime. *Geophysical Research Letters* 22(1):25–28. doi:10.1029/94GL02791.

Ormö J., Melero-Asensio I., Housen K. R., Wünnemann K., Elbeshausen D., and Collins G. S. 2015. Scaling and reproducibility of craters produced at the Experimental Projectile Impact Chamber (EPIC), Centro de Astrobiología, Spain. *Meteoritics & Planetary Science* 50(12):2067–2086. doi:10.1111/maps.12560.

Ortiz J. L., Sada P. V., Bellot Rubio L. R., Aceituno F. J., Gutiérrez P. J., and Thiele U. 2000. Optical detection of meteoroidal impacts on the Moon. *Nature* 405(6789):921–923. doi:10.1038/35016015.

Osinski G. R. and Pierazzo E., editors. 2013. *Impact cratering: Processes and products*. Chichester, West Sussex: Wiley-Blackwell. 316 p.

Petrovic J. J. 2001. Review Mechanical properties of meteorites and their constituents. *Journal of Materials Science* 36(7):1579–1583.

Piekutowski A. J. 1980. Formation of bowl-shaped craters. *(Abstract)* 11th Lunar and Planetary Science Conference. Lunar and Planetary Institute, LPI, Houston:2129–2144.

Pierazzo E., Artemieva N. A., Asphaug E., Baldwin E. C., Cazamias J., Coker R., Collins G. S., Crawford D. A., Davison T. M., Elbeshausen D., Holsapple K. A., Housen K. R., Korycansky D. G., and Wünnemann K. 2008. Validation of numerical codes for impact and explosion cratering:: Impacts on strengthless and metal targets. *Meteoritics & Planetary Science* 43(12):1917–1938.

Pierazzo E., Artemieva N. A., and Ivanov B. A. 2005. Starting conditions for hydrothermal systems underneath Martian craters:: Hydrocode modeling. In *Large Meteorite Impacts III*, edited by Kenkmann T., Hörz F., and Deutsch A.

Pierazzo E., Kring D. A., and Melosh H. J. 1998. Hydrocode simulation of the Chicxulub impact event and the production of climatically active gases. *Journal of Geophysical Research* 103(E12):28607–28625. doi:10.1029/98JE02496.

Pierazzo E. and Melosh H. J. 2000. Understanding oblique impacts from experiments, observations, and modeling. *Annual Review of Earth and Planetary Sciences* 28:141–167. doi:10.1146/annurev.earth.28.1.141.

Pike R. J. 1974. Ejecta from large craters on the Moon:: Comments on the Geometric Model of McGetchin et al. *Earth and Planetary Science Letters* 23:265–274.

Poelchau M. H., Kenkmann T., Hoerth T., Schäfer F., Rudolf M., and Thoma K. 2014. Impact cratering experiments into quartzite, sandstone and tuff: The effects of projectile size and target properties on spallation. *Icarus* 242:211–224. doi:10.1016/j.icarus.2014.08.018.

Poelchau M. H., Kenkmann T., Thoma K., Hoerth T., Dufresne A., and Schäfer F. 2013. The MEMIN research unit: Scaling impact cratering experiments in porous sandstones. *Meteoritics & Planetary Science* 48(1):8–22. doi:10.1111/maps.12016.

Poelchau M. H., Michalski C., Deutsch A., Thoma K., Schäfer F., and Kenkmann T. 2015. Experimental cratering in Carrara marble:: Latest Results from the MEMIN research unit. *Proceedings of the Lunar and Planetary Science Conference* 46(LPI Contribution No. 1832):#2447.

Polanskey C. A. and Ahrens T. J. 1990. Impact spallation experiments: Fracture patterns and spall velocities. *Icarus* 87(1):140–155. doi:10.1016/0019-1035(90)90025-5.

Popova O. P., Jenniskens P., Emel'yanenko V., Kartashova A., Biryukov E., Khaibrakhmanov S., Shuvalov V. V., Rybnov Y., Dudorov A. E., Grokhovsky V. I., Badyukov D. D., Yin Q.-Z., Gural P. S., Albers J., Granvik M., Evers L. G., Kuiper J., Kharlamov V., Solovyov A., Rusakov Y. S., Korotkiy S., Serdyuk I., Korochantsev A. V., Larionov M. Y., Glazachev D., Mayer A. E., Gisler G., Gladkovsky S. V., Wimpenny J., Sanborn M. E., Yamakawa A., Verosub K. L., Rowland D. J., Roeske S., Botto N. W., Friedrich J. M., Zolensky M. E., Le L., Ross D., Ziegler K., Nakamura T., Ahn I., Lee J. I., Zhou Q., Li X.-H., Li Q.-L., Liu Y., Tang G.-Q., Hiroi T., Sears D., Weinstein I. A., Vokhmintsev A. S., Ishchenko A. V., Schmitt-Kopplin P., Hertkorn N., Nagao K., Haba M. K., Komatsu M., and Mikouchi T. 2013. Chelyabinsk airburst, damage assessment, meteorite recovery, and characterization. *Science* 342(6162):1069–1073. doi:10.1126/science.1242642.

Prieur N., Rolf T., Luther R., Wünnemann K., Xiao Z., and Werner S. 2017. The effect of target properties on transient crater scaling for simple craters. *Journal of Geophysical Research: Planets* 122:1704–1726.

Raducan S., Luther R., Davison T. M., and Collins G. S. (submitted). The Role of Asteroid Strength, Porosity and Internal Friction in Impact Momentum Transfer. *Icarus*.

Raith M., Ebert M., Pinkert K., and Große C. U. 2018. Nondestructive imaging of hypervelocity impact-induced damage zones beneath laboratory-created craters by means of ultrasound travel-time tomography. *Meteoritics & Planetary Science* 80. doi:10.1111/maps.13113.

Rivard W. W. and Torrey M. D. 1978. *KFIX: A program for transient two dimensional two fluid flow*. Report LA-NUREG-6623.

Robertson P. B. and Grieve R. A. F. 1977. Shock attenuation at terrestrial impact structures. In *Impact and explosion cratering:: Planetary and*

terrestrial implications (Proceedings of the Symposium on Planetary Cratering Mechanics), edited by Roddy D. J., Pepin P. O., and Merill R. B. New York: Pergamon Press. pp. 687–702.

Rybacki E., Evans B., Janssen C., Wirth R., and Dresen G. 2013. Influence of stress, temperature, and strain on calcite twins constrained by deformation experiments. *Tectonophysics* 601:20–36. doi:10.1016/j.tecto.2013.04.021.

Schaller C. J. and Melosh H. J. 1998. Venusian Ejecta Parabolas: Comparing Theory with Observations. *Icarus* 131(1):123–137. doi:10.1006/icar.1997.5855.

Schedl A. 2006. Applications of twin analysis to studying meteorite impact structures. *Earth and Planetary Science Letters* 244(3-4):530–540. doi:10.1016/j.epsl.2006.02.018.

Schmidt R. M. 1980. Meteor Crater:: Energy of formation - Implications of centrifuge scaling. *Proceedings of the Lunar and Planetary Science Conference* 11:2099–2128.

Schneebeli M., Pielmeier C., and Johnson J. B. 1999. Measuring snow microstructure and hardness using a high resolution penetrometer. *Cold Regions Science and Technology* 30(1-3):101–114. doi:10.1016/S0165-232X(99)00030-0.

Schneebeli M. and Sokratov S. A. 2004. Tomography of temperature gradient metamorphism of snow and associated changes in heat conductivity. *Hydrological Processes* 18(18):3655–3665. doi:10.1002/hyp.5800.

Schneider E. and Schäfer F. 2001. Hypervelocity impact research - acceleration technology and applications -. *Advances in Space Research* 28(9):1417–1424. doi:10.1016/S0273-1177(01)00448-3.

Schneider E. and Wagner G. A. 1976. Shatter cones produced experimentally by impacts in limestone targets. *Earth and Planetary Science Letters* 32(1):40–44. doi:10.1016/0012-821X(76)90182-5.

Schröter J. H. 1791. *Selenotopographische Fragmente zur genauern Kenntniss der Mondfläche, ihrer erlittenen Veränderungen und*

Atmosphäre, sammt den dazu gehörigen Specialcharten und Zeichnungen. Lilienthal: by Joh. Georg Rosenbusch.

Schultz P. H. 1988. Cratering on Mercury:: A Relook. In *Mercury: [papers presented at the Mercury Conference, held 6 - 9 Aug. 1986 in Tucson, Ariz.]*, edited by Vilas F. Tucson, Ariz.: Univ. of Arizona Pr.

Schultz P. H. 1992. Atmospheric Effects On Ejecta Emplacement. *Journal of Geophysical Research* 97(E7):11,623-11,662.

Schultz P. H., Eberhardy C. A., Ernst C. M., A'Hearn M. F., Sunshine J. M., and Lisse C. M. 2007. The Deep Impact oblique impact cratering experiment. *Icarus* 190(2):295–333. doi:10.1016/j.icarus.2007.06.006.

Senft L. E. and Stewart S. T. 2008. Impact crater formation in icy layered terrains on Mars. *Meteoritics & Planetary Science* 43(12):1993–2013. doi:10.1111/j.1945-5100.2008.tb00657.x.

Shuvalov V. V. 1999. Multi-dimensional hydrodynamic code SOVA for interfacial flows:: Application to the thermal layer effect. *Shock Waves* 9(6):381–390. doi:10.1007/s001930050168.

Shuvalov V. V. 2011. Ejecta deposition after oblique impacts: An influence of impact scale. *Meteoritics & Planetary Science* 46(11):1713–1718. doi:10.1111/j.1945-5100.2011.01259.x.

Shuvalov V. V. and Dypvik H. 2013. Distribution of ejecta from small impact craters. *Meteoritics & Planetary Science* 48(6):1034–1042. doi:10.1111/maps.12127.

Snape J. F., Curran N. M., Whitehouse M. J., Nemchin A. A., Joy K. H., Hopkinson T., Anand M., Bellucci J. J., and Kenny G. G. 2018. Ancient volcanism on the Moon: Insights from Pb isotopes in the MIL 13317 and Kalahari 009 lunar meteorites. *Earth and Planetary Science Letters* 502:84–95. doi:10.1016/j.epsl.2018.08.035.

Sommer F., Reiser F., Dufresne A., Poelchau M. H., Hoerth T., Deutsch A., Kenkmann T., and Thoma K. 2013. Ejection behavior characteristics in experimental cratering in sandstone targets. *Meteoritics & Planetary Science* 48(1):33–49. doi:10.1111/maps.12017.

Spohn T., Knollenberg J., Ball A. J., Banaszkiewicz M., Benkhoff J., Grott M., Grygorczuk J., Hüttig C., Hagermann A., Kargl G., Kaufmann E.,

Kömle N., Kührt E., Kossacki K. J., Marczewski W., Pelivan I., Schrödter R., and Seiferlin K. 2015. Thermal and mechanical properties of the near-surface layers of comet 67P/Churyumov-Gerasimenko. *Science* 349(6247):aab0464. doi:10.1126/science.aab0464.

Staron P. J., Adams E. E., and Miller D. A. 2014. Nonequilibrium thermodynamics of kinetic metamorphism in snow. *Cold Regions Science and Technology* 97:60–71. doi:10.1016/j.coldregions.2013.10.007.

Stöffler D., Gault D. E., Wedekind J., and Polkowski G. 1975. Experimental hypervelocity impact into quartz sand:: Distribution and shock metamorphism of ejecta. *Journal of Geophysical Research* 80:4062–4077.

Stöffler D. and Ryder G. 2001. Stratigraphy and Isotope Ages of Lunar Geologic Units: Chronological Standard for the Inner Solar System. In *Chronology and Evolution of Mars*, edited by Kallenbach R., Geiss J., and Hartmann W. K. Dordrecht: Springer Netherlands. pp. 9–54.

Sturm M. and Benson C. S. 1997. Vapor transport, grain growth and depth-hoar development in the subarctic snow. *Journal of Glaciology* 43(143):42–59.

Sturm M. and Holmgren J. 1998. Differences in compaction behaviour of three climate classes of snow. *Annals of Glaciology* 26:125–130.

Sturm M., Holmgren J., and Liston G. E. 1995. A seasonal cover classification system for local to global applications. *Journal of Climate* 8:1261–1283.

Sturm S., Kenkmann T., and Hergarten S. 2016. Ejecta thickness and structural rim uplift measurements of Martian impact craters: Implications for the rim formation of complex impact craters. *Journal of Geophysical Research: Planets* 121(6):1026–1053. doi:10.1002/2015JE004959.

Suggs R. M., Moser D. E., Cooke W. J., and Suggs R. J. 2014. The flux of kilogram-sized meteoroids from lunar impact monitoring. *Icarus* 238:23–36. doi:10.1016/j.icarus.2014.04.032.

Szurgot M. 2014. Thermal Properties of Chelyabinsk Meteorite. *Meteoritics & Planetary Science* (77th-Annual Meteoritical Society Meeting, Casablanca, Morocco (abstract #5012)):77:5012id.

Thomas N., Sierks H., Barbieri C., Lamy P. L., Rodrigo R., Rickman H., Koschny D., Keller H. U., Agarwal J., A'Hearn M. F., Angrilli F., Auger A.-T., Barucci M. A., Bertaux J.-L., Bertini I., Besse S., Bodewits D., Cremonese G., Da Deppo V., Davidsson B., Cecco M. de, Debei S., El-Maarry M. R., Ferri F., Fornasier S., Fulle M., Giacomini L., Groussin O., Gutiérrez P. J., Guttler C., Hviid S. F., Ip W.-H., Jorda L., Knollenberg J., Kramm J.-R., Kührt E., Küppers M., La Forgia F., Lara L. M., Lazzarin M., Moreno J. J. L., Magrin S., Marchi S., Marzari F., Massironi M., Michalik H., Moissl R., Mottola S., Naletto G., Oklay N., Pajola M., Pommerol A., Preusker F., Sabau L., Scholten F., Snodgrass C., Tubiana C., Vincent J.-B., and Wenzel K.-P. 2015. The morphological diversity of comet 67P/Churyumov-Gerasimenko. *Science* 347(6220):aaa0440-aaa0440. doi:10.1126/science.aaa0440.

Thompson S. L. 1990. *ANEOS Analytic Equations of State for Shock Physics Codes Input Manual*. SAND89-2951.

Thompson S. L. and Lauson H. S. 1972. Improvements in the Chart D radiation-hydrodynamic code 3:: Revised analytical equations of state (Report SC-RR-71 0714. Sandia National Laboratory, Albuquerque, New Mexico):119.

Thomsen J. M., Austin M. G., Ruhl S. F., Schultz P. H., and Orphal D. L. 1979. Calculational investigation of impact cratering dynamics:: Early time material motions. *Proceedings of the Lunar and Planetary Science Conference* 10:2741–2756.

Tillotson J. H. 1962. *Metallic equation of state for hypervelocity impact*. GA-3216 AD0486711.

Tsujido S., Arakawa M., Suzuki A. I., and Yasui M. 2015. Ejecta velocity distribution of impact craters formed on quartz sand: Effect of projectile density on crater scaling law. *Icarus* 262:79–92. doi:10.1016/j.icarus.2015.08.035.

Turner F. J. and Weiss L. E. 1963. *Structural Analysis of Metamorphic Tectonites*. New York: McGraw-Hill.

Valentine G. A. and Wohletz K. H. 1989. Numerical models of Plinian eruption columns and pyroclastic flows. *Journal of Geophysical Research* 94(B2):1867. doi:10.1029/JB094iB02p01867.

Vervack R. J., Jr., and Melosh H. J. 1992. Wind interaction with falling ejecta Origin of the parabolic features on Venus. *Geophysical Research Letters* 19(6):525–528. doi:10.1029/91GL02812.

Wada K., Senshu H., and Matsui T. 2006. Numerical simulation of impact cratering on granular material. *Icarus* 180(2):528–545. doi:10.1016/j.icarus.2005.10.002.

Wänke H., Brückner J., Dreibus G., Rieder R., and Ryabchikov I. 2001. Chemical Composition of Rocks and Soils at the Pathfinder Site. *Space Science Reviews* 96(1/4):317–330. doi:10.1023/A:1011961725645.

Wegener A. 1921. *Die Entstehung der Mondkrater*. Braunschweig, Germany: Friedr. Vieweg & Sohn.

Winkler R., Poelchau M. H., Moser S., and Kenkmann T. 2016. Subsurface deformation in hypervelocity cratering experiments into high-porosity tuffs. *Meteoritics & Planetary Science* 51(10):1849–1870. doi:10.1111/maps.12694.

Wood C. A., Lorenz R., Kirk R., Lopes R., Mitchell K., and Stofan E. 2010. Impact craters on Titan. *Icarus* 206(1):334–344. doi:10.1016/j.icarus.2009.08.021.

Wünnemann K., Collins G. S., and Melosh H. J. 2006. A strain-based porosity model for use in hydrocode simulations of impacts and implications for transient crater growth in porous targets. *Icarus* 180(2):514–527. doi:10.1016/j.icarus.2005.10.013.

Wünnemann K., Collins G. S., and Osinski G. R. 2008. Numerical modelling of impact melt production in porous rocks. *Earth and Planetary Science Letters* 269(3-4):530–539. doi:10.1016/j.epsl.2008.03.007.

Wünnemann K. and Ivanov B. A. 2003. Numerical modelling of the impact crater depth–diameter dependence in an acoustically fluidized target.

Planetary and Space Science 51(13):831–845. doi:10.1016/j.pss.2003.08.001.

Wünnemann K. and Lange M. A. 2002. Numerical modeling of impact-induced modifications of the deep-sea floor. *Deep Sea Research Part II: Topical Studies in Oceanography* 49(6):969–981. doi:10.1016/S0967-0645(01)00148-5.

Wünnemann K., Morgan J. V., and Jödicke H. 2005. Is Ries crater typical for its size? An analysis based upon old and new geophysical data and numerical modeling. In *Large Meteorite Impacts III*, edited by Kenkmann T., Hörz F., and Deutsch A. pp. 67–83.

Wünnemann K., Nowka D., Collins G. S., Elbeshausen D., and Bierhaus M. 2011. Scaling of impact crater formation on planetary surfaces – insights from numerical modelling. *Proceedings of the Hypervelocity Impact Symposium* 11:1–16.

Wünnemann K., Zhu M.-H., and Stöffler D. 2016. Impacts into Quartz Sand: Crater Formation, Shock Metamorphism, and Ejecta Distribution in Laboratory Experiments and Numerical Models. *Meteoritics & Planetary Science* (in press).

Yamamoto S., Hasegawa S., Suzuki A. I., and Matsunaga T. 2017. Impact velocity dependence of transient cratering growth. *Journal of Geophysical Research: Planets* 122(5):1077–1089. doi:10.1002/2016JE005252.

Yanagisawa M. and Kisaichi N. 2002. Lightcurves of 1999 Leonid Impact Flashes on the Moon. *Icarus* 159(1):31–38. doi:10.1006/icar.2002.6931.

Yoshikawa M., Kawaguchi J., Fujiwara A., and Tsuchiyama A. 2015. Hayabusa Sample Return Mission. In *Asteroids IV*, edited by Michel P., DeMeo F. E., and Bottke W. F. University of Arizona Press.

Zahnle K. J. 1990. Atmospheric chemistry by large impacts. In *Global Catastrophes in Earth History; An Interdisciplinary Conference on Impacts, Volcanism, and Mass Mortality*, edited by Sharpton V. L. and Ward, Peter, D. Geological Society of America. pp. 271–288.

Zel′dovich J. B. and Raizer J. P., editors. 2002. *Physics of shock waves and high-temperature hydrodynamic phenomena*. Mineola, NY: Dover Publ. 916 p.

Zhu M.-H., Wünnemann K., and Artemieva N. A. 2017. Effects of Moon's Thermal State on the Impact Basin Ejecta Distribution. *Geophysical Research Letters* 44(22):11. doi:10.1002/2017GL075405.

Zhu M.-H., Wünnemann K., and Potter R. W. K. 2015. Numerical modeling of the ejecta distribution and formation of the Orientale basin on the Moon. *Journal of Geophysical Research: Planets* 120(12):2118–2134. doi:10.1002/2015JE004827.

Zwiessler R., Kenkmann T., Poelchau M. H., Nau S., and Hess S. 2016. High Strain Rate response testing with the Split-Hopkinson-Pressure bar technique. *Meteoritics & Planetary Science* 51(79th Annual Meeting of the Meteoritical Society August 7-12, 2016, #6276).

Zwiessler R., Kenkmann T., Poelchau M. H., Nau S., and Hess S. 2017. On the use of a split Hopkinson pressure bar in structural geology: High strain rate deformation of Seeberger sandstone and Carrara marble under uniaxial compression. *Journal of Structural Geology* 97:225–236. doi:10.1016/j.jsg.2017.03.007.

12 Appendix

12.1 Publications at scientific conferences and workshops related to this thesis

Luther R., Wünnemann K. (2018), *Influence of Target Properties on Ejecta Scaling Relationshships* (abstract), European Planetary Science Congress, 16.-21. September, 2018 in Berlin, Germany. id.EPSC2018-139.

Kenkmann, T., Winkler R., Poelchau M. H., Wirth R., **Luther R.**, Schaefer F. (2018), *Impact-Induced Twinning in Calcite as Revealed by MEMIN Experiments with Marble* (abstract), 81. Annual Meeting of the Meteoritical Society, 22.-27. August, 2018 in Moscow, Russia. LPI Contribution No. 2067, S.6147.

Luther R., Artemieva N., Wünnemann K. (2017), *Simulation of ejecta-atmosphere interaction* (abstract), European Planetary Science Congress, 17.-22. September, 2017 in Riga, Latvia. id.EPSC2017-182.

Engelmann J., Wünnemann K., **Luther R.**, Zhu M.-H.., (2017), *Quantification of shock-induced melting and its distribution in the Ejecta* (abstract), European Planetary Science Congress, 17.-22. September, 2017 in Riga, Latvia. id.EPSC2017-251.

Luther R., Artemieva N., Collins G. S., Wünnemann K., (2017), *On the deposition of impact ejecta: influences by target properties and atmospheric interaction* (abstract), 77. Jahrestagung der Deutschen Geophysikalischen Gesellschaft, 27.-30. March, 2017 in Potsdam, Germany.

Luther R., Prieur N. C., Wünnemann K., Werner S. C. (2017), *Crater Formation and Shock Melt Production for the 17th March 2013 Lunar Impact Flash Event* (abstract), 48. Lunar and Planetary Science Conference, 20.-24. March, 2017 in The Woodlands, USA. LPI Contribution No. 1964, S.3012.

Luther R., Artemieva N., Collins G. S., Wünnemann K., (2017), *Impact Ejecta Mechanics: Influence of Target Properties and Atmospheric Interaction on Ejecta Deposition* (abstract), 48. Lunar and Planetary Science Conference, held March 20-24, 2017 at The Woodlands, USA. LPI Contribution No. 1964, S.1942.

Wünnemann K., Engelmann J., **Luther R.**, Hamann C., (2017), *Impact-Induced Shock Melting and Ejection of Material in an Asteroidal Environment – Implications for the Deficit in Melt Agglutinates in Itokawa Samples* (abstract), 48. Lunar and Planetary Science Conference, 20.-24. March, 2017 in The Woodlands, USA. LPI Contribution No. 1964, p.2023.

Luther R., Wünnemann K., (2017), *Numerical simulation of impact cratering events: What is the fate of the ejected material?* (abstract), 2nd Leibniz MMS Days, 22.-24. February, 2017 in Hannover, Germany.

Luther R., Prieur N.C., Tasdelen E.,Wünnemann K., Werner S. C. (2016), *Shock melting, crater formation, and ejecta distribution in the 17th March 2013 Lunar Impact Event* (abstract), 79. Annual Meeting of the Meteoritical Society, 7.-12. August, 2016 in Berlin, Germany. LPI Contribution No. 1921, S.6494.

Luther R., Zhu M.-H.,Wünnemann K., Artemieva N. (2016), *Impact Eject Mechanics: Atmospheric Interaction and Fragment-Size Distribution from Numerical Modeling* (abstract), 47. Lunar and Planetary Science Conference, 21.-25. March, 2016 in The Woodlands, USA. LPI Contribution No. 1903, S.1950.

Stickle A. M., Barnouin O. S., Bruck S. M., Cheng A., El Mir C., Ernst C. M., Michel P., Oklay N., Owen M., Price M., Rainey E. S. G., Ramesh K. T., Schwartz S. R., Vincent J., Wünnemann K., **AIDA Impact Simulation Working Group** (2016), *Impact Simulation Benchmarking for the Double Asteroid Redirect Test (DART)* (abstract), 47. Lunar and Planetary Science Conference, 21.-25. March, 2016 in The Woodlands, USA. LPI Contribution No. 1903, S.2832.

Luther R., Yener A., Wünnemann K. (2015), *Production of Climatically Active Gases during the Chicxulub Impact Event* (abstract), GeoBerlin – Dynamic Earth from Alfred Wegener to today and beyond, 4.-7. October, 2015 in Berlin, Germany. Annual Meeting of DGGV and DMG. DOI: http://doi.org/10.2312/GFZ.LIS.2015.003.

Luther R., Lukashin A., Artemieva N., Shuvalov V., Wünnemann K. (2015), Snow Funnel Creation due to Chelyabinsk Meteorite Fragments (abstract), GeoBerlin – Dynamic Earth from Alfred Wegener to today and beyond, 4.-7. October, 2015 in Berlin, Germany. Annual Meeting of DGGV and DMG. DOI: http://doi.org/10.2312/GFZ.LIS.2015.003.

Luther R., Wünnemann K., Artemieva N. (2015), Numerical Simulation of Non-ballistic Ejection Processes as a Function of Material Properties (abstract), Bridging the Gap III: Impact Cratering in Nature, Experiments, and Modelling, 21.-26. September, 2015 in Freiburg, Germany. LPI Contribution No. 1861, S.1068.

Luther R., Lukashin A., Artemieva N., Shuvalov V., Wünnemann K. (2015), *Snow Compaction during the Chelyabinsk Meteorite Fall* (abstract), 46. Lunar and Planetary Science Conference, 16.-20. March, 2015 in The Woodlands, USA. LPI Contribution No. 1832, S.1724.

Güldemeister N., **Luther R.**, Wünnemann K. (2014), Numerical modeling of seismic signals generated by hypervelocity impacts in comparison to experiments on the laboratory scale (abstract), GeoFrankfurt – Earth System Dynamics, 21.-24. September, 2014 in Frankfurt, Germany. SDGG 85 (2014).

Lukashin A., **Luther R.**, Artemieva N., Shuvalov V., Wünnemann K. (2014), Thermal History of Small Fragments During the Chelyabinsk Meteorite Fall (abstract), 77. Annual Meeting of the Meteoritical Society, 7.-12. September, 2014 in Casablanca, Marokko. LPI Contribution No. 1800, id.5156, Meteoritics & Planetary Science 49, A244, Special Issue, September 2014.

Eidesstattliche Erklärung

Hiermit erkläre ich, dass ich die vorliegende Dissertation mit dem Titel

Numerical Modelling of Impact Crater Formation: Material Excavation and Interaction between Ejecta and Atmosphere

selbstständig verfasst und angefertigt habe und keine anderen als die angegebenen Quellen und Hilfsmittel verwendet habe. Geistiges Eigentum anderer Autoren wurde als solches gekennzeichnet.
Des Weiteren versichere ich, dass ich an keiner anderen Stelle ein Prüfungsverfahren beantragt bzw. die Dissertation in dieser oder anderer Form an keiner anderen Fakultät als Dissertation vorgelegt habe.

Ort, Datum Unterschrift

Lebenslauf

Der Lebenslauf ist nur in der Gutachterversion enthalten.

Danksagung

Vor fünf Jahren begann dieses Abenteuer durch eine weitergeleitete E-Mail mit Hinweis auf eine Stelle am Naturkundemuseum zu Berlin (Danke Jürgen Oberst!). Kurzentschlossen bewarb ich mich knapp vor Bewerbungsschluss auf diese Reise ins Ungewisse, die mir tiefe Einblicke in die Welt der Asteroideneischläge, aber auch in die Welt der Programmierung und der *segmentation faults***,** bringen sollte. Ohne den Ansatz „das wird schon klappen, wenn du dich reinkniest“, hätte ich aus diesem Zug sehr früh aussteigen müssen; und natürlich, wenn ich nicht solch unglaublich starke Unterstützung gehabt hätte.

Kai Wünnemann: Dir danke ich, dass du mich damals als Bewerber ausgesucht und mir einen so einmaligen Arbeitsplatz in historischem Gemäuer (fast) zwischen den Füßen solch alter Titanen (Brachiosaurus brancai, oder doch Giraffatitan?) gegeben hast. Zusammen haben wir über urkomisch eingestellte Modelle gelacht, die nie ein Rechner zu simulieren wagte. Ohne deine vielen Erklärungen und Rückfragen hätte ich nicht einmal die Hälfte dessen erreicht, was auf den 300 vorigen Seiten steht, bzw. sich mir im Kopf eingeprägt hat. Zusammen sind wir nach Houston, Oslo, oder Freiburg gefahren, wo du mir spannende Kollegen vorgestellt hast. Du hattest immer ein offenes Ohr für alle Probleme. Ich danke dir von ganzem Herzen!

Natasha Artemieva: Dir danke ich aufrichtig für all die Unterstützung, ohne die unsere Staubpartikel nicht annähernd so schön chaotisch durch die Modelle wabern würden, wie sie es letztendlich tun. Du hast die Geduld aufgebracht, mir auf dem langen Programmierweg zur Seite zu stehen und all die Fragen, die unweigerlich kommen mussten, auszuhalten. So manche ungeplante Modellexplosion schien unentwegt erneut Programmierfortschritte in Frage zu stellen. Doch am Ende kamen wir zu einer Lösung. Und auch wenn es einmal nicht um Staub und Winde, sondern um Materiezustände verpackt in Fortran 77 ging, warst du mit deinem Wissen und deiner langjährigen Erfahrung für einen Rat zur Stelle. Einen ganz besonderen und vor allem herzlichen Dank an dich!

Lena Noack: Danke, dass du die Co-Betreuung, das Gutachten und den Vizevorsitz der Kommission übernimmst.

Gareth S. Collins und Menghua „Peter“ Zhu: Euch danke ich für die vielen fruchtvollen Diskussionen über Auswurfmassen und die richtigen Kriterien, um diese zu bestimmen. Zwei Punkte oder drei, ein Radius Höhe oder mehr, das waren unsere Fragen. Gareth, dir danke ich auch für die großartige Unterstützung bei Problemen atmosphärischer Stabilität bei iSALE, welche meine Staubteilchen hart durchgeschüttelt hätten.

Tom Davison und Dirk Elbeshausen: Euch danke ich, dass ihr so hervorragende Routinen entwickelt habt, ohne die keines der Modelle so schön anzusehen und zu erfahren wäre. Ohne ViMoD gelang keine Einschätzung der Modellqualität, und ohne pySALEPlot wären die Daten immer noch komprimiert auf einer verborgenen Festplatte.

Danke an die MEMIN Gruppe und an alle Co-Autoren für die großartige Arbeit. Insbesondere danke ich den Mit-Doktoranden Rebecca Winkler, Christopher Hamann, Matthias Ebert, Jakob Wilk, Nils C. Prieur und Sabina Raducan sowie Thomas Kenkmann, Michael Poelchau und Stephanie Werner für die gute Zusammenarbeit, die Diskussionen, und die tollen Momente. Die Besuche in Freiburg (Danke Rebecca, Matthias, Thomas und Michael) und in Oslo (Danke an Nils, Stephanie und Tobias Rolf) waren für mich eine große Bereicherung.

Nicole Güldemeister und Michael Bierhaus: Euch danke ich alleine schon dafür, dass ihr mir im ersten Monat noch so viele Informationen mitgegeben habt, dass ich die Zeit danach in eurer Abwesenheit meistern konnte. Ohne diese Starthilfe wäre der Anfang schwer geworden. Darüber hinaus danke ich allen Kollegen aus der Arbeitsgruppe für die tolle Zeit, in der immer eine gute Grundstimmung herrschte. Danke an die neueren MfN-iSALEr Lukas Manske, Tomke Fröchtenicht (inzwischen Lompa) und Elena Martellato, die wahren Geologen/Geochemiker/Mineralogen Christopher, Lutz Hecht, Astrid Kowitz, Matthias, Felix Kaufmann, Ulli Raschke, Patrice Zaag, Sanni Siegert, Tanja Mohr-Westheide und Marie Hofmann, den einstigen Chef W. Uwe Reimold, dem ich im Ries meine Unwissenheit in Bezug auf Steine (verpackt in schönen Fragen) darstellte, an Dieter Stöffler

für die weitergegebenen Erfahrungen, an die Kuratoren im Team Ralf-Thomas Schmitt und Ansgar Greshake, an Friederike Schwarz und Rita Schmidt im Sekretariat, ohne die kein „Verwaltungsakt“ funktionieren (oder verstanden werden) könnte, und ganz klar an Sebastian Block, der von mir nie verschont wurde, wenn der Cluster mal nicht erreichbar war, Linux nicht mit Windows sprach, Word nicht mit OpenOffice konnte, oder der Rechner nicht mehr wollte. Danke euch allen.

Natürlich danke ich meiner Lebensgefährtin, meinen Kindern, meinen Eltern und Großeltern - meiner Familie, die mir eine ständige Stütze war, mir über schwierige Strecken hinweggeholfen hat und mich immer weiter motiviert und an mich geglaubt hat, auch wenn die Fortschritte ins Stocken kamen. Außerdem danke ich euch für das zugewandte Zuhören bei komplizierten Programmier- sowie physikalischen Fragen von denen inhaltlich nicht immer alles leicht zu verstehen war! Lola, Leonardo, Ludovico, diese Aufgabe ist vollbracht. Einen riesen Dank an euch!